University of Alberta

New Ternary Rare-Earth Antimonides and Germanides:
Bonding, Structures, and Physical Properties

by

Haiying Bie

A thesis submitted to the Faculty of Graduate Studies and Research
in partial fulfillment of the requirements for the degree of

Doctor of Philosophy

Department of Chemistry

Fall, 2009
Edmonton, Alberta

Examining Committee

Prof. Arthur Mar, Chemistry

Prof. Josef Takats, Chemistry

Prof. Jonathan G. C. Veinot, Chemistry

Prof. Mariusz Klobukowski, Chemistry

Prof. Douglas Ivey, Chemical and Materials Engineering

Prof. Holger Kleinke, Chemistry, University of Waterloo

In memory of my dearest father

Abstract

This thesis focuses on the synthesis, structures, and physical properties of ternary rare-earth antimonides and germanides. These ternary compounds exhibit diverse polyanionic substructures with classical and non-classical Sb–Sb bonding, Ge–Ge bonding, or both. The Zintl-Klemm concept and band structure calculations were applied to understand their structures and bonding. Electrical resistivities and magnetic properties were measured for these compounds.

The compounds $RE_2Ti_7Sb_{12}$ (*RE* = La–Nd) and $RE_2Ti_{11-x}Sb_{14+x}$ (*RE* = Sm, Gd, Tb, Yb), which were synthesized by arc-melting, adopt different structures depending on the size of the *RE* atoms. Both consist of a complex arrangement of $TiSb_n$ polyhedra, linked to form a 3D framework with large cavities in which the *RE* atoms reside. Hypervalent Sb–Sb bonds are manifested in disordered Sb fragments in $RE_2Ti_7Sb_{12}$, and 1D linear chains, zig-zag chains, and pairs in $RE_2Ti_{11-x}Sb_{14+x}$.

A series of compounds, $RECrGe_3$ (*RE* = La–Nd, Sm), was synthesized by the Sn-flux method. They adopt a hexagonal perovskite structure type, in which chains of face-sharing Cr-centred octahedra are linked by triangular Ge_3 clusters. These unusual single-bonded Ge_3 substructures can be rationalized simply by the Zintl-Klemm concept. Electrical resistivity measurements show metallic behaviour with prominent transitions coincident with ferromagnetic transitions (T_c ranging from 62 to 155 K) found in magnetic measurements. Band structure calculations show the presence of a narrow, partially filled band with high DOS at E_f, in agreement with the observation that $LaCrSb_3$ is an itinerant ferromagnet.

With a different number of d-electrons in the *M* site, the isostructural *RE*VGe_3 compounds exhibit antiferromagnetic behaviour. The doped quaternary compounds $LaCr_{1-x}V_xGe_3$ and $LaCr_{1-x}Mn_xGe_3$ exhibit depressed Curie temperatures.

The structures of *RE*Cr_xGe_2 compounds (*RE* = Sm, Gd–Er) are built up by inserting transition-metal atoms into the square pyramidal sites of a hypothetical "*RE*Ge_2" host structure ($ZrSi_2$-type). The presence of extensive anionic Ge substructures in the form of 1D zigzag chains and 2D square sheets can be explained by the Zintl-Klemm concept. Magnetic measurements indicated antiferromagnetic ordering with low T_N ranging from 3 to 17 K.

Compounds involving a p-block element as the second component were prepared. In $RE_{12}Ge_{7-x}Sb_{21}$ (*RE* = La–Pr), a complex 3D polyanionic framework with Ge pairs, five-atom-wide Sb ribbons, and 2D Ge/Sb layers is present. The bonding exemplifies the competition of valence electron transfer from the *RE* atoms to metalloids with similar electronegativities. Full electron transfer from the *RE* atoms to the anionic substructure cannot be assumed. Magnetic measurements on $Ce_{12}Ge_{6.5}Sb_{21}$ indicate antiferromagnetic coupling. The metal-rich compounds $RE_5Tt_xSb_{3-x}$ (*Tt* = Si, Ge) adopt the orthorhombic β-Yb_5Sb_3-type structure with a range of solid solubility of $0.9 \leq x \leq 1.6$. They are not electron-precise and do not obey the Zintl-Klemm concept.

Acknowledgements

This thesis could not be completed without the help and support of many people and here I acknowledge them deeply.

My deepest gratitude goes first and foremost to my supervisor, Prof. Arthur Mar for his guidance and encouragement over the years. He provided an excellent research environment where I can try out all of my ideas, gave me precious suggestions with his rich chemistry and crystallography knowledge, and created opportunities for me to learn more techniques. He taught me not only chemistry but also English and I thank you, Arthur, for correcting my writing all the time.

I'm extremely grateful to Dr. Mar's previous postdocs, Oksana Zelinska and Andriy Tkachuk, who taught me everything at the very beginning of my research. I also thank all members in the Mar group, who kept me happy everyday. They are the most easy-going labmates I have ever met. I am so glad to work with them. Thanks, Pete, for showing me the cool technique of XPS and helping me collect some XPS spectra. Thanks, Mike, for correcting my strong accent all the time. It's my great pleasure to work with him for his 403 research.

I deeply appreciate the instructions from Dr. Bob Macdonald who taught me how to collect single-crystal X-ray diffraction data. Thanks for giving me many practical opportunities. Thank you for your kindness and patience. In addition, I thank Bob and Mike who collected many diffraction datasets for me very efficiently.

Special thanks are given to my dearest parents for their endless love in my life and encouragement in my studies. Without their support, I would not have finished my Ph.D. studies and make my dreams come true. I wish my dad could have seen this exciting moment of my life. I thank my husband for his particular support and for clearing out all obstacles during my writing.

I thank Prof. Ron Cavell for giving me an opportunity to use HXMA and SGM at the Canadian Light Source. I thank Ms. Christina Barker in the Department of Chemical and Materials Engineering for assistance with the EDX analysis. I thank the General Chemistry lab supervisor, Dr. Norman Gee, who made teaching run efficiently, and the University of Alberta and the Department of Chemistry for allowing me to be a TA and to get financial support over the years. I thank all my committee members Prof. Takats, Prof. Veinot, Prof. Klobukowski, Prof. Ivey, and Prof. Kleinke for serving on my Ph.D. committee and for reading through this thesis.

Finally, I thank many friends who encouraged me and gave me many suggestions, particularly to Yanjie who helped me with many questions I had for band structure calculations. Here, I want to express my greatest appreciation to them and wish them the best.

Table of Contents

Chapter 1. Introduction

1.1. Background.....1

1.1.1. Importance of Intermetallics.....1

1.1.2. Electron Counting Rules.....2

1.1.2.1 Hume-Rothery Phases.....2

1.1.2.2 Zintl-Klemm Concept.....3

1.1.3. Sb substructures.....5

1.1.3.1 Classical Sb–Sb Bonding.....5

1.1.3.2 Non-Classical (Hypervalent) Sb–Sb Bonding.....9

1.1.4. Ge substructures.....17

1.1.4.1 Classical Ge–Ge Bonding.....17

1.1.4.2 Non-Classical (Hypervalent) Ge–Ge Bonding.....18

1.1.5. Research Motivation.....22

1.2. Synthesis.....23

1.3. Characterization.....27

1.3.1. EDX (Energy Dispersive X-ray) Analysis.....27

1.3.2. X-ray Diffraction.....28

1.3.2.1. Powder X-ray Diffraction.....30

1.3.2.1. Single-Crystal X-ray Diffraction.....32

1.4. Band Structure Calculation.....33

1.5. Physical Properties.....35

1.5.1. Electrical Properties.....35

1.5.2. Magnetic Properties.....39

1.5.2.1. Diamagnetism….....41

1.5.2.2. Paramagnetism….....43

1.5.2.3. Pauli Paramagnetism.....44

1.5.2.4. Ferromagnetism (FM)….....45

1.5.2.5. Ferrimagnetism….....46

1.5.2.6. Antiferromagnetism (AFM).....46

1.5.2.7. RKKY Interaction and de Gennes Factor.....47

1.5.2.8. Itinerant d-Electron Magnetism.....48

1.6. Thesis Outline.....49

1.7. References.....50

Chapter 2. Ternary Rare-Earth Titanium Antimonides: Phase Equilibria in the *RE*–Ti–Sb (*RE* = La, Er) Systems and Crystal Structures of $RE_2Ti_7Sb_{12}$ (*RE* = La, Ce, Pr, Nd)

2.1. Introduction….....56

2.2. Experimental Section…….....……..59

2.2.1. Synthesis.....59

2.2.2. Structure Determination.....61

2.3. Results and Discussion.....…….…..….....66

2.3.1. Phase Diagrams.....66

2.3.2. Crystal Structure of $RE_2Ti_7Sb_{12}$.....69

2.3.3. Structural Relationships.....72

2.3.4. Bonding.....75

2.4. Conclusions.....76

2.5. References.....78

Chapter 3. Ternary Rare-Earth Titanium Antimonides $RE_2Ti_{11-x}Sb_{14+x}$ (*RE* = Sm, Gd, Tb, Yb)

3.1. Introduction.....81

3.2. Experimental Section.....84

3.2.1. Synthesis 84

3.2.2. Structure Determination.....86

3.2.3. Electrical Resistivity.....93

3.3. Results and Discussion.....93

3.4. Conclusions.....103

3.5. References.....104

Chapter 4. Structures and Physical Properties of Rare-Earth Chromium Germanides $RECrGe_3$ (*RE* = La–Nd, Sm)

4.1. Introduction.....106

4.2. Experimental Section 107

4.2.1. Synthesis.....107

4.2.2. Structure Determination.....108

4.2.3. Electrical and Magnetic Properties 109

4.2.4. Band Structure Calculation 110

4.3. Results and Discussion.....112

4.3.1. Crystal Structure 112

4.3.2. Physical Properties 115

4.3.3. Electronic Structure 124

4.4. Conclusions.....127

4.5. References.....129

Chapter 5. Structure and Magnetic Properties of Hexagonal Perovskite-type Rare-Earth Vanadium Germanides *RE*VGe_3 (*RE* = La–Nd)

5.1. Introduction.....131

5.2. Experimental Section.....132

5.2.1. Synthesis.....132

5.2.2. Structure Determination 133

5.2.3. Magnetic Measurements.....137

5.2.4. Band Structure Calculation.....137

5.3. Results and Discussion.....137

5.3.1. Structure and Bonding.....137

5.3.2. Magnetic Properties.....140

5.3.3. Electronic Structure.....146

5.4. Conclusions…….....149

5.5. References.....150

Chapter 6. Structure and Magnetic Properties of Rare-Earth Chromium Germanides *RE*Cr_xGe_2 (*RE* = Sm, Gd–Er)

6.1. Introduction.....152

6.2. Experimental Section.....153

6.2.1. Synthesis.....153

6.2.2. Structure Determination.....154

6.2.3. Band Structure Calculation.....155

6.2.4. Magnetic Measurements.....160
6.3. Results and discussion.....160
6.3.1. Crystal Structure.....160
6.3.2. Electronic Structure.....163
6.3.3. Magnetic Properties.....165
6.4. Conclusions.....173
6.5. References.....174

Chapter 7. Ge Pairs and Sb Ribbons in Rare-Earth Germanium Antimonides $RE_{12}Ge_{7-x}Sb_{21}$ (*RE* = La–Pr)

7.1. Introduction.....176
7.2. Experimental Section.....178
7.2.1. Synthesis.....178
7.2.2. Structure Determination.....179
7.2.3. Band Structure Calculation.....185
7.2.4. Magnetic Measurements.....185
7.3. Results and Discussion.....185
7.3.1. Phase Composition.....185
7.3.2. Structure and Bonding.....186
7.3.3. Magnetic Properties.....199
7.4. Conclusions.....201
7.5. References.....203

Chapter 8: Structures and Magnetic Properties of $RE_5Tt_xSb_{3-x}$ (*RE* = La–Nd; *Tt* = Si, Ge)

8.1. Introduction.....205

8.2. Experimental Section.....206

8.2.1. Synthesis.....206

8.2.2. Structure Determination.....208

8.2.3. Band Structure Calculation.....218

8.2.4. Magnetic Measurements.....218

8.3. Results and Discussion.....219

8.3.1. Phase Diagram.....219

8.3.2. Structure and Bonding.....222

8.3.3. Magnetic Properties.....230

8.4. Conclusions.....235

8.5. References.....236

Chapter 9: Conclusions

9.1. Structure and Bonding.....238

9.2. Limits of the Zintl-Klemm Concept.....243

9.3. Physical Properties.....245

9.4. Future Directions.....247

9.5. References.....248

Appendices

Appendix 1: Supplementary Data for Chapter 4 249

Appendix 2: Supplementary Data for Chapter 7.....254

Appendix 3: Supplementary Data for Chapter 8.....257

List of Tables

Table 1–1	Summary of Sb substructures formed by the classical Sb–Sb single bond in A_xSb_y (A = alkali, alkaline earth metals) and their charge assignments.	8
Table 1–2	Summary of Ge substructures formed by the classical Ge–Ge single bond in A_xGe_y (A = alkali, alkaline earth metals) and their charge assignments.	19
Table 1–3	Theoretical effective magnetic moments for the free RE^{3+} ions.	42
Table 2–1	Known ternary rare-earth antimonides in *RE*–*M*–Sb systems (M = transition metal).	58
Table 2–2	Cell parameters for $RE_2Ti_7Sb_{12}$ (RE = La, Ce, Pr, Nd).	61
Table 2–3	Crystallographic data for $La_2Ti_7Sb_{12}$.	63
Table 2–4	Atomic coordinates and equivalent isotropic displacement parameters (Å^2) for $La_2Ti_7Sb_{12}$.	64
Table 2–5	Selected interatomic distances (Å) in $La_2Ti_7Sb_{12}$.	65
Table 3–1	Homoatomic Ti–Ti and Sb–Sb bonds in Ti–Sb binary system.	83
Table 3–2	Crystallographic data for $RE_2Ti_{11-x}Sb_{14+x}$ (RE = Sm, Tb, Yb).	88

Table 3–3	Atomic coordinates and equivalent isotropic displacement parameters ($Å^2$) for $RE_2Ti_{11-x}Sb_{14+x}$ (*RE* = Sm, Tb, Yb).	89
Table 3–4	Selected interatomic distances (Å) in $RE_2Ti_{11-x}Sb_{14+x}$ (*RE* = Sm, Tb, Yb).	91
Table 4–1	Crystallographic data for $RECrGe_3$ (*RE* = La–Nd, Sm).	111
Table 4–2	Atomic coordinates and equivalent isotropic displacement parameters ($Å^2$) for $RECrGe_3$ (*RE* = La–Nd, Sm).	112
Table 4–3	Selected interatomic distances (Å) in $RECrGe_3$ (*RE* = La–Nd, Sm).	112
Table 4–4	Summary of resistivity and magnetism data for $RECrGe_3$ (*RE* = La–Nd, Sm).	116
Table 5–1	Crystallographic data for $REVGe_3$ (*RE* = La–Nd).	134
Table 5–2	Atomic coordinates and isotropic displacement parameters ($Å^2$) for $REVGe_3$ (*RE* = La–Nd).	135
Table 5–3	Selected interatomic distances (Å) in $REVGe_3$ (*RE* = La–Nd).	135
Table 5–4	Hexagonal unit cell parameters for $LaV_{1-x}Cr_xGe_3$ and $LaCr_{1-x}Mn_xGe_3$ compounds.	141
Table 5–5	Summary of magnetic data for $REVGe_3$ (*RE* = Ce–Nd).	143
Table 6–1	Crystallographic data for $RECr_xGe_2$ (*RE* = Sm, Gd–Er).	157

Table 6–2	Atomic coordinates and equivalent isotropic displacement parameters ($Å^2$) for $RECr_xGe_2$ (RE = Sm, Gd–Er).	158
Table 6–3	Selected interatomic distances (Å) in $RECr_xGe_2$ (RE = Sm, Gd–Er).	159
Table 6–4	Summary of magnetic data for $RECr_{0.3}Ge_2$ (RE = Gd–Er).	168
Table 7–1	Crystallographic data for $RE_{12}Ge_{7-x}Sb_{21}$ (RE = La–Pr).	182
Table 7–2	Atomic coordinates and equivalent isotropic displacement parameters ($Å^2$) for $RE_{12}Ge_{7-x}Sb_{21}$ (RE = La–Pr).	183
Table 7–3	Selected interatomic distances (Å) in $RE_{12}Ge_{7-x}Sb_{21}$ (RE = La–Pr).	184
Table 8–1	Atomic compositions (%) determined from X-ray diffraction data and electron probe microanalysis data for $RE_5Tt_xSb_{3-x}$ (RE = La–Nd; Tt = Si, Ge).	207
Table 8–2	Crystallographic data for $RE_5Tt_xSb_{3-x}$ (RE = La–Nd; Tt = Si, Ge).	211
Table 8–3	Atomic coordinates and equivalent isotropic displacement parameters ($Å^2$) for $RE_5Tt_xSb_{3-x}$ (RE = La–Nd; Tt = Si, Ge).	213
Table 8–4	Ranges of interatomic distances (Å) in $RE_5Tt_xSb_{3-x}$ (RE = La–Nd; Tt = Si, Ge).	216
Table 8–5	Average integrated crystal orbital Hamilton population (–ICOHP) (eV $bond^{-1}$) in different models for $La_5Ge_xSb_{3-x}$.	230

Table 8–6	Summary of magnetic data for $RE_5Tt_xSb_{3-x}$ (*RE* = Pr, Nd; *Tt* = Si, Ge).	231
Table 9–1	Summary of the bonding characters of all compounds synthesized in this thesis.	239
Table A1–1	Crystallographic data for $RECrGe_3$ (*RE* = La–Nd, Sm) from Rietveld refinements on arc-melted samples.	251
Table A2–1	Crystallographic data for $Pr_{12}Ge_{6.48(1)}Sb_{21}$ refined in space group *Imm2*.	254
Table A2–2	Atomic coordinates and equivalent isotropic thermal displacement parameters for $Pr_{12}Ge_{6.48(1)}Sb_{21}$ refined in space group *Imm2*.	255
Table A3–1	Synthesis and cell parameters of $La_5Ge_xSb_{3-x}$ phases.	257
Table A3–2	Interatomic distances (Å) in $RE_5Tt_xSb_{3-x}$ (*RE* = La–Nd; *Tt* = Si, Ge).	258

List of Figures

Figure 1–1	The relative location of polar intermetallic phases in terms of electronegativity difference.	4
Figure 1–2	The formed Sb substructures by classical Sb–Sb single bond in A_xSb_y binaries.	7
Figure 1–3	The Lewis structure and simple MO diagram for Sb_3^{7-}.	11
Figure 1–4	The Sb substructures formed by non-classical Sb–Sb bonding.	12
Figure 1–5	Crystal structures of: (a) $YbSb_2$ showing zig-zag chains and 2D sheets; (b) $RESb_2$ showing reduced Sb pairs and 2D sheets viewed along the *a* axis. The blue and red spheres are *RE* and Sb atoms, respectively.	14
Figure 1–6	Crystal structure of $Gd_6Ge_{5-x}Sb_{11+x}$ (x = 0.67) viewed along the *a* direction. The blue, green, and red spheres are Gd, Ge, and Sb atoms, respectively.	15
Figure 1–7	Crystal structure of Ce_2GeSb_3 showing zig-zag chains and Ge/Sb sheets viewed along the *c* axis. The blue, green, and red spheres are Ce, Ge, and Sb atoms, respectively.	16
Figure 1–8	The Ge substructures formed by Ge–Ge single bonds in A_xGe_y Zintl binaries.	20
Figure 1–9	Crystal structure of REM_xGe_2 viewed along the *a* axis. The blue, green, and red spheres are *RE*, *M*, and Ge	21

atoms, respectively.

Figure 1–10 The arc melters in our lab used for the arc-melting: (a) Centorr 5TA tri-arc melter; b) Edmund Bühler arc melter. 25

Figure 1–11 The reaction tubes for direct reaction: (a) fused silica tube; (b) alumina tube. 25

Figure 1–12 The principle of EDX analysis. 28

Figure 1–13 The constructive interference to satisfy the Bragg law. 30

Figure 1–14 The setup of four-probe arrangement of resistivity measurement. 36

Figure 1–15 The resistivity (ρ) changes as a function of temperature (*T*) in: (a) metal; (b) semiconductor or insulator; (c) superconductor. 37

Figure 1–16 (a) The magnetic spin arrangements; (b) the temperature dependence of susceptibility; and (c) the temperature dependence of the inverse susceptibility (satisfying the Curie or Curie-Weiss law) in paramagnetic (PM), ferromagnetic (FM), and antiferromagnetic (AFM) materials. 43

Figure 1–17 Schematic band structure for a Pauli paramagnet: (a) spin-up and spin-down initial state; (b) non-equilibrium state in the presence of a magnetic field; (c) equilibrium state. 45

Figure 1–18	Schematic band structure for an itinerant ferromagnet according to Stoner theory: (a) nonmagnetic state; (b) magnetic state.	49
Figure 2–1	Isothermal sections at 800 ºC of the La–Ti–Sb and Er–Ti–Sb phase diagram.	67
Figure 2–2	The powder X-ray diffraction pattern containing binary TiSb (red lines) and ternary $La_2Ti_7Sb_{12}$ (blue lines) phases.	69
Figure 2–3	Structure of $La_2Ti_7Sb_{12}$ viewed down the *c* direction. The blue, green, and red spheres are La, Ti, and Sb atoms, respectively.	73
Figure 2–4	The 2D Ti layers by Ti–Ti bonding in $La_2Ti_7Sb_{12}$ viewed along the *c* axis.	73
Figure 2–5	One possible local ordering of the partially occupied Sb sites (0.50 for Sb2 and Sb3; 0.25 for Sb5 and Sb6) within an edge-sharing chain of Ti1-centred octahedra extended along the *c* direction in $La_2Ti_7Sb_{12}$.	74
Figure 2–6	Comparison of the structures of (a) $NdTi_3(Sn_xSb_{1-x})_4$, (b) $La_2Ti_7Sb_{12}$, and (c) La_3TiSb_5. Face-sharing Ti-centred octahedra are shown as ball-and-stick representations, and corner-sharing (or isolated) octahedra as polyhedral representations.	75
Figure 3–1	The powder X-ray diffraction pattern showing the $Sm_2Ti_{11}Sb_{14}$ phase (blue lines) and Sm_3TiSb_5 phase	85

(red lines).

Figure 3–2 Structure of $RE_2Ti_{11-x}Sb_{14+x}$ (*RE* = Sm, Tb, Yb) viewed down the *b* direction, emphasizing the Ti–Sb framework. In the split sites Sb5/Sb6 and Sb7/Sb8, only one member of each set is shown. The blue, green, and red spheres are *RE*, Ti, and Sb atoms, respectively. Ti5 atom is shown in purple. 95

Figure 3–3 Chains of Ti-centred pentagonal bipyramids or octahedra extending down the *b* direction, with possible local orderings of the split Sb sites (Sb5/Sb6 and Sb7/Sb8) and half-occupied Ti5 site. 97

Figure 3–4 Monocapped square antiprismatic coordination around *RE* atom in $RE_2Ti_{11-x}Sb_{14+x}$ (*RE* = Sm, Tb, Yb). Distances shown (in Å) are for $Sm_2Ti_{11}Sb_{14}$. 98

Figure 3–5 Structure of $RE_2Ti_{11-x}Sb_{14+x}$ (*RE* = Sm, Tb, Yb) in terms of two-dimensional slabs alternately stacked along the *c* direction consisting of (i) Ti3-centred octahedra (yellow) and *RE*-centred monocapped square antiprisms (magenta) (at z = 0, ½) or (ii) Ti1- and Ti2-centred pentagonal bipyramids (cyan) (at z = ¼, ¾). Remaining voids are filled by Ti4 and Ti5 atoms. 98

Figure 3–6 The Sb substructures in $Sm_2Ti_{11}Sb_{14}$: zig-zag chains, 1D linear chains, and pairs. 102

Figure 3–7 Electrical resistivity of single crystals of $Sm_2Ti_{11}Sb_{14}$ and $Yb_2Ti_{10.6}Sb_{14.4}$. 102

Figure 4–1	Structure of *RE*$CrGe_3$ (*RE* = La–Nd, Sm) viewed down the *c*-direction showing the chains of face-sharing $CrGe_6$ octahedra and anticuboctahedral geometry of rare-earth atoms. The blue, green, and red spheres represent *RE*, Cr, and Ge atoms, respectively.	114
Figure 4–2	$LaCrGe_3$: (a) electrical resistivity, (b) field-cooled (fc) and zero-field-cooled (zfc) dc magnetic susceptibility (inset: inverse susceptibility plot), and (c) isothermal magnetization at 2 and 300 K.	118
Figure 4–3	$CeCrGe_3$: (a) electrical resistivity, (b) field-cooled (fc) and zero-field-cooled (zfc) dc magnetic susceptibility (inset: inverse susceptibility plot), and (c) isothermal magnetization at 2 and 300 K.	119
Figure 4–4	$PrCrGe_3$: (a) electrical resistivity, (b) field-cooled (fc) and zero-field-cooled (zfc) dc magnetic susceptibility (inset: inverse susceptibility plot), and (c) isothermal magnetization at 2 and 300 K.	121
Figure 4–5	$NdCrGe_3$: (a) electrical resistivity, (b) field-cooled (fc) and zero-field-cooled (zfc) dc magnetic susceptibility (inset: inverse susceptibility plot), and (c) isothermal magnetization at various temperatures.	122
Figure 4–6	$SmCrGe_3$: (a) field-cooled (fc) and zero-field-cooled (zfc) dc magnetic susceptibility (inset: inverse susceptibility plot), and (b) isothermal magnetization at various temperatures.	123

Figure 4–7 Magnetic ordering temperatures for *RE*$CrGe_3$ plotted versus the de Gennes factor. 124

Figure 4–8 (a) Total density of states (DOS) for non-spin-polarized $LaCrGe_3$ and its (b) La, (c) Cr, and (d) Ge contributions. The dashed curve in (c) indicates the contribution of 3d states to the Cr partial DOS. The Fermi level is marked by a horizontal line at 0 eV. 125

Figure 4–9 Crystal orbital Hamilton population (COHP) curves (solid line) and integrated COHP curves (dotted line) for (a) Cr–Ge, (b) Ge–Ge, and (c) Cr–Cr contacts in non-spin-polarized $LaCrGe_3$. The Fermi level is marked by a horizontal line at 0 eV. 125

Figure 4–10 Total density of states for spin-polarized $LaCrGe_3$. The Fermi level is marked by a horizontal line at 0 eV. 127

Figure 5–1 Rietveld refinement results for *RE*VGe_3 (*RE* = La-Nd). The observed profile is indicated by red circles and the calculated profile by the black solid lines. Bragg peak positions are located by the vertical green tick marks. (The second set of tick marks corresponds to trace amounts of $LaGe_{2-x}$ present in $LaVGe_3$.) The difference plot is shown at the bottom in blue. 136

Figure 5–2 Structure of *RE*VGe_3 (*RE* = La–Nd) viewed down the *c* direction, emphasizing the V–Ge framework. The octahedral coordination around V atoms and the anticuboctahedral coordination around *RE* atoms are also highlighted. The blue, green, and red spheres are 139

RE, V, and Ge atoms, respectively.

Figure 5–3 Plots of hexagonal cell parameters and *c/a* ratio vs *x* for two series of solid solutions, $LaV_{1-x}Cr_xGe_3$ and $LaCr_{1-x}Mn_xGe_3$. 142

Figure 5–4 The dc magnetic susceptibility plots for $LaV_{1-x}Cr_xGe_3$ and $LaCr_{1-x}Mn_xGe_3$. 142

Figure 5–5 Magnetic data for (a)–(b) $CeVGe_3$, (c)–(d) $PrVGe_3$, and (e)–(f) $NdVGe_3$. The left panels show the zero-field-cooled dc magnetic susceptibility and its inverse as a function of temperature (with the insets highlighting low-temperature transitions in the ac magnetic susceptibility), and the right panels show isothermal magnetization curves at various temperatures. 144

Figure 5–6 (a) Total density of states (DOS) and its La, V, and Ge projections in $LaVGe_3$. (b) Crystal orbital Hamilton populations (COHP) curves (solid lines) and integrated COHP curves (dashed lines) for V–Ge, Ge–Ge, and V–V contacts in $LaVGe_3$. The horizontal lines at 0 eV mark the Fermi level. 147

Figure 6–1 Rietveld refinement results for $RECr_{0.3}Ge_2$ (*RE* = (a) Tb, (b) Ho, (c) Er). The observed profile is indicated by red circles and the calculated profile by the black line. Bragg peak positions are located by the vertical tick green marks. The difference plot is shown at the bottom by blue lines. 156

Figure 6–2 Plot of cell parameters vs. x for $CeNiSi_2$-type phase observed in reactions with nominal composition of $DyCr_xGe_2$. 161

Figure 6–3 Average structure of $RECr_xGe_2$ (RE = Sm, Gd–Er) viewed down the c-direction, and an excised $[Cr_xGe_2]$ slab viewed down the b-direction. The large blue spheres are RE atoms, the green spheres are Cr atoms, and the red spheres are Ge atoms. 163

Figure 6–4 (a) Total density of states (DOS) for Y_4CrGe_8 and its Y, Cr, and Ge contributions; (b) Crystal orbital Hamilton population (COHP) curves for Ge1–Ge1 contacts in the zig-zag chains, Ge2–Ge2 interactions in the square sheets, and Cr–Ge contacts in the square pyramidal geometry. The Fermi level is marked by a horizontal line at 0 eV. 165

Figure 6–5 Magnetic data for $RECr_{0.3}Ge_2$ (RE = Gd–Er). The left panels show the zero-field-cooled dc magnetic susceptibility and its inverse as a function of temperature (with the insets highlighting low-temperature transitions in the ac magnetic susceptibility), and the right panels show isothermal magnetization curves at various temperatures. 167

Figure 6–6 Zero-field-cooled dc magnetic susceptibility for several members of $DyCr_xGe_2$ (x = 0.25, 0.35, 0.45). The inset highlights the low-temperature transitions. 170

Figure 6–7 The RE arrangements in $RECr_xGe_2$. 172

Figure 6–8	Magnetic ordering temperatures for $RECr_{0.3}Ge_2$ plotted vs the de Gennes factor.	172
Figure 7–1	Structure of $RE_{12}Ge_{7-x}Sb_{21}$ (RE = La–Pr) viewed down the a direction. The blue spheres are RE atoms, the green spheres are Ge atoms, and the red spheres are Sb atoms. The solid lines between RE atoms outline the RE_6 trigonal prisms. The Ge3 site is only half-occupied.	188
Figure 7–2	Deconstruction of the polyanionic network in $RE_{12}Ge_{7-x}Sb_{21}$ (RE = La–Pr) built up of ribbons containing Ge and Sb atoms extending along the a direction. The interatomic distances shown (in Å) here are for $Pr_{12}Ge_{6.5}Sb_{21}$.	189
Figure 7–3	Coordination environments around the Ge atoms in $RE_{12}Ge_{7-x}Sb_{21}$ (RE = La–Pr).	191
Figure 7–4	Coordination environments around the RE atoms in $RE_{12}Ge_{7-x}Sb_{21}$ (RE = La–Pr). Here $Pr_{12}Ge_{7-x}Sb_{21}$ is shown as an example.	193
Figure 7–5	Derivation of $RE_{12}Ge_{7-x}Sb_{21}$ from the structures of $RE_6Ge_{5-x}Sb_{11+x}$ and $RE_{12}Ga_4Sb_{23}$, viewed in projection down the shortest cell axis. The large lightly shaded circles are RE atoms, the small solid circles are Ge or Ga atoms, and the medium open circles are Sb atoms. Circles with thicker rims indicate atoms located in planes displaced by half the short axis parameter.	195
Figure 7–6	Total density of states (DOS) for $La_{12}Ge_7Sb_{21}$ (solid line) and its La, Ge, and Sb projections. The Fermi	198

level is marked by the horizontal line at 0 eV.

Figure 7–7 Crystal orbital Hamilton population (COHP) curves (solid line) and integrated COHP curves (dotted line) for (a) Ge–Sb, (b) Ge–Ge, and (c) Sb–Sb contacts in $La_{12}Ge_7Sb_{21}$. The Fermi level is marked by the horizontal line at 0 eV. 198

Figure 7–8 Magnetic data for $Ce_{12}Ge_{6.5}Sb_{21}$. (a) Magnetic susceptibility and its inverse, with a fit to the modified Curie-Weiss law indicated by the solid line. (b) Isothermal magnetization at different temperatures. 200

Figure 7–9 Hypothetical structure of $RE_{20}Ge_{11}Sb_{33}$, with assemblies of nine condensed RE_6 trigonal prisms. The labelling scheme is the same as in Figure 7–5. 202

Figure 8–1 Plot of cell parameters vs. x for the β-Yb_5Sb_3-type phase obtained in reactions with nominal composition $La_5Ge_xSb_{3-x}$. In addition to the ternary phase, La_5Sb_3 and La_4Sb_3 were also formed below $x = 0.9$, and La_4Ge_3 was formed above $x = 1.6$. 208

Figure 8–2 Isothermal section at 800 °C for the La–Si–Sb system. The ternary phase is identified to be $La_5Si_xSb_{3-x}$, with a homogeneity width estimated to be similar to that in $La_5Ge_xSb_{3-x}$ ($0.9 \le x \le 1.6$). 221

Figure 8–3 Structure of $RE_5Tt_xSb_{3-x}$ (RE = La–Nd; Tt = Si, Ge), emphasizing the connectivity of RE_6 trigonal prisms, viewed down the b direction. The blue circles are RE 223

atoms, the green circles are *Tt*2 atoms (4*c*), and the red circles are mixture of *Tt*1 and Sb atoms (8*d*).

Figure 8–4 (a) One-dimensional ribbons of [RE_2Tt] rhombs and columns of confacial RE_6 trigonal prisms extending along the *b* direction. (b) Local coordination environments around the *Tt*2 (4*c*) and *Tt*1/Sb1 (8*d*) sites. 224

Figure 8–5 Density of states (DOS) and its La, Ge, and Sb projections for ordered models of (a) $La_5Ge_{0.5}Sb_{2.5}$, (b) La_5GeSb_2, and (c) $La_5Ge_{1.5}Sb_{1.5}$. The horizontal line at 0 eV marks the Fermi level. 228

Figure 8–6 Crystal orbital Hamilton population (COHP) curves (solid line) and integrated COHP curves (dotten line) for (a) La–La, (b) La–Ge, and (c) La–Sb contacts in La_5GeSb_2. The horizontal line at 0 eV marks the Fermi level. 229

Figure 8–7 Magnetic data for $Pr_5Ge_xSb_{3-x}$ (x = 1.2, 1.7). (a) Magnetic susceptibility and its inverse, with a fit to the Curie-Weiss law indicated for $Pr_5Ge_{1.2}Sb_{1.7}$ by the solid line. (b) Isothermal magnetization at different temperatures for $Pr_5Ge_{1.2}Sb_{1.7}$. (c) Isothermal magnetization at different temperatures for $Pr_5Ge_{1.7}Sb_{1.3}$. 232

Figure 8–8 Magnetic data for (a)–(b) $Pr_5Si_{1.2}Sb_{1.8}$, (c)–(d) $Nd_5Si_{1.2}Sb_{1.8}$, and (e)–(f) $Nd_5Ge_{1.2}Sb_{1.8}$. The left panels show the zero-field-cooled dc magnetic susceptibility 234

and its inverse as a function of temperature (with the insets highlighting low-temperature transitions in the ac magnetic susceptibility), and the right panels show isothermal magnetization curves at various temperatures.

Figure 9–1 The electron transfers in (a) *RE*–(Ti, V, Cr)–(Ge, Sb) and (b) *RE*–(Si, Ge)–Sb compounds. The width and arrows indicates the magnitude and direction of electron transfer. 241

Figure A1–1 Rietveld refinement results for *RE*$CrGe_3$ (*RE* = La–Nd, Sm). The observed profile is indicated by black crosses and the calculated profile by the solid red line. Bragg peak positions are located by the vertical blue tick marks. The difference plot is shown at the bottom. 250

Figure A1–2 Plots of ac magnetic susceptibility for *RE*$CrGe_3$ (*RE* = La–Nd, Sm). 252

Figure A1–3 Plots of isothermal magnetization for *RE*$CrGe_3$ (*RE* = La–Nd, Sm). 253

Figure A2–1 Molar magnetic susceptibility for $La_{12}Ge_{6.7}Sb_{21}$ in an applied field of 1 T. 256

Figure A3–1 Density of states (DOS) and its La, Ge, and Sb projections for La_5GeSb_2, with La 4f orbitals being downfolded. The horizontal line at 0 eV marks the Fermi level. 260

Figure A3–2 Rietveld refinement results for pure samples of $La_5Ge_xSb_{3-x}$, with x = (a) 1.0, (b) 1.2, (c) 1.3, and (d) 1.6. The observed profile is indicated by circles and the calculated profile by the solid line. Bragg peak positions are located by the vertical tick marks. The difference plot is shown at the bottom 261

Figure A3–3 Rietveld refinement results for (a) $Ce_5Si_{1.4}Sb_{1.6}$, (b) $Nd_5Si_{1.2}Sb_{1.8}$, and (c) $Ce_5Ge_{0.9}Sb_{2.1}$. The observed profile is indicated by circles and the calculated profile by the solid line. Bragg peak positions are located by the vertical tick marks. The difference plot is shown at the bottom. Trace amounts of Ce_2Sb are also present in (a) and (c). 262

Figure A3–4 Molar magnetic susceptibility for $La_5Si_{1.2}Sb_{1.8}$ and $La_5Ge_{1.2}Sb_{1.8}$ in an applied field of 1 T. 263

List of Abbreviations and Symbols

1D	one-dimensional
2D	two-dimensional
3D	three-dimensional
2θ	diffraction angle
a, b, c, V	unit cell constants, volume
AFM	antiferromagnetic
ASA	atomic spheres approximation
C	Curie constant
CEF	crystalline electric field
COHP	crystal orbital Hamilton population
CPS	curved position sensitive
d(1)	theoretical metallic bond length
DFT	density functional theory
dG	de Gennes factor
d_{hkl}	interplanar spacing
d_{ij}	observed distance
d(*n*)	observed distance
DOS	density of states
EDX	energy-dispersive X-ray analysis
E_g	band gap
F	structure factor
F_c	calculated structure factor

FM	ferromagnetic
F_o	observed structure factor
g	Landé factor
H	applied magnetic field
hkl	Miller indices
I	current
J	total angular momentum quantum number
l	length between two inner leads
L	total orbital angular momentum quantum number
LDA	local density approximation
M	magnetization; transition metal
n	bond order; non-bonding; number of charge carrriers
σ	bonding; conductivity; standard deviation
σ^*	antibonding
θ	Weiss temperature
ρ	resistivity
ρ_{calcd}	calculated density
$(\Delta\rho)_{max}$, $(\Delta\rho)_{min}$	maximum and minimum difference electron density
PPMS	Physical Property Measurement System
PM	paramagnetic
R	residual factor
R_{ij}	theoretical distance

R_{int}	residual for averaged symmetry equivalent reflections
RKKY	Ruderman-Kittel-Kasuya-Yosida model
R_w	weighted residual factor
S	total spin angular momentum quantum number
SEM	scanning electron microscopy
TB-LMTO	tight-binding linear muffin-tin orbital
T_c	critical temperature
T_N	Neél temperature
μ	mobility of charge carriers; absorption coefficient
μ_B	Bohr magneton
μ_{eff}	effective magnetic moment
U_{eq}	equivalent isotropic displacement parameter
U_{ij}	anisotropic displacement parameter
V	applied voltage
vec	valence electron concentration
w	weighting scheme
λ	wavelength
χ	susceptibility
χ_o	temperature-independent susceptibility
χ^P	Pauling electronegativity
x, y, z	atomic coordinates
Z	number of formula units in the unit cell

Chapter 1

Introduction

1.1. Background

1.1.1. Importance of Intermetallics

Intermetallic compounds (or intermetallics) are alloys formed from a mixture of two or more elements (at least one metal); they have a definite composition and a crystal structure type different from the constituent elements.[1] With their ordered crystal structures and mixed bonding character (metallic and polar covalent), these compounds display many interesting physical properties and have been paid increasing attention over the years. These properties include mechanical hardness, high-temperature stability, and resistance to oxidation or corrosion, which make them exceptional candidates for industrial applications.[1,2] Thus, intermetallics have been widely used as novel electrical and magnetic materials. Current important commercial applications include superconductors (e.g., Nb_3Sn), and permanent magnets (e.g., $SmCo_5$, Sm_2Co_{17}, and $Nd_2Fe_{14}B$).[1] Because metals constitute most of the elements in the periodic table, there are potentially a huge number of intermetallic compounds whose structures and properties can be adjusted through appropriate combination of the elements. Nevertheless, "*intermetallic phases have long been among the black sheep in the*

family of chemical compounds,"[3] because understanding how their structures relate to bonding and properties is still an unresolved question.

1.1.2. Electron Counting Rules

Unlike organic and organometallic compounds where the octet rule or 18 e^- rule is normally obeyed, intermetallics defy such simple electron-counting schemes because their bonding involves a mixture of polar covalent and metallic character and electrons are more delocalized. Many researchers have dedicated much experimental and theoretical effort to understanding the bonding in intermetallics.

1.1.2.1. Hume-Rothery Phases

Early in the history of intermetallics, William Hume-Rothery studied a series of binary alloys combining Cu, Ag, or Au with other metallic elements of similar electronegativities, such as Zn, Sn, Al, or Ga. He arranged the resulting compounds according to their average valence electron concentration (*vec*), and found that those with the same *vec* adopt the same structural type regardless of the type of element and their composition.[4,1b] For example, Cu_5Zn_8 and Cu_9Al_4, having the same *vec* of 1.61, both crystallize in the γ-brass type structure.[5,6] Although this *Hume-Rothery rule* applies well to these binary alloys, which show typical metallic behaviour, these alloys only represent a tiny portion of

intermetallic compounds. This rule could not be used effectively to explain other types of alloys and new rules need to be discovered.

1.1.2.2. Zintl-Klemm Concept

Shortly after Hume-Rothery's work, Eduard Zintl started to examine compounds of the electropositive alkali or alkaline earth metals with an electronegative element from group 13, 14, or 15. These compounds are quite different from the Hume-Rothery intermetallics because of the larger electronegativity difference between elements. Even though the electronegativity difference ($\Delta\chi^P \sim 1.0$) is not large enough to invoke ionic bonding, he nevertheless proposed the occurrence of complete electron transfer from the electropositive to the electronegative component, similar to typical ionic compounds such as NaCl ($\Delta\chi^P = 2.1$).[7] For instance, the compound NaTl would be formulated as Na^+Tl^-, so that Tl^- possesses the same number of valence electrons as carbon. The advantage of this concept is that it relates the electron counting scheme to a structure, since the Tl atoms in NaTl are arranged in a 3D diamond network, identical to that of carbon. The octet rule is retained, with each Tl atom participating in four $2c–2e^-$ bonds, just like the C atoms in diamond, an idea that Klemm termed the *pseudoatom concept*.[4,8,9] Intermetallic compounds (not just the original binary phases studied by Zintl) that conform to this electron-counting rule are now commonly termed *Zintl phases*.

The *Zintl-Klemm concept* represents one of the most successful ideas in solid state chemistry that can be used as a starting point to understand bonding in polar intermetallics. All valence electrons of a donor (electropositive metal) atom are assumed to be transferred to an acceptor (electronegative element) atom, and the resulting anionic substructure can be rationalized by the octet rule (8–*N* rule). If there are not enough electrons assigned to the anions to satisfy the octet rule, homoatomic covalent bonding occurs to form extended anionic substructures (or polyanions). If there are more than 8 available electrons for each anion, the excess electrons participate in forming cation-cation bonds (polycations), which is usually the case for electropositive metal-rich compounds.[10]

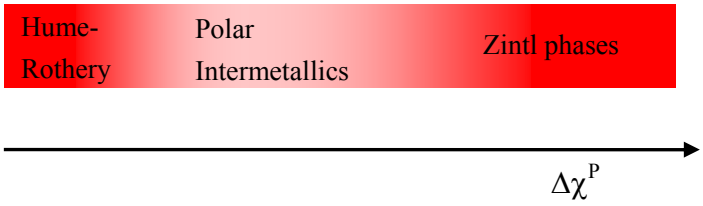

Figure 1–1. The relative location of polar intermetallic phases in terms of electronegativity difference.

Of course, the Hume-Rothery rule (average *vec* rule) and Zintl-Klemm concept (8–*N* rule) are only applicable to limiting classes of intermetallics in which the electronegativity difference between components is either small or large, respectively. Do compounds with intermediate electronegativity difference also satisfy the Zintl-Klemm concept, and at what point does it fail? To answer these

questions, many polar intermetallics containing an electropositive metal (alkali, alkaline-earth, rare-earth, or transition metal) and an electronegative metal (p-block elements) have been examined (Figure 1–1). Antimony (χ^P = 1.9) with five valence electrons and germanium (χ^P = 1.8) with four valence electrons are metalloids with large χ, whose compounds exhibit a rich structural chemistry containing various polyanionic substructures. These polyanionic interactions have a significant impact on the electronic structure (e.g., band gap), and thus their physical properties. In the following section, the different polyanionic Sb and Ge substructures will be reviewed. (Structural data are taken from Inorganic Crystal Structure Database.) Selected examples will be discussed to address the applicability of the Zintl-Klemm concept.

1.1.3. Sb Substructures

1.1.3.1. Classical Sb–Sb Bonding

In binary compounds of the alkali or alkaline-earth metals A_xSb_y, classical Sb–Sb single bonds (2c–2e$^-$) of 2.8–2.9 Å distances are typically observed. The various substructures formed are summarized in Table 1–1 and Figure 1–2. In accordance with the octet rule, Sb ($5s^2$ $5p^3$) can form isolated Sb^{3-}, one-bonded (1b) Sb^{2-}, two-bonded (2b) Sb^-, or three-bonded (3b) Sb^0.

Isolated Sb^{3-} anions are usually observed in antimonides A_xSb_y that are metal-rich. In these cases, the metal atoms provide enough electrons to

completely reduce Sb atoms to Sb^{3-} anions, while the remaining electrons are used to form metal-metal bonds (polycations). For instance, in Ca_2Sb (La_2Sb-type structure), the normal oxidation state of +2 for Ca is not adopted because it would imply an impossible charge of –4 for Sb. The correct assignment is based on the assumption that each Sb atom possesses 8 e^- (Sb^{3-}) (without any Sb–Sb bonds formed) and the Ca atoms participate in partial Ca–Ca metallic bonds (with a Ca–Ca distance of 3.302 Å).[11a]

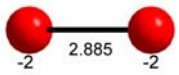

Pair in Ba_5Sb_4

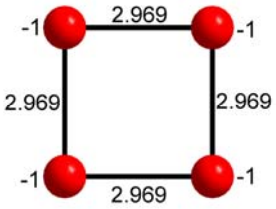

Square in $Sr_{11}Sb_{10}$

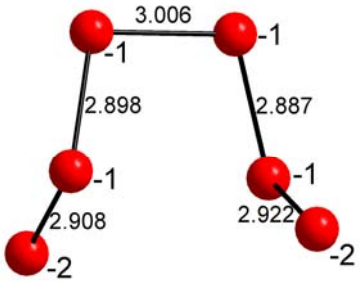

6-atom cluster in Sr_2Sb_3

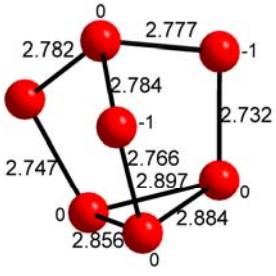

7-atom cluster in Cs_3Sb_7

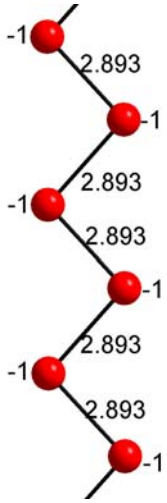

Zig-zag chain in $SrSb_2$

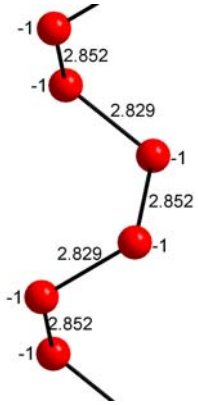

Helical chain in KSb

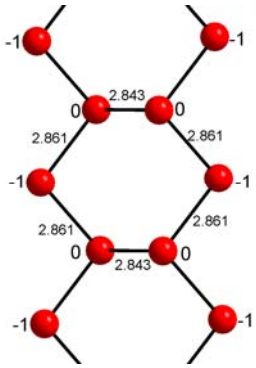

Connected double zig-zag chain in KSb_2

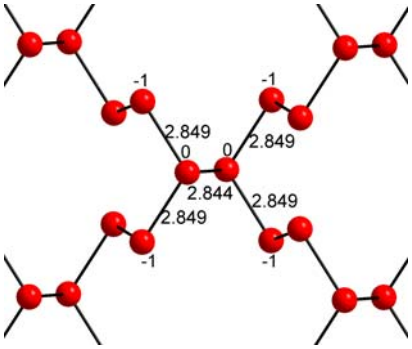

2D layer in $BaSb_3$

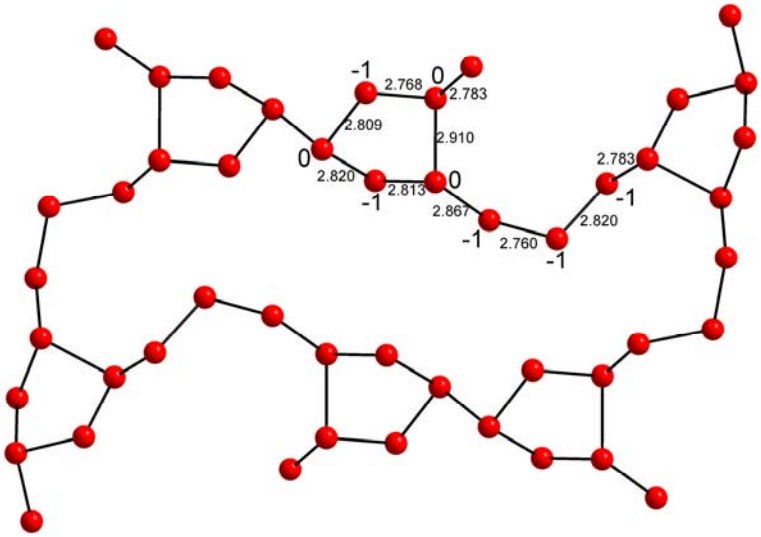

2D layer in Cs_5Sb_8

Figure 1–2. The formed Sb substructures by classical Sb–Sb single bond in A_xSb_y binaries.

Table 1–1. Summary of Sb substructures formed by the classical Sb–Sb single bond in A_xSb_y (A = alkali, alkaline earth metals) and their charge assignments.

Compound	Structure type	Sb substructures	Bond distance (Å)	Charge assignment
A_2Sb (A = Ca, Sr) [11]	La_2Sb	isolated Sb^{3-} anion	None	$(A^{2+})_2(Sb^{3-})(e^-)$
A_3Sb (A = Na, K, Rb) [12]	$IrAl_3$	isolated Sb^{3-} anion	None	$(A^{+})_3(Sb^{3-})$
A_5Sb_3 (A = Ca, Ba, Sr) [13]	Mn_5Si_3	isolated Sb^{3-} anion	None	$(A^{2+})_5(Sb^{3-})_3(e^-)$
Ba_5Sb_4 [14]	Sm_5Ge_4	isolated pair, Sb^{3-} anion	2.885	$(Ba^{2+})_5(Sb^{3-})_2(Sb_2^{4-})$
Cs_2Sb [15]	Cs_2Sb	isolated pair	2.923	$(Cs^{+})_2(Sb^{2-})$
$A_{11}Sb_{10}$ (A = Ca, Sr) [16]	$Ca_{11}Sb_{10}$	isolated square, Sb^{3-} anion, pair	2.969	$(A^{2+})_{11}(Sb^{3-})_4(Sb^{-})_2(Sb^{2-})_4$
A_2Sb_3 (A = Sr, Ba) [17]	Sr_2Sb_3	isolated 6-atom cluster	2.88–3.0	$(A^{2+})_4(Sb_6^{8-})$
Cs_3Sb_7 [15]	Cs_3Sb_7	isolated 7-atom cluster	2.73–2.89	$(Cs^{+})_3(Sb_7^{3-})$
ASb_2 (A = Ca, Sr) [18]	$CaSb_2$	two 1D zig-zag chain	2.893	$(A^{2+})(Sb^{-})_2$
ASb (A = K, Na) [19]	LiAs	1D helical chain	2.829, 2.852	$(A^{+})(Sb^{-})$
KSb_2 [20]	KSb_2	2b, 3b–double zig-zag chain	2.843, 2.861	$(K^{+})(Sb^{0})(Sb^{-})$
$BaSb_3$ [21]	$SrAs_3$	2b, 3b–formed 2D layer	2.844, 2.849	$(Ba^{2+})(Sb^{0})(Sb^{-})_2$
Cs_5Sb_8 [22]	Cs_5Sb_8	2b, 3b–formed 2D layer	2.76–2.91	$(Cs^{+})_5(Sb^{0})_3(Sb^{-})_5$

Polyanionic Sb substructures have been observed in the form of Sb_2^{4-} pairs (in Ba_5Sb_4),[14] Sb_4^{4-} squares (in $Sr_{11}Sb_{10}$),[16b] Sb_6^{8-} fragments (in Sr_2Sb_3),[17b] Sb_7^{3-} clusters (in Cs_3Sb_7),[15] $^1_\infty[Sb]^{1-}$ chains (in $SrSb_2$ and KSb),[18b,19a] $^1_\infty[Sb_2]^{1-}$ double chains (in KSb_2),[20] $^2_\infty[Sb_3]^{2-}$ layers (in $BaSb_3$),[21] and $^2_\infty[Sb_8]^{5-}$ layers (in Cs_5Sb_8).[22] The charges conform exactly to the Zintl-Klemm concept. For example, in KSb, the assumption of full electron transfer leads to the formulation K^+Sb^-, and in agreement with predictions, each Sb atom is two-bonded to form a helical chain that is reminiscent of the structure of isoelectronic Te.[19a]

With their large electronegativity difference between *A* and Sb, these binary antimonides can be considered to be typical Zintl phases, and the Zintl-Klemm concept is well-suited to explain their structure and bonding.

1.1.3.2. Non-Classical (Hypervalent) Sb–Sb Bonding

In antimonides containing the less electropositive rare-earth elements or transition metals, longer Sb–Sb distances between 3.0 and 3.2 Å are usually observed, corresponding to non-classical Sb–Sb bonds. One way to quantify these bonds is to calculate their bond order through either the Pauling equation:[7]

$$\log n = [d(1) - d(n)] / 0.60 \qquad \text{(Equation 1–1)}$$

where $d(1) = 2.782$ Å, $d(n)$ is the observed distance (in Å), and n is the bond order, or the bond-valence equation:[23,24]

$$\nu_{ij} = \exp\left[\left(R_{ij} - d_{ij}\right)/0.37\right] \qquad \text{(Equation 1–2)}$$

where R_{ij} = 2.81 Å, d_{ij} is the observed distance (in Å), and ν_{ij} is the bond valence. According to these equations, a bond distance of 3.0 Å corresponds roughly to a bond order or bond valence of 0.5, that is, a "half-bond".

The simplest example, that of a linear Sb_3^{7-} cluster with Sb–Sb distances of 3.196(2) Å, is found in $Ca_{14}AlSb_{11}$ compound, in which the oxidation states of the metal centres are Ca (+2) and Al (+3).[25] Charge balance then implies that the eleven Sb atoms should bear a total charge of 31–. There are eight isolated Sb^{3-} anions per formula unit (giving a 24– charge), so the linear Sb_3 cluster should carry a charge of 7–. This Sb_3^{7-} unit is isoelectronic to I_3^- and XeF_2 (22 valence electrons), both of which have been described as electron-rich species containing hypervalent bonds. A molecular orbital (MO) diagram can be constructed to explain this bonding (Figure 1–3).[26,27] If a Lewis structure is drawn for Sb_3^{7-} (22 e^-), the lone pairs on each atom can be assumed to occupy the s orbital and two perpendicular p orbitals ($6e^- \times 3 = 18\ e^-$). Four electrons remain to be distributed over three axial p orbitals. Assuming that no significant s-p mixing takes place, these three p orbitals combine to form three MOs. The four electrons occupy the bonding (σ) and non-bonding (n) MOs, so that each of the Sb–Sb bonds can be considered to be "half-bonds", consistent with the estimation from bond order or bond valence equations above. Despite the simplicity of this MO model, the bonding character of these Sb–Sb bonds is nicely explained.

More rigorous calculations performed by Kleinke and co-workers for the Sb_3^{7-} fragment in $Ca_{14}AlSb_{11}$ confirm this model in general.[28]

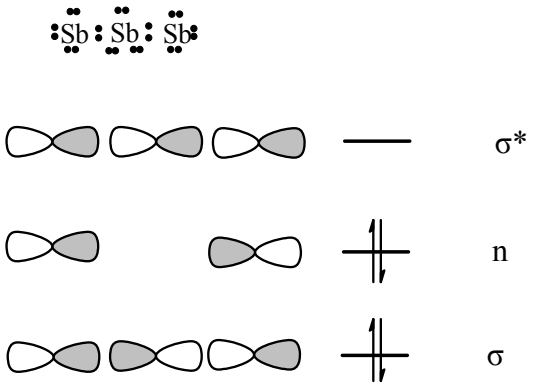

Figure 1–3. The Lewis structure and simple MO diagram for Sb_3^{7-}.

Typical extended Sb substructures exhibiting this non-classical Sb–Sb bonding include 1D linear and zigzag chains, 1D ribbons, and 2D square nets (Figure 1–4). Hoffmann and coworkers have analyzed these substructures and provided general electron-counting rules: 7 electrons for two-bonded (2b-Sb^{2-}) and 6 electrons for four-bonded (4b-Sb^{-}) antimony atoms that participate in hypervalent bonding.[27a,29]

Examples of 1D linear chains are found in the isostructural compounds RE_3MSb_5 (*RE* = La–Nd, Sm; *M* = Ti, Zr, Hf)[30] and U_3MSb_5 (*M* = Ti, Zr, Hf).[36] The crystal structure consists of chains of Sb atoms (Sb–Sb 3.0–3.2 Å) and columns of face-sharing MSb_6 octahedra separated by *RE* atoms. In the formula,

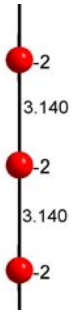

1D linear chain in La_3TiSb_5 [30]

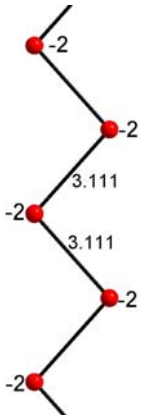

1D zig-zag chain in Ce_2GeSb_3 [31]

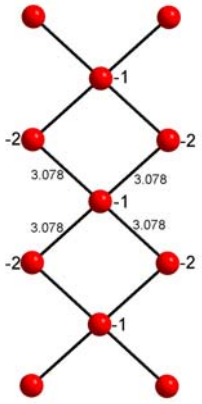

3-atom wide ribbon in $Gd_6Ge_{5-x}Sb_{11+x}$ [32]

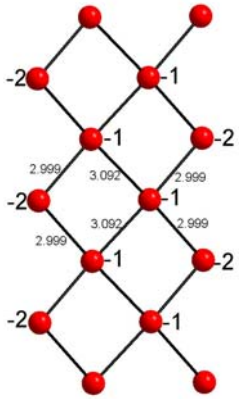

4-atom wide ribbon in $Gd_6Zn_{1+x}Sb_{14}$.[33]

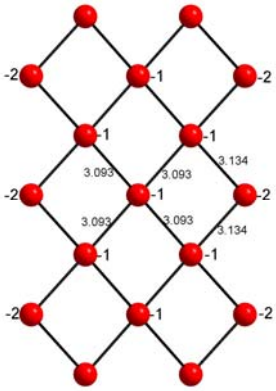

5-atom wide ribbon in $La_{12}Ga_8Sb_{21}$.[34]

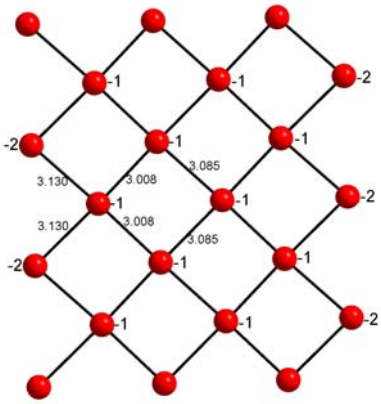

6-atom wide ribbon in $Pr_{12}Ga_4Sb_{23}$.[34]

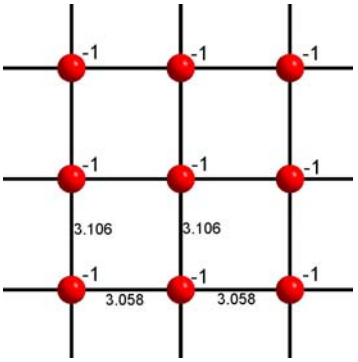

2D layer in $LaCrSb_3$.[35]

Figure 1–4. The Sb substructures formed by non-classical Sb–Sb bonding.

out of the five Sb atoms, two participate in the linear chains (2b-Sb^{2-}) and three are isolated (0b-Sb^{3-}). According to the Zintl-Klemm concept and with the assumption that the *RE* and *M* (group 4) atoms transfer all of their valence electrons, the formulation $(RE^{3+})_3(M^{4+})(Sb^{2-})_2(Sb^{3-})_3$ accounts well for the bonding. Although this model works well for RE_3MSb_5 when *M* = Ti, Zr, Hf (group 4), it fails for other isostructural compounds such as RE_3NbSb_5, and U_3MSb_5 (*M* = Sc, V, Cr, Mn) unless the charge assignments for the metal atoms need to be revised.[30,37] The presence of variable oxidation states adopted by a transition metal may lead to these ambiguous assignments, although magnetic measurements may provide useful information. Moreover, the idea of full electron transfer may break down for antimonides containing transition metals whose electronegativities are close to or even greater than that of Sb.

Many antimonides exhibit 2D square sheets, such as the binary compound $YbSb_2$, which adopts the $ZrSi_2$-type structure.[38] In addition to 1D zigzag chains (Sb–Sb 2.964 Å single bonds), it contains 2D square sheets (Sb–Sb 3.119 Å hypervalent bonds) (Figure 1–5). Magnetic measurements suggest that the oxidation state of Yb is +2.[39] The 2b-Sb (single bond) in the 1D zigzag chain carries a charge of 1– and 4b-Sb (hypervalent bond) in 2D square sheets has a charge of 1–, leading to the charge-balanced formulation $(Yb^{2+})(Sb^{1-})(Sb^{1-})$. Thus, $YbSb_2$ conforms to the Zintl-Klemm concept. When divalent Yb is substituted by trivalent *RE* (*RE* = La–Nd, Sm, Gd, Tb), one extra electron is

provided to the Sb substructures. As a result, the Sb atoms in the 1D chain are reduced (from Sb^{1-} to Sb^{2-}) and broken into Sb_2 pairs with single bonds ($d_{(Sb–Sb)}$ = 2.788 Å in $SmSb_2$). The formulation is now $(RE^{3+})(Sb^{2-})(Sb^{1-})$, so $RESb_2$ ($LaSb_2$) still follows the electron-counting rule.[40]

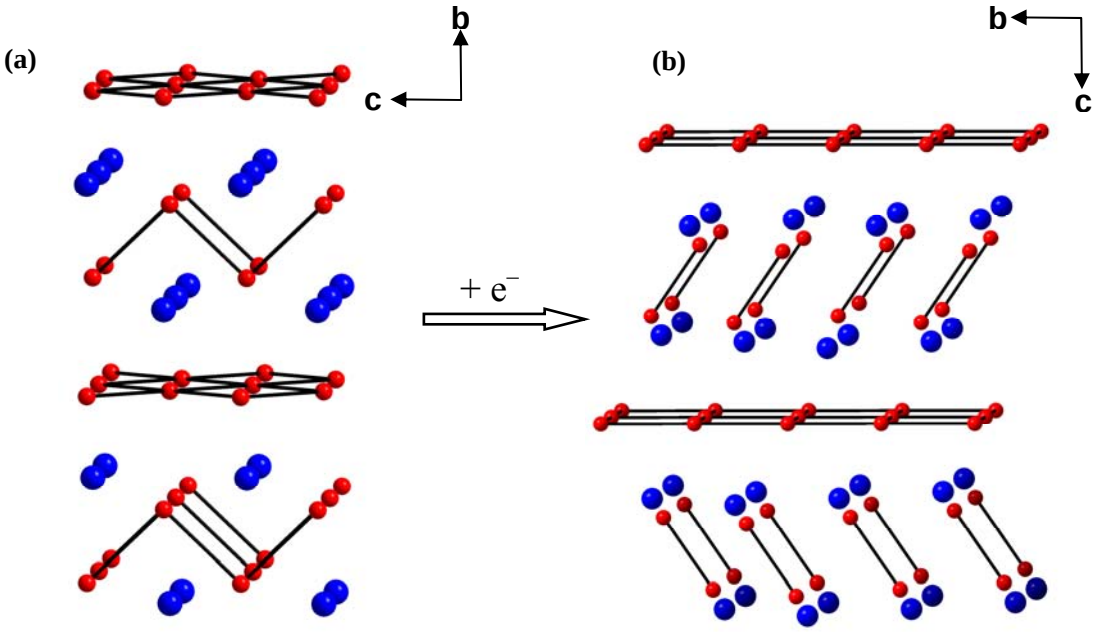

Figure 1–5. Crystal structures of: (a) $YbSb_2$ showing zig-zag chains and 2D sheets; (b) $RESb_2$ showing reduced Sb pairs and 2D sheets viewed along the *a* axis. The blue and red spheres represent *RE* and Sb atoms, respectively.

Despite the many successful applications of the Zintl-Klemm concept, it fails for many of the ternary rare-earth p-block-element antimonides, which contain complex polyanionic substructures.[29] In these compounds, the similar sizes of the p-block and Sb atoms usually leads to the disorder (partial occupancies or substitutional mixing), complicating the charge assignment.

Moreover, incomplete electron transfer from the *RE* atoms arising from the smaller electronegativity differences makes these charge assignments questionable.

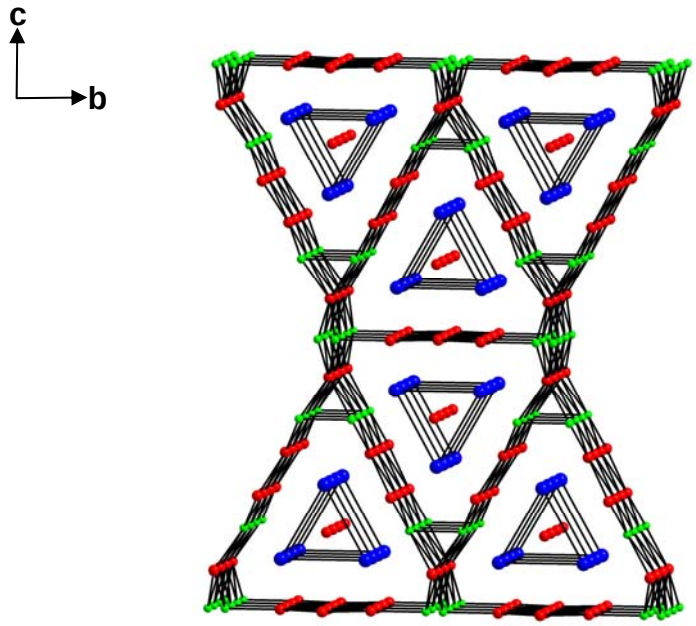

Figure 1–6. Crystal structure of $Gd_6Ge_{5-x}Sb_{11+x}$ (x = 0.67) viewed along *a* direction. The blue, green, and red spheres are Gd, Ge, and Sb atoms, respectively.

Let us look at two examples. The structure of $Gd_6Ge_{5-x}Sb_{11+x}$ (x = 0.67) consists of a complex 3D polyanionic Ge–Sb framework outlining large channels, which are filled by columns of face-sharing Sb-centred RE_6 trigonal prisms (Figure 1–6).[32] This polyanionic framework can be broken down through a "retrotheoretical approach"[27b] into isolated Sb^{3-} species, three-atom-wide Sb ribbons $(Sb_3)^{5-}$, and a 2D kinked layer containing Ge and Sb atoms. One of the sites is occupied by a mixture of Ge and Sb atoms, making it difficult to assign a

charge. If only Ge atoms are assumed to occupy this site, giving rise to the stoichiometric formula $Gd_6Ge_5Sb_{11}$, and the remaining units are assigned their usual charge, then the anionic substructure consists of two isolated Sb^{3-} anions, three-atom-wide ribbons $(Sb_3)^{5-}$, and 2D kinked sheets $(Ge_5Sb_6)^{6-}$ per formula unit. The total 17– charge on this anionic substructure cannot be balanced by the 18+ charge provided by the six Gd^{3+} ions, unless the assumption of full electron transfer is incorrect.

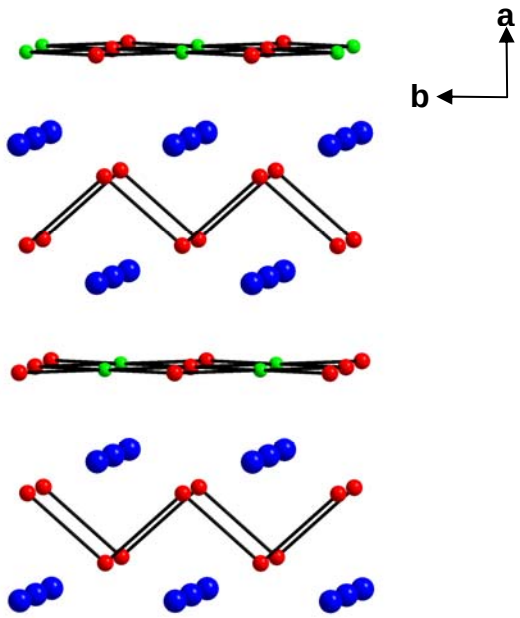

Figure 1–7. Crystal structure of Ce_2GeSb_3 showing zig-zag chains and Ge/Sb sheets viewed along the *c* axis. The blue, green, and red spheres are Ce, Ge, and Sb atoms, respectively.

Although doubtful, Ce_2GeSb_3 has been reported to be isostructural to $YbSb_2$, with half of the Sb atoms in the 2D square sheets being replaced by Ge atoms (Figure 1–7).[31] The Sb–Sb distance in the 1D zigzag chain is 3.111 Å

(hypervalent bond), which is much longer than that in $YbSb_2$ (2.946 Å), so the Sb atoms in this chain are assigned to be 2–. If the long Ge–Sb distance of 3.166 Å in the substituted square sheet is treated as a hypervalent bond, then the assignment is $(GeSb)^{3-}$. Thus, the overall 7– charge on the anionic substructure $(GeSb)^{3-}(Sb)^{2-}(Sb)^{2-}$ cannot be balanced by the 6+ charge provided by two trivalent Ce atoms. The Zintl-Klemm concept cannot rationalize this structure.

1.1.4. Ge Substructures

1.1.4.1. Classical Ge–Ge Bonding

Ge is a metalloid element located at the Zintl border, with similar electronegativity ($\chi^P = 1.8$) and atomic radius ($R_1 = 1.242$ Å) as Sb ($\chi^P = 1.9$, $R_1 = 1.391$ Å),[7] but with four valence electrons instead of five. Like other pairs of elements (Li/Mg, Be/Al, B/Si) positioned diagonally in the periodic table, there is the possibility for similar behaviour between Ge and Sb, but the relationship is generally weak. For example, some germanides and antimonides adopt the same structure type, such as RE_4Sb_3/RE_4Ge_3 (anti-Th_3P_4-type) and RE_5Sb_3/RE_5Ge_3 (Mn_5Si_3-type).[41,42] Ternary compounds such as U_3TiGe_5 and U_3TiSb_5 are also isostructural.[43,36]

To complete its octet, a Ge ($4s^24p^2$) atom needs to acquire four additional electrons, in contrast to three for Sb. Thus, it can form isolated Ge^{4-},

one-bonded (1b) Ge^{3-}, two-bonded (2b) Ge^{2-}, three-bonded (3b) Ge^{-}, or four-bonded (4b) Ge^{0} species. A classical Ge–Ge single bond distance is typically between 2.5 and 2.6 Å. The Ge substructures found in binary germanides A_xGe_y formed with the highly electropositive alkali or alkaline-earth metals are summarized in Figure 1–8 and their assigned charges are listed in Table 1–2. Because the electronegativity differences are still quite large, these binary germanides generally satisfy the Zintl-Klemm concept and can be considered to be Zintl phases.

When less electropositive *RE* metals substitute for alkali or alkaline-earth metals, the assumption of full electron transfer is brought into question once again. Thus, for example, whereas the alkaline-earth germanides AE^{2+}(2b-Ge^{2-}) (*AE* = Ca, Sr, Ba)[57] containing zigzag Ge chains satisfy the Zintl-Klemm concept, the isostructural rare-earth germanides *RE*Ge (*RE* = Pr, Nd, Sm, Gd–Er)[61] do not, with the apparent donation of only two valence electrons from these nominally trivalent *RE* metals.

1.1.4.2. Non-Classical (Hypervalent) Ge–Ge Bonding

Hypervalent Ge–Ge bonds are also observed in germanides containing less electropositive rare-earth or transition metals, and the bonding model is similar to those discussed for the antimonides above.

Table 1–2. Summary of Ge substructures formed by the classical Ge–Ge single bond in A_xGe_y (A = alkali, alkaline earth metals) and their charge assignments.

Compound	Structure type	Ge substructures	Bond distance (Å)	Charge assignment
Mg_2Ge [44]	CaF_2	isolated Ge^{4-}	None	$(Mg^{2+})_2(Ge^{4-})$
Ca_2Ge [45]	Co_2P	isolated Ge^{4-}	None	$(Ca^{2+})_2(Ge^{4-})$
Ba_2Ge [46], Sr_2Ge [47]	$PbCl_2$	isolated Ge^{4-}	None	$(Ba^{2+})_2(Ge^{4-})$
Li_7Ge_2 [48]	Li_7Ge_2	pairs	2.624	$(Li^{+})_7$(1b-Ge^{3-})(Ge^{4-})
Ba_5Ge_3 [49]	Ba_5Si_3	pairs	2.563	$(Ba^{2+})_5$(1b-Ge^{3-})$_2(Ge^{4-})$
Sr_5Ge_3 [50], Ca_5Ge_3 [51]	Cr_5B_3	pairs	2.591	$(Sr^{2+})_5$(1b-Ge^{3-})$_2(Ge^{4-})$
Ba_3Ge_4 [52]	Ba_3Si_4	butterfly	2.564	$(Ba^{2+})_3$(3b-Ge^{-})$_2$(2b-Ge^{2-})$_2$
$BaGe_2$ [53], $SrGe_2$ [54]	$BaSi_2$	tetragonal cluster	2.5–2.6	Ba^{2+}(3b-Ge^{-})$_2$
NaGe [55]	NaGe	tetragonal cluster	2.537, 2.544	Na^{+}(3b-Ge^{-})
KGe, RbGe [56]	KGe	tetragonal cluster	2.555, 2.579	K^{+}(3b-Ge^{-})
AGe (A = Ca, Sr, Ba) [57]	CrB	1D zig-zag chain	2.627	A^{2+}(2b-Ge^{2-})
$CaGe_2$ [58]	$CaSi_2$	3b, 2D brick-like layer	2.519	Ca^{2+}(3b-Ge^{-})$_2$
$BaGe_2$ (h.p.) [59]	$ThSi_2$	3b, 3D network	2.453, 2.684	Ba^{2+}(3b-Ge^{-})$_2$
LiGe [60]	LiGe	3b, 3D network	2.554, 2.601	Li^{+}(3b-Ge^{-})

Pair in Ba_5Ge_3

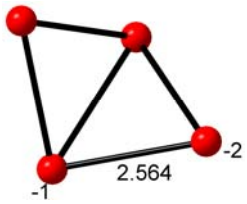

Butterfly in Ba_3Ge_4

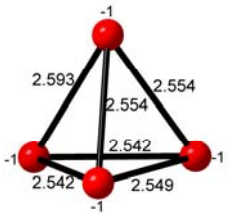

Tetragonal cluster in $BaGe_2$

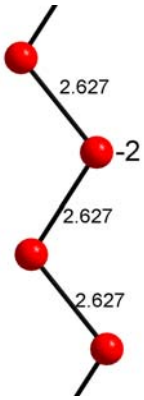

1D Zig-zag chain in BaGe

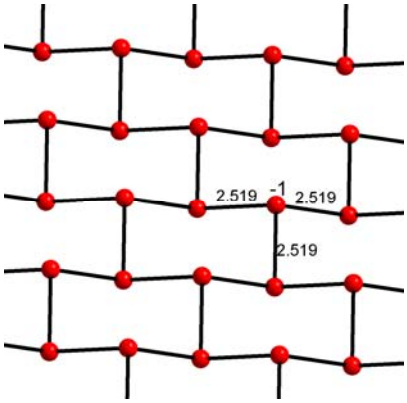

3b, 2D brick-like layer in $CaGe_2$

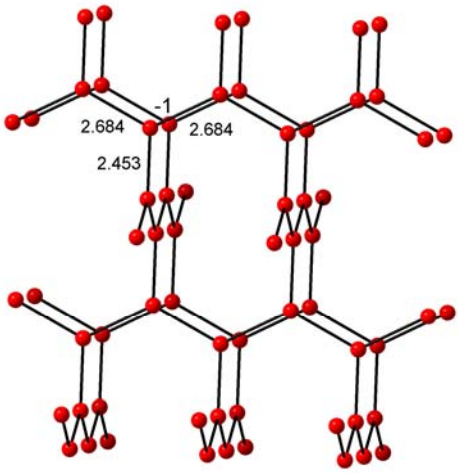

3b, 3D network in $BaGe_2$ (h.p.)

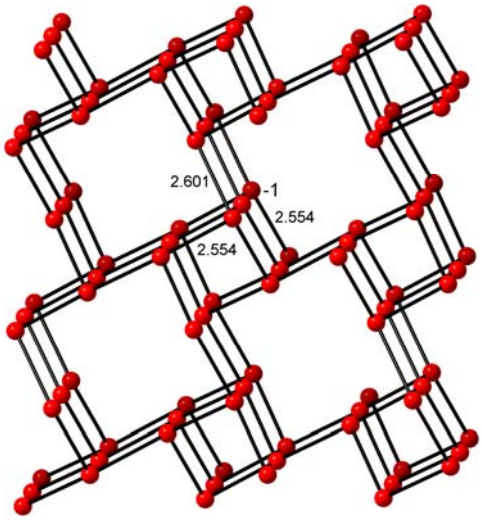

3b, 3D network in LiGe

Figure 1–8. The Ge substructures formed by Ge–Ge single bonds in A_xGe_y Zintl binaries.

The 2D Ge square sheets are observed in MGe$_2$ compounds (M = Zr, Hf), which adopt the same structure type (ZiSi$_2$) as YbSb$_2$ discussed before.[62] The Ge atoms appear in two arrangements: a zigzag chain containing single bonds (2.580, 2.590 Å) and a square sheet containing hypervalent bonds (2.669, 2.685 Å). Thus, the charge formulation M^{4+}(2b-Ge)$^{2-}$(Ge^{2-}) is satisfactory. In contrast, the isostructural compound TmGe$_2$ is also known (Ge–Ge 2.544, 2.780 Å),[63] but the presence of a trivalent *RE* metal cannot be rationalized with the Zintl-Klemm concept.

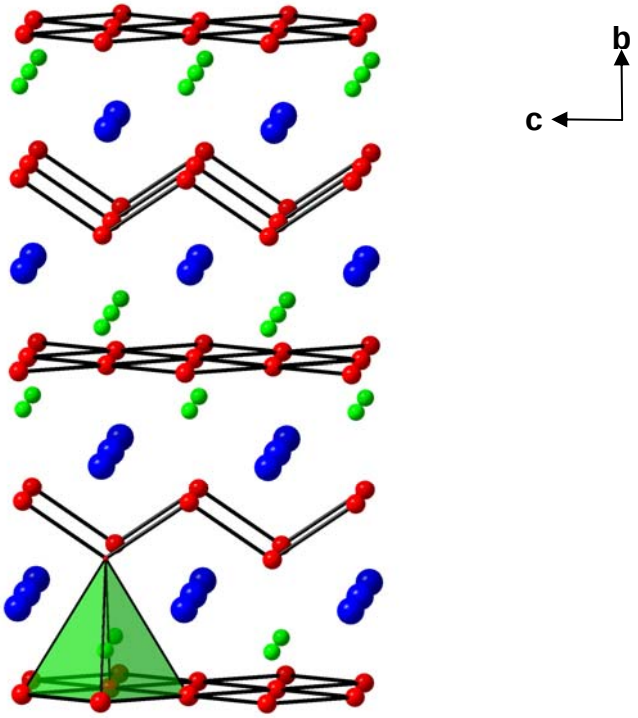

Figure 1–9. Crystal structure of REM_xGe$_2$ viewed along the *a* axis. The blue, green, and red spheres are *RE*, *M*, and Ge atoms, respectively.

A series of ternary germanides REM_xGe$_2$ (M = Mn, Fe, Co, Ni, Cu, Ru, Rh,

Pd, Re, Ir, Pt)[64] is known in which additional transition metal atoms *M* are inserted between the 1D zigzag chains and 2D square sheets of Ge atoms found in the host structure of $M\text{Ge}_2$ above, as shown in Figure 1–9. Each *M* atom is surrounded by five Ge atoms in a square pyramidal geometry, the four basal atoms belonging to the square sheet and the one apical atom belonging to the chain. Because these germanides are non-stoichiometric, with a wide homogeneity range *x*, a formulation such as $RE^{3+}(M_x)^{+}(2b\text{-Ge}_{\text{chain}})^{2-}(\text{Ge}_{\text{square sheet}})^{2-}$ seems to be incompatible with the Zintl-Klemm concept.

1.1.5. Research Motivation

From the above survey on antimonides and germanides, we have seen that the Zintl-Klemm concept works well to explain the bonding and structures for compounds containing highly electropositive elements such as alkali and alkaline earth metals, and begins to fail for those containing transition metals or rare-earth metals because of their smaller electronegativity differences. The assumption of complete electron transfer is questionable. Notwithstanding the weak diagonal relationship of Ge and Sb, different polyanionic substructures are observed because of the different number of valence electrons. Generally speaking, the p-block elements located further to the left in the periodic table (such as the group 13 elements) lie at the Zintl border where it is more likely to find polyhedral clusters exhibiting multicentre electron-deficient bonding described using Wade's

rules. In contrast, the group 15 elements, like Sb, tend to adopt more electron-rich hypervalent bonding in non-classical anionic substructures. Ge is located between these regions in the periodic table, and may exhibit mixed above bonding character.

The goal of this thesis is to synthesize and characterize new ternary rare-earth antimonides and germanides to test the limits of the Zintl-Klemm concept, because the most challenging substructures are found in these compounds. Given the presence of unpaired f-electrons in rare-earth metals and d-electrons in transition metals, these compounds may also exhibit interesting magnetic properties. Moreover, the measurement of magnetic properties may provide a way to identify the oxidation states of rare-earth and transition metals, thus aiding the assignment of the formal charge. Therefore, physical properties such as resistivity and magnetic properties of the synthetically available compounds were measured. By relating structures and bonding to physical properties using band structure calculations, we hope novel materials with desired properties can be designed.

1.2. Synthesis

The synthesis of intermetallic compounds typically requires high temperature or sometimes even high pressure in order to overcome the large kinetic barriers in solid state reactions. Because there is practically no way to

predict the composition and structure of an unknown solid state compound, synthesis of a new ternary intermetallic compound generally proceeds by investigation of the ternary phase diagram. Samples with selected stoichiometries of the elements are first prepared by arc-melting. In an arc-melter (Figure 1–10), the intense electric arc generated under high potential and with large current is directed at the reactants, which are placed on a water-cooled copper base under argon atmosphere in the presence of Ti (which absorbs traces of oxygen). Melting occurs essentially instantaneously, and the alloys are normally melted twice to ensure homogeneity. Because of the low boiling point of Sb (1587 °C), a 5–7 at. % excess of Sb is added to compensate for its volatilization during arc-melting. After arc-melting, the alloys are sealed within evacuated fused-silica tubes and annealed at 800 °C for at least two weeks to ensure that equilibrium is reached. The alloys are then quenched in cold water and subsequently analyzed (see later). If a new ternary phase is identified and its composition is accurately determined, it becomes important to attempt to prepare single crystals for subsequent structure determination and property measurements.

For the growth of single crystals, it is common to simply mix powders of the elements in the correct stoichiometric ratios, load them into evacuated fused-silica tubes (to prevent reaction with oxygen), heat to high temperatures (typically up to 1000 °C) for a long time, and slowly cool the tubes (Figure 1–11a). To prevent

reaction of starting materials with the silica tube, especially at high temperatures, the samples are sometimes placed within inner alumina crucibles (Figure 1–11b).

Figure 1–10. The arc melters in our lab used for the arc-melting: (a) Centorr 5TA tri-arc melter; (b) Edmund Bühler arc melter.

Figure 1–11. The reaction tubes for direct reaction: (a) fused silica tube; (b) alumina tube.

Solid-state reactions may be quite slow, requiring several weeks or more to go to completion because of the slow diffusion rate and small contact area of

reactants.[65] However, it is certainly possible to choose reaction temperatures until the system is molten, accelerating the reaction rates as well as facilitating the growth of crystals from the melt. In addition, it may be possible to add a flux, which effectively acts as a solvent, to enhance the reaction rate. Suitable fluxes with low melting points include Al (660 °C), Ga (30 °C), In (157 °C), Sn (232 °C) and Pb (328 °C). Sometimes a "reactive flux" participates in the reaction to form an unwanted byproduct containing the flux element. Choosing an appropriate non-reactive flux is done on a case-by-case basis, depending on the type of reactants, temperature, and other factors. General guidelines for choosing a flux are available in an excellent review.[66] In the case of antimonides, experience in our research group has shown that Sn (mp 232 °C) serves as an effective flux for the growth of antimonide crystals, such as RE_3TiSb_5 and $RECrSb_3$.[30,35] In the case of germanides, previous literature suggests the use of In flux,[67] but we are also interested in extending the use of Sn flux to these systems. Upon completion of the reaction, the Sn flux can be centrifuged off while still molten and any remaining Sn in the solid can be removed by treatment with HCl.

The choice of a heating program for the synthesis must be considered carefully. Although phase diagram information is still largely lacking for many ternary antimonide and germanide systems, phase diagrams for the binary systems may be consulted for initial guidance on the appropriate reaction temperature. Generally a pre-heating step is advisable in which the reactants are heated quickly

to a temperature at which at least one element is starting to melt. The reaction begins but at this moderate temperature it does not go out of control if exothermic. Next, the reactants are taken to a higher temperature and held there for a sufficiently long time to attain complete reaction. Finally, if the growth of single crystals is desired, the system is slowly cooled from the melt (with or without flux). However, there may be some disadvantages for slow cooling, since phase transitions or decomposition may occur at lower temperatures, or incomplete reaction may lead to the formation of byproducts that are difficult to remove.

1.3. Characterization

1.3.1. Energy Dispersive X-ray (EDX) Analysis

The elemental composition of an intermetallic phase is typically determined by energy-dispersive X-ray (EDX) analysis on a scanning electron microscope (SEM). The principle behind this technique is illustrated in Figure 1–12.[68] When the surface of the solid is bombarded with a high-energy incident electron beam, core-shell electrons in atoms are ionized, leaving a hole. The atom relaxes by a process in which electrons from higher energy levels fill this vacancy. In the course of this relaxation process, X-ray photons of a particular wavelength and energy are emitted, and detected in an energy-dispersive spectrometer. Because the X-ray energy is characteristic of the energy difference between the two levels of a specific element, this technique provides a means for qualitative analysis of elements. If the intensity of the emitted X-ray is also measured, then

a quantitative analysis can also be obtained. EDX can thus be used to determine the elemental composition of a single crystal or to identify phases in a multiphase alloy sample. However, the accuracy of quantitative EDX analysis depends critically on sample preparation and the availability of standards. Ideally, surfaces must be highly polished to minimize geometric effects. If pure elements are used as standards, a typical ~5% error may be expected. EDX analysis was conducted on a Hitachi S-2700 scanning electron microscope with use of an acceleration voltage of 20 kV. More precise measurements were performed on a JEOL 8900 electron microprobe which has a higher electron beam current.

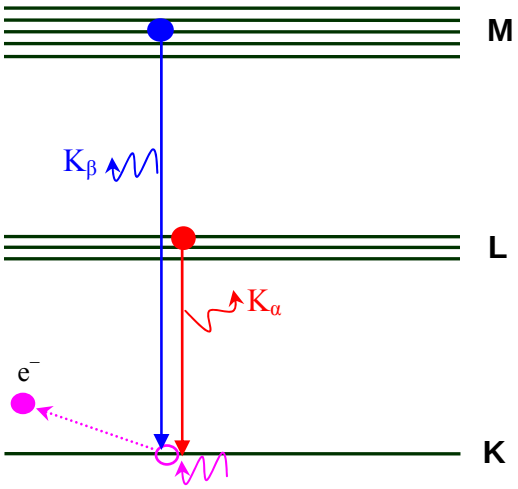

Figure 1–12. The principle of EDX analysis.

1.3.2. X-ray Diffraction

In molecular chemistry, NMR and IR spectroscopy are normally the most important characterization techniques to determine the structure of a compound.

However, this is generally not the case for extended solids. In particular, these spectroscopic techniques are useless for intermetallic compounds, which may contain many heavy and highly magnetic elements. Thus, X-ray diffraction is clearly the most important and powerful technique to determine the crystal structures of solid state compounds, and has been widely applied to many types of materials.

The basic principle behind X-ray diffraction can be summarized through Bragg's law (Figure 1–13).[65,69] A crystal consists of a periodic arrangement of atoms, and may be thought of as consisting of many planes of atoms separated by a constant spacing d_{hkl}. When incident X-rays of a specific wavelength (e.g. Mo Kα, λ = 0.71073 Å) strike a crystal (containing interatomic distances of a similar magnitude, say, 1 to 3 Å), constructive interference will occur only if Bragg's law is satisfied:

$$\sin \theta = \lambda / 2d_{hkl} \qquad \text{(Equation 1–3)}$$

where λ is the wavelength, d_{hkl} is the interplanar spacing, and θ (or 2θ) is the diffraction angle. The generated diffraction patterns contain diffraction angles, which provide information about the unit cell geometry, and the intensities, which provide information about the location of atoms within the unit cell. X-ray diffraction can be performed on either powder or single-crystal samples, each with its own advantages and disadvantages.

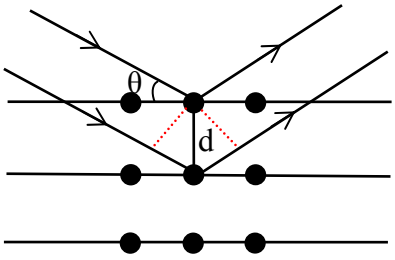

Figure 1–13. The constructive interference to satisfy the Bragg law.

1.3.2.1 Powder X-ray Diffraction

Although the ideal situation is to analyze single crystals through X-ray diffraction, this is often not possible, either because they are difficult to grow synthetically or because a crystal tested on a diffractometer is somehow unsuitable due to its poor quality (e.g., weak intensities, overlapping lattices, powder arcs, twinning). In such circumstances, powder X-ray diffraction may be used.

In powder X-ray diffraction, reflections that are normally distinguishable in 3D space are projected onto a 1D pattern, such that overlapping reflections may appear at the same diffraction angle. Thus, it is usually very difficult to determine a crystal structure directly from powder X-ray diffraction, especially when the structure is of a new or unknown type. Nevertheless, powder X-ray diffraction serves as a very useful and rapid method for phase analysis, because each crystalline phase has a characteristic pattern. By matching experimental with simulated powder patterns, we can fingerprint different phases within a

sample. If a new compound is suspected to have a structure that resembles that of a known one, then they will have similar powder patterns, with only slight differences in diffraction angles and intensities. It is then possible to refine the structure of such a new compound by the Rietveld method, yielding precise cell parameters, atomic positions, and displacement parameters.[70] In a multiphase sample, it is also possible to perform a quantitative analysis to determine the percent composition of each phase.

Experimentally, a finely ground powder sample is mounted and smoothed onto a sample holder. Powder X-ray diffraction data were collected on an Inel powder diffractometer equipped with a curved position-sensitive (CPS) detector, which allows reflections to be collected simultaneously over a wide 2θ range (0 to 120°) with the step size of 0.029°. For qualitative phase analysis, a rapid data collection (1 hour or less) is sufficient, but a longer time (3 hours or more) may be needed to obtain accurate high-resolution data required for Rietveld refinement. Among the many freely available and user-friendly software packages for full-profile Rietveld refinement (e.g., Fullprof,[71] GSAS,[72] and LHPM-Rietica[73]), the latter was used for all refinements performed in this thesis. Initial positions were taken from the reported isostructural compound. The least-squares refinement includes scale factor, background, zero point, cell parameters, pseudo-Voigt peak profile parameters, atomic coordinates, and isotropic displacement parameters and preferred orientation.

1.3.2.2 Single-Crystal X-ray Diffraction

Excellent textbooks for understanding the principles behind single-crystal X-ray diffraction are available.[65,69,74] The intent here is simply to provide some details about how data were collected and how structures were refined in the following discussion.

In general, a single crystal of high quality and suitable size (<0.5 mm) was picked and mounted on a glass fiber attached to a brass pin. The crystal was then mounted on a goniometer head and centred optically with the aid of a camera on a Bruker Platform / SMART 1000 CCD-equipped diffractometer. A few frames were collected to determine if the crystal diffracts well. If the crystal was found to be suitable, unit cell parameters and an orientation matrix were determined. A full data set was collected with an ω-scan of 0.3° per frame for a 20-second exposure time. Because the compounds studied normally contain many heavy elements, absorption corrections were critical and the crystal faces and dimensions were carefully measured. Data reduction and integration was performed using the program SAINT. A numerical face-indexed absorption correction was applied with use of the program SADABS. The SHELXTL package was used to solve and refine the crystal structure.[75] A space group was initially chosen based on systematic extinctions and intensity statistics. If a compound adopts a known structure type (slightly shifted unit cell parameters and the same space group), the coordinates for each atom can be taken from the

known structure and used as a starting model for the refinement. For compounds with new structures, direct methods or Patterson (heavy atom) methods were used to locate the atomic positions. Full-matrix least-squares refinements were carried out on F^2.[69] A good refinement is judged not only by low residual factors (less than 8%) and goodness-of-fit (close to 1), but also low standard uncertainties in the metrical parameters (bond lengths and angles), reasonable displacement parameters, and sensible chemical bonding and coordination environments.

1.4. Band Structure Calculation

Because a goal of this thesis is to understand the bonding in antimonides and germanides, it is important to determine the detailed electronic structure of these compounds. Earlier we attributed different bonding character (e.g. classical vs. non-classical Sb–Sb bonds) largely through correlation with interatomic distances or simple electron-counting schemes. How can the strength of a bond be quantified more precisely? Unlike a molecule, where a molecular orbital diagram is (relatively) simple to calculate, a solid has many energy levels because it is inherently an infinite structure. Although it is possible, in principle, to calculate the electronic structure of a solid from quantum mechanical methods by solving the many-body Schrödinger equation in a crystal, this is too complicated because of the numerous interactions between a very large number of electrons.

One approach to simplifying this problem is to apply density functional theory (DFT). Thus, the problem of numerous interacting electrons is greatly reduced to one in which there is an effective one-particle Kohn-Sham equation which combines the Coulomb potential of nuclei, the Hartree potential, and the exchange-correlation potential.[76]

The Stuttgart tight-binding linear muffin-tin orbital (TB-LMTO) program has been employed for band structure calculations in this thesis.[77a] In this method, the potential function is modeled by dividing up the space within the unit cell into "muffin-tin" spheres, with one sphere of some specified radius centred at each atomic site. Empty spaces between atoms are filled by adding empty spheres with zero potential. The local density approximation (LDA) and atomic spheres approximation (ASA) for exchange-correlation energy are made in this calculation.[77b]

The band structure calculation generates density of states (DOS) and crystal orbital Hamilton population (COHP) curves.[78] The DOS curve provides, among other things, information about the general electrical properties (insulator, semiconductor, or metal) according to the separation between valence and conduction bands, and orbital character of states. The COHP curve gives information about the bond strength and bonding character according to how the atomic orbitals overlap.

1.5. Physical Properties

Because intermetallics can be used in many applications as electrical, magnetic, or thermal materials, as described earlier, it is of interest to measure the physical properties of any new compounds discovered. Moreover, the electrical and magnetic properties can give information about the electronic structure and oxidation states, which may be useful for further support of bonding models (e.g. electron-counting rules).

1.5.1. Electrical Properties

Electrical properties, electronic structures, and crystal structures are closely related to each other. Classical Zintl phases, where there is a large electronegativity difference between the electropositive and electronegative elements, should lead to semiconductor behaviour. Hume-Rothery phases, where electrons are delocalized within the whole structure, exhibit metallic behaviour. However, the prediction of electrical properties is not obvious for compounds intermediate between these extremes. The intermetallics studied in this thesis have less polar character than in traditional Zintl phases, and could exhibit either metallic or semiconductor properties. Resistivity measurements provide a way to understand crystal structures, to test the validity of the proposed bonding schemes, and to help us understand their electronic structures.

The electrical resistivity data in this thesis were measured by a four-probe

method on a Quantum Design PPMS-9T system.[79] Large regular-shaped crystals, if available, were selected and mounted to four graphite fibers attached to gold wires with Ag paint. The resistivity data were measured at variable temperatures between 2 and 300 K by controlling the flow of liquid nitrogen and helium in the PPMS system. At each temperature, the resistivity of a material is calculated by:

$$\rho = \frac{VA}{Il} \qquad \text{(Equation 1–4)}$$

where V is the applied voltage, I is the current, A is the cross-sectional area, and l is the length between the two inner leads (Figure 1–14). From this measurement, the electrical resistivity as a function of temperature (2 to 300 K) is obtained. On the basis of this dependence, solid-state materials can usually be classified into four categories: metal, semiconductor, insulator, and superconductor (Figure 1–15). Because metallic behaviour was typically observed in the compounds studied in this thesis, it will be given more focus.

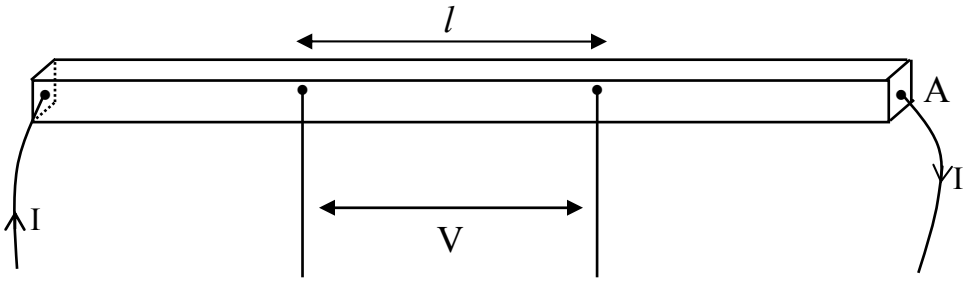

Figure 1–14. The setup of four-probe arrangement of resistivity measurement.

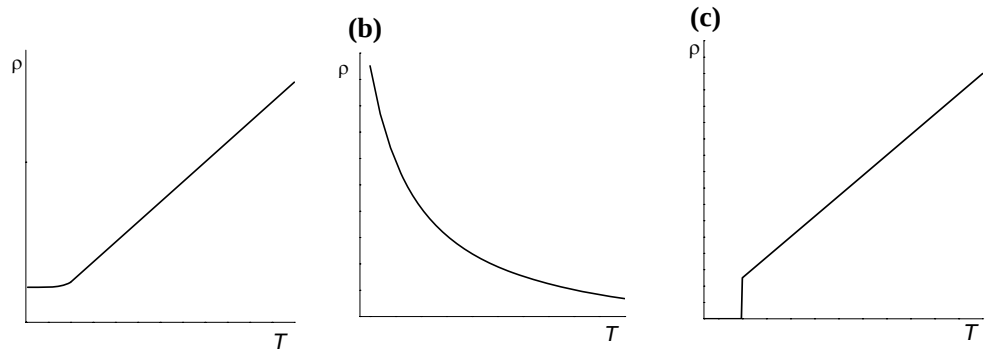

Figure 1–15. The resistivity (ρ) changes as a function of temperature (*T*) in: (a) metal; (b) semiconductor or insulator; (c) superconductor.

To understand the origins of metallic behaviour, it is helpful to recast the electrical resistivity by its inverse, the electrical conductivity, which is governed by the following equation:[65,74]

$$\sigma = \frac{1}{\rho} = ne\mu \qquad \text{(Equation 1–5)}$$

where n is the number of charge carriers, μ is their mobility, and e is the charge on the carriers, which are electrons in this case. In metals, where valence electrons experience nearly zero potential and are free to move within the solid, the number of charge carriers, n, is very large and almost constant. Thus, the conductivity is mainly controlled by the mobility of electrons, μ, which is mostly impeded by scattering with phonons (i.e. lattice vibrations). As the temperature is decreased, the scattering is diminished, thereby enhancing the mobility. At low temperatures, the conductivity increases (or the resistivity decreases). However,

except in very pure samples, the resistivity does not approach zero even when the temperature is very low because of scattering with impurities or defects, but rather reaches a plateau representing a residual resistivity value.

In many intermetallic compounds that also undergo magnetic ordering, it is often observed that there is a corresponding electronic transition in the resistivity curve. The occurrence of spin ordering or magnetic phase transitions will change the orientation of the conduction electrons, as reflected in a change in slope in the resistivity curve. That is, there is a loss of "spin-disorder scattering", another mechanism that controls the flow of electrons, so the resistivity often diminishes below the magnetic ordering temperature. Another phenomenon often observed in intermetallics containing Ce is that the resistivity reaches a local minimum at some temperature. Termed the *Kondo effect*, this feature was explained by Jun Kondo who proposed that localized spins from impurities interact with the conduction electrons, leading to resonant scattering of the conduction electrons and thus increasing resistivity.[80]

Other classes of materials are insulators and semiconductors, which have a completely filled valence band and an empty conduction band, separated by a band gap (E_g). The division between insulators and semiconductors is somewhat arbitrary, based on the value of E_g. For insulators, the band gap is greater than ~3 eV and there are essentially no electrons in the conduction band. The number of carriers n is zero and therefore the conductivity is extremely low for insulators.

For semiconductors, the band gap is between 0 and 3 eV. Because of this smaller band gap, electrons in the valence band can be promoted to the conduction band by thermal or optical activation. The number of carriers *n* increases exponentially with temperature, thus leading to the increased resistivity with decreased temperature. Superconductors, of course, represent a much more interesting class of electronic materials, where the electrical resistivity drops to zero at some critical temperature T_c, but this is not the focus of this thesis.

1.5.2. Magnetic Properties

Ternary rare-earth transition-metal antimonides and germanides exhibit interesting magnetic properties because of the co-existence of unpaired f-electrons and d-electrons. Magnetic investigations not only help us to determine the oxidation states of magnetic centres, but more importantly, they also provide a way to identify the properties that might be useful in industrial applications.

The magnetic properties of synthesized pure materials were measured in our lab on a Quantum Design 9T Physical Properties Measurement System (PPMS). After a powder sample is placed and centred in the magnetometer, the magnetization (*M*) is measured in the presence of an applied external magnetic field (*H*). The magnetic susceptibility (χ) is a measure of how the magnetization (*M*) of a material reacts to an applied magnetic field (*H*):

$$\chi = \frac{M}{H} \qquad \text{(Equation 1–6)}$$

Three different sequences have been used to characterize the magnetic behaviour of a pure sample: (i) dc magnetic susceptibility as a function of temperature (which is controlled by the flow liquid He and N_2) at a fixed field, (ii) magnetization at a function of applied field (which is controlled by the voltage applied to the superconductor), at a fixed temperature, and (iii) ac susceptibility as a function of temperature, at a fixed frequency. The dc susceptibility curve can provide information about the magnetic ordering temperature, the general magnetic behaviour, and experimental effective magnetic moments, which can help us to identify the oxidation state of a magnetic centre. The ac susceptibility curve is obtained without the application of external magnetic field, thus giving a more accurate measurement of the transition temperature of a material. The dc magnetization curve can help us to identify the magnetic behaviour of a material at different temperature. For all pure phases in this thesis, these three curves are measured to understand their magnetic behaviour.

Here, several basic equations and principles of magnetism are introduced.[81] In a free ion or atom, the magnetism originates from the orbital (*L*) and spin (*S*) angular momentum of the unpaired electrons. Both factors are combined into the Landé factor *g*:

$$g = 1 + \frac{J(J+1) + S(S+1) - L(L+1)}{2J(J+1)} \qquad \text{(Equation 1–7)}$$

where J is the total angular momentum quantum number. For a transition-metal ion, the d-orbital angular momentum (L) is often quenched by a crystal field effect, so the Landé factor g reduces to 2. However, for rare-earth metals with unpaired f electrons, since the f-orbitals are closer to the nucleus and not influenced by the crystal field effect, both L and S contribute to the value of g. The effective magnetic moment for a free atom or ion can be calculated as follows:

$$\mu_{eff} = g\sqrt{J(J+1)} \qquad \text{(Equation 1–8)}$$

where μ_{eff} is in units of Bohr magnetons (μ_B). The theoretical effective magnetic moment can be calculated and compared with the experimental value, thus providing a means to determine oxidation states of the magnetic centres, as will be discussed later. Table 1–3 lists the theoretical effective magnetic moment for the free trivalent *RE* ions.

Magnetic materials can be classified into several major types according to different spin arrangements, as shown in Figure 1–16, which will be discussed below.[81–83]

1.5.2.1. Diamagnetism

Diamagnetism is a property of all materials arising from the paired electrons in the core levels of atoms. The magnetization is a small and negative value, which is independent on applied field and temperature.

Table 1–3. Theoretical effective magnetic moments for the free RE^{3+} ions.

ion	configuration	term symbol	μ_{eff}(calc) = $g\,[J\,(J+1)]^{1/2}$
Ce^{3+}	$4f^1$	$^2F_{5/2}$	2.54
Pr^{3+}	$4f^2$	$^3H_4$	3.58
Nd^{3+}	$4f^3$	$^4I_{9/2}$	3.62
Pm^{3+}	$4f^4$	$^5I_4$	2.68
Sm^{3+}	$4f^5$	$^6H_{5/2}$	0.84
Eu^{3+}	$4f^6$	$^7F_0$	0
Gd^{3+}	$4f^7$	$^8S_{7/2}$	7.94
Tb^{3+}	$4f^8$	$^7F_6$	9.72
Dy^{3+}	$4f^9$	$^6H_{15/2}$	10.63
Ho^{3+}	$4f^{10}$	$^5I_8$	10.60
Er^{3+}	$4f^{11}$	$^4I_{15/2}$	9.59
Tm^{3+}	$4f^{12}$	$^3H_6$	7.57
Yb^{3+}	$4f^{13}$	$^2F_{7/2}$	4.54

(a)

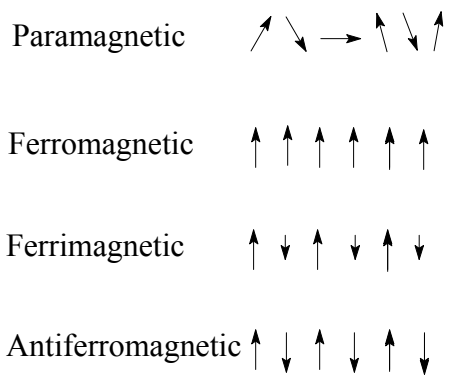

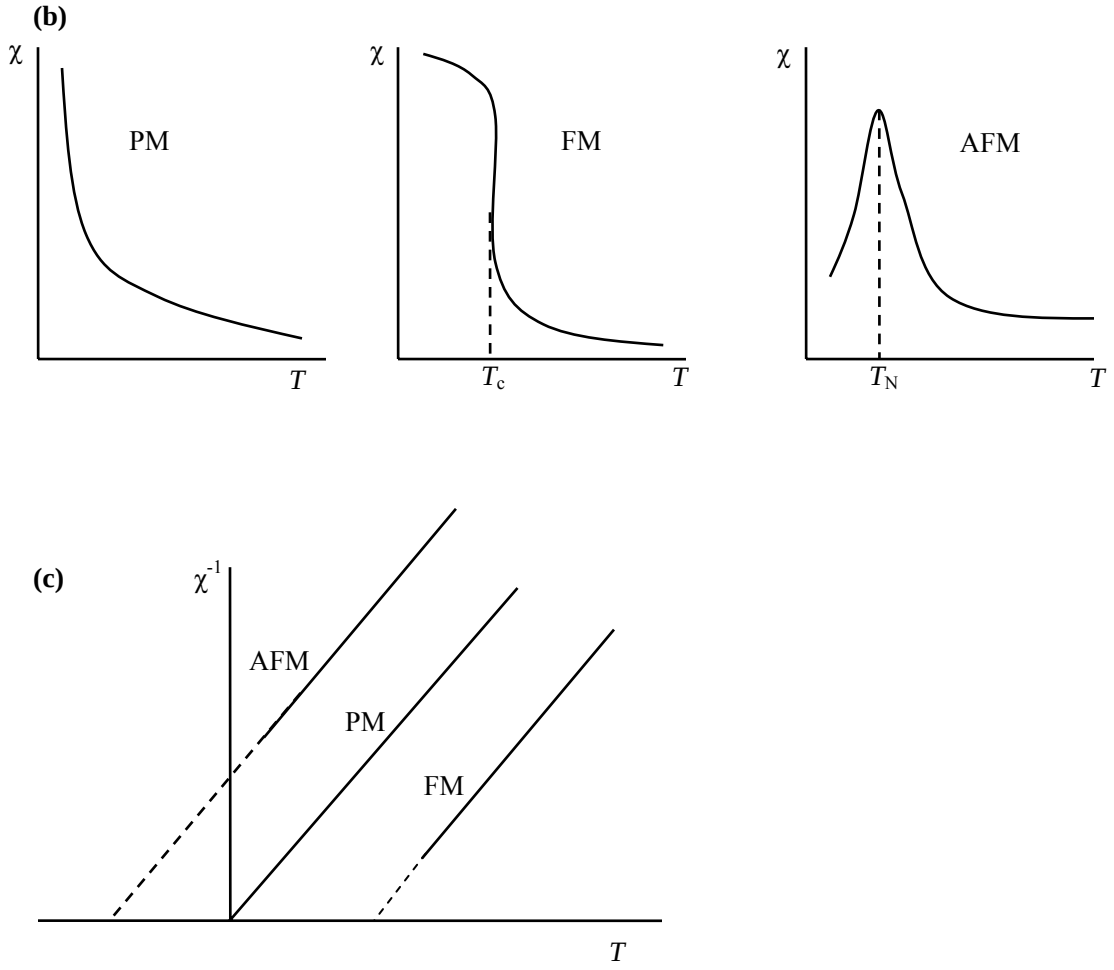

Figure 1–16. **(**a) The magnetic spin arrangements; (b) the temperature dependence of susceptibility; and (c) the temperature dependence of the inverse susceptibility (satisfying the Curie or Curie-Weiss law) in paramagnetic (PM), ferromagnetic (FM), and antiferromagnetic (AFM) materials.

1.5.2.2. Paramagnetism (PM)

Paramagnetic materials have unpaired electrons that are not coupled with each other. The spins are randomly oriented in the absence of an applied magnetic field. However, in the presence of a magnetic field, the spins try to align along the applied field direction, and the magnetization has a linear

relationship to the applied external magnetic field *H*. The susceptibility for paramagnetic materials increases with decreasing temperature because of less randomization of the spins. The susceptibility curve follows the Curie Law: [83]

$$\chi = \frac{C}{T} \qquad \text{(Equation 1–9)}$$

where *T* is the temperature and *C* is the Curie constant. From the Curie constant, we can calculate the experimental effective magnetic moment:

$$\mu_{eff} = 2.828\sqrt{C} \qquad \text{(Equation 1–10)}$$

The number of unpaired electrons on a magnetic centre (usually transition metal or rare-earth metal) and its oxidation state can be determined from Equation 1–7 and 1–8 above.

1.5.2.3. Pauli Paramagnetism

Pauli paramagnetism arises in metals or metallic materials with paired electrons delocalized in the whole material. When a magnetic field is applied, the spin-up electrons and spin-down electrons are re-oriented and exchanged, leading to a slight excess of spins aligned parallel to the field. The susceptibility generated by the excess number of spins is positive, small, and temperature-independent (Figure 1–17).

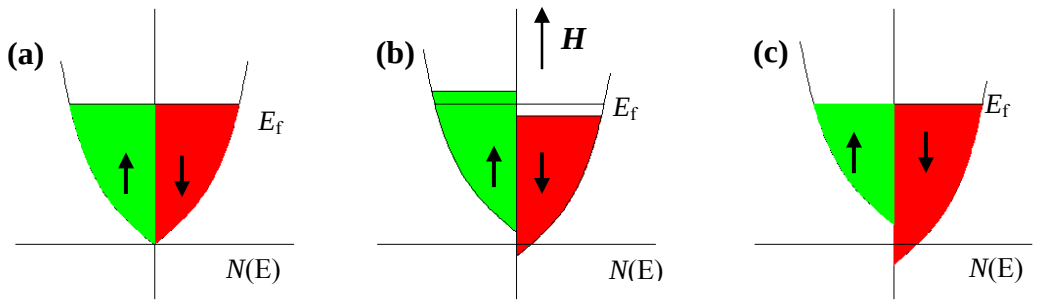

Figure 1–17. Schematic band structure for a Pauli paramagnet: (a) spin-up and spin-down initial state; (b) non-equilibrium state in the presence of a magnetic field; (c) equilibrium state.

1.5.2.4. Ferromagnetism (FM)

When magnetic moments of all individual magnetic centres in a material are ordered, and spontaneously aligned parallel to each other, ferromagnetic behaviour is said to be exhibited. The magnetic susceptibility is highly temperature-dependent, and increases dramatically at a critical temperature (T_c), below which spins align with each other spontaneously. Above T_c, the spins are arranged randomly due to the increased thermal energy, preventing the ferromagnetic ordering. Because of these spin-spin interactions, the susceptibility does not follow the Curie law, but rather the Curie-Weiss law: [83]

$$\chi = \frac{C}{T - \theta} \qquad \text{(Equation 1–11)}$$

or the modified Curie-Weiss law:

$$\chi = \chi_0 + \frac{C}{T - \theta} \qquad \text{(Equation 1–12)}$$

where θ is the Weiss temperature and χ_o is a temperature-independent term that may be included to account for contribution from conduction electrons. When

the inverse magnetic susceptibility curve is fit to the Curie-Weiss law or the modified version, a ferromagnetic material will generate a positive Weiss temperature, with the absolute value reflecting the strength of the coupling.

A domain structure forms in ferromagnetic materials to minimize the total energy. Within each domain, the spins are all aligned, but different domains are aligned randomly with respect to each other. Walls between neighbouring domains can be moved when an external magnetic field is applied, leading to an irreversible behaviour manifested by a hysteresis loop in the magnetization curves, a unique characteristic of ferromagnetic materials.

1.5.2.5. Ferrimagnetism

When magnetic moments of neighbouring magnetic centres are ordered in an anti-parallel orientation but the sum of the moments does not equal zero, the material is said to exhibit ferrimagnetism. Although spins are aligned in the similar way as in AFM, the magnetic properties of ferrimagnets generally resemble those of ferromagnets: both exhibit spontaneous magnetization with saturation and increasing susceptibility when the temperature is lowered.

1.5.2.6. Antiferromagnetism (AFM)

When unpaired electrons are aligned anti-parallel to each other, antiferromagnetic behaviour is said to be exhibited. In such a material, the susceptibility first increases when the temperature is lowered, because the spins

begin to align with the field. Below a critical temperature called the Néel temperature (T_N) characteristic of an antiferromagnet, however, the susceptibility then decreases as the spins begin to favour an anti-parallel ordering. Unlike ferromagnets, a negative Weiss temperature is observed after fitting to the Curie-Weiss law.

1.5.2.7. RKKY Interaction and de Gennes Factor[84]

When electrons behave as local moments, they can interact between each other through a direct exchange, arising from a Coulomb interaction between orbitals of neighbouring atoms. In compounds containing rare-earth atoms as the only source of unpaired electrons, this direct exchange is not effective unless the overlap between 4f orbitals is good, that is, if the atoms are in close contact. In contrast, ternary rare-earth transition-metal intermetallic compounds contain at least two sources of unpaired electrons: the more localized 4f electrons of the rare-earth atoms, and the more delocalized (itinerant) d electrons of the transition-metal atoms. The interaction between 4f electrons can now occur through the polarization of conduction electrons of the transition-metal component, a mechanism proposed by Ruderman, Kittel, Kasuya, and Yosida (RKKY). In this RKKY model, which applies to both AFM and FM materials where there is spin polarization of the conduction electrons, the magnetic ordering temperature (T_N or T_C) is predicted to have a linear relationship with the de Gennes factor, dG, for a series of isostructural rare-earth compounds:

$$dG = (g-1)^2 J(J+1) \qquad \text{(Equation 1–13)}$$

However, this relationship may not hold if the ordering temperature is affected by a crystalline electric field (CEF).

1.5.2.8. Itinerant d-Electron Magnetism[76,83,85]

The conduction electrons originating from the transition-metal component play an important role in influencing the magnetic interaction between 4f local magnetic moments in rare-earth transition-metal intermetallic compounds. In general, the localized moment magnetism model is able to explain a diluted rare-earth system successfully, but not the magnetic properties of conduction electrons. For example, the metallic elements Fe, Co, and Ni exhibit strong FM behaviour, with magnetic moments that do not correspond to an integer number of electrons predicted by localized moment model. The magnetism in these types of materials can be explained by the Stoner theory (Figure 1–18). In a partially filled energy band with high DOS, the large exchange energy removes the degeneracy of the spin-up and spin-down electrons, leading to an imbalance of numbers of spins. (The exchange energy is minimized when all electrons have the same spin.) This phenomenon is similar to what observed in Pauli paramagnetism, but occurs spontaneously. It originates from the delocalized conduction electrons in the narrow, partially filled *d*-band. The electrons near E_f are not stable and rearranged thus generating the ferromagnetic behaviour. This theory explains the observed smaller saturated magnetic moments for

3d-transition-metal-containing systems but it only applies for ferromagnetic materials.

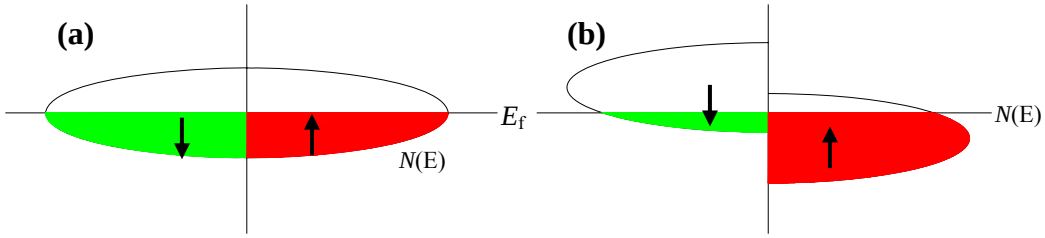

Figure 1–18. Schematic band structure for an itinerant ferromagnet according to Stoner theory: (a) nonmagnetic state; b) magnetic state.

1.6. Thesis Outline

Ternary rare-earth transition metal antimonides and germanides *RE*–*M*–(Sb or Ge) are now relatively well known for later transition metals *M*, but systems containing earlier transition metals, such as Ti, V, and Cr, have not been well studied. This thesis presents several new compounds in these systems. The body of this work is based on papers already published or in submission.

Chapters 2 and **3** present the crystal structures, bonding, and physical properties of $RE_2Ti_7Sb_{12}$ (*RE* = La–Nd) and $RE_2Ti_{11-x}Sb_{14+x}$ (*RE* = Sm, Gd, Tb and Yb) found in *RE*–Ti–Sb systems.

Chapters 4 and **5** discuss the structures, bonding, and physical properties of two series of hexagonal perovskite-type compounds $RECrGe_3$ (*RE* = La–Nd, Sm) and $REVGe_3$ (*RE* = La–Nd).

Chapter 6 addresses the bonding, structures, and magnetic properties of

non-stoichiometric $CeNiSi_2$-type $RECr_xGe_2$ (*RE* = Sm, Gd–Er) compounds.

Chapters 7 and **8** present attempts to integrate Ge and Sb, which have different numbers of valence electrons, to form new compounds in the *RE*–Ge–Sb system. Two new series of compounds, $RE_{12}Ge_{7-x}Sb_{21}$ and $RE_5Ge_xSb_{3-x}$, have been synthesized. Their structures, bonding, and physical properties are discussed.

Chapter 9 summarizes the work in a conclusion and offers ideas for future directions.

1.7. References

(1) Sauthoff, G. *Intermetallics*; VCH: Weinheim, 1995.

(2) a) Ferro, R.; Saccone, A. *Intermetallic Chemistry*; Cahn, R. W., Ed. Elsevier: Pergamon Materials Series, Oxford, 2008; b) Pfeiler, W., Ed. *Alloy Physics*; Wiley–VCH: Weinheim, 2007; c) Westbrook, J. H., Fleischer, R. L., Eds. *Intermetallic Compounds: Principles and Practice*; Wiley: Chichester, 2002; Vol. 3, pp 469–561.

(3) Nesper, R. *Angew. Chem. Int. Ed.* **1991**, *30*, 789–817.

(4) Kauzlarich, S. M., Ed. *Chemistry, Structure and Bonding of Zintl Phases and Ions*; VCH Publishers: New York, 1996.

(5) Brandon, K. J.; Brizard, R. Y.; Chieh, P. C.; McMillan, R. K.; Pearson, W. B. *Acta Crytallogr. Sect. B,* **1974**, *B30*, 1412–1417.

(6) Heidenstam, O.; Johansson, A.; Westman, S. *Acta Chem. Scand.* **1968**, *22*, 653–661.

(7) Pauling scale electronegativity and Pauling metallic radii R_1 have been used for reference in this thesis. Data are from: Pauling, L. *The Nature of the Chemical Bond,* 3rd ed.; Cornell University Press: Ithaca, NY, 1960.

(8) Zintl, E.; Woltersdorf, G. *Z. Elektrochem.* **1935**, *41*, 876.

(9) a) Klemm, W. *Proc. Chem. Soc. (London)*, **1959**, 329; b) Schäfer, H.; Eisenmann, B.; Müller, W. *Angew. Chem. Int. Ed.* **1973**, *12*, 694.

(10) Müller, U. *Inorganic Structural Chemistry*, 2nd ed.; Wiley: Chichester, 2007.

(11) a) Eisenmann, B.; Schäfer, H. *Z. Naturforsch., B: Anorg. Chem. Org. Chem.* **1974**, *29 (1-2)*, 13–15; b) Martinez-Ripoll, M.; Haase, A.; Brauer, G. *Acta Crystallogr., Sect. B*, **1973**, *29(8)*, 1715–1717.

(12) a) Brauer, G.; Zintl, E. *Z. phys. Chem., Abt. B,* **1937**, *37*, 323–352; b) Chikawa, J.; Imamura, S.; Tanaka, K.; Shiojiri, M. *J. Phys. Soc. Jpn.* **1961**, *16*, 1175–1180.

(13) Hurng, W.-M.; Corbett, J. D. *Chem. Mater.* **1989**, *1*, 311–319.

(14) Brechtel, E.; Cordier G.; Schäfer, H. *Z. Naturforsch., B: Anorg. Chem. Org. Chem.* **1981**, *36B(10)*, 1341–1342.

(15) Hirschle, C.; Röhr, C. *Z. Anorg. Allg. Chem.* **2000**, *626(9)*, 1992–1998.

(16) a) Deller, K.; Eisenmann, B. *Z. Naturforsch., B: Anorg. Chem. Org. Chem.* **1976**, *31B(1)*, 29–34; b) Rehr, A.; Kauzlarich, S. M. *Acta Crystallogr., Sect. C* **1994**, C*50(12)*, 1859–1861.

(17) a) Eisenmann, B. *Z. Naturforsch., B: Anorg. Chem. Org. Chem.* **1979**, *34B(8)*, 1162–1164; b) Eisenmann, B.; Jordan, H.; Schäfer, H. *Z. Naturforsch., B: Anorg. Chem. Org. Chem.* **1985**, *40B(12)*, 1603–1606.

(18) a) Deller, K.; Eisenmann, B. *Z. Anorg. Allg. Chem.* **1976**, *425(2)*, 104–108; b) Deller, K.; Eisenmann, B. *Z. Naturforsch., B: Anorg. Chem. Org. Chem.* **1976**, *31B(8)*, 1146–1147.

(19) a) Hönle, W.; Von Schnering, H. G. *Z. Kristallogr.* **1981**, *155,* 307–314; b) Cromer, D. T. *Acta Crystallogr.* **1959**, *12*, 41–45.

(20) Rehr, A.; Guerra, F.; Parkin, S.; Hope, H.; Kauzlarich, S. M. *Inorg. Chem.* **1995**, *34(24)*, 6218–6220.

(21) Deller, K.; Eisenmann, B. *Z. Naturforsch., B: Anorg. Chem. Org. Chem.* **1978**, *33B(6)*, 676–681.

(22) Emmerling, F.; Hirschle, C.; Röhr, C. *Z. Anorg. Allg. Chem.* **2002**, *628*, 559–563.

(23) Brown, I. D. *Structure and Bonding in Crystals*; O'Keeffe, M.; Navrotsky, A., Eds.; Academic Press: New York, 1981; Vol. 2, pp 1–30.

(24) O'Keeffe, M.; Brese, N. E. *J. Am. Chem. Soc.* **1991**, *113*, 3226–3229.

(25) a) Brock, S. L.; Weston, L. J.; Olmstead, M. M.; Kauzlarich, S. M. *J. Solid State Chem.*. **1993**, *107*, 513–523; b) Cordier, G.; Schäfer, H.; Stelter, M. *Z. Anorg. Allg. Chem.* **1984**, *519*, 183–188.

(26) Kleinke, H. Nonclassical Sb–Sb Bonding in Transition Metal Antimonides. In *Inorganic Chemistry in Focus II*; Meyer, G., Naumann, D., Wesemann, L., Eds.; Wiley-VCH: Weinheim, Germany, 2005; pp 167–191.

(27) a) Papoian, G. A.; Hoffmann, R. *Angew. Chem. Int. Ed.* **2000**, *39*, 2408–2448; b) Papoian, G. A.; Hoffmann, R. *J. Am. Chem. Soc.* **2001**, *123*, 6600–6608.

(28) Xu, J.; Kleinke, H. *J. Comput. Chem.* **2008**, *29(13)*, 2134–2143.

(29) Mills, A. M.; Lam, R.; Ferguson, M. J.; Deakin, L.; Mar, A. *Coord. Chem. Rev.* **2002**, *233–234*, 207–222.

(30) a) Bolloré, G.; Ferguson, M. J.; Hushagen, R. W.; Mar, A. *Chem. Mater.* **1995**, *7(12)*, 2229–2231; b) Moore, S. H.; Deakin, L.; Ferguson, M. J.; Mar, A. *Chem. Mater.* **2002**, *14(11)*, 4867–4873.

(31) Stetskiv, A. O.; Pavlyuk, V. V.; Bodak, O. I. *Pol. J. Chem.* **1998**, *72*, 956–958.

(32) Lam, R.; McDonald, R.; Mar, A. *Inorg. Chem.* **2001**, *40*, 952–959.

(33) Liu, Y.; Chen, L.; Li, L.-H.; Wu, L.-M; Zelinska, O. Ya.; Mar, A. *Inorg. Chem.* **2008**, *47*, 11930–11941.

(34) a) Mills, A. M.; Mar, A. *Inorg. Chem.* **2000**, *39*, 4599–4607; b) Mills, A. M.; Deakin, L.; Mar, A. *Chem. Mater.* **2001**, *13(5)*, 1778–1788.

(35) a) Ferguson, M. J.; Hushagen, R. W.; Mar, A. *J. Alloys Compd.* **1997**, *249(1-2)*, 191–198; b) Brylak, M.; Jeitschko, W. *Z. Naturforsch*., *B*: *Chem. Sci.* **1995**, *50(6)*, 899–904.

(36) a) Tkachuk, A. V.; Crerar, S. J.; Wu, X.; Muirhead, C. P. T.; Deakin, L.; Mar, A. *Mater. Res. Soc. Symp. Proc.* **2005**, *848*, 75–82; b) Tkachuk, A. V.; Muirhead, C. P. T.; Mar, A. *J. Alloys Compd.* **2006**, *418*, 39–44.

(37) a) Mar, A.; Tougait, O.; Potel, M.; Noël, H.; Lopes, E. B. *Chem. Mater.* **2006**, *18(18)*, 4533–4540; b) Brylak, M.; Jeitschko, W. *Z. Naturforsch*., *B*: *Chem. Sci.* **1994**, *49(6)*, 747–752.

(38) Wang, R.; Bodnar, R.; Steinfink, H. *Inorg. Chem.* **1966**, *5(8)*, 1468–1470.

(39) Bodnar, R. E.; Steinfink, H.; Narasimhan, K. S. V. L. *J. Appl. Phys.* **1968**, *39*, 1485–1489.

(40) Wang, R.; Steinfink, H. *Inorg. Chem.* **1967**, *6(9)*, 1685–1692.

(41) a) Wang, Y.; Calvert, L. D.; Taylor, J. B. *Acta Crystallogr., Sect. B* **1980**, *36*, 221–222; b) Hohnke, D.; Parthé, E. *Acta Crystallogr.* **1966**, *21*, 435–437.

(42) a) Yakinthos, J. K.; Semitelou, I. P. *J. Magn. Magn. Mater.*, **1983**, *36(1-2)*, 136–140; b) Gladyshevskii, E. I. *Zh. Strukt. Khim.* **1964**, *5(6)*, 919–921.

(43) Boulet, P.; Gross, G. M.; André, G.; Bourée, F.; Noël, H. *J. Solid State Chem.* **1999**, *144(2)*, 311–317.

(44) Grosch, G. H.; Range, K. J. *J. Alloys Compd.* **1996**, *235*, 250–255.

(45) Migas, D. B.; Miglio, L.; Shaposhnikov, V. L.; Borisenko, V. E. *Phys. Rev. B* **2003**, *67*, 205203.

(46) Turban, K.; Schäfer, H. *Z. Naturforsch., B: Anorg. Chem. Org. Chem.* **1973**, *28 (3-4)*, 220–222.

(47) Bruzzone, G.; Franceschi, E. *J. Less-Common Met.* **1978**, *57*, 201–208.

(48) Hopf, V.; Müller, W.; Schäfer, H. *Z. Naturforsch., B: Anorg. Chem. Org. Chem.* **1972**, *27 (10)*, 1157–1160.

(49) Nesper, R.; Zürcher, F. *Z. Kristallogr. – New Cryst. Struct.* **1999**, *214(1)*, 22.

(50) Nesper, R.; Zürcher, F. *Z. Kristallogr. – New Cryst. Struct.* **1999**, *214(1)*, 21.

(51) Mudring, A.-V.; Corbett, J. D. *J. Am. Chem. Soc.* **2004**, *126*, 5277–5281.

(52) Zürcher, F.; Nesper, R. *Angew. Chem. Int. Ed.* **1998**, *37*, 3314–3318.

(53) Vaughey, J. T.; Miller, G. J.; Gravelle, S.; Leon-Escamilla, E. A.; Corbett, J. D. *J. Solid State Chem.* **1997**, *133*, 501–507.

(54) Palenzona, A.; Pani, M. *J. Alloys Compd.* **2005**, *402*, 136–140.

(55) Witte, J.; von Schnering, H. G. *Z. Anorg. Allg. Chem.* **1964**, *327*, 260–273.

(56) Busmann, E. *Z. Anorg. Allg. Chem.* **1961**, *313*, 90–106.

(57) Merlo, F.; Fornasini, M. L. *J. Less-Common Met.* **1967**, 13, 603–610.

(58) Tobash, P. H.; Bobev, S. *J. Solid State Chem.* **2007**, *180*, 1575–1581.

(59) Evers, J.; Oehlinger, G.; Weiss, A. *Z. Naturforsch*., *B*: *Anorg*. *Chem*. *Org*. *Chem*. **1977**, *32B (11)*, 1352–1353.

(60) Menges, E.; Hopf, V.; Schäfer, H.; Weiss, A. *Z. Naturforsch*., *B*: *Anorg*. *Chem*. *Org*. *Chem*. **1969**, *24 (10)*, 1351–1352.

(61) Hohnke, D.; Parthé, E. *Acta Crystallogr.* **1966**, *20*, 572–581.

(62) Smith, J. F.; Bailey, D. M. *Acta Crystallogr.* **1957**, *10*, 341–342.

(63) Tobash, P. H.; Meyers, J. J.; DiFilippo, G.; Bobev, S.; Ronning, F.; Thompson, J. D.; Sarrao, J. L. *Chem. Mater.* **2008**, *20*, 2151–2159.

(64) a) François, M.; Verturini, B.; Malaman, B.; Roques, J. *J. Less-Common Met.* **1990**, *160*, 197–213; b) Verturini, B.; François, M.; Malaman, B.; Roques, J. *J. Less-Common Met.* **1990**, *160*, 215–228.

(65) Smart, L.; Moore, E. *Solid State Chemistry: An Introduction*, 2nd ed.; Chapman & Hall: London, 1996.

(66) Kanatzidis, M. G.; Pöttgen, R.; Jeitschko, W. *Angew Chem. Int. Ed.* **2005**, *44(43)*, 6996–7023.

(67) Salvador, J. R.; Bilc, D.; Gour, J. R.; Mahanti, S. D.; Kanatzidis, M. G. *Inorg. Chem.* **2005**, *44*, 8670–8679.

(68) Russ, J. C. *Fundamentals of energy dispersive X-ray analysis*; Butterworths: London, 1984.

(69) Massa, W. *Crystal Structure Determination*, 2nd ed.; Springer–Verlag: Berlin, 2004.

(70) a) Rietveld, H. M. *J. Appl. Crystallogr.* **1969**, *2*, 65–71; b) Pecharsky, V. K.; Zavalij, P. Y. *Fundamentals of Powder Diffraction and Structural Characterization of Materials*; Kluwer Academic Publishers: Boston, USA, 2003.

(71) Rodriguez-Carvajal, J. *Phys. B* **1993**, *192*, 55. (http://www.ccp14.ac.uk/tutorial/fullprof/index.html.)

(72) a) Larson, A. C.; Von Dreele, R. B. *Los Alamos National Laboratory Report LAUR*, **1994**, 86-748; b) Toby, B. H. *J. Appl. Crystallogr.* **2001**, *34*, 210-213. (www.ccp14.ac.uk/solution/gsas).

(73) Hunter, B. *LHPM-Rietica*, version 1.7.7, International Union of Crystallography Commission on Powder Diffraction Newsletter, no. 20 (summer), 1998 (www.rietica.org).

(74) West, A. R. *Basic Solid State Chemistry*, 2nd ed.; Wiley: New York, 1999.

(75) Sheldrick, G. M. *SHELXTL*, version 6.12; Bruker AXS Inc.: Madison, WI, 2001.

(76) Dronkowski, R. *Computational Chemistry of Solid State Materials*; Wiley-VCH: Weinheim, 2005.

(77) a) Tank, R.; Jepsen, O.; Burkhardt, A.; Andersen, O. K. *TB-LMTO-ASA Program*, version 4.7, Max Planck Institut für Festkörperforschung, Stuttgart, Germany, 1998; b) Tank, R. W.; Arcangeli, C. *Phys. Stat. Sol.* **2000**, *b217*, 89-130.

(78) Dronskowski, R.; Blöchl, P. E. *J. Phys. Chem.* **1993**, *97*, 8617-8624.

(79) Cheetham, A. K., Day, P., Eds. *Solid State Chemistry: Techniques*; Oxford University Press: Oxford, 1987.

(80) a) Kondo, J. *Progr. Theoret. Phys.* **1964**, *32*, 37; b) Lee, H.-O. *Ferromagnetism in the Kondo Lattice $CeNiSb_3$ and $CeZn_xSb_2$ (x=0.64, 0.66)*, Ph.D. Thesis in University of California, Davis, Physics, 2006.

(81) Kittel, C. *Introduction to Solid State Physics*, 7th ed.; Wiley: New York, 1996.

(82) Morrish, A. H. *The Physical Principles of Magnetism*; Wiley: New York, 1965.

(83) Spaldin, N. A. *Magnetic Materials: Fundamentals and Device Applications*; Cambridge University Press: Cambridge, 2003.

(84) a) Majlis, N. *The Quantum Theory of Magnetism*; World Scientific: Singapore, 2000; b) Jia, S. *Magnetic properties of RT_2Zn_{20} (R = rare earth, T = Fe, Co, Ru, Rh, Os and Ir)*, Ph.D. Thesis in Iowa State University, Physics, 2008.

(85) Jiles, D. *Introduction to Magnetism and Magnetic Materials*, 2nd ed.; CRC Press: New York, 1998.

Chapter 2

Ternary Rare-Earth Titanium Antimonides: Phase Equilibria in the *RE*–Ti–Sb (*RE* = La, Er) Systems and Crystal Structures of $RE_2Ti_7Sb_{12}$ (*RE* = La, Ce, Pr, Nd) *

2.1. Introduction

Ternary rare-earth transition-metal antimonides *RE*–*M*–Sb represent a rich and varied class of materials exhibiting diverse structures and physical properties owing to the coexistence of unpaired *f* and *d* electrons.[1] Table 2–1 summarizes, to our knowledge, all the ternary antimonides in *RE*–*M*–Sb systems that have been prepared to date.[1–7] A great diversity of anionic Sb substructures has been observed in the form of isolated squares, 1D chains, and 2D square sheets. Systems containing a late transition metal have been the subject of most previous studies, with the focus on their bonding and physical properties. Generally speaking, their electron counting schemes do not obey the simple Zintl-Klemm concept because the electron transfer to Sb from the less electropositive rare-earth and transition metals is incomplete, and the transition metal centres can adopt multiple oxidation states, as discussed in

*A version of this chapter has been published. Haiying Bie, Devon S.H. Moore, Davin G. Piercey, Andriy V. Tkachuk, Oksana Ya. Zelinska, Arthur Mar, 2007. Journal of Solid State Chemistry, 180, 2216—2224. Except for the Er–Ti–Sb phase diagram, which was investigated by D.G. Piercey, all work presented in this chapter was completed by myself with the experimental assistance of A.V. Tkachuk and O. Ya. Zelinska.

In contrast, systems containing an early transition metal remain poorly investigated. When *M* is a group 4, 5, or 6 element, the only compounds known so far are RE_3MSb_5 (*M* = Ti, Zr, Hf, Nb),[2,8–10] $REMSb_3$ (*M* = V, Cr),[10–27] and *RE*ZrSb.[28–31] In the Sb-rich phases, homoatomic Sb–Sb substructures are an interesting feature, in the form of 1D chains in RE_3MSb_5 or 2D square sheets in $REMSb_3$. The compounds RE_3MSb_5 (*M* = Ti, Zr, Hf) are metallic Zintl phases formulated as $(RE^{3+})_3(M^{4+})(Sb^{3-})_3(Sb^{2-})_2$, in conformity with the Zintl-Klemm concept, as discussed in Chapter 1. The crystal structure of $RECrSb_3$ phases consists of two interesting Sb substructures: (i) square sheets with Sb(3)–Sb(3) distances of 3.0581(5) and 3.1065(1) Å; (ii) pairs between Sb(1) and Sb(2) with a long distance of 3.175(2) Å. Therefore, the charge can be balanced as follows: $(RE^{3+})(Cr^{3+})(Sb(1)^{2.5-})(Sb(2)^{2.5-})(Sb(3)^{-})$. Unfortunately the situation is less clear in the case of metal-rich compounds *RE*ZrSb, which adopt the CeScSi-type structure, an ordered variant of the La_2Sb-type structure. There is no significant Sb–Sb bonding present in the structure, and thus Sb is considered as isolated Sb^{3-}. Thus, the *RE* and Zr atoms do not transfer all their valence electrons, a situation that is often observed in metal-rich antimonides, and metal-metal (Zr–Zr) bonds are dominant. Given the absence of phase diagram information except for Dy–Zr–Sb (800 ºC),[29] it is not clear if other compounds exist in these systems.

Table 2–1. Known ternary rare-earth antimonides in *RE*–*M*–Sb systems (*M* = transition metal).[1,2]

Ti	V	Cr	Mn	Fe	Co	Ni	Cu	Zn
RE_3TiSb_5	$REVSb_3$	$RECrSb_3$	$REMn_2Sb_2$ $RE_{14}MnSb_{11}$ RE_6MnSb_{15} $REMn_xSb_2$	RE_6FeSb_2 $RE_6Fe_{13}Sb$ $REFe_4Sb_{12}$ $REFe_3Sb_2$ $REFe_xSb_2$ $REFeSb_3$ [3]	$RE_6Co_{13}Sb$ $RECo_4Sb_{12}$ $RECo_xSb_2$ $RECoSb_3$ [3b,4]	$RENi_2Sb_2$ $RENiSb$ RE_5Ni_2Sb $RENi_xSb_2$ $RENiSb_3$ [5] β-$RENiSb_3$ [6]	$RECu_2Sb_2$ $RECuSb$ $RE_3Cu_3Sb_4$ $RECu_xSb_2$ RE_6CuSb_{15}	$REZn_2Sb_2$ $RE_{14}ZnSb_{11}$ $REZn_xSb_2$ RE_6ZnSb_{15} $RE_6Zn_{1+x}Sb_{14+y}$ [7]
Zr	**Nb**	**Mo**	**Tc**	**Ru**	**Rh**	**Pd**	**Ag**	**Cd**
RE_3ZrSb_5 $REZrSb$	RE_3NbSb_5			$RERu_4Sb_{12}$	$RERh_2Sb_2$ $RERhSb$ $RE_3Rh_3Sb_4$	$RE_8Pd_{24}Sb$ RE_5Pd_2Sb $RE_2Pd_9Sb_3$ $REPdSb$ $REPd_2Sb_2$ $RE_3Pd_6Sb_5$ $REPd_xSb_2$ $REPd_2Sb$	$REAgSb$ $REAg_xSb_2$	$RECd_2Sb_2$ $RECd_xSb_2$

Systematic investigations on *RE*–Ti–Sb systems are presented in this chapter. The complete phase diagrams for a representative early (*RE* = La) and late rare earth (*RE* = Er) have been established at 800 ºC. A new ternary phase, $RE_2Ti_7Sb_{12}$ (*RE* = La, Ce, Pr, Nd) has been identified and its crystal structure was determined by single-crystal X-ray diffraction. It adopts a new structure type in which Ti-centred octahedra and homoatomic Ti–Ti and Sb–Sb bonding figure prominently.

2.2. Experimental Section

2.2.1. Synthesis

The phase diagrams of the La–Ti–Sb and Er–Ti–Sb systems were investigated by arc-melting of 80 and 50 alloys, respectively, which were prepared in the arc melter as described in Chapter 1. Starting materials were pieces of the rare-earth elements (La, 99.9%, Hefa; Er, 99.9%, Cerac), Ti sponge (99.9%, Fisher), and Sb pieces (99.999%, Alfa-Aesar). The alloys were melted twice to ensure homogeneity. The final compositions of the alloys were determined with the assumption that the weight losses observed during arc-melting (up to at. 5%) were attributed to volatilization of Sb alone. The alloys were then sealed in evacuated fused-silica tubes and annealed at 800 ºC. After the heat treatment, the tubes were quenched in cold water. Products were then characterized by powder X-ray diffraction technique. Polished samples embedded in resin were

examined by metallographic analyses. Elemental compositions of each phase were determined by energy-dispersive X-ray (EDX) analysis on a Hitachi S-2700 scanning electron microscope.

A new ternary phase found in the La–Ti–Sb system was initially believed to be the antimonide analogue of the RETi$_3$(Sn$_x$Sb$_{1-x}$)$_4$ phase.[32] To obtain crystals of this phase (subsequently identified as La$_2$Ti$_7$Sb$_{12}$), mixtures of La pieces (99.9%, Hefa), Ti powder (99.98%, Cerac), and Sb powder (99.995%, Cerac) in the molar ratio 1:3:4 were placed in an alumina crucible jacketed by an outer fused-silica tube. The tubes then were heated to 650 ºC over 1 d, heated to 1050 ºC over 1 d, kept at that temperature for 2 d, slowly cooled to 800 ºC over 4 d, kept at that temperature for 12 d, and then slowly cooled to 20 ºC over 4 d. The major phase from these reactions was La$_3$TiSb$_5$,[8] which was difficult to distinguish from La$_2$Ti$_7$Sb$_{12}$ as all crystals obtained were small. Among five crystals selected for single-crystal X-ray diffraction analysis, only one gave the unit cell of the title La$_2$Ti$_7$Sb$_{12}$ phase and none of them gave the expected unit cell for "LaTi$_3$Sb$_4$". The yield could not be improved by attempts of different synthetic conditions, e.g., reactant stoichiometry or temperature program.

Isostructural compounds RE_2Ti$_7$Sb$_{12}$ with RE = Ce, Pr, Nd were obtained (in combination with RE_3TiSb$_5$) by arc-melting at the stoichiometric ratio of 2:7:12 and annealing at 900 ºC over a relatively long time of 20 d. Use of different compositions near the target composition did not improve the phase purity

substantially. Cell parameters are listed in Table 2–2.

2.2.2. Structure Determination

Single-crystal X-ray diffraction data were collected on a Bruker Platform / SMART 1000 CCD diffractometer at 22 °C using ω scans. Structure solution and refinement were carried out with use of the SHELXTL (version 6.12) program package.[33] Face-indexed numerical absorption corrections were applied. Crystal data and further details of the data collection are given in Table 2–3.

Table 2–2. Cell parameters for $RE_2Ti_7Sb_{12}$ (*RE* = La, Ce, Pr, Nd) [a]

Compound	*a* (Å)	*b* (Å)	*c* (Å)	*V* (Å^3)
$La_2Ti_7Sb_{12}$	10.5332(5)	20.733(1)	4.4338(2)	968.26(8)
$Ce_2Ti_7Sb_{12}$	10.497(1)	20.692(2)	4.4160(5)	959.1(2)
$Pr_2Ti_7Sb_{12}$	10.474(2)	20.689(4)	4.3896(9)	951.2(3)
$Nd_2Ti_7Sb_{12}$	10.427(2)	20.697(3)	4.3812(7)	945.5(3)

[a] Obtained from powder X-ray diffraction data.

For $La_2Ti_7Sb_{12}$, the intensity pattern indicated Laue symmetry and systematic absences consistent with the orthorhombic space groups *Cmmm*, *Cmm*2, and *C*222. Intensity statistics (mean $|E^2-1|$ = 0.946) favoured the centrosymmetric space group *Cmmm*. Initial atomic positions for the La, Ti, and most of the Sb atoms in the structure were found by direct methods. The Sb2 and Sb3 sites exhibited large displacement parameters, suggesting partial occupancy. Two additional

prominent peaks remaining in the difference electron density map were assigned as partially occupied Sb5 and Sb6 sites. When allowed to refine freely, the occupancies of these sites converged to 0.50(1) for Sb2, 0.50(1) for Sb3, 0.21(1) for Sb5, and 0.19(1) for Sb6. The occupancies of these sites (Sb2/Sb6 and Sb3/Sb5) are correlated because of chemically impossible short distances between them and symmetry-equivalent positions, and are limited to a maximum of 0.50 for Sb2 and Sb3, and 0.25 for Sb5 and Sb6. All other sites were essentially fully occupied (0.97(1)–1.06(1)), except for Ti3, whose occupancy converged to 0.85(2). The Sb1 site exhibits an elongated displacement parameter, which could be resolved into two very closely separated split sites (< 0.4 Å), each half-occupied. If all these partial occupancies are taken at face value, the resulting formula is "$La_2Ti_{6.8}Sb_{11.8}$". Other orthorhombic space groups in which one or more mirror planes are removed (*Cmm*2, *C*222) as well as lower-symmetry monoclinic space groups (*C*2/*m*, *Cm*) were considered, but these failed to lead to ordered structural models. To arrive at a simple model for a local interpretation of the disorder implied by the partially occupied Sb sites, we have retained the structure in *Cmmm* but with the occupancies fixed at 0.50 for Sb2 and Sb3, 0.25 for Sb5 and Sb6, and 1.00 for all remaining atoms, and with the Sb1 site unsplit. This model thus neglects the slight substoichiometry inherent in the Sb5, Sb6, and Ti3 sites. The formula corresponding to this simplified structural model is "$La_2Ti_7Sb_{12}$" and will be referred to as such in the remaining discussion. Atomic positions were standardized with the program STRUCTURE TIDY.[34] Final

values of the positional and displacement parameters are given in Table 2–4. Selected interatomic distances are listed in Tables 2–5.

Table 2–3. Crystallographic data for $La_2Ti_7Sb_{12}$.

Formula	$La_2Ti_7Sb_{12}$
Formula mass (amu)	2074.12
Space group	*Cmmm* (No. 65)
Cell parameters (Å)	a = 10.5446(10), b = 20.768(2), c = 4.4344(4)
V (Å^3), Z	971.1(2), 2
ρ_{calcd} (g cm^{-3})	7.093
Crystal dimensions (mm)	0.08 × 0.05 × 0.04
Radiation	Graphite monochromated Mo $K\alpha$, λ = 0.71073 Å
μ(Mo K_α) (mm^{-1})	233.26
Transmission factors	0.176–0.454
2θ limits	3.92° ≤ 2θ ≤ 66.32°
Data collected	–15 ≤ h ≤ 15, –31 ≤ k ≤ 31, –6 ≤ l ≤ 6
No. of data collected	6703
No. of unique data, including $F_o^2 < 0$	1083 (R_{int} = 0.058)
No. of unique data, with $F_o^2 > 2\sigma(F_o^2)$	889
No. of variables	52
$R(F)$ for $F_o^2 > 2\sigma(F_o^2)$ [a]	0.040
$R_w(F_o^2)$ [b]	0.100
Goodness of fit	1.064
$(\Delta\rho)_{max}$, $(\Delta\rho)_{min}$ (e Å^{-3})	3.01, –3.21

[a] $R(F) = \sum \| |F_o| - |F_c| \| / \sum |F_o|$.

[b] $R_w(F_o^2) = \left[\sum \left[w(F_o^2 - F_c^2)^2 \right] / \sum w F_o^4 \right]^{1/2}$; $w^{-1} = \left[\sigma^2(F_o^2) + (Ap)^2 + Bp \right]$ where $p = \left[\max(F_o^2, 0) + 2F_c^2 \right] / 3$.

Table 2–4. Atomic coordinates and equivalent isotropic displacement parameters (Å^2) for $La_2Ti_7Sb_{12}$.

Atom	Wyckoff position	Occupancy	*x*	*y*	*z*	U_{eq} (Å^2) [a]
La	4*i*	1	0	0.38857(4)	0	0.0087(2)
Ti1	8*p*	1	0.1451(2)	0.11989(9)	0	0.0136(4)
Ti2	4*e*	1	1/4	1/4	0	0.0103(4)
Ti3	2*a*	1	0	0	0	0.0167(7)
Sb1	8*q*	1	0.29146(9)	0.16415(5)	1/2	0.025(2)
Sb2	8*o*	0.50	0.2596(1)	0	0.1173(3)	0.0135(3)
Sb3	8*n*	0.50	0	0.22999(6)	0.1373(3)	0.0080(2)
Sb4	4*j*	1	0	0.08027(5)	1/2	0.0150(2)
Sb5	4*j*	0.25	0	0.2208(3)	1/2	0.033(1)
Sb6	4*h*	0.25	0.2328(6)	0	1/2	0.037(1)
Sb7	2*c*	1	1/2	0	1/2	0.013(3)

[a] U_{eq} is defined as one-third of the trace of the orthogonalized U_{ij} tensor.

Table 2–5. Selected interatomic distances (Å) in $La_2Ti_7Sb_{12}$.

La–Sb7 (×2)	3.2050(6)	Sb1–Sb5	3.247(5)
La–Sb1 (×4)	3.3091(7)	Sb1–Sb5	3.291(2)
La–Sb3	3.349(1)	Sb1–Sb6	3.465(3)
La–Sb2 (×2)	3.471(1)	Sb2–Sb2	3.394(3)
Ti1–Sb2	2.816(2)	Sb2–Sb6	2.752(2)
Ti1–Sb4 (×2)	2.816(1)	Sb2–Sb7	3.050(1)
Ti1–Sb3	2.818(2)	Sb2–Sb7	3.731(3)
Ti1–Sb1 (×2)	2.854(1)	Sb3–Sb3	3.216(3)
Ti2–Sb3 (×2)	2.7373(4)	Sb3–Sb5	2.833(1)
Ti2–Sb1 (×4)	2.8785(6)	Sb4–Sb4	3.334(3)
Ti3–Sb4 (×4)	2.7740(6)	Sb4–Sb5	2.918(6)
Ti3–Sb2 (×2)	2.787(1)	Sb4–Sb6	2.968(5)
Ti1–Ti1	3.059(4)	Sb6–Sb7	2.817(6)
Ti1–Ti2	2.920(2)		
Ti1–Ti3	2.922(2)		

2.3. Results and Discussion

2.3.1. Phase Diagrams

Apart from the existence of RE_3TiSb_5 (*RE* = La, Ce, Pr, Nd, Sm) phases, which were first discovered in Sn-flux reactions,[8] little else is known about the ternary *RE*–Ti–Sb systems. The termination of the RE_3TiSb_5 series at *RE* = Sm suggests that the phase behaviour will differ for early vs. late *RE* elements. For this reason, a representative early and late *RE* member were chosen for more comprehensive phase diagram investigations. Figure 2–1 shows the isothermal sections at 800 ºC of the La–Ti–Sb and Er–Ti–Sb systems. The highly antimony-rich compositions (> 70 at. % Sb) in the ternary phase diagrams were not examined.

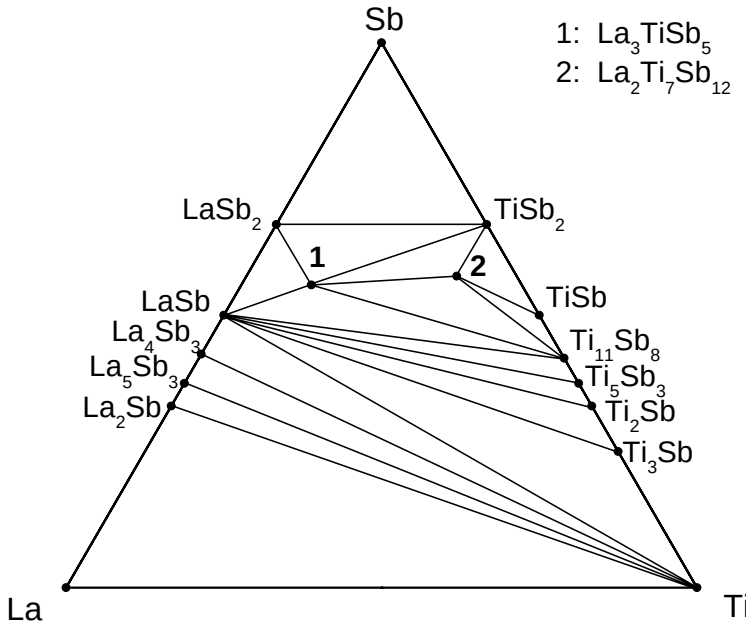

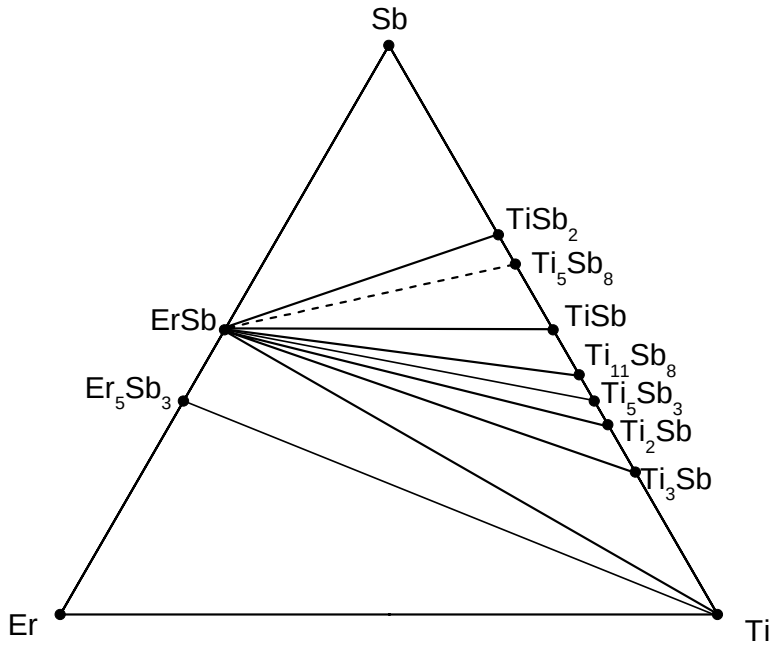

Figure 2–1. Isothermal sections at 800 ºC of the La–Ti–Sb and Er–Ti–Sb phase diagram.

In the *RE*–Sb sections of both systems, all previously known binary phases were observed except for Er_4Sb_3 and the high-pressure phase $ErSb_2$.[35,36] In the Ti–Sb sections of both systems, the existence of six binary phases was confirmed: cubic Ti_3Sb,[37] Ti_2Sb,[38] Ti_5Sb_3,[39,40] $Ti_{11}Sb_8$,[41] TiSb,[37] and $TiSb_2$.[42] The phases Ti_2Sb and $Ti_{11}Sb_8$ were reported recently.[38,41] Other phases (Ti_4Sb, $Ti_{2.5}Sb$, Ti_6Sb_5) reported in earlier investigations were not observed under the conditions used here. Ti_4Sb was initially formulated as "$Ti_3(Ti_{0.2}Sb_{0.8})$",[43] but later attempts to reproduce its synthesis by arc-melting failed,[37] so perhaps it is a metastable phase. $Ti_{2.5}Sb$ was originally prepared in carbon crucibles and heated in a high-pressure furnace or an induction furnace,[43] but neither

arc-melting nor heating at 1400–1600 ºC yielded this phase.[37] The existence of $Ti_{2.5}Sb$ can also be discounted, on the basis of the stability of Ti_2Sb with respect to disproportionation to Ti_3Sb and Ti_5Sb_3.[38] Ti_6Sb_5 was originally prepared by arc-melting but its structure was unknown.[37] It is probably the phase now identified as $Ti_{11}Sb_8$,[41] given the similarity of their cell constants and powder X-ray diffraction patterns. Within the Er–Ti–Sb phase diagram, formation of the phase Ti_5Sb_8[45] was sometimes observed in combination with TiSb and $TiSb_2$ at 800 ºC in the 50–67 at. % Sb region. When the annealing temperature was raised to 1000 ºC, the expected equilibrium mixture of Ti_5Sb_8 with one of TiSb or $TiSb_2$ was formed. Ti_5Sb_8 has been indicated previously to be stable with respect to disproportionation (to TiSb and $TiSb_2$) between 900 ºC and 1100 ºC.[45] The non-equilibrium formation of Ti_5Sb_8 suggests that the annealing time of one week in the Er–Ti–Sb phase investigation may not have been sufficiently long. Although the structures of several mixed-metal representatives (M',Ti)$_5Sb_8$ (M' = Zr, Hf, Nb, Mo) are known,[46] crystallographic details for the end-member Ti_5Sb_8 itself have not been reported previously.[45] Cell parameters obtained here from a single-crystal X-ray structure determination on tetragonal Ti_5Sb_8 are a = 6.492(4) Å, c = 26.514(15) Å, and V = 1117.3(18) Å^3.[47]

In the Er–Ti–Sb system, no ternary compounds were found at 800 ºC. In the La–Ti–Sb system, in addition to the previously known phase La_3TiSb_5,[8] the new compound $La_2Ti_7Sb_{12}$ was discovered, as revealed by EDX analyses of

polished samples and by unidentified powder X-ray diffraction pattern of ground samples (Figure 2–2).

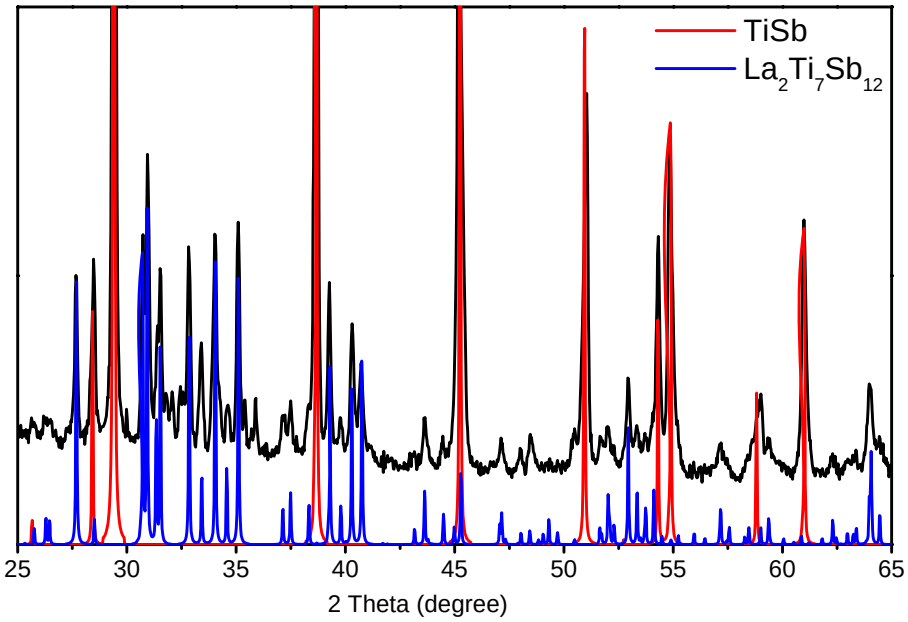

Figure 2–2. The powder X-ray diffraction pattern containing binary TiSb (red lines) and ternary $La_2Ti_7Sb_{12}$ (blue lines) phases.

2.3.2. Crystal Structure of $RE_2Ti_7Sb_{12}$

The compounds $RE_2Ti_7Sb_{12}$ (*RE* = La, Ce, Pr, Nd) adopt a new structure type. The structure of $La_2Ti_7Sb_{12}$ projected down the *c* direction is shown in Figure 2–3. It consists of a complex three-dimensional framework of linked $TiSb_6$ octahedra. The Sb2 and Sb3 sites each have an occupancy of 0.50, but to clarify the presence of these $TiSb_6$ octahedra, the figure portrays one possible idealized model in which half of these sites are occupied in an ordered fashion and the other half are not shown. Three types of Ti-centred octahedra are then evident, each forming infinite chains through edge-sharing with their symmetry

equivalents along the *c* direction. They differ in their connectivity along the *a* direction: The Ti1-centred octahedra are connected in pairs by sharing a common face (Sb4–Sb4–Sb3), the Ti2-centred octahedra are connected to form zigzag chains through corner-sharing of *trans* Sb3 atoms, and the Ti3-centred octahedra remain isolated. Lastly, the Ti1-, Ti2-, and Ti3-centred octahedra are connected by face-sharing along the [110] and [$1\bar{1}0$] directions. The Ti–Sb distances range from 2.7373(4) Å to 2.8785(6) Å, the shortest being similar to the sum of the Pauling radii ($r_{Ti} + r_{Sb}$ = 1.324 + 1.391 = 2.715 Å)[48] and the longest being similar with those found in $TiSb_6$ octahedra in TiSb (2.846 Å)[37] and La_3TiSb_5 (2.859(1) Å).[8] The occurrence of face-sharing octahedra brings the Ti centres in close contact with each other to form 2D layers, at distances (2.920(2)–3.059(4) Å) that may be indicative of weak metal-metal bonding (Figure 2–4).

The network of $TiSb_6$ octahedra outlines channels that are occupied by the La and Sb7 atoms. The coordination geometry of Sb atoms around the La centres is approximately tricapped trigonal prismatic, corresponding to CN9 (4 Sb1, 2 Sb7, 0.50 × 4 Sb2, 0.50 × 2 Sb3), with La–Sb distances of 3.2050(6)–3.471(1) Å. Surrounding Sb7 in a distorted planar environment are four Sb2 atoms (with the half-occupancy of the Sb2 sites taken into account), two that are within weak Sb–Sb bonding distances (3.050(1) Å) and two that are too far to be bonding (3.731(3) Å), on average.

Close to the half-occupied Sb2 and Sb3 sites are two other sites, Sb5 and Sb6, each of which has occupancy of 0.25. These partially occupied Sb sites correspond to a complicated disorder. Figure 2–5 shows one possible local interpretation for this disorder within a chain of edge-sharing Ti1-centred octahedra extending along the *c* direction. Full occupation of these sites is clearly precluded by the impossibly short Sb–Sb distances that would result. However, the level of partial occupancy is understandable on the basis that a minimum Sb–Sb distance cannot be less than ~2.7 Å. Distances of 2.8–2.9 Å are indicative of Sb–Sb single bonds, longer distances of ~3.0–3.2 Å typically suggest hypervalent Sb–Sb bonds, and the values greater than 3.2 Å have been implicated as non-innocent.[49] Within this edge-sharing octahedral chain, the apices are formed by the Sb2 and Sb3 sites; fixing their occupancy at 0.50 maintains CN6 around the Ti1 centres. An Sb5 atom must then lie between a pair of Sb3 atoms, and an Sb6 atom between a pair of Sb2 atoms, forming linear trimers containing rather short Sb–Sb contacts (Sb3–Sb5, 2.833(1) Å; Sb2–Sb6, 2.752(2) Å). These short distances are likely a result of matrix effects, analogous to the situation in $Ti_{11}Sb_8$ where similar Sb–Sb distances of 2.759(2) and 2.838(2) Å are found in linear Sb chains.[41] Even if long-range ordering of these trimers ensues within an individual edge-sharing octahedral chain, this ordering need not be in registry in other different chains, leading to the observed average disordered structure.

2.3.3. Structural Relationships

Although not evident at first inspection, the structures of $La_2Ti_7Sb_{12}$, $NdTi_3(Sn_xSb_{1-x})_4$, and RE_3TiSb_5 show interesting relationships to each other. We focus on sectioned layers consisting of linked Ti-centred octahedra. In $NdTi_3(Sn_xSb_{1-x})_4$, such a layer consists of alternating, perfectly linear chains of corner-sharing and of face-sharing octahedra, extended along the *a* direction (Figure 2–6a). Proceeding to $La_2Ti_7Sb_{12}$, the layer is derived by removing every second Ti centre from half of the chains of corner-sharing octahedra and every third and fourth one from all the chains of face-sharing octahedra (Figure 2–6b). Thus, the layer in $La_2Ti_7Sb_{12}$ may be regarded as a defect variant of that in $NdTi_3(Sn_xSb_{1-x})_4$. The corner-sharing octahedral chains are no longer perfectly linear but adopt a zigzag configuration. Moreover, the cavity that is formed by removal of some of the corner-sharing octahedra is occupied by new Sb atoms. The shortest Ti–Ti interactions in these structures are associated with occurrence of the face-sharing octahedra, when Ti centres can approach each other most closely, by geometrical arguments. An alternative possibility of a defect structure is to remove all the corner-sharing octahedra, which results in isolated chains of only face-sharing octahedra, as occurs in the hexagonal structure of La_3TiSb_5 (Figure 2–6c).

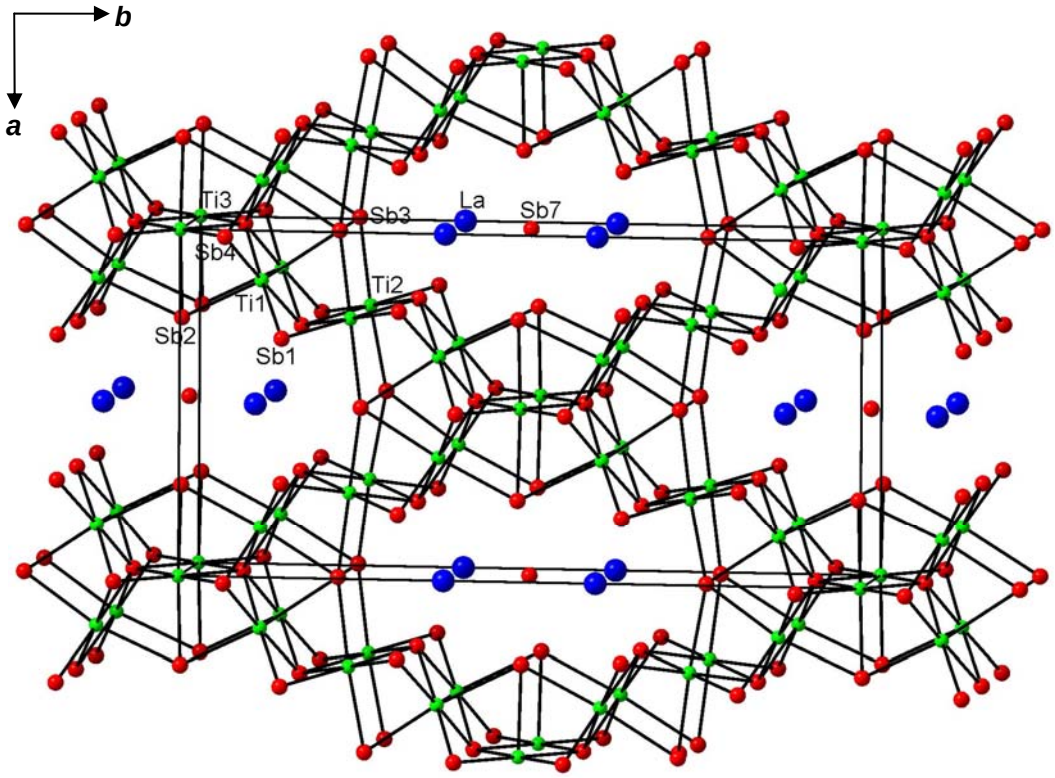

Figure 2–3. Structure of $La_2Ti_7Sb_{12}$ viewed down the *c* direction. The blue, green, and red spheres are La, Ti, and Sb atoms, respectively.

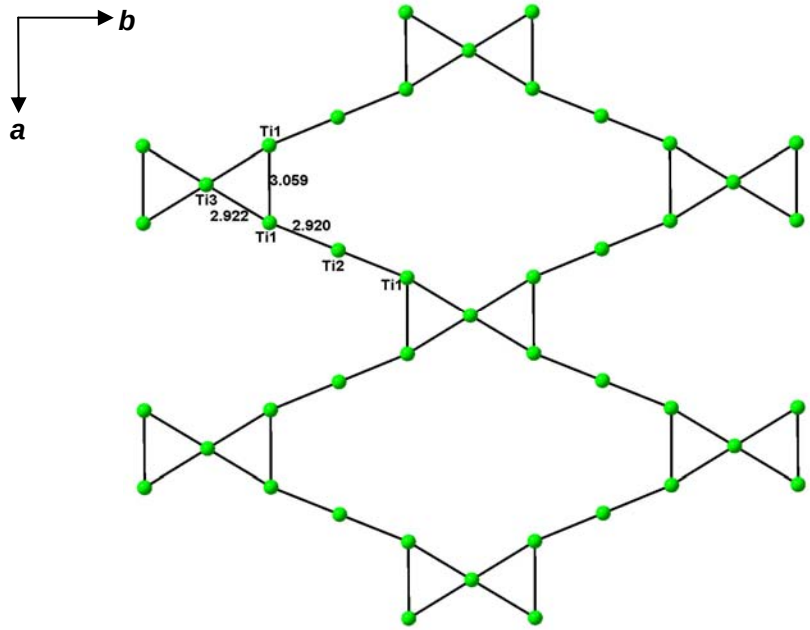

Figure 2–4. The 2D Ti layers formed by Ti–Ti bonding in $La_2Ti_7Sb_{12}$, viewed along the *c* axis.

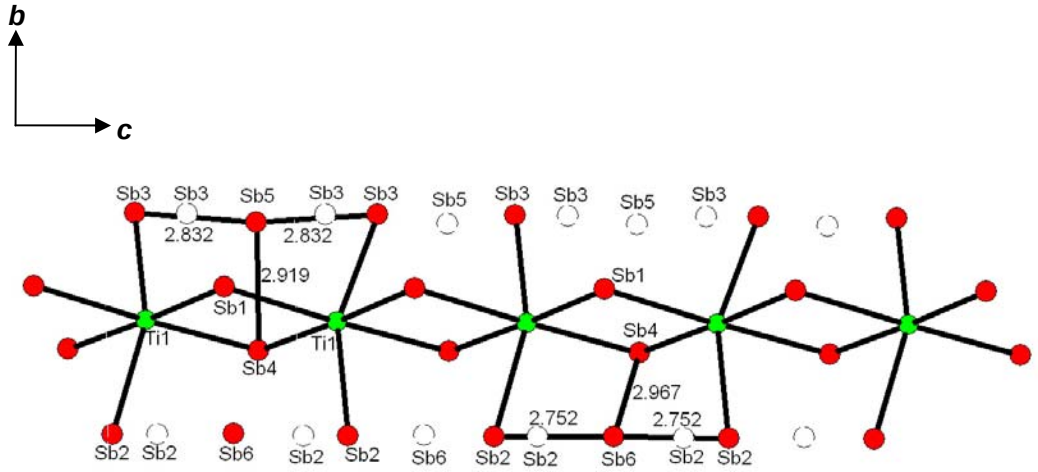

Figure 2–5. One possible local ordering of the partially occupied Sb sites (0.50 for Sb2 and Sb3; 0.25 for Sb5 and Sb6) within an edge-sharing chain of Ti1-centred octahedra extended along the *c* direction in $La_2Ti_7Sb_{12}$.

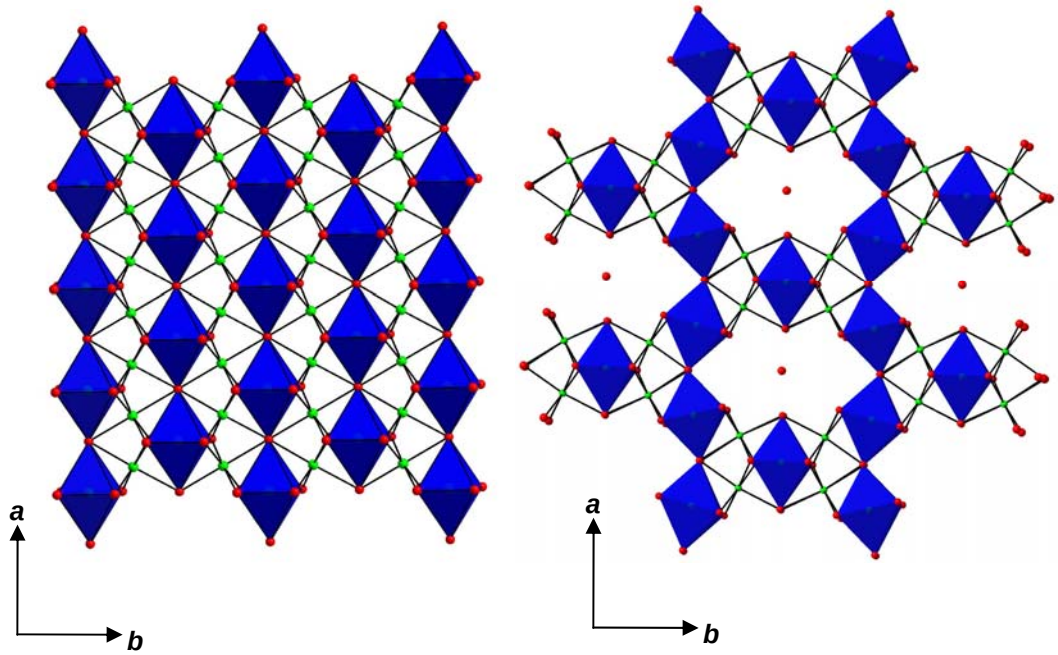

(a) $NdTi_3(Sn_xSb_{1-x})_4$ (*Fmmm*) (b) $La_2Ti_7Sb_{12}$ (*Cmmm*)

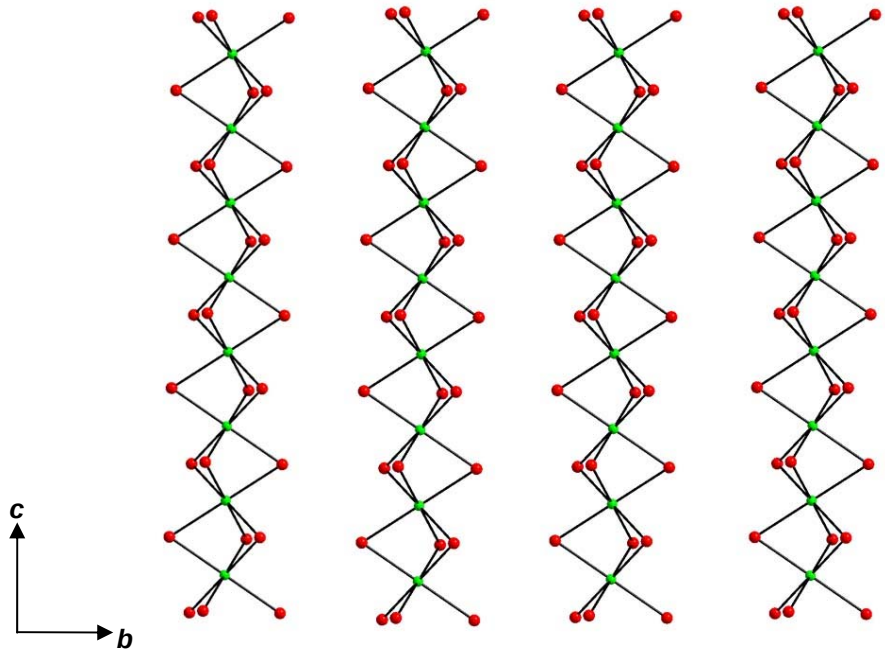

(c) La_3TiSb_5 ($P6_3/mcm$)

Figure 2–6. Comparison of the structures of (a) $NdTi_3(Sn_xSb_{1-x})_4$, (b) $La_2Ti_7Sb_{12}$, and (c) La_3TiSb_5. Face-sharing Ti-centred octahedra are shown as ball-and-stick representations, and corner-sharing (or isolated) octahedra as polyhedral representations.

2.3.4. Bonding

Following the Zintl-Klemm concept, RE_3TiSb_5 can be formulated as $(RE^{3+})_3(M^{4+})(Sb^{3-})_3(Sb^{2-})_2$, which is consistent with the occurrence of 1D Sb zig-zag chains containing hypervalent bonds. If $NdTi_3(Sn_xSb_{1-x})_4$ is idealized as the hypothetical antimonide "$NdTi_3Sb_4$" and Sb–Sb interactions beyond 3.2 Å are assumed to be insignificant, the charge-balanced formula

$(Nd^{3+})(Ti^{3+})_3(Sb^{3-})_4$ implies that the Ti atoms will have a partially filled d configuration, consistent with the occurrence of Ti–Ti distances (~2.9 Å) that may indicate metal-metal bonding. Introduction of a small amount of Sn into the Sb sites will not change this conclusion.

However, for $La_2Ti_7Sb_{12}$, the situation is even more complicated, since both Ti–Ti (2.9–3.0 Å) and Sb–Sb distances (2.8–3.2 Å) are probably operative. If no Ti–Ti bonding is assumed, then compliance with a charge-balanced formulation $(La^{3+})_2(Ti^{4+})_7(Sb^{2.8-})_{12}$ leads to the conclusion that some Sb–Sb bonding must be present. Conversely, if no Sb–Sb bonding is assumed, then the impossible formula $(La^{3+})_2(Ti^{4.3+})_7(Sb^{3-})_{12}$ leads by *reductio ad absurdum* to the same conclusion. A more rigorous analysis through use of the bond valence equation[50,51] leads to charges of 2.8– for Sb1, 1.8– for Sb2, 2.2– for Sb3, 2.4– for Sb4, 0.8– for Sb5, 0.4– for Sb6, and 1.3– for Sb7, resulting in the formulation $(La^{3+})_2(Ti^{2.84+})_7(Sb_{12})^{25.9-}$.

2.4. Conclusions

The present work has revealed new phases $RE_2Ti_7Sb_{12}$ among the *RE*–Ti–Sb systems. It exemplifies that phase diagram investigation is an efficient way to identify new phases in an unknown system. Despite the complexity of the structure of $RE_2Ti_7Sb_{12}$, which includes many disordered

fragments of homoatomic Sb assemblies and extensive Ti–Ti bonding network, the Zintl-Klemm concept provides a simple way to understand its bonding.

Isostructural phases containing other early rare-earth elements can be obtained. However, the range of *RE* substitution is only limited to the early *RE* elements (*RE* = La, Ce, Pr, Nd). Although the Er–Ti–Sb system was found to contain no ternary phases, it is still worthwhile investigating systems containing other late *RE* elements, such as Yb, whose propensity for divalency may lead to different phase behaviour. These results will be discussed in the next chapter.

2.5. References

(1) Sologub, O. L.; Salamakha, P. S. In *Handbook on the Physics and Chemistry of Rare Earths*, Vol. 33; Gschneidner, K. A., Jr., Bünzli, J.-C. G., Pecharsky, V. K., Eds.; Elsevier: Amsterdam, 2003; pp 35–146.

(2) Ferguson, M. J.; Hushagen, R. W.; Mar, A. *J. Alloys Compd.* **1997**, *249*, 191–198.

(3) a) Liu, J.; Liu, W.; Zong, B.; Wang, L.; Cui, X.; Li, J. *J. Alloys Compd.* **2008**, *456*, 101–104; b) Chykhrij, S. I.; Smetana, V. B. *Inorg. Mater.* **2006**, *42*, 503–507 (*Transl. Izv. Akad. Nauk SSSR, Neorg. Mater.* **2006**, *42*, 563–567); c) Qin, P.; Nong, L.; Zhang, J.; Qin, H.; Liao, J.; Zeng, L. *Key Eng. Mater.* **2007**, *353–358*, 3043–3046.

(4) Cai, W.-Z.; Wu, L.-M.; Li, L.-H.; Chen, L. *Eur. J. Inorg. Chem.* **2009**, 230–237.

(5) Thomas, E. L.; Macaluso, R. T.; Lee, H. O.; Fisk, Z.; Chan, J. Y. *J. Solid State Chem.* **2004**, *177*, 4228–4236.

(6) Thomas, E. L.; Gautreaux, D. P.; Lee, H. O.; Fisk, Z.; Chan, J. Y. *Inorg. Chem.* **2007**, *46*, 3010–3016.

(7) Liu, Y.; Chen, L.; Li, L.-H.; Wu, L.-M.; Zelinska, O. Ya.; Mar, A. *Inorg. Chem.* **2008**, *47*, 11930–11941.

(8) Bolloré, G.; Ferguson, M. J.; Hushagen, R. W.; Mar, A. *Chem. Mater.* **1995**, *7* 2229–2231.

(9) Moore, S. H. D.; Deakin, L.; Ferguson, M. J.; Mar, A. *Chem. Mater.* **2002**, *14*, 4867–4873.

(10) Tkachuk, A. V.; Crerar, S. J.; Wu, X.; Muirhead, C. P. T.; Deakin, L.; Mar, A. *Mater. Res. Soc. Symp. Proc.* **2005**, *848*, 75–82.

(11) Brylak, M.; Jeitschko, W. *Z. Naturforsch. B: Chem. Sci.* **1995**, *50*, 899–904.

(12) Hartjes, K.; Jeitschko, W.; Brylak, M. *J. Magn. Magn. Mater.* **1997**, *173*,109–116.

(13) Raju, N. P.; Greedan, J. E.; Ferguson, M. J.; Mar, A. *Chem. Mater.* **1998**, *10*, 3630–3635.

(14) Leonard, M.; Saha, S.; Ali, N. *J. Appl. Phys.* **1999**, *85*, 4759–4761.

(15) Leonard, M. L.; Dubenko, I. S.; Ali, N. *J. Alloys Compd.* **2000**, *303–304*, 265–269.

(16) Dubenko, I. S.; Hill, P.; Ali, N. *J. Appl. Phys.* **2001**, *89*, 7326–7328.

(17) Jackson, D. D.; Torelli, M.; Fisk, Z. *Phys. Rev. B* **2001**, *65*, 014421-1–014421-7.

(18) Granado, E.; Martinho, H.; Sercheli, M. S.; Pagliuso, P. G.; Jackson, D. D.; Torelli, M.; Lynn, J. W.; Rettori, C.; Fisk, Z.; Oseroff, S. B. *Phys. Rev. Lett.* **2002**, *89*, 107204-1–107204-4.

(19) Shim, J. H.; Min, B. I. *J. Magn. Magn. Mater.* **2004**, *272–276*, e241–e242.

(20) Richter, M.; Rusz, J.; Rosner, H.; Koepernik, K.; Opahle, I.; Nitzsche, U.; Eschrig, H. *J. Magn. Magn. Mater.* **2004**, *272–276*, e251–e252.

(21) Deakin, L.; Ferguson, M. J.; Mar, A.; Greedan, J. E.; Wills, A. S. *Chem. Mater.* **2001**, *13*, 1407–1412.

(22) Jackson, D. D.; Fisk, Z. *J. Magn. Magn. Mater.* **2003**, *256*, 106–116.

(23) Deakin, L.; Mar, A. *Chem. Mater.* **2003**, *15*, 3343–3346.

(24) Jackson, D. D.; Fisk, Z. *J. Alloys Compd.* **2004**, *377*, 243–247.

(25) Crerar, S. J.; Deakin, L.; Mar, A. *Chem. Mater.* **2005**, *17*, 2780–2784.

(26) Jackson, D. D.; Fisk, Z. *Phys. Rev. B* **2006**, *73*, 024421/1–024421/7.

(27) MacFarlane, W. A.; Chow, K. H.; Salman, Z.; Tkachuk, A. V.; Mar, A. *Physica B* **2006**, *374–375*, 71–74.

(28) Morozkin, A. V.; Sviridov, I. A. *J. Alloys Compd.* **2001**, *320*, L1–L2.

(29) Morozkin, A. V.; Sviridov, I. A.; Leonov, A. V. *J. Alloys Compd.* **2002**, *335*, 139–141.

(30) Welter, R.; Morozkin, A. V.; Halich, K. *J. Magn. Magn. Mater.* **2003**, *257*, 44–50.

(31) Morozkin, A. V.; Halich, K.; Welter, R.; Ouladdiaf, B. *J. Alloys Compd.* **2005**, *393*, 34–40.

(32) Bie, H.; Moore, D. S. H.; Piercey, D. G.; Tkachuk, A. V.; Zelinska, O. Ya.; Mar, A. *J. Solid State Chem.* **2007**, *180*, 2216–2224.

(33) Sheldrick, G. M. *SHELXTL*, Version 6.12; Bruker AXS Inc.: Madison, WI, 2001.

(34) Gelato, L. M.; Parthé, E. *J. Appl. Crystallogr.* **1987**, *20*, 139–143.

(35) Abdusalyamova, M. N.; Vlasov, N. A.; Goryachev, Yu. M. *Inorg. Mater.* (*Transl. Izv. Akad.*

Nauk SSSR, Neorg. Mater.) **1984**, *20*, 1242–1245.

(36) Eatough, N. L.; Hall, H. T. *Inorg. Chem.* **1969**, *8*, 1439–1445.

(37) Kjekshus, A.; Grønvold, F.; Thorbjørnsen, J. *Acta Chem. Scand.* **1962**, *16*, 1493–1510.

(38) Derakhshan, S.; Assoud, A.; Kleinke, K. M.; Dashjav, E.; Qiu, X.; Billinge, S. J. L.; Kleinke, H. *J. Am. Chem. Soc.* **2004**, *126*, 8295–8302.

(39) Berger, R. *Acta Chem. Scand. Ser. A: Phys. Inorg. Chem.* **1977**, *31*, 889–890.

(40) Kaiser, J. W.; Haase, M. G.; Jeitschko, W. *Z. Anorg. Allg. Chem.* **2001**, *627*, 2369–2376.

(41) Bobev, S.; Kleinke, H. *Chem. Mater.* **2003**, *15*, 3523–3529.

(42) Armbrüster, M.; Cardoso Gil, R.; Burkhardt, U.; Grin, Yu. *Z. Kristallogr. – New Cryst. Struct.* **2004**, *219*, 209–210.

(43) Nowotny, H.; Funk, R.; Pesl, J. *Monatsh. Chem.* **1951**, *82*, 513–525.

(44) Auer-Welsbach, H.; Nowotny, H.; Kohl, A. *Monatsh. Chem.* **1958**, *89*, 154–159.

(45) Zhu, Y.; Kleinke, H. *Z. Anorg. Allg. Chem.* **2002**, *628*, 2233.

(46) Kleinke, H. *Inorg. Chem.* **2001**, *40*, 95–100.

(47) Bie, H.; Mar, A. unpublished result.

(48) Pauling, L. *The Nature of the Chemical Bond*, 3rd ed.; Cornell University Press: Ithaca, NY, 1960.

(49) Papoian, G. A.; Hoffmann, R. *Angew. Chem. Int. Ed.* **2000**, *39*, 2408–2448.

(50) Brown, I. D. In *Structure and Bonding in Crystals*; O'Keeffe, M.; Navrotsky, A., Eds.; Academic Press: New York, 1981; Vol. 2, pp 1–30.

(51) O'Keeffe, M.; Brese, N. E. *J. Am. Chem. Soc.* **1991**, *113*, 3226–3229.

Chapter 3

Ternary Rare-Earth Titanium Antimonides $RE_2Ti_{11-x}Sb_{14+x}$ (*RE* = Sm, Gd, Tb, Yb)*

3.1. Introduction

Ternary rare-earth transition-metal antimonides *RE*–*M*–Sb exhibit a rich structural chemistry.[1] Bonding character in these polar intermetallic compounds is more complicated to explain than that in classical Zintl phases, where complete valence electron transfer is assumed. As seen earlier in Chapter 2, the existence of two phases in the *RE*–Ti–Sb systems has now been established for the earlier *RE* metals: RE_3TiSb_5 (*RE* = La–Nd, Sm)[2,3] and $RE_2Ti_7Sb_{12}$ (*RE* = La–Nd).[4] No other ternary phases were revealed in the La–Ti–Sb phase diagram at 800 ºC besides the two indicated above.[4] A tin-stabilized phase, $RETi_3(Sn_xSb_{1-x})_4$ (x = 0.1), also forms for *RE* = Nd and Sm.[4] Although complete electron transfer does not seem to apply to disordered $RE_2Ti_7Sb_{12}$ and $RETi_3(Sn_xSb_{1-x})_4$, it provides a way to explain the occurrence of the significant homoatomic (Ti–Ti and Sb–Sb) bonding in the structures.

Unlike the later transition metals, Ti is electron poor with only four valence

*A version of this chapter has been published. Haiying Bie and Arthur Mar, 2008. Inorganic Chemistry, 47, 6763—6770.

electrons. Much of the interest in these antimonides relates to the search for new thermoelectric materials.[5,6] The different substructures found in these binary antimonides are summarized in Table 3–1. In binary metal-rich titanium antimonides, not only can the Ti atoms reduce Sb atoms completely to isolated Sb^{3-}, but extra electrons will also develop Ti–Ti bonding in the structure. These compounds include cubic Ti_3Sb, [7] Ti_2Sb, [8] Ti_5Sb_3, [9,10] and TiSb.[7] However, not all Sb atoms may be completely reduced and Sb–Sb bonding does exist in some metal-rich antimonides.[5,6] For example, in $Ti_{11}Sb_8$, the Sb7 atoms form 1D linear chains with distances of 2.759(2) and 2.838(2) Å.[11] In contrast, in metal-poor titanium antimonides, Ti–Ti bonding should not be expected. Thus, in Ti_5Sb_8, there is no significant Ti–Ti bonding observed, and the charge can be balanced as $(Ti^{4+})_5(Sb^{2.5-})_8$, consistent with the presence of an Sb_6 fragment (only $d_{(Sb–Sb)} < 3.2$ Å is considered), although this scheme is considered too simple.[12] Interestingly, in $TiSb_2$, both Ti–Ti and Sb–Sb bonds are present. If the observed Sb pairs ($d_{(Sb–Sb)} = 2.852$ Å) are assumed to be single bonds, as proposed by Armbrüster and coworkers, the formulation can be written as $Ti^{4+}(Sb^{2-})_2$.[13] Thus the Zintl-Klemm concept seems unable to reconcile the existence of Ti–Ti bonding (2.904 Å) with a Ti^{4+} species.

Table 3–1. Homoatomic Ti–Ti and Sb–Sb bonds in Ti–Sb binary system.

Compound	Structure	Ti units	$d_{Ti–Ti}$ (Å)	Sb units	$d_{Sb–Sb}$ (Å) < 3.2 Å
Ti_3Sb [7]	β-W	chains	2.61	isolated $Sb^{3–}$	none
Ti_2Sb [8]	La_2Sb	planar nets	2.82	isolated $Sb^{3–}$	none
Ti_5Sb_3 [9,10]	β-Yb_5Sb_3	butterfly clusters	2.84–2.99	isolated $Sb^{3–}$	none
TiSb [7]	NiAs	chains	3.15	isolated $Sb^{3–}$	none
$Ti_{11}Sb_8$ [11]	$Cr_{11}Ge_8$	chains, pairs	2.7–2.9	1D linear chains	2.76, 2.84
Ti_5Sb_8 [12]	$Zr_{2.4}Ti_{2.6}Sb_8$	none	~ 3.2	6-atom fragment	3.19
$TiSb_2$ [13]	$CuAl_2$	chains	2.90	pairs	2.85

In this chapter, we investigate *RE*–Ti–Sb systems for later *RE* elements. No ternary phases were found in the Er–Ti–Sb phase diagram,[4] but it is not clear if this also holds true for other systems containing a later *RE* metal. In attempts to substitute *RE* atoms with Sm, an unidentified new phase was observed which adopts a different structure. Here, we describe the synthesis of this phase, $RE_2Ti_{11-x}Sb_{14+x}$, which forms for *RE* = Sm, Gd, Tb, and Yb. The structure type is new, featuring a complex framework built up from six- and seven-coordinate Ti-centred polyhedra.

3.2. Experimental Section

3.2.1. Synthesis

In attempts to extend the $RE_2Ti_7Sb_{12}$ (*RE* = La–Nd) series to later *RE* members, a new phase was identified in a reaction intended to prepare "$Sm_2Ti_7Sb_{12}$", as determined by powder X-ray diffraction and EDX analysis. Similar reactions were carried out for *RE* = Gd–Er and Yb, but were successful for only *RE* = Gd, Tb, and Yb. Reactions were conducted by arc-melting mixtures of the elements with overall stoichiometry "$RE_2Ti_7Sb_{12}$" (~ 9% *RE*, 34% Ti, 57% Sb) in the arc melter. Starting materials were pieces of the rare-earth elements (99.9%, Hefa), Ti sponge (99.9%, Fisher), and Sb pieces (99.999%, Alfa-Aesar). The powder X-ray diffraction patterns of the as-melted ingots were

in good agreement with those calculated from the single-crystal data (Figure 3–1).

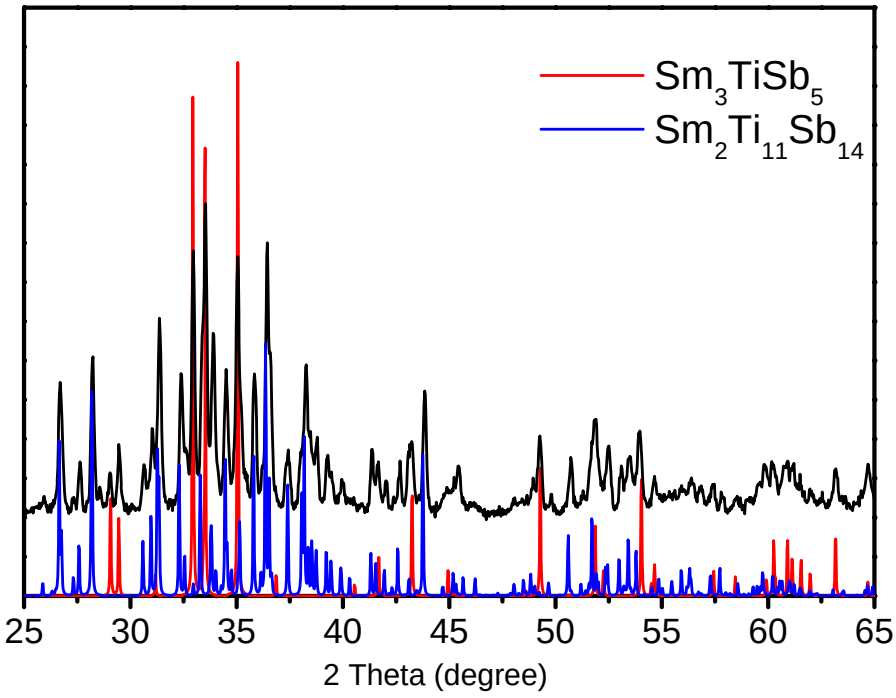

Figure 3–1. The powder X-ray diffraction pattern showing the $Sm_2Ti_{11}Sb_{14}$ phase (blue lines) and Sm_3TiSb_5 phase (red lines).

Single crystals of the title compounds were obtained after annealing the arc-melted samples, which were placed within alumina crucibles and then sealed within fused-silica tubes under vacuum. The tubes were heated to 650 ºC over 1 day, heated to 1050 ºC over 1 day, kept at that temperature for 2 days, slowly cooled to 800 ºC over 4 days, kept at that temperature for 12 days, and then slowly cooled to 20 ºC over 4 days. EDX analyses on these crystals gave approximate chemical compositions (8–13% *RE*, 38–43% Ti, 46–52% Sb) that were consistent with the formulas ultimately refined from the structure determinations. The ideal elemental composition for "$RE_2Ti_{11}Sb_{14}$" (7% *RE*,

41% Ti, 52% Sb) is not readily distinguishable from that for "$RE_2Ti_7Sb_{12}$" (9% *RE*, 34% Ti, 57% Sb), given that the uncertainties in quantitative EDX analyses. For $Gd_2Ti_{11-x}Sb_{14+x}$, suitable samples for single-crystal X-ray diffraction were unavailable, but its unit cell parameters refined from the powder X-ray diffraction pattern were found to be a = 15.899(1) Å, b = 5.7198(5) Å, and c = 12.938(1) Å.

In lieu of arc-melting, direct reactions of the elements close to the loading composition "$RE_2Ti_{11}Sb_{14}$" (*RE* = Sm, Gd–Er, Yb) with a similar heating profile as above were also attempted. These reactions generally resulted in the formation of binary phases, except for the occasional observation of small crystals of the ternary phase in the case of *RE* = Yb. Given that Yb has the lowest melting point of the late *RE* metals, we cannot rule out the possibility that the other ternary phases, including those of the "missing" *RE* members, may be accessible through a different heating treatment.

3.2.2. Structure Determination

Single crystals were selected for X-ray diffraction analysis and intensity data were collected on a Bruker Platform / SMART 1000 CCD diffractometer at 22 °C using ω scans. Structure solution and refinement were carried out with use of the SHELXTL (version 6.12) program package.[14] Face-indexed numerical absorption corrections were applied. Crystal data and further details of the data collection are given in Table 3–2.

For $Sm_2Ti_{11}Sb_{14}$, the intensity pattern, systematic absences and statistics favoured the centrosymmetric orthorhombic space group *Pnma*. Initial atomic positions for the Sm, Ti, and most of the Sb atoms were found by direct methods. The difference electron density map revealed additional peaks which were assigned as two sets of split Sb sites: Sb5/Sb6 and Sb7/Sb8. When allowed to refine freely and no restrictions are placed on the total occupancy within a set of split Sb sites, the occupancies converged to 0.52(2) for Sb5, 0.48(2) for Sb6, 0.53(2) for Sb7, and 0.47(2) for Sb8. In subsequent refinements, these occupancies were fixed at exactly 0.50. All other sites were found to be fully occupied except for Ti5, which exhibited an anomalously large displacement parameter and which is located too close to Sb6 (2.36 Å) and Sb7 (2.30 Å). The occupancy of Ti5 converged to 0.44(1) when refined, but was fixed at exactly 0.50 to simplify interpretation of the disorder inherent in the crystal structure, as described later. Intensity data on the same crystal were recollected to determine if site ordering sets in at low temperature (–80 ºC). However, these data led to essentially the same disordered structure solution as at room temperature.

Other subgroups of *Pnma* were considered ($P2_12_12_1$, $P2_1/c$, $P2_1/m$, $Pmn2_1$, $Pna2_1$, and $Pmc2_1$) to ascertain if the disorder problems result from an incorrect choice of space group with too high symmetry. In all cases, the same features of split Sb sites and partial Ti5 occupancy persists. Careful re-examination of the CCD frames of intensity data for the original crystal as well as other separately mounted crystals also provided no evidence for superstructure reflections.

Table 3–2. Crystallographic data for $RE_2Ti_{11-x}Sb_{14+x}$ (*RE* = Sm, Tb, Yb).

Formula	$Sm_2Ti_{11}Sb_{14}$	$Tb_2Ti_{10.41(1)}Sb_{14.59(1)}$	$Yb_2Ti_{10.58(1)}Sb_{14.42(1)}$
Formula mass (amu)	2532.10	2593.55	2608.87
Space group	*Pnma* (No. 62)	*Pnma* (No. 62)	*Pnma* (No. 62)
a (Å)	15.8865(6)	15.8693(18)	15.9529(9)
b (Å)	5.7164(2)	5.7036(6)	5.7135(3)
c (Å)	12.9244(5)	12.9309(15)	12.9442(7)
V (Å^3)	1173.71(8)	1170.4(2)	1179.82(11)
Z	2	2	2
ρ_{calcd} (g cm^{-3})	7.165	7.359	7.344
Crystal dimensions (mm)	0.23× 0.07 × 0.06	0.11 × 0.08 × 0.05	0.19 × 0.12 × 0.06
Radiation	Graphite monochromated Mo *K*α, λ = 0.71073 Å		
μ(Mo *K*α) (mm^{-1})	24.19	25.77	27.35
Transmission factors	0.056–0.282	0.076–0.292	0.043–0.248
2θ limits	4.06°≤2θ≤ 66.28°	4.06° ≤ 2θ≤ 66.26°	4.06° ≤ 2θ ≤ 66.24°
Data collected	–23 ≤ *h* ≤ 23, –8 ≤ *k* ≤ 8, –19 ≤ *l* ≤ 19	–24 ≤ *h* ≤ 24, –8 ≤ *k* ≤ 8, –19 ≤ *l* ≤ 19	–23 ≤ *h* ≤ 24, –8 ≤ *k* ≤ 8, –19 ≤ *l* ≤ 19
No. of data collected	15628	15600	15686
No. of unique data, including $F_o^2 < 0$	2403 (R_{int} = 0.038)	2396 (R_{int} = 0.082)	2410 (R_{int} = 0.036)
No. of unique data, with $F_o^2 > 2\sigma(F_o^2)$	2194	1866	2179
No. of variables	92	92	93
R(*F*) for $F_o^2 > 2\sigma(F_o^2)$ [a]	0.019	0.033	0.024
$R_w(F_o^2)$ [b]	0.042	0.061	0.050
Goodness of fit	1.101	1.052	1.151
$(\Delta\rho)_{max}$, $(\Delta\rho)_{min}$ (e Å^{-3})	1.06, –1.64	2.19, –2.12	1.50, –2.02

[a] $R(F) = \sum \| |F_o| - |F_c| \| / \sum |F_o|$.

[b] $R_w(F_o^2) = \left[\sum \left[w(F_o^2 - F_c^2)^2 \right] / \sum w F_o^4 \right]^{1/2}$; $w^{-1} = \left[\sigma^2(F_o^2) + (Ap)^2 + Bp \right]$ where $p = \left[\max(F_o^2, 0) + 2F_c^2 \right] / 3$.

Table 3–3. Atomic coordinates and equivalent isotropic displacement parameters (Å^2) for $RE_2Ti_{11-x}Sb_{14+x}$ (*RE* = Sm, Tb, Yb).

atom	Wyckoff position	occupancy	*x*	*y*	*z*	U_{eq} (Å^2) [a]
			$Sm_2Ti_{11}Sb_{14}$			
Sm	4*c*	1	0.3619(1)	¼	0.0530(1)	0.0110(1)
Ti1	4*c*	1	0.3745(1)	¼	0.7064(1)	0.0122(2)
Ti2	4*c*	1	0.0870(1)	¼	0.7532(1)	0.0115(1)
Ti3	8*d*	1	0.3520(1)	0.0073(1)	0.4860(1)	0.0096(1)
Ti4	4*c*	1	0.1881(1)	¼	0.3718(1)	0.0108(1)
Ti5	4*c*	0.50	0.0156(1)	¼	0.1525(2)	0.0222(4)
Sb1	4*c*	1	0.2494(1)	¼	0.8516(1)	0.0095(1)
Sb2	4*c*	1	0.4980(1)	¼	0.5622(1)	0.0114(1)
Sb3	4*c*	1	0.2127(1)	¼	0.5858(1)	0.0104(1)
Sb4	8*d*	1	0.0322(1)	0.5001(1)	0.3688(1)	0.0116(1)
Sb5	4*c*	0.50	0.3511(1)	¼	0.2906(2)	0.0103(3)
Sb6	4*c*	0.50	0.3720(1)	¼	0.3012(2)	0.0100(2)
Sb7	4*c*	0.50	0.1601(1)	¼	0.1637(1)	0.0104(2)
Sb8	4*c*	0.50	0.1867(1)	¼	0.1623(1)	0.0113(2)
			$Tb_2Ti_{10.41(1)}Sb_{14.59(1)}$			
Tb	4*c*	1	0.3618(1)	¼	0.0531(1)	0.0096(1)
Ti1	4*c*	1	0.3743(1)	¼	0.7053(1)	0.0082(3)
Ti2	4*c*	1	0.0878(1)	¼	0.7525(1)	0.0053(3)
*M*3	8*d*	0.853(3) Ti, 0.147(3) Sb	0.3511(1)	0.0080(1)	0.4860(1)	0.0063(3)
Ti4	4*c*	1	0.1880(1)	¼	0.3728(1)	0.0081(3)
Ti5	4*c*	0.50	0.0161(2)	¼	0.1532(2)	0.0118(6)

Sb1	4*c*	1	0.2505(1)	¼	0.8520(1)	0.0082(1)
Sb2	4*c*	1	0.4980(1)	¼	0.5621(1)	0.0086(1)
Sb3	4*c*	1	0.2114(1)	¼	0.5859(1)	0.0088(1)
Sb4	8*d*	1	0.0320(1)	0.5002(1)	0.3703(1)	0.0104(1)
Sb5	4*c*	0.50	0.3502(2)	¼	0.2889(4)	0.0087(5)
Sb6	4*c*	0.50	0.3718(2)	¼	0.2999(4)	0.0096(5)
Sb7	4*c*	0.50	0.1609(1)	¼	0.1639(2)	0.0099(4)
Sb8	4*c*	0.50	0.1887(1)	¼	0.1625(2)	0.0087(4)
			$Yb_2Ti_{10.58(1)}Sb_{14.42(1)}$			
Yb	4*c*	1	0.3634(1)	¼	0.0518(1)	0.0139(1)
Ti1	4*c*	1	0.3723(1)	¼	0.7058(1)	0.0132(2)
*M*2	4*c*	0.789(3) Ti, 0.211(3) Sb	0.0897(1)	¼	0.7498(1)	0.0134(2)
Ti3	8*d*	1	0.3517(1)	0.0062(1)	0.4855(1)	0.0108(1)
Ti4	4*c*	1	0.1880(1)	¼	0.3709(1)	0.0121(2)
Ti5	4*c*	0.50	0.0162(1)	¼	0.1546(2)	0.0120(3)
Sb1	4*c*	1	0.2499(1)	¼	0.8524(1)	0.0118(1)
Sb2	4*c*	1	0.4975(1)	¼	0.5630(1)	0.0116(1)
Sb3	4*c*	1	0.2133(1)	¼	0.5838(1)	0.0134(1)
Sb4	8*d*	1	0.0328(1)	0.0006(1)	0.3672(1)	0.0138(1)
Sb5	4*c*	0.50	0.3497(1)	¼	0.2898(2)	0.0117(3)
Sb6	4*c*	0.50	0.3709(1)	¼	0.3003(2)	0.0133(2)
Sb7	4*c*	0.50	0.1600(1)	¼	0.1634(1)	0.0139(2)
Sb8	4*c*	0.50	0.1894(1)	¼	0.1611(1)	0.0108(2)

[a] U_{eq} is defined as one-third of the trace of the orthogonalized U_{ij} tensor.

Table 3–4. Selected interatomic distances (Å) in $RE_2Ti_{11-x}Sb_{14+x}$ (*RE* = Sm, Tb, Yb) [a]

	$Sm_2Ti_{11}Sb_{14}$	$Tb_2Ti_{10.41(1)}Sb_{14.59(1)}$	$Yb_2Ti_{10.58(1)}Sb_{14.42(1)}$
RE–Sb5/Sb6	3.076(2) / 3.212(2)	3.055(5) / 3.196(5)	3.088(3) / 3.218(3)
RE–Sb8/Sb7	3.122(1) / 3.510(1)	3.089(2) / 3.495(2)	3.114(1) / 3.551(1)
RE–Sb3 (×2)	3.1231(2)	3.1084(4)	3.1348(2)
RE–Sb1	3.1569(4)	3.1440(7)	3.1528(5)
RE–Sb4 (×2)	3.2228(3)	3.2121(6)	3.2303(4)
RE–Sb4 (×2)	3.2462(3)	3.2333(6)	3.2415(4)
Ti1–Sb2	2.7062(9)	2.699(2)	2.7213(10)
Ti1–Sb1	2.7324(8)	2.730(2)	2.7237(10)
Ti1–Sb4 (×2)	2.9395(8)	2.965(1)	2.9509(9)
Ti1–Sb7/Sb8 (×2)	2.9624(4)/ 3.0722(5)	2.955(1) / 3.072(1)	2.9543(4) / 3.0768(6)
Ti1–Sb3	3.0058(9)	3.011(2)	2.988(1)
*M*2–Sb2	2.7330(9)	2.788(2)	2.8350(8)
*M*2–Sb4 (×2)	2.8481(7)	2.858(1)	2.8573(7)
*M*2–Sb1	2.8776(9)	2.885(2)	2.8793(8)
*M*2–Sb3	2.9441(9)	2.914(2)	2.9157(9)
*M*2–Sb6/Sb5 (×2)	2.9665(7)/ 3.0611(8)	2.987(2) / 3.054(2)	2.9972(9) / 3.0599(10)
*M*3–Sb7/Sb8	2.735(1) / 2.782(1)	2.738(3) / 2.788(3)	2.734(1) / 2.782(1)
*M*3–Sb6/Sb5	2.780(2) / 2.880(2)	2.793(4) / 2.898(4)	2.790(3) / 2.892(2)
*M*3–Sb1	2.7884(6)	2.787(1)	2.7816(7)
*M*3–Sb2	2.8691(6)	2.878(1)	2.8846(8)
*M*3–Sb2	2.8761(6)	2.882(1)	2.8903(8)
*M*3–Sb3	2.9139(6)	2.914(1)	2.9049(8)
Ti4–Sb8/Sb7	2.708(2) / 2.726(2)	2.719(3) / 2.735(3)	2.716(2) / 2.723(2)
Ti4–Sb3	2.7938(8)	2.781(2)	2.785(1)
Ti4–Sb5/Sb6	2.794(2) / 3.061(2)	2.793(4) / 3.065(4)	2.785(3) / 3.058(2)

Ti4–Sb4 (×2)	2.8599(7)	2.857(1)	2.8568(9)
Ti4–Sb1 (×2)	3.0367(3)	3.0261(6)	3.0334(4)
Ti5–Sb7/Sb8	[2.300(2)] / 2.720(2)	[2.302(4)] / 2.741(3)	[2.296(2)] / 2.765(2)
Ti5–Sb6/Sb5	[2.359(2)] / 2.715(2)	[2.369(4)] / 2.738(4)	[2.391(3)] / 2.753(2)
Ti5–Sb2	2.790(2)	2.799(3)	2.832(2)
Ti5–Sb2 (×2)	3.0948(8)	3.093(1)	3.1008(8)
Ti5–Sb4 (×2)	3.150(2)	3.160(3)	3.110(2)
Ti1–*M*3 (×2)	3.190(1)	3.176(2)	3.190(1)
*M*3–*M*3	2.774(1)	2.761(2)	2.786(1)
*M*3–*M*3	2.942(1)	2.943(2)	2.927(1)
Sb2–Sb2 (×2)	3.2803(3)	3.2740(6)	3.2903(4)
Sb4–Sb4	2.8572(4)	2.8492(9)	2.8494(5)
Sb4–Sb4	2.8592(4)	2.8544(9)	2.8641(5)
Sb5–Sb8	3.094(2)	3.040(4)	3.051(2)

[a] Sites *M*2 and *M*3 contain a mixture of Ti and Sb whose proportions depend on the *RE* member (See Table 3–3). Split sites Sb5/Sb6 and Sb7/Sb8 are each half-occupied.

Similar procedures applied to the data sets for the Tb and Yb compounds revealed that some of the other Ti sites had unusually small displacement parameters, suggesting that they are disordered with Sb atoms. In the Tb compound, the *M*3 site contains 0.85 Ti and 0.15 Sb, corresponding to an overall formula of $Tb_2Ti_{10.4}Sb_{14.6}$. In the Yb compound, the *M*2 site contains 0.79 Ti and 0.21 Sb, corresponding to an overall formula of $Yb_2Ti_{10.6}Sb_{14.4}$.

Atomic positions were standardized with the program STRUCTURE TIDY.[15] Final values of the positional and displacement parameters are given in Table 3–3. Selected interatomic distances are listed in Table 3–4.

3.2.3. Electrical Resistivity

Block-shaped single crystals of $Sm_2Ti_{11}Sb_{14}$ and $Yb_2Ti_{10.6}Sb_{14.4}$ were selected for electrical resistivity measurements after their identities were confirmed by EDX analysis. Given the small dimensions of these crystals, only two-point measurements were made on a Quantum Design Physical Property Measurement System (PPMS) equipped with an ac transport controller (Model 7100), from 2 to 300 K. The current was 100 μA and the frequency was 16 Hz. Measurements were performed twice to confirm reproducibility.

3.3. Results and Discussion

The structure of $RE_2Ti_{11-x}Sb_{14+x}$ (*RE* = Sm, Gd, Tb, Yb) is quite complex,

exhibiting several types of disorder: (i) split Sb sites, (ii) partial occupancy of one of the Ti sites, and (iii) mixing of Ti and Sb atoms. For simplicity, we first examine the structure of $Sm_2Ti_{11}Sb_{14}$, which exhibits only the first two types of disorder. Figure 3–2 shows the three-dimensional framework assembled by linking Ti-centred polyhedra with Sb atoms at the vertices, yielding cavities that are filled with Sm atoms. Within the two sets of split, half-occupied Sb sites (Sb5/Sb6 and Sb7/Sb8), only one member of each set is portrayed. There are five distinct Ti sites, one (Ti3) centred within octahedra ($TiSb_6$, CN6) and four (Ti1, Ti2, Ti4, Ti5) within pentagonal bipyramids ($TiSb_7$, CN7). Chains are formed that extend along the *b* direction by sharing opposite faces of the Ti-centred octahedra or by sharing equatorial vertices of the Ti-centred pentagonal bipyramids (Figure 3–3). The source of the disorder becomes apparent upon inspection of the chains containing the Ti5 sites, which are only half-occupied. In the other chains, the distances from the Ti centres to the Sb sites (including the half-occupied ones) are 2.7–3.0 Å, in good agreement with the sum of the Pauling radii (2.715 Å)[18] and with similar distances in $La_2Ti_7Sb_{12}$ (2.7373(4)–2.8785(6) Å).[4] In contrast, the half-occupancy of the Ti5 site arises because of the need to maintain reasonable Ti5–Sb distances: if Ti5 is occupied, the axial sites occupied must be Sb5 and Sb8 (2.715(2)–2.720(2) Å) but not Sb6 and Sb7 (2.300(2)–2.359(2) Å); if Ti5 is vacant, the axial sites can relax to Sb6 and Sb7.

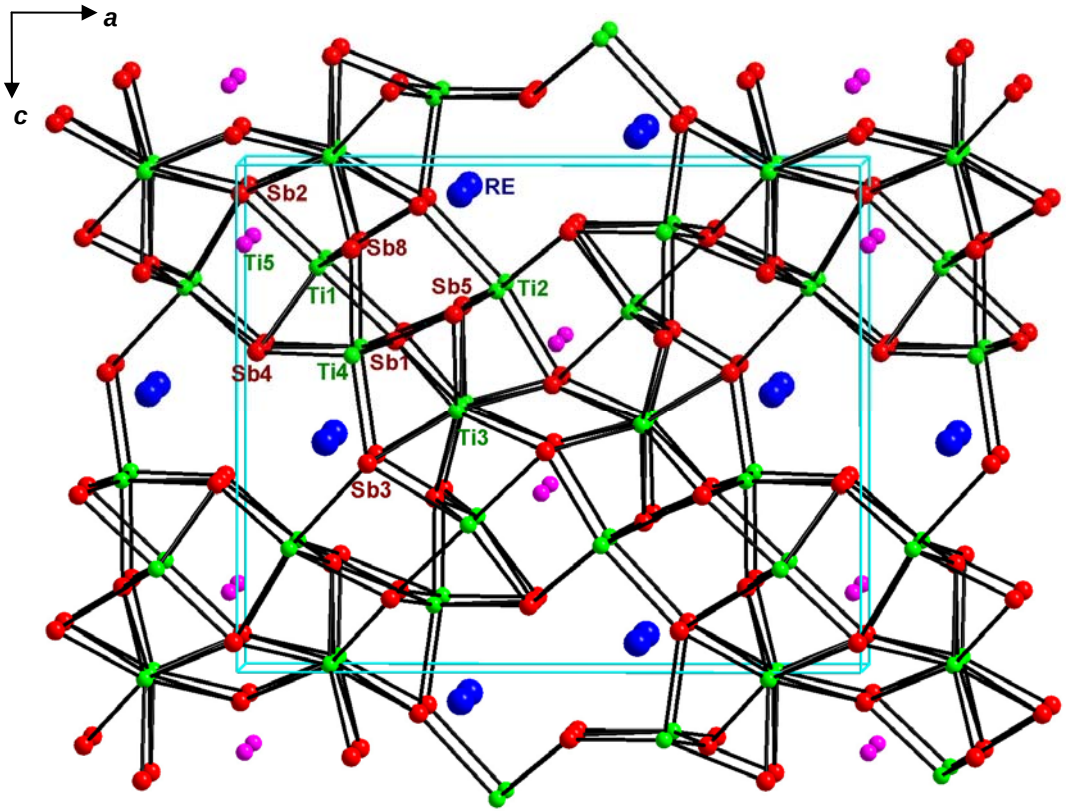

Figure 3–2. Structure of $RE_2Ti_{11-x}Sb_{14+x}$ (*RE* = Sm, Tb, Yb) viewed down the *b* direction, emphasizing the Ti–Sb framework. In the split sites Sb5/Sb6 and Sb7/Sb8, only one member of each set is shown. The blue, green, and red spheres are *RE*, Ti, and Sb atoms, respectively. Ti5 atom is shown in purple.

Associated with this disorder is the coordination environment around the Sm atom (Figure 3–4). The geometry is nine-coordinate, in the form of a monocapped square antiprism (the squares being Sb4–Sb4–Sb4–Sb4 and Sb3–Sb1–Sb3–Sb5/Sb6, and the cap being Sb8/Sb7). The Sm–Sb5 and Sm–Sb8 distances are the shortest (3.076(2) and 3.122(1) Å, respectively) within the polyhedron, at the lower limit of reasonable Sm–Sb contacts (cf. 3.13(2)–3.48(2) Å in $SmSb_2$ and 3.14 Å in SmSb).[16,17] Occupation of the alternate Sb sites

allows a more reasonable Sm–Sb6 distance to be recovered (3.212(2) Å) but considerably lengthens the Sm–Sb7 distance (3.510(1) Å). The occurrence of split Sb sites may thus be attributed to a structural compromise to balance the competing needs to achieve reasonable Ti5–Sb and Sm–Sb contacts.

The separation between Ti sites corresponds to approximately half the *b* parameter in the face-sharing octahedral chains or exactly the *b* parameter in the vertex-sharing pentagonal bipyramidal chains (Figure 3–3). The Ti3–Ti3 distances (2.774(1)–2.942(1) Å) within the face-sharing octahedral chains are similar to those found in related structure of $Ti_{11}Sb_8$ (2.707(4)–2.890(4) Å) where metal-metal bonding interactions have been confirmed to be present.[11] Common to all the vertex-sharing pentagonal bipyramidal chains, the Sb4 atoms form a linear skewer with 2.8572(4)–2.8592(4) Å distances also suggestive of Sb–Sb bonding.

The full three-dimensional structure is densely packed and may be built up from alternately stacking two types of slabs along the *c* direction (Figure 3–5). At $z = 0$ and ½, the slabs consist of double chains of face-sharing Ti3-centred octahedra and of *RE*-centred polyhedra. At $z = ¼$ and ¾, the slabs consist of double chains of Ti1- and Ti2-centred pentagonal pyramids. Within this arrangement of densely packed polyhedra, the remaining voids are then either fully occupied by Ti4 atoms or half-occupied by Ti5 atoms.

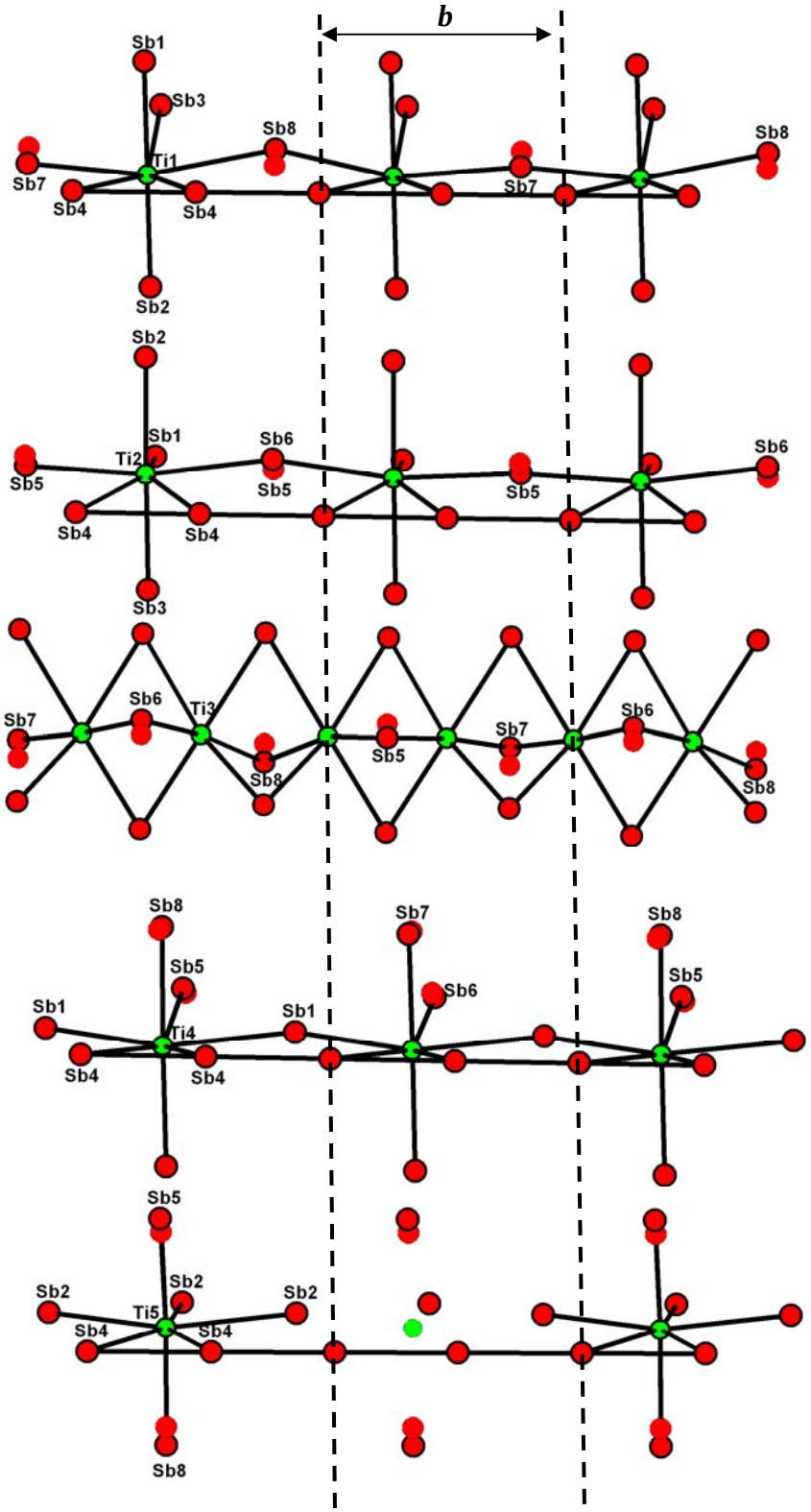

Figure 3–3. Chains of Ti-centred pentagonal bipyramids or octahedra extending down the *b* direction, with possible local orderings of the split Sb sites (Sb5/Sb6 and Sb7/Sb8) and half-occupied Ti5 site.

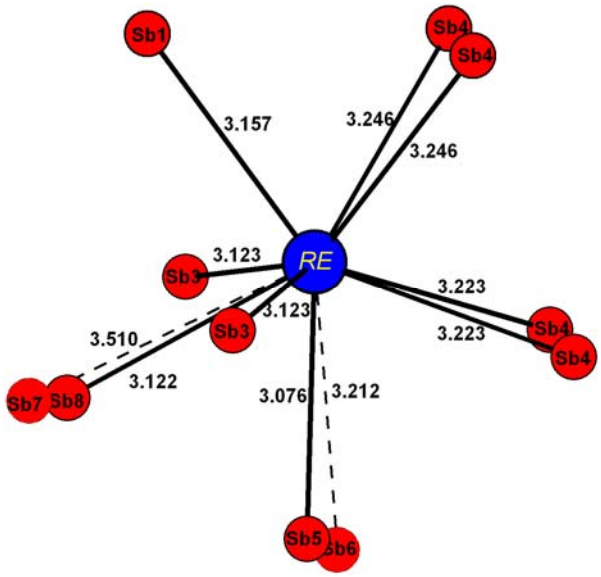

Figure 3–4. Monocapped square antiprismatic coordination around *RE* atom in $RE_2Ti_{11-x}Sb_{14+x}$ (*RE* = Sm, Tb, Yb). Distances shown (in Å) are for $Sm_2Ti_{11}Sb_{14}$.

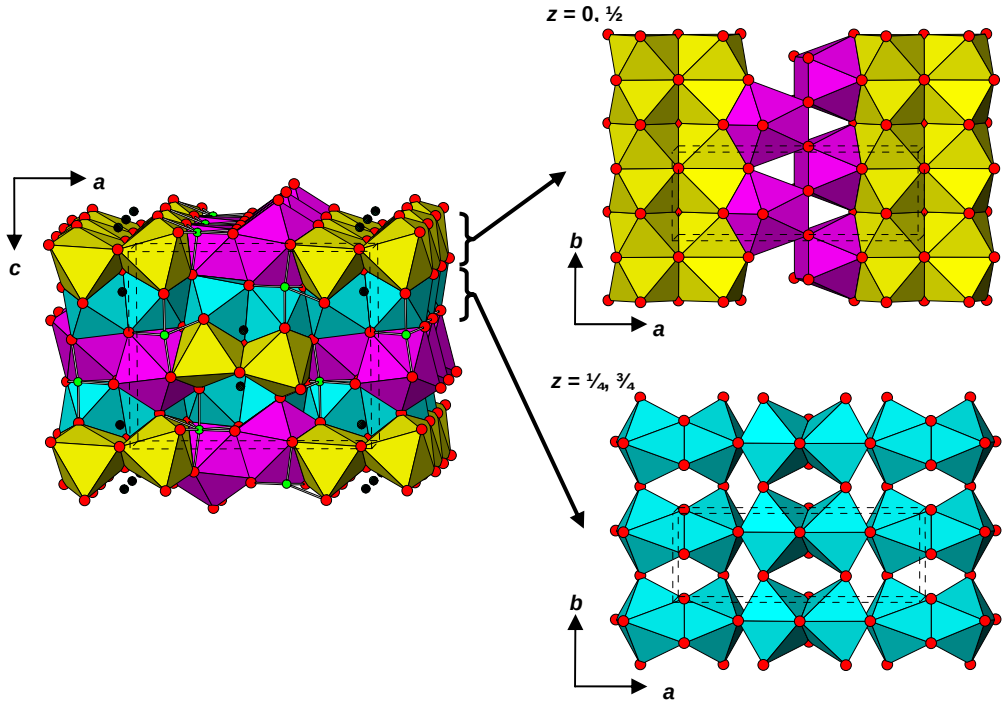

Figure 3–5. Structure of $RE_2Ti_{11-x}Sb_{14+x}$ (*RE* = Sm, Tb, Yb) in terms of two-dimensional slabs alternately stacked along the *c* direction consisting of (i) Ti3-centred octahedra (yellow) and *RE*-centred monocapped square antiprisms (magenta) (at z = 0, ½) or (ii) Ti1- and Ti2-centred pentagonal bipyramids (cyan) (at z = ¼, ¾). Remaining voids are filled by Ti4 and Ti5 atoms.

The clear demarcation between $RE_2Ti_{11-x}Sb_{14+x}$ (*RE* = Sm, Gd, Tb, Yb) and $RE_2Ti_7Sb_{12}$ (*RE* = La, Ce, Pr, Nd) suggests that there are critical limits on the size of the *RE* atom. In both cases, the *RE* atoms are surrounded by Sb atoms in nine-coordinate geometry, but the *RE*–Sb distances decrease significantly from $RE_2Ti_7Sb_{12}$ (e.g., 3.205(1)–3.471(1) Å in $La_2Ti_7Sb_{12}$)[4] to $RE_2Ti_{11-x}Sb_{14+x}$ (e.g., 3.076(2)–3.2462(3) Å in $Sm_2Ti_{11}Sb_{14}$), a manifestation of the lanthanide contraction. Substitution of Sm with later rare-earth metals leads to an additional disorder involving mixing of Ti and Sb atoms, giving the formulas $Tb_2Ti_{10.4}Sb_{14.6}$ and $Yb_2Ti_{10.6}Sb_{14.4}$. The substitution of such seemingly chemically disparate elements for each other may seem surprising, even though Ti and Sb are not too dissimilar in size (with metallic radii R_1 of 1.324 Å and 1.391 Å, respectively).[18] However, this type of disorder is now emerging to be a recurring feature of several transition-metal antimonides such as $Ti_{11-x}Sb_{8-y}$,[11] $Hf_6Ni_{1-x}Sb_{2+x}$,[19] $Zr_5M_{1-x}Sb_{2+x}$ (*M* = Fe, Co, Ni),[20] and $Hf_{10}M_xSb_{6-x}$ (*M* = V–Cu),[21] and points to the importance of size effects in controlling the stability of these structures. In $Tb_2Ti_{10.4}Sb_{14.6}$, 15% of the atoms in the "Ti3" site are replaced by slightly larger Sb atoms, which could be interpreted as a counteracting response against an overall contraction of the structure. In $Yb_2Ti_{10.6}Sb_{14.4}$, 21% of the atoms in a different site, "Ti2", are replaced by Sb atoms, and interestingly, the cell parameters and bond distances have now increased (relative to $Tb_2Ti_{10.4}Sb_{14.6}$). The interruption of the $RE_2Ti_{11-x}Sb_{14+x}$ series after *RE* = Tb and its resumption at *RE* = Yb argues strongly for the presence of divalent Yb, in contrast to trivalent

RE for the other members, to offset the structural contraction. Unfortunately, pure samples could not be obtained for further magnetic measurements to confirm its oxidation state. (The trend in size can be inferred from the Shannon-Prewitt (ionic) radii for RE^{3+} (CN9), which decrease from 1.36 to 1.30 Å for La^{3+} to Nd^{3+}, 1.27 to 1.24 Å for Sm^{3+} to Tb^{3+}, and then to 1.18 Å for Yb^{3+}.[22] The radius for Yb^{2+} (only specified up to CN8) is 1.28 Å.) The $RE_2Ti_{11-x}Sb_{14+x}$ structure thus appears to be stable only within a rather limited range of permitted *RE* sizes. It remains unclear why the site preference for the Sb admixture differs in the Tb vs. Yb members; indeed both sites might be simultaneously susceptible to this mixing, giving rise to a limited range of solid solubility. Because the original syntheses were performed with a deficiency of Ti relative to the final refined compositions, and the weight loss from Sb volatilization that occurs during arc-melting is variable (typically ranging from ~3 to ~8 at. %), the final composition that is attained may well differ depending on the synthetic conditions. If the "Ti2" and "Ti3" sites are assumed to be the only ones that can accommodate mixing with Sb atoms, to a maximum of 50%, then the limits of solid solubility in $RE_2Ti_{11-x}Sb_{14+x}$ can be estimated to lie within the range $0 < x < 3$.

Neglecting distances beyond 3.3 Å, the Sb substructures present in $RE_2Ti_{11-x}Sb_{14+x}$ consist of: (i) 1D linear chains formed by Sb4–Sb4 bond ($d_{(Sb4–Sb4)}$ = 2.86 Å); (ii) 1D zig-zag chains formed by hypervalent Sb2–Sb2 bond ($d_{(Sb2–Sb2)}$ = 3.28 Å); (iii) pairs formed by hypervalent Sb5–Sb8 bond ($d_{(Sb5–Sb8)}$ = 3.09 Å) (Figure 3–6). The charges are assigned as 2– for the hypervalent 2b-Sb2

atoms; 2.5– for the hypervalent 1b-Sb5 and Sb8 atoms; 3– for the isolated Sb1, Sb3, Sb6 and Sb7 atoms; and 2– for the hypervalent 2b-Sb4 atoms in linear chains (which are incompatible with sp^3 hybridization, similar to the situation in $Ti_{11}Sb_8$).[11] The resulting overall negative charge of 35– in the idealized formula $RE_2Ti_{11}Sb_{14}$ must be balanced by an equal positive charge on the *RE* and Ti atoms. If trivalent *RE* is assumed, the eleven Ti atoms should bear a charge of 29+, or 2.6+ per Ti atom, consistent with the short Ti–Ti bond distances (e.g. $d_{(Ti3–Ti3)}$ = 2.77 Å).

Resistivity measurements on $Sm_2Ti_{11}Sb_{14}$ and $Yb_2Ti_{10.6}Sb_{14}$ reveal typical metallic behaviour (Figure 3–7), with only a very weak temperature dependence characteristic of disordered materials. In $Sm_2Ti_{11}Sb_{14}$, the resistivity ratio is already quite low (ρ_{300}/ρ_2 = 1.7), whereas in $Yb_2Ti_{10.6}Sb_{14.4}$, the resistivity is nearly temperature-independent (ρ_{300}/ρ_2 = 1.1), consistent with significant scattering of conduction electrons by defects.

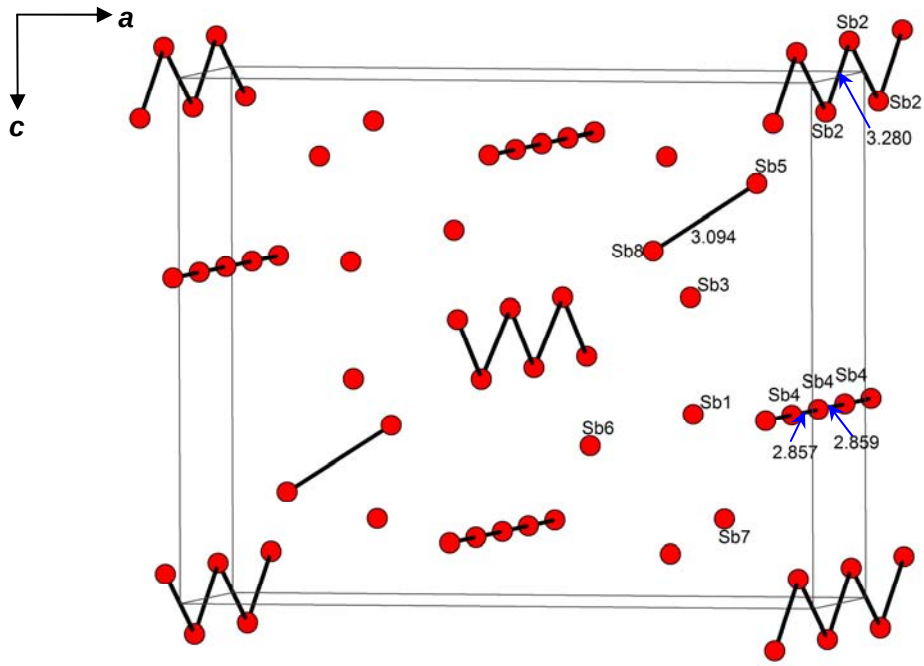

Figure 3–6. The Sb substructures in $Sm_2Ti_{11}Sb_{14}$: zig-zag chains, 1D linear chains, and pairs.

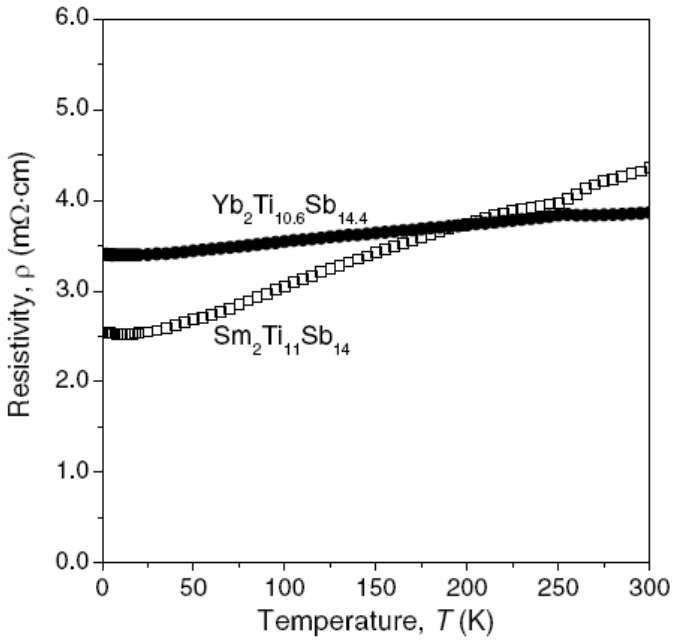

Figure 3–7. Electrical resistivity of single crystals of $Sm_2Ti_{11}Sb_{14}$ and $Yb_2Ti_{10.6}Sb_{14.4}$.

3.4. Conclusions

$RE_2Ti_{11-x}Sb_{14+x}$ (*RE* = Sm, Gd, Tb, Yb) extends the body of known ternary phases in the *RE*–Ti–Sb systems, which was previously restricted to RE_3TiSb_5 (La–Nd, Sm) and $RE_2Ti_7Sb_{12}$ (La–Nd). Homoatomic Ti-Ti and Sb-Sb bonding interactions are an important component in the structures of all these phases, but disorder between titanium and antimony atoms can ensue in response to size demands of the *RE* component. Further work is in progress to examine the remaining ternary systems containing the other *RE* metals, such as Eu.

3.5. References

(1) Sologub, O. L.; Salamakha, P. S. In *Handbook on the Physics and Chemistry of Rare Earths*; Gschneidner, K. A., Jr., Bünzli, J.-C. G., Pecharsky, V. K., Eds.; Elsevier: Amsterdam, 2003; Vol. 33, pp 35–146.

(2) Bolloré, G.; Ferguson, M. J.; Hushagen, R. W.; Mar, A. *Chem. Mater.* **1995**, *7*, 2229–2231.

(3) Moore, S. H. D.; Deakin, L.; Ferguson, M. J.; Mar, A. *Chem. Mater.* **2002**, *14*, 4867–4873.

(4) Bie, H.; Moore, S. H. D.; Piercey, D. G.; Tkachuk, A. V.; Zelinska, O. Ya.; Mar, A. *J. Solid State Chem.* **2007**, *180*, 2216–2224.

(5) Kleinke, H. *Chem. Soc. Rev.* **2000**, *29*, 411–418.

(6) Kleinke, H. Nonclassical Sb–Sb Bonding in Transition Metal Antimonides. In *Inorganic Chemistry in Focus II*; Meyer, G., Naumann, D., Wesemann, L., Eds.; Wiley-VCH: Weinheim, Germany, 2005; pp 167–191.

(7) Kjekshus, A.; Grønvold, F.; Thorbjørnsen, J. *Acta Chem. Scand.* **1962**, *16*, 1493–1510.

(8) Derakhshan, S.; Assoud, A.; Kleinke, K. M.; Dashjav, E.; Qiu, X.; Billinge, S. J. L.; Kleinke, H. *J. Am. Chem. Soc.* **2004**, *126*, 8295–8302.

(9) Berger, R. *Acta Chem. Scand. Ser. A: Phys. Inorg. Chem.* **1977**, *31*, 889–890.

(10) Kaiser, J. W.; Haase, M. G.; Jeitschko, W. *Z. Anorg. Allg. Chem.* **2001**, *627*, 2369–2376.

(11) Bobev, S.; Kleinke, H. *Chem. Mater.* **2003**, *15*, 3523–3529.

(12) a) Zhu, Y.; Kleinke, H. *Z. Anorg. Allg. Chem.* **2002**, *628*, 2233; b) Kleinke, H. *Inorg. Chem.* **2001**, *40*, 95–100.

(13) a) Armbrüster, M.; Cardoso Gil, R.; Burkhardt, U.; Grin, Yu. *Z. Kristallogr. – New Cryst. Struct.* **2004**, *219*, 209–210; b) Armbrüster, M.; Schnelle, W.; Schwarz, U.; Grin, Y. *Inorg. Chem.* **2007**, *46*, 6319–6328.

(14) Sheldrick, G. M. *SHELXTL*, version 6.12; Bruker AXS Inc.: Madison, WI, 2001.

(15) Gelato, L. M.; Parthé, E. *J. Appl. Crystallogr.* **1987**, *20*, 139–143.

(16) Wang, R.; Steinfink, H. *Inorg. Chem.* **1967**, *6*, 1685–1692.

(17) Iandelli, A. *Z. Anorg. Allg. Chem.* **1956**, *288*, 81–86.

(18) Pauling, L. *The Nature of the Chemical Bond*, 3rd ed.; Cornell University Press: Ithaca, NY, 1960.

(19) Kleinke, H. *J. Alloys Compd.* **1998**, *270*, 136–141.

(20) Kwon, Y.–U.; Sevov, S. C.; Corbett, J. D. *Chem. Mater.* **1990**, *2*, 550–556.

(21) Kleinke, H.; Ruckert, C.; Felser, C. *Eur. J. Inorg. Chem.* **2000**, 315–322.

(22) Shannon, R. D. *Acta Crystallogr., Sect. A* **1976**, *32*, 751–767.

Chapter 4

Structures and Physical Properties of Rare-Earth Chromium Germanides *RE*$CrGe_3$ (*RE* = La–Nd, Sm)*

4.1. Introduction

The wide variety of magnetic properties displayed by intermetallic compounds containing rare-earth (*RE*) and transition metals (*M*) arises from different interactions between the localized f-electrons of the *RE* atoms, through the possible intermediary of the d-electrons of the *M* atoms. Our own work on ternary rare-earth transition-metal antimonides has revealed compounds such as *RE*$CrSb_3$ that exhibit magnetic ordering.[1] Because Ge and Sb have similar electronegativities and atomic radii (as noted in Chapter 1), exemplifying what might be regarded as a diagonal relationship in the periodic table, we were interested in extending this work to ternary germanides. Numerous ternary *RE*–*M*–Ge phases have now been identified, especially with the later transition metals from the Fe, Co, Ni, and Cu; in contrast, much less is known about those containing an early transition metal.[2] In the *RE*–(Ti, V, or Cr)–Ge systems, the only known phases so far are *RE*$TiGe_3$,[3–7] *RE*$TiGe_3$,[8,9] $RE_2Ti_3Ge_4$,[10–12] $Sc_xV_{5-x}Ge_3$,[13] $Sc_2V_3Ge_4$,[14,15] $Sc_{1+x}V_{5-x}Ge_5$,[15] $Sc_2Cr_4Ge_5$,[16] $Sc_7Cr_{4+x}Ge_{10-x}$,[16,17] $ScCrGe_2$,[16]

*A version of this chapter has been published. Haiying Bie, Oksana Ya. Zelinska, Andriy V. Tkachuk, and Arthur Mar, 2008. Chemistry of Materials, 47, 6763—6770. All work presented in this chapter was completed by myself with the experimental assistance from O. Ya. Zelinska and A.V. Tkachuk.

La_5CrGe_3,[18] $Nd_2Cr_9Ge_8$,[19] $Sm_{117}Cr_{52}Ge_{112}$,[20] and $RECr_6Ge_6$.[21,22] Among these phases, $RETiGe_3$ (*RE* = La, Ce, Pr)[9] is worthy of attention because it represents an unusual example of an intermetallic phase adopting the hexagonal perovskite structure type,[23] which consists of 1D chains of face-sharing octahedra and is normally found for chalcogenides and halides. $CeTiGe_3$ was shown to order ferromagnetically with a low Curie temperature (T_c) of 14 K and was proposed to be a dense Kondo lattice compound.[9]

In this chapter, we report the new series $RECrGe_3$ (*RE* = La–Nd, Sm) also adopting the hexagonal perovskite structure type. These compounds are also ferromagnetic, but the substitution of Cr for Ti increases the ordering temperatures significantly in $RECrGe_3$ because of magnetic interactions involving the Cr moments.

4.2. Experimental Section

4.2.1. Synthesis

Starting materials were *RE* pieces (99.9%, Hefa), Cr powder (99.8%, Alfa-Aesar), and Ge powder (99.999%, Cerac). Single crystals of $RECrGe_3$ used for structure determination were grown from mixtures of *RE*, Cr, Ge, and Sn in the molar ratio 3:1:5:10, contained in evacuated fused-silica tubes. The presence of excess Sn, which acts as a flux, aids in improving crystal quality. The samples were heated at 850 ºC for 4 d, heated at 500 ºC for 4 d, and then cooled to room temperature over 1 d. After treatment with 6 M HCl to dissolve the Sn flux, needle-shaped crystals of $RECrGe_3$ could be obtained for *RE* = La–Nd, with

typical lengths of up to ~0.5 mm. EDX analysis on these crystals showed the presence of all three elements in ratios (18–22% *RE*, 17–25% Cr, 56–61% Ge) consistent with the formulas obtained from the structure determinations.

Powder samples of *RE*$CrGe_3$ (*RE* = La–Nd, Sm) could be obtained by arc melting of stoichiometric mixtures of the elements in the form of pieces or rods (99.9% or better). The arc-melted ingots were then sealed in evacuated fused-silica tubes and annealed at 800 ºC for 20 d, followed by quenching in cold water. Powder X-ray diffraction patterns of the arc-melted samples were in good agreement with those calculated from the single-crystal data. The samples were phase-pure, except for that with *RE* = Sm, which contained a small amount of Ge (~8%).

Attempts were made to extend the *RE*$CrGe_3$ series to other *RE* members. Our investigations revealed that the *RE*$CrGe_3$ phase could not be formed for *RE* = Gd–Yb at 800 ºC.

4.2.2. Structure Determination

Single-crystal intensity data for *RE*$CrGe_3$ (*RE* = La–Nd) were collected on a Bruker Platform / SMART 1000 CCD diffractometer at 22 °C using ω scans. Structure solution and refinement were carried out with use of the SHELXTL (version 6.12) program package.[24] Face-indexed numerical absorption corrections were applied. Laue symmetry and systematic absences were consistent with the hexagonal space groups $P6_3mc$, $P62c$, and $P6_3/mmc$. The centrosymmetric space group $P6_3/mmc$ was chosen and initial atomic positions

were found by direct methods. Refinements proceeded in a straightforward manner. Refinements on the occupancy factors confirmed that all sites are fully occupied with reasonable displacement parameters. Atomic positions were standardized with the program STRUCTURE TIDY.[25]

Powder X-ray diffraction data collected for *RE*$CrGe_3$ (*RE* = La–Nd, Sm) were also refined with the full-profile Rietveld method using the program LHPM-Rietica.[26] Initial positions were taken from the single-crystal structures determined above. The final cycle of least-squares refinement included scale factor, background, zero point, cell parameters, pseudo-Voigt peak profile parameters, atomic coordinates, and isotropic displacement parameters. Fits to the powder patterns are shown in Figure A1–1 and the Rietveld refinement results are summarized in Table A1–1 in Appendix 1.

Crystal data from the single-crystal structure determinations of *RE*$CrGe_3$ (*RE* = La–Nd) and the Rietveld refinement of $SmCrGe_3$ are given in Table 4–1. Final values of the positional and displacement parameters are given in Table 4–2. Interatomic distances are listed in Table 4–3.

4.2.3. Electrical and Magnetic Properties

Electrical resistivities from 2 to 300 K were measured on needle-shaped single crystals of *RE*$CrGe_3$ (*RE* = La–Nd) that had been used for the single-crystal structure determinations by standard four-probe techniques as discussed in Chapter 1. The current was 100 μA and the frequency was 16 Hz. Given the habit of the crystals, the resistivity could only be easily measured along the needle

axis, which corresponds to the crystallographic *c* axis. All measurements were repeated at least twice.

Measurements of dc magnetic susceptibility were made on powders of *RE*$CrGe_3$ (*RE* = La–Nd, Sm) between 2 and 300 K on a Quantum Design 9T–PPMS dc magnetometer / ac susceptometer. Susceptibility values were corrected for contributions from the holder and sample diamagnetism. Measurements of ac magnetic susceptibility were made with a driving amplitude of 1 Oe and frequencies between 1000 and 5000 Hz.

4.2.4. Band Structure Calculation

Tight-binding linear muffin tin orbital (TB-LMTO) band structure calculations were performed on $LaCrGe_3$ within the local density and atomic spheres approximations using the Stuttgart TB-LMTO program.[27] The basis sets consisted of La 6s, 6p, 5d, 4f; Cr 4s, 4p, 3d; and Ge 4s, 4p, 4d orbitals, with the La 6p and Ge 4d orbitals being downfolded. Integrations in reciprocal space were carried out with an improved tetrahedron method over 95 independent *k* points within the first Brillouin zone. Non-spin-polarized and spin-polarized calculations were carried out.

Table 4–1. Crystallographic data for *RE*$CrGe_3$ (*RE* = La–Nd, Sm).

Formula	$LaCrGe_3$	$CeCrGe_3$	$PrCrGe_3$	$NdCrGe_3$	$SmCrGe_3$
Formula mass (amu)	408.68	409.89	410.68	414.01	420.11
Space group			$P6_3/mmc$ (No. 194)		
a (Å)	6.2004(7)	6.150(2)	6.1416(6)	6.1264(4)	6.0812(3)
c (Å)	5.7660(6)	5.7222(19)	5.7039(5)	5.6914(4)	5.6594(3)
V (Å^3)	191.97(4)	187.45(11)	186.32(3)	185.00(2)	181.25(2)
Z	2	2	2	2	2
ρ_{calcd} (g cm^{-3})	7.070	7.262	7.320	7.432	7.694
Radiation		Mo $K\alpha$, λ = 0.71073 Å			Cu $K\alpha_1$, λ = 1.54056 Å
μ (mm^{-1})	36.59	38.22	39.31	40.46	169.79
2θ range	7.58–66.08°	7.66–66.20°	7.66–66.02°	7.68–52.68°	10.00–100.00°
No. of data collected	2235 (R_{int} = 0.055)	2237 (R_{int} = 0.051)	2191 (R_{int} = 0.049)	1395 (R_{int} = 0.047)	3103 data points
No. of unique data	165 (159 with $F^2 > 2\sigma(F^2)$)	161 (161 with $F^2 > 2\sigma(F^2)$)	160 (160 with $F^2 > 2\sigma(F^2)$)	93 (93 with $F^2 > 2\sigma(F^2)$)	49 Bragg reflections
No. of variables	10	10	10	10	19
Residuals [a]	$R(F)$ ($F^2 > 2\sigma(F^2)$) = 0.024, $R_w(F^2)$ = 0.052	$R(F)$ ($F^2 > 2\sigma(F^2)$) = 0.028, $R_w(F^2)$ = 0.070	$R(F)$ ($F^2 > 2\sigma(F^2)$) = 0.032, $R_w(F^2)$ = 0.075	$R(F)$ ($F^2 > 2\sigma(F^2)$) = 0.024, $R_w(F^2)$ = 0.064	R_B = 0.050, R_p = 0.046, R_{wp} = 0.065
Goodness of fit	1.299	1.079	1.334	1.064	2.56

[a] $R(F) = \sum \| F_o | - | F_c \| / \sum |F_o|$; $R_w(F_o^2) = \left[\sum \left[w(F_o^2 - F_c^2)^2 \right] / \sum w F_o^4 \right]^{1/2}$; $R_B = \sum |I_o - I_c| / \sum I_o$; $R_p = \sum |y_o - y_c| / \sum y_o$;
$R_{wp} = \left[\sum [w(y_o - y_c)] / \sum w y_o^2 \right]^{1/2}$, $w^{-1} = \left[\sigma^2(F_o^2) + (Ap)^2 + Bp \right]$ where $p = \left[\max(F_o^2, 0) + 2F_c^2 \right] / 3$.

Table 4–2. Atomic coordinates and equivalent isotropic displacement parameters (Å^2) for *RE*CrGe$_3$ (*RE* = La–Nd, Sm).[a]

	$LaCrGe_3$	$CeCrGe_3$	$PrCrGe_3$	$NdCrGe_3$	$SmCrGe_3$
RE at 2*d* (⅓, ⅔, ¾)					
U_{eq} (or U_{iso})	0.0082(3)	0.0099(4)	0.0063(4)	0.0101(6)	0.006(1)
Cr at 2*a* (0, 0, 0)					
U_{eq} (or U_{iso})	0.0077(4)	0.0094(5)	0.0052(5)	0.0096(8)	0.013(3)
Ge at 6*h* (*x*, 2*x*, ¼)					
x	0.1934(1)	0.1931(1)	0.1934(1)	0.1932(2)	0.1889(3)
U_{eq} (or U_{iso})	0.0078(3)	0.0104(4)	0.0063(4)	0.0101(6)	0.002(1)

[a] U_{eq} is defined as one-third of the trace of the orthogonalized U_{ij} tensor. U_{iso} applies to $SmCrGe_3$.

Table 4–3. Selected interatomic distances (Å) in *RE*CrGe$_3$ (*RE* = La–Nd, Sm).

	$LaCrGe_3$	$CeCrGe_3$	$PrCrGe_3$	$NdCrGe_3$	$SmCrGe_3$
RE–Ge (×6)	3.1134(4)	3.0880(11)	3.0839(3)	3.0761(2)	3.0496(3)
RE–Ge (×6)	3.2514(5)	3.2277(10)	3.2173(5)	3.2107(7)	3.213(2)
Cr–Ge (×6)	2.5278(7)	2.5054(11)	2.5027(9)	2.4957(13)	2.442(3)
Cr–Cr (×2)	2.8830(3)	2.8611(9)	2.8519(3)	2.8457(2)	2.8297(1)
Ge–Ge (×2)	2.6038(14)	2.588(2)	2.5792(18)	2.575(3)	2.635(6)

4.3. Results and Discussion

4.3.1. Crystal Structure

The *RE*CrGe$_3$ series forms for the early rare-earths (*RE* = La–Nd, Sm) and is the most Ge-rich phase found in the *RE*–Cr–Ge systems so far. The structure

consists of chains of face-sharing Cr-centred octahedra, $^{1}_{\infty}[CrGe_{6/2}]$, aligned along the *c* direction, separated by *RE* atoms (Figure 4–1). The *RE* atoms are coordinated by twelve Ge atoms in an anticuboctahedral geometry. On progressing from the La to the Sm member, the *RE*–Ge distances generally decrease regularly from 3.1134(4) Å (around the planar hexagonal waist) and 3.2514(5) Å (in a trigonal prism) to 3.0496(3) Å and 3.213(2) Å because of the lanthanide contraction. The surprisingly variable Cr–Ge distances within the Cr-centred octahedra range from 2.5278(7) Å for $LaCrGe_3$ to 2.442(3) Å for $SmCrGe_3$, in good agreement with distances found in $Cr_{11}Ge_8$ and $Cr_{11}Ge_9$,[28,29] and slightly longer than the sum of the single-bond metallic radii (Cr, 1.186 Å; Ge, 1.242 Å).[30] Face-sharing of octahedra is normally disfavoured in solid state structures because of the repulsions experienced by cationic centres in close proximity, unless charges are small or another overriding factor such as metal-metal bonding is present. Both effects are probably occurring in *RE*$CrGe_3$, where the Cr–Cr distances along the face-sharing octahedral chains (2.8830(3)–2.8297(1) Å) are suggestive of weak metal-metal bonding. Despite the appearance of a 1D structure, an interesting feature is that these chains are linked by Ge–Ge interactions in the form of triangular clusters so that strong bonding really extends in all three dimensions in the structure (Figure 4–1). Consistent with single bonds, these Ge–Ge distances are quite short (2.6038(14)–2.575(3) Å), slightly longer those in the covalently bonded Ge–Ge dimers in Gd_2MgGe_2 (2.525(3) Å),[31] and relatively invariant with *RE* substitution.

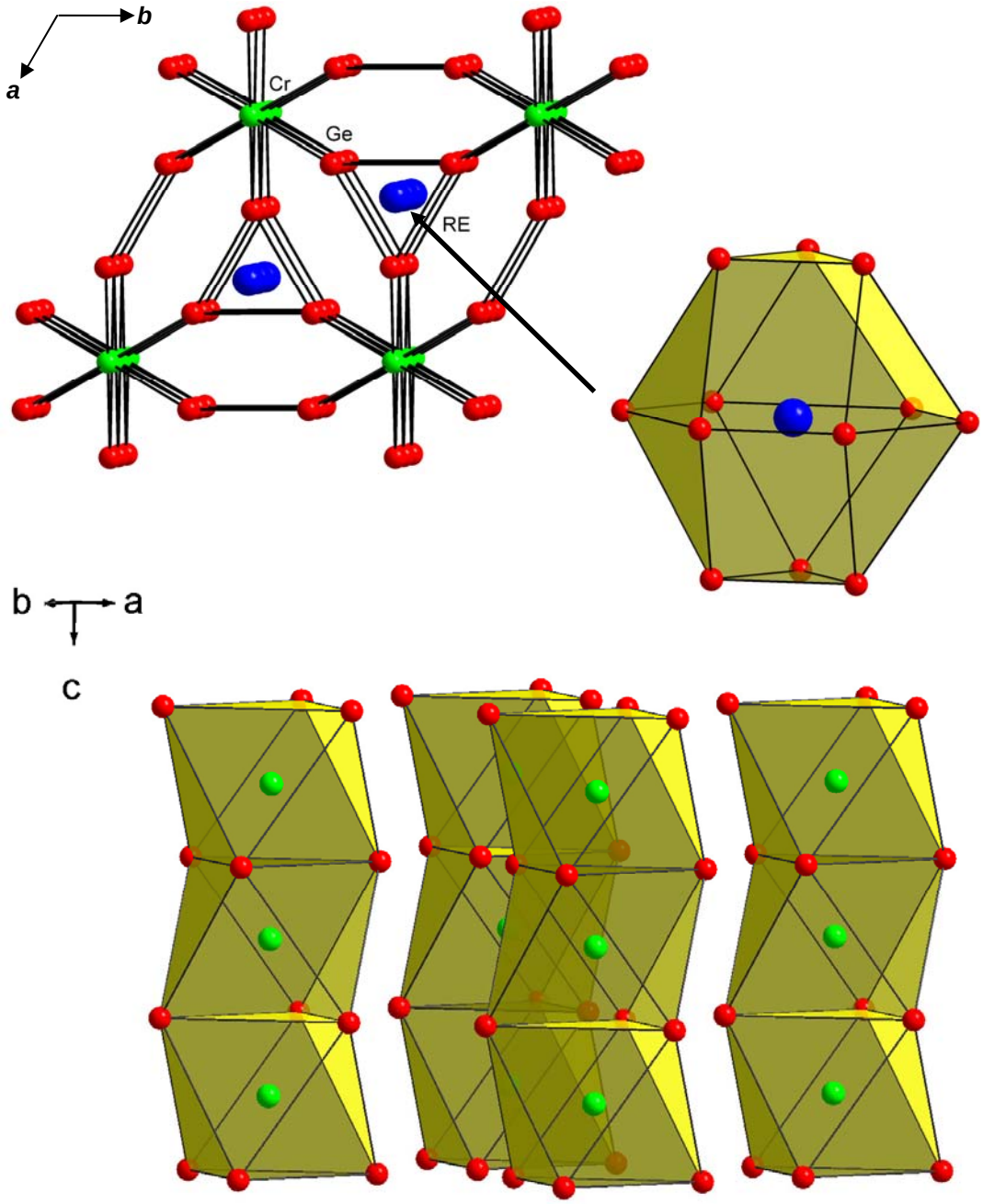

Figure 4–1. Structure of *RE*$CrGe_3$ (*RE* = La–Nd, Sm) viewed down the *c*-direction showing the chains of face-sharing $CrGe_6$ octahedra and anticuboctahedral geometry of rare-earth atoms. The blue, green, and red spheres represent *RE*, Cr, and Ge atoms, respectively.

The structure of *RE*$CrGe_3$ can be identified as a hexagonal perovskite ($BaNiO_3$-type or $BaVS_3$-type),[32,33] which is more commonly adopted by chalcogenides ABQ_3 and halides ABX_3. This and the isostructural *RE*$TiGe_3$ series[9] are the only examples known so far of an intermetallic representative of a hexagonal perovskite. Whereas isolated Q^{2-} or X^{1-} species can be regarded to be present in the more ionic representatives, the same cannot be said for *REM*Ge_3 (*M* = Ti, Cr), which must necessarily have a polyanionic substructure. If charges of RE^{3+} and Cr^{3+} are assumed in *RE*$CrGe_3$ in the Zintl-Klemm formalism, the electron transfer to the anionic framework is insufficient to provide each Ge atom with an octet. A hypothetical Ge^{2-} species would then require formation of two additional homoatomic Ge–Ge bonds per atom, on average, to satisfy the octet rule. Although the degree of charge transfer in *REM*Ge_3 is expected to be much less pronounced and the notion of localized electrons is questionable, this Zintl-Klemm formalism provides, surprisingly, a satisfying rationalization for the occurrence of triangular Ge_3 clusters, consistent with this prediction of two-bonded Ge atoms.

4.3.2. Physical Properties

Interesting magnetic properties may be anticipated by the presence of Cr atoms in chains, which could interact via *RE* atoms. Moreover, given the quasi-1D structure, these properties may be expected to exhibit a high anisotropy. As an initial study of the bulk properties of these *RE*$CrGe_3$ materials, the following magnetic results pertain to powder samples only, while electrical resistivities have been measured for single crystals along the *c* direction. Table 4–4 summarizes the magnetic and electrical data.

Table 4–4. Summary of resistivity and magnetism data for *RE*$CrGe_3$ (*RE* = La–Nd, Sm).

	$LaCrGe_3$	$CeCrGe_3$	$PrCrGe_3$	$NdCrGe_3$	$SmCrGe_3$
ρ_{300K} (μΩ·cm)	410	1020	330	400	
ρ_{2K} (μΩ·cm)	75	910	130	110	
ρ_{300K}/ρ_{2K}	5.5	1.1	2.5	3.6	
T_c (K) from:					
ρ vs. *T* plot	80	70	90	103	
$d(\chi T)/dT$ vs. *T* plot	78	66	97	122	155
χ'_{ac} vs. *T* plot	78	62	92	123	155
χ_o (emu/mol)	3.0×10^{-5}	3.2×10^{-4}	7.2×10^{-4}	1.0×10^{-3}	4.6×10^{-4}
θ_p (K)	95	86	110	134	157
μ_{eff} (μ_B/f.u.)	1.4	1.7	2.1	1.8	1.1

$LaCrGe_3$. The electrical resistivity falls linearly with decreasing temperature, characteristic of normal metallic behaviour, but at ~80 K, it abruptly drops and then levels off to a residual value of 75 μΩ·cm at 2 K (Figure 4–2a). Correspondingly, the dc magnetic susceptibility increases rapidly below a similar transition temperature, with the zero-field-cooled (zfc) and field-cooled (fc) curves diverging below this point (Figure 4–2b) because of magnetic domain effects. These observations clearly indicate ferromagnetic behaviour, below a Curie temperature of T_c = 78 K, as located more precisely from plots of $d(\chi T)/dT$ vs. *T* or χ'_{ac} vs. *T* (Figure A1–2). There appears to be a low-temperature downturn in the susceptibility near ~10 K of uncertain origin. The isothermal magnetization curve at 300 K increases linearly with field, consistent with paramagnetic behaviour above T_c (Figure 4–2c). On the other hand, at 2 K, the magnetization saturates very quickly to M_s = 0.9 μ_B/f.u., with little hysteresis as seen by the small remanent magnetization of M_{rem} = 0.1 μ_B/f.u, consistent with soft ferromagnetic behaviour below T_c. The inverse susceptibility in the high-

temperature regime was fit to the modified Curie-Weiss law, $\chi = C/(T-\theta_p) + \chi_o$ (inset of Figure 4–2b), giving a positive Weiss parameter of $\theta_p = 95$ K, implying ferromagnetic coupling, and a modest temperature-independent term of $\chi_o = 3.0 \times 10^{-5}$ emu/mol. The effective magnetic moment calculated from the Curie constant is 1.4 μ_B/f.u. Since trivalent La provides no unpaired electrons, the magnetic moment can be attributed solely to the d-electrons of the Cr atoms. However, this value is significantly lower than would be expected based on Cr^{4+} (2.8 μ_B) or Cr^{3+} ions (3.8 μ_B), clearly in repudiation of a local moment picture for the Cr atoms. These observations for $LaCrGe_3$ are similar to those reported previously for $LaCrSb_3$, which was identified to be a band ferromagnet with T_c = ~125 K and which also has an apparently depressed Cr moment.[34] Despite their identical chemical formulas and the presence of face-sharing Cr-centred octahedra in both structures, they differ in that the Cr–Cr distances are somewhat longer (3.08 Å) and the chains are connected to form layers in $LaCrSb_3$.[35]

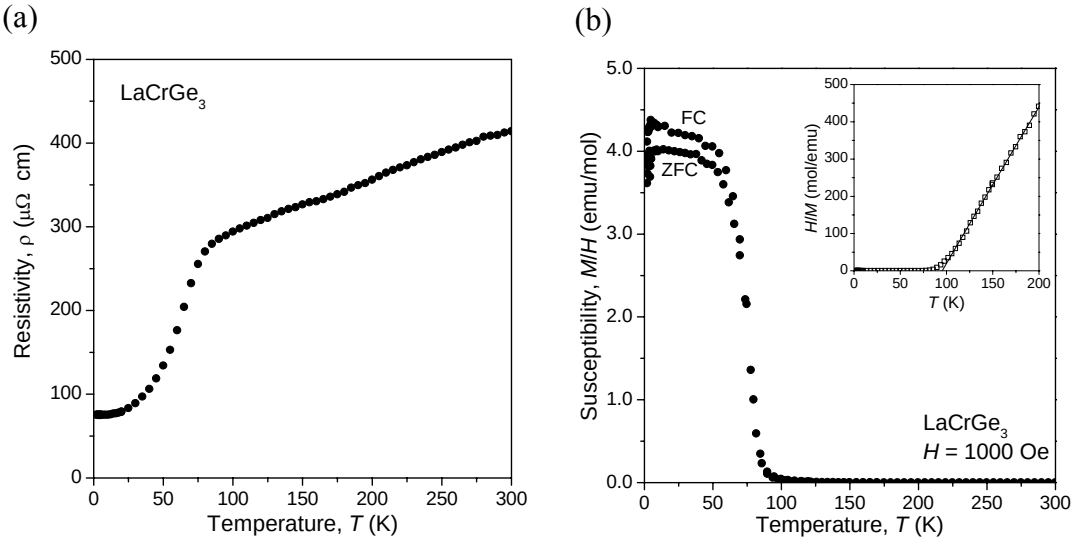

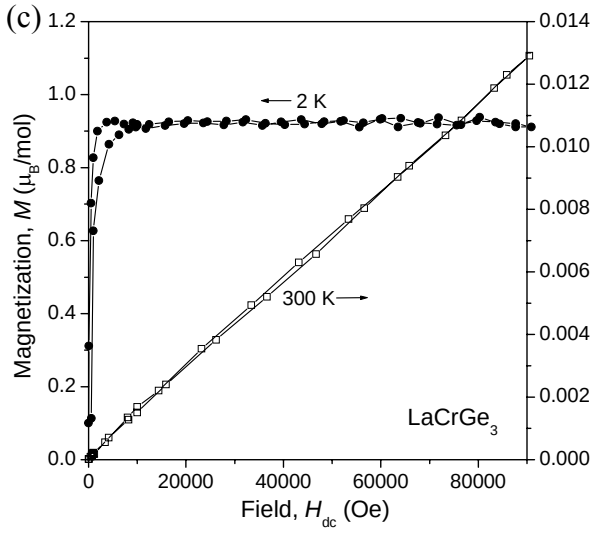

Figure 4–2. $LaCrGe_3$: (a) electrical resistivity, (b) field-cooled (fc) and zero-field-cooled (zfc) dc magnetic susceptibility (inset: inverse susceptibility plot), and (c) isothermal magnetization at 2 and 300 K.

$CeCrGe_3$. The electrical resistivity profile for $CeCrGe_3$ is distinctly different from that of $LaCrGe_3$. With decreasing temperature, the resistivity gradually increases to a maximum at ~70 K, then falls to a shallow minimum centred around 25 K before rising again to 910 μΩ·cm at 2 K (Figure 4–3a). This profile resembles that found in other Ce-containing intermetallics such as $CeTiGe_3$ (which is isostructural to $CeCrGe_3$),[9] $CePdSb_2$,[36] and $CeAgSb_2$,[36,37] which have been proposed to be dense Kondo lattice compounds, except that the resistivity does not decrease as much in the low-temperature regime in $CeCrGe_3$. The rapid upturn in the dc magnetic susceptibility at a similar temperature (Figure 4–3b) and the saturation behaviour of the isothermal magnetization at 2 K (Figure 4–3c) again imply ferromagnetism. The Curie temperature located from $d(\chi T)/dT$ vs. T or χ'_{ac} vs. T plots is 66 K or 62 K, respectively, slightly lower than the transition temperature in the electrical resistivity curve. Fitting of the high-temperature inverse susceptibility to the modified Curie-Weiss law gave θ_p = 86

K. Interestingly, the effective magnetic moment of 1.7 μ_B/f.u in $CeCrGe_3$ is not significantly higher than that (1.4 μ_B/f.u) in $LaCrGe_3$, despite the nominal introduction of a 4f moment, if trivalent cerium is assumed (which has a free-ion moment of 2.5 μ_B). In fact, this value remains less than that (2.6 μ_B/f.u) in $CeTiGe_3$, which has a much lower ordering temperature (T_c = 14 K) and a negative Weiss parameter (θ_p = –36 K).[9] These observations suggest strong interactions of Cr d-moments with the Ce f-moments in $CeCrGe_3$, in a non-trivial arrangement that will need to be determined by further study such as neutron diffraction.

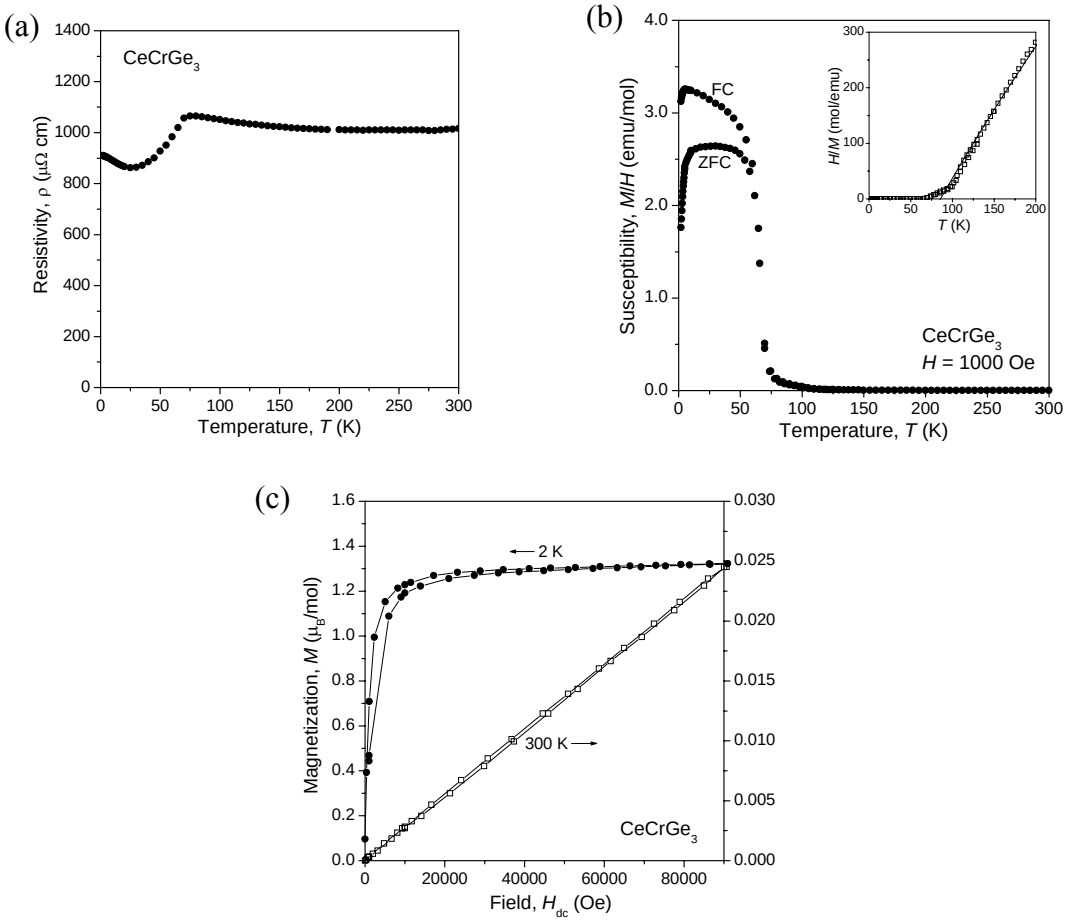

Figure 4–3. $CeCrGe_3$: (a) electrical resistivity, (b) field-cooled (fc) and zero-field-cooled (zfc) dc magnetic susceptibility (inset: inverse susceptibility plot), and (c) isothermal magnetization at 2 and 300 K.

$PrCrGe_3$ and $NdCrGe_3$. The electrical resistivity plots for $PrCrGe_3$ (Figure 4–4a) and $NdCrGe_3$ (Figure 4–5a) are similar in profile and absolute values, with sharp transitions at 90 K and 103 K, respectively. These transitions coincide with the rapid upturns in the dc magnetic susceptibility, at 97 K (Figure 4–4b) and 122 K (Figure 4–5b), respectively. Additional transitions are seen in the susceptibility at low temperatures. In $PrCrGe_3$, all isothermal magnetization curves below T_c exhibit saturation behaviour (the 2 K curve is shown in Figure 4–4c; further curves are in Figure A1–3), with no striking changes seen in their profiles other than the expected increase in saturation magnetization as the temperature is decreased. In $NdCrGe_3$, however, the isothermal magnetization curve at 2 K exhibits strong hysteresis (M_{rem} = 1.4 μ_B/f.u), which becomes less pronounced at higher temperature (Figure 4–5c). The increasing importance of the role of f-electrons can be surmised from the dramatic low-temperature downturns in the zfc curves of the magnetic susceptibility on progressing from $LaCrGe_3$ to $NdCrGe_3$, which may be related to different degrees of magnetic anisotropy associated with the rare earth. The effective magnetic moment (determined from fits of the high-temperature susceptibility to the modified Curie-Weiss law) also decreases on going from $PrCrGe_3$ (2.1 μ_B/f.u.) to $NdCrGe_3$ (1.8 μ_B/f.u.), suggesting a distinct change in the nature of magnetic interactions between the *RE* and Cr moments.

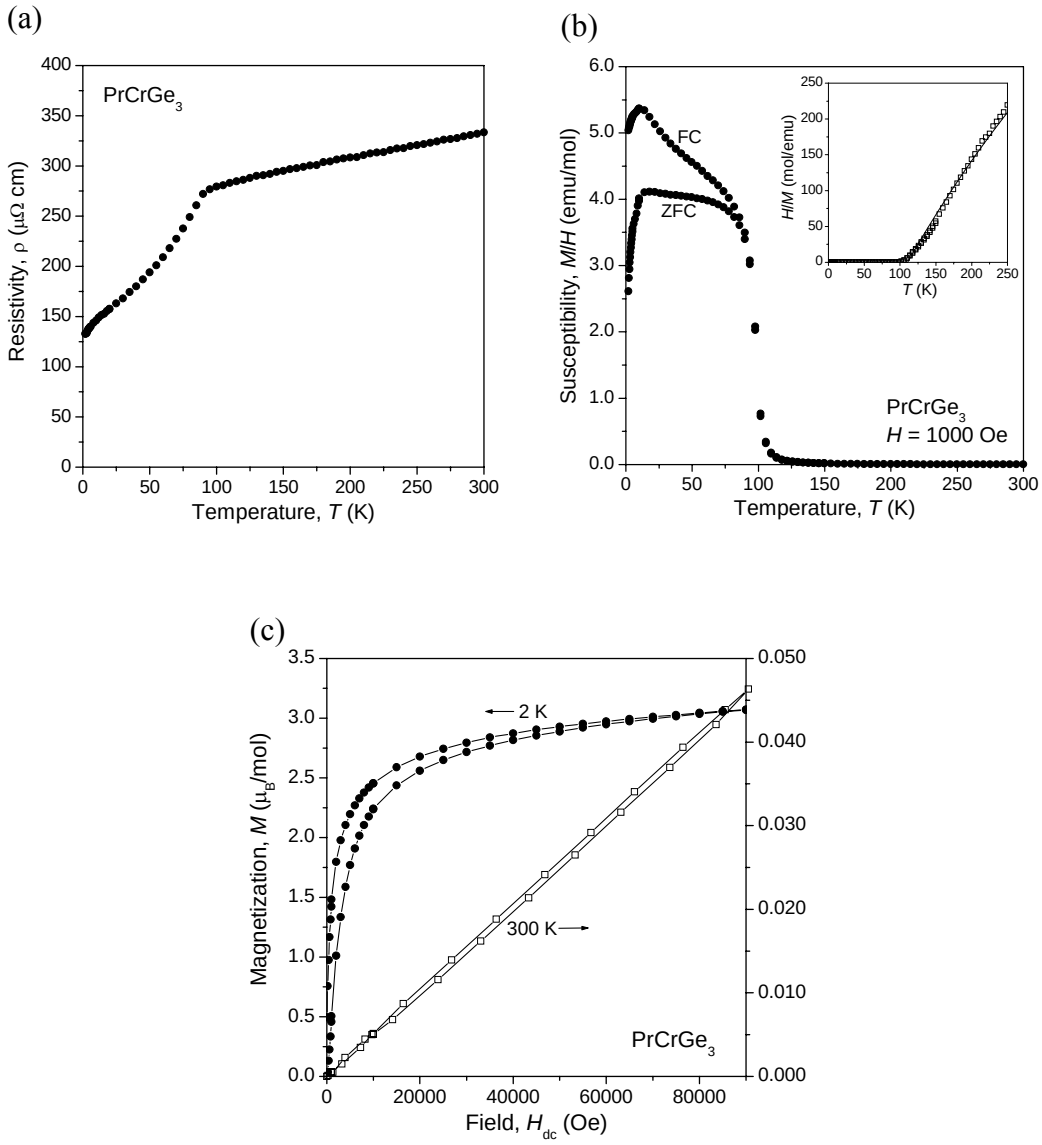

Figure 4–4. $PrCrGe_3$: (a) electrical resistivity, (b) field-cooled (fc) and zero-field-cooled (zfc) dc magnetic susceptibility (inset: inverse susceptibility plot), and (c) isothermal magnetization at 2 and 300 K.

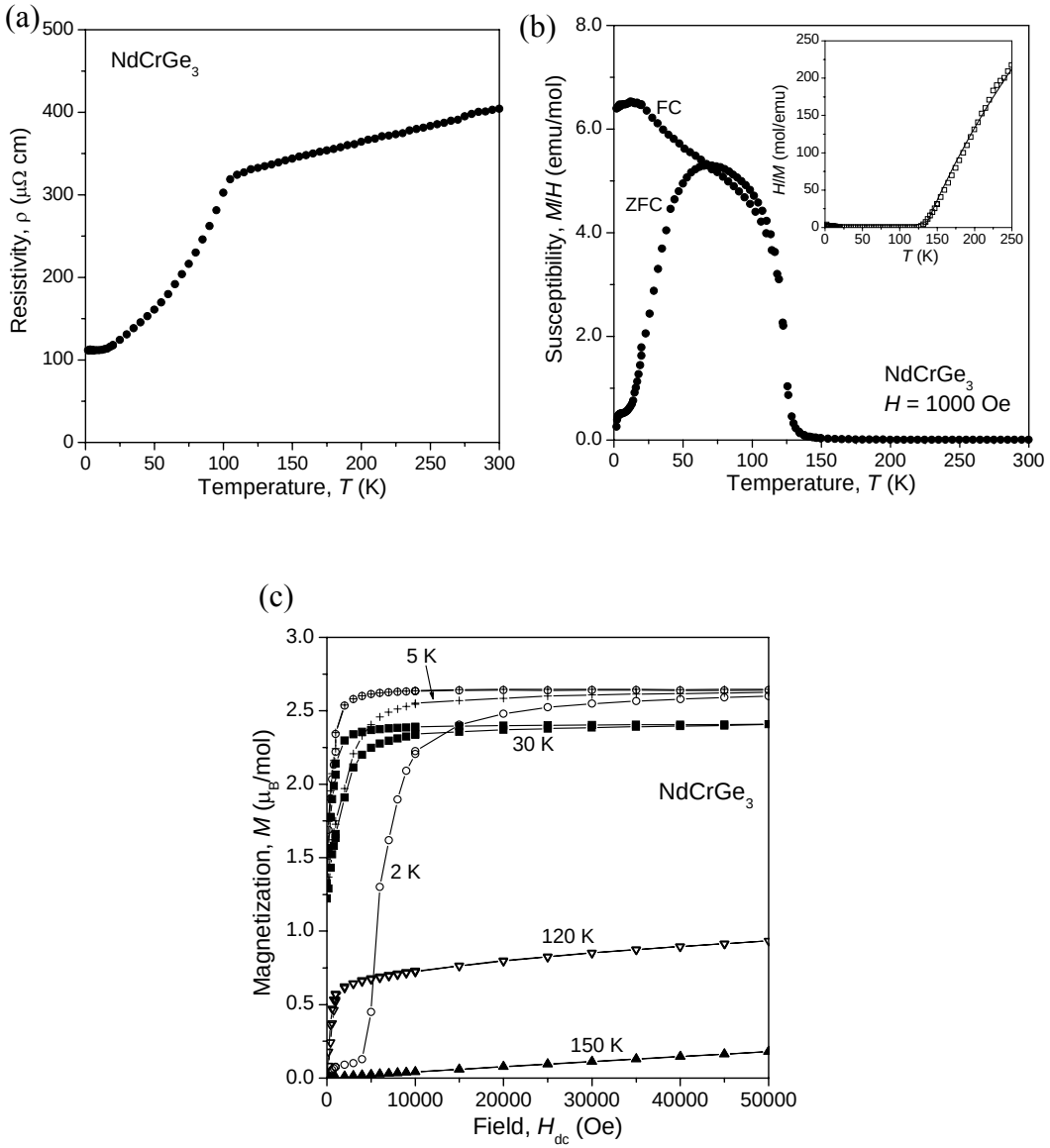

Figure 4–5. $NdCrGe_3$: (a) electrical resistivity, (b) field-cooled (fc) and zero-field-cooled (zfc) dc magnetic susceptibility (inset: inverse susceptibility plot), and (c) isothermal magnetization at various temperatures.

$SmCrGe_3$. The resistivity of $SmCrGe_3$ was not measured owing to lack of suitably sized crystals, but it may be predicted to have a similar profile as other *RE*$CrGe_3$ members. Inspection of the dc magnetic susceptibility shows that the Curie temperature is now increased to 155 K (Figure 4–6). The low-temperature

transition at 55 K becomes quite prominent. Below this transition, the isothermal magnetization at 2 K first appears to saturate at 0.3 μ_B, but then increases abruptly at 60 kOe to saturate again at 1.0 μ_B. At 5 K, the curve only shows saturation at 1.0 μ_B.

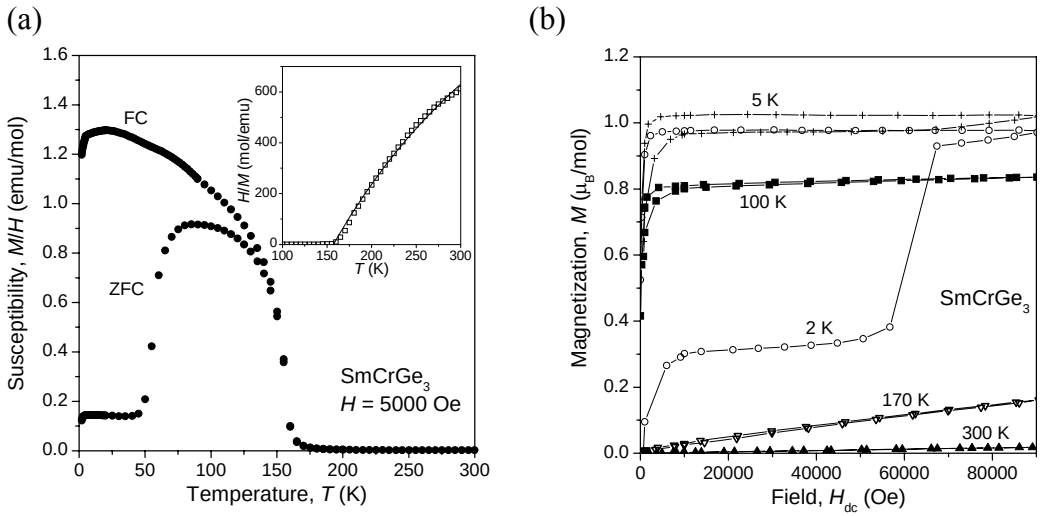

Figure 4–6. $SmCrGe_3$: (a) field-cooled (fc) and zero-field-cooled (zfc) dc magnetic susceptibility (inset: inverse susceptibility plot), and (b) isothermal magnetization at various temperatures.

In general, all *RE*$CrGe_3$ compounds studied here are metallic and exhibit a prominent kink in their electrical resistivity curves that is clearly magnetic in origin, as it coincides with a ferromagnetic transition seen in the magnetic susceptibility curves. The sudden decrease in resistivity arises because of a loss of spin-disorder scattering as ferromagnetic ordering sets in. This ferromagnetic ordering arises from interaction between the *RE* atoms, mediated through Cr moments. The Curie temperatures are found to be roughly proportional to the de Gennes factor, $(g - 1)^2(J(J + 1))$ (Figure 4–7), implying that the localized 4f

electrons on the *RE* atoms interact indirectly with each other through polarization of the conduction electrons (RKKY interaction). This correlation and the low observed effective magnetic moments also suggest that Cr d-electrons are highly delocalized in conduction bands.

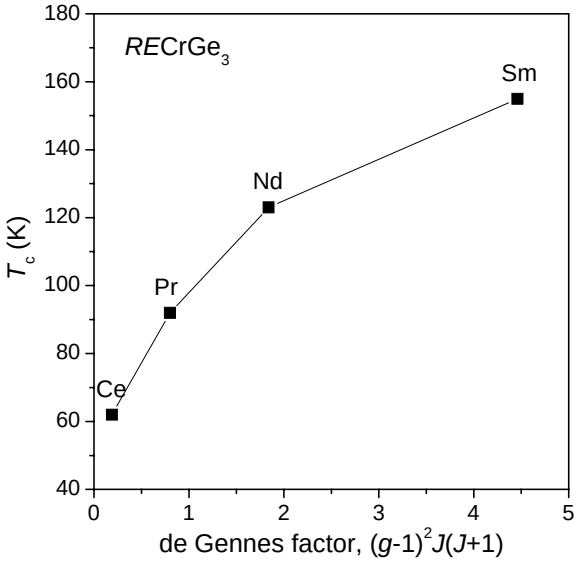

Figure 4–7. Magnetic ordering temperatures for *RE*$CrGe_3$ plotted versus the de Gennes factor.

4.3.3. Electronic Structure

To gain insight on the bonding and properties of *RE*$CrGe_3$, a band structure calculation was carried out for $LaCrGe_3$. Figure 4–8 shows the density of states (DOS) curve for $LaCrGe_3$, as well as its contributions from La, Cr, and Ge. In general agreement with the Zintl-Klemm formulation $(La^{3+})(Cr^{3+})(Ge^{2-})_3$ derived from the simple electron counting scheme proposed earlier, most of the La states are unoccupied and located above the Fermi level, whereas the Cr- and Ge-based bands are partially filled. Strong covalent bonding is implied by the

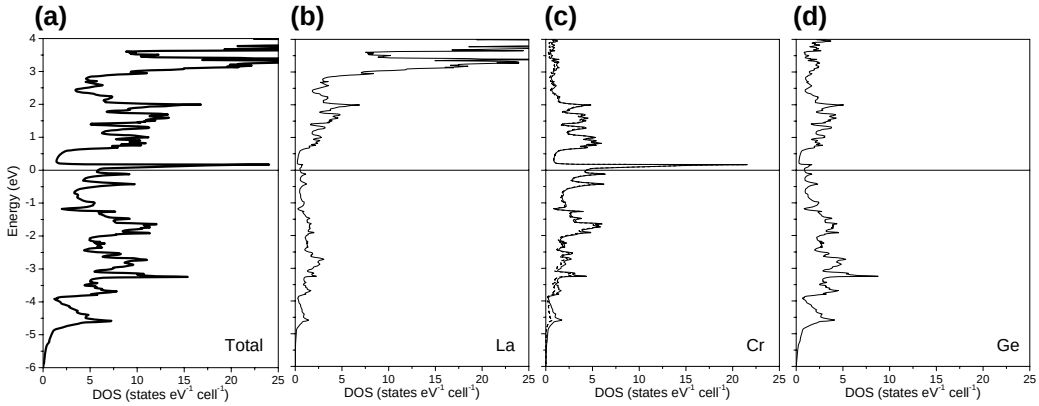

Figure 4–8. (a) Total density of states (DOS) for non-spin-polarized $LaCrGe_3$ and its (b) La, (c) Cr, and (d) Ge contributions. The dashed curve in (c) indicates the contribution of 3d states to the Cr partial DOS. The Fermi level is marked by a horizontal line at 0 eV.

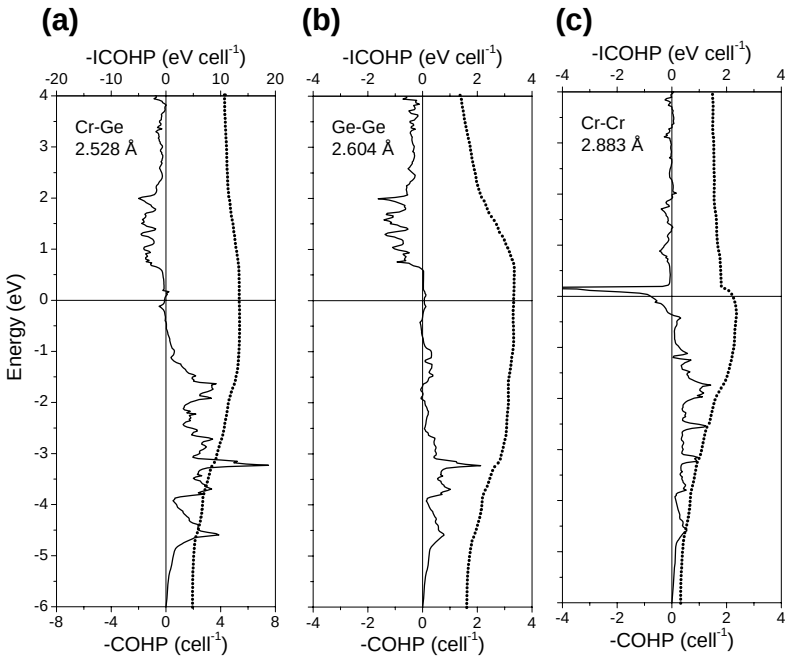

Figure 4–9. Crystal orbital Hamilton population (COHP) curves (solid line) and integrated COHP curves (dotted line) for (a) Cr–Ge, (b) Ge–Ge, and (c) Cr–Cr contacts in non-spin-polarized $LaCrGe_3$. The Fermi level is marked by a horizontal line at 0 eV.

mixing of Cr and Ge states over a wide energy range (from –6 eV upward). As seen in the crystal orbital Hamilton population (COHP) curves, Cr–Ge bonding within the Cr-centred octahedra is optimized through complete filling of bonding levels, giving an integrated –COHP of 2.2 eV/bond up to the Fermi level, beyond which are only unoccupied antibonding levels (Figure 4–9a). Occupation of bonding levels at similar energies and nonbonding levels near the Fermi level account for the Ge–Ge bonds within the triangular clusters, giving an integrated –COHP of 1.1 eV/bond (Figure 4–9b). Perhaps the most striking feature of the band structure is the presence of a very large spike in the DOS near the Fermi level, just below a pseudogap. This spike is almost entirely based on Cr d-states (Figure 4–8c). A partially filled narrow band with high DOS at the Fermi level is one of the characteristic features of a band ferromagnet, consistent with the experimentally observed metallic and ferromagnetic behaviour of $LaCrGe_3$. Moreover, inspection of the COHP curve for the Cr–Cr contacts along the face-sharing octahedral chains reveals that, while there is still net metal-metal bonding overall (integrated –COHP of 1.1 eV/bond), the states at the Fermi level are strongly antibonding (Figure 4–9c). The electronic instability inherent in this type of situation has been proposed as an alternative way to view the driving force for band ferromagnetism.[38] Figure 4–10 shows the results of a spin-polarized calculation on $LaCrGe_3$. The DOS curve for the majority spin states (↑) is shifted down relative to that for the minority spin states (↓), with the narrow Cr d band now appearing below the Fermi level. The magnetic state is more stable than the non-magnetic state by 0.076 eV/cell. The calculated magnetic moment

of 1.3 μ_B is derived almost exclusively from Cr 3d states, and agrees well with the experimental moment of 1.4 μ_B for $LaCrGe_3$. By extension, we can make the supposition that the Cr d states are also delocalized in narrow d-bands in the other *RE*$CrGe_3$ members to account for the depressed magnetic moments, and the *RE* f-states will also be polarized and contribute to the effective moment.

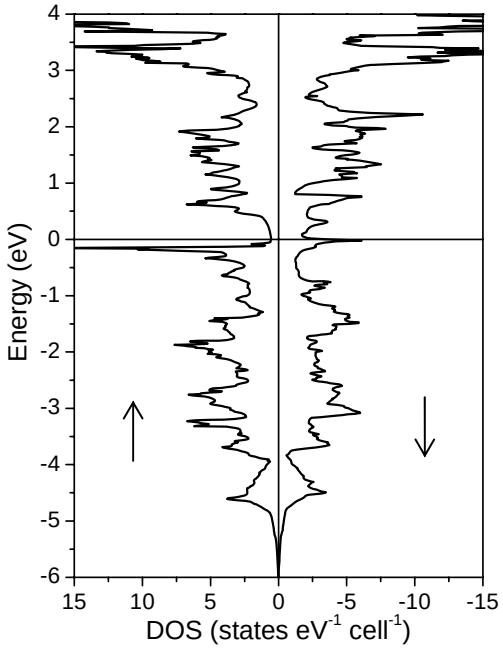

Figure 4–10. Total density of states for spin-polarized $LaCrGe_3$. The Fermi level is marked by a horizontal line at 0 eV.

4.4. Conclusions

This investigation has uncovered a new series of intermetallic germanides that have several points of interest: (i) the adoption of a hexagonal perovskite type structure, normally found for halides and chalcogenides, is unusual for an intermetallic compound, (ii) all rare-earth members studied thus far are metallic

and ferromagnetic with relatively high transition temperatures, and (iii) more complex magnetic behaviour is signaled by other transitions at low temperature or low field. Although the degree of charge transfer in *RE*$CrGe_3$ is expected to be much less pronounced because of smaller electronegativity difference and the idea of localized electrons is questionable (metallic behaviour), the Zintl-Klemm formalism $RE^{3+}Cr^{3+}(2b\text{-}Ge^{2-})_3$ provides a satisfying rationalization for the occurrence of triangular Ge_3 clusters.

The conduction electrons from the transition-metal component play an important role in influencing the magnetic interaction between 4f local magnetic moments in rare-earth transition-metal intermetallic compounds. Since both *RE*$TiGe_3$ and *RE*$CrGe_3$ compounds are isostructural and exhibit interesting ferromagnetic behaviour, it is worthwhile to synthesize isostructural *RE*VGe_3 compounds and investigate their magnetic properties. The results will be introduced in the next chapter.

4.5. References

(1) Crerar, S. J.; Deakin, L.; Mar, A. *Chem. Mater.* **2005**, *17*, 2780–2784 and references therein.

(2) Salamakha, P. S.; Sologub, O. L.; Bodak, O. I. In *Handbook on the Physics and Chemistry of Rare Earths*; Gschneidner, K. A., Jr., Eyring, L., Eds.; Elsevier: Amsterdam, 1999; Vol. 27, pp 1–223.

(3) Morozkin, A. V.; Seropegin, Yu. D.; Leonov, A. V.; Sviridov, I. A.; Tskhadadze, I. A.; Nikitin, S. A. *J. Alloys Compd.* **1998**, *267*, L14–L15.

(4) Nikitin, S. A.; Tskhadadze, I. A.; Telegina, I. V.; Morozkin, A. V.; Seropegin, Yu. D. *J. Magn. Magn. Mater.* **1998**, *182*, 375–380.

(5) Welter, R.; Vernière, A.; Venturini, G.; Malaman, B. *J. Alloys Compd.* **1999**, *283*, 54–58.

(6) Morozkin, A. V.; Seropegin, Yu. D.; Sviridov, I. A. *J. Alloys Compd.* **1999**, *285*, L5–L7.

(7) Vernière, A.; Klosek, V.; Welter, R.; Venturini, G.; Isnard, O.; Malaman, B. *J. Magn. Magn. Mater.* **2001**, *234*, 261–273.

(8) Morozkin, A. V. *J. Alloys Compd.* **2004**, *370*, L1–L3.

(9) Manfrinetti, P.; Dhar, S. K.; Kulkarni, R.; Morozkin, A. V. *Solid State Commun.* **2005**, *135*, 444–448.

(10) Morozkin, A. V.; Seropegin, Yu. D.; Portnoy, V. K.; Leonov, A. V.; Sviridov, I. A. *J. Alloys Compd.* **1998**, *278*, L8–L9.

(11) Morozkin, A. V. *J. Alloys Compd.* **1999**, *287*, 185–188.

(12) Nirmala, R.; Sankaranarayanan, V.; Sethupathi, K.; Rangarajan, G.; Morozkin, A. V.; Kundaliya, D. C.; Malik, S. K. *J. Appl. Phys.* **2004**, *95*, 7079–7081.

(13) Kotur, B. Ya.; Bodak, O. I.; Sikiritsa, M.; Bruvo, M. *Dopov. Akad. Nauk Ukr. RSR, Ser. B* **1983**, *10*, 46–49.

(14) Kotur, B. Ya.; Bodak, O. I.; Zavodnik, V. E. *Sov. Phys. Crystallogr.* **1986**, *31*, 513–516 (*Transl. Kristallografiya* **1986**, *31*, 868–873).

(15) Kotur, B. Ya. *Inorg. Mater.* **1987**, *23*, 493–496 (*Transl. Izv. Akad. Nauk SSSR, Neorg. Mater.* **1987**, *23*, 558–561).

(16) Kotur, B. Ya.; Kravs, A. B.; Andrusyak, R. I. *Russ. Metall.* **1988**, *(6)*, 192–195 (*Transl. Izv. Akad. Nauk SSSR, Metally* **1988**, *6*, 198–201).

(17) Kotur, B. Ya.; Andrusyak, R. I.; Zavodnik, V. E. *Sov. Phys. Crystallogr.* **1988**, *33*, 141–142 (*Transl. Kristallografiya* **1988**, *33*, 240–241).

(18) Guloy, A. M.; Corbett, J. D. *Inorg. Chem.* **1993**, *32*, 3532–3540.

(19) Bodak, O. I.; Gladyshevskii, E. I.; Salamakha, P. S.; Pecharskii, V. K.; Bruskov, V. A. *Sov. Phys. Crystallogr.* **1989**, *34*, 774–775 (*Transl. Kristallografiya* **1989**, *34*, 1285–1287).

(20) Morozkin, A. V.; Seropegin, Yu. D.; Portnoy, V. K.; Sviridov, I. A.; Leonov, A. V. *Mater. Res. Bull.* **1998**, *33*, 903–908.

(21) Brabers, J. H. V. J.; Buschow, K. H. J.; de Boer, F. R. *J. Alloys Compd.* **1994**, *205*, 77–80.

(22) Schobinger-Papamantellos, P.; Rodríguez-Carvajal, J.; Buschow, K. H. J. *J. Alloys Compd.* **1997**, *256*, 92–96.

(23) Müller, U. *Inorganic Structural Chemistry*; Wiley: Chichester, 1993.

(24) Sheldrick, G. M. *SHELXTL*, version 6.12; Bruker AXS Inc.: Madison, WI, 2001.

(25) Gelato, L. M.; Parthé, E. *J. Appl. Crystallogr.* **1987**, *20*, 139–143.

(26) Hunter, B. *LHPM-Rietica*, version 1.7.7, International Union of Crystallography Commission on Powder Diffraction Newsletter, no. 20 (summer), 1998 (www.rietica.org).

(27) Tank, R.; Jepsen, O.; Burkhardt, A.; Andersen, O. K. *TB-LMTO-ASA Program*, version 4.7, Max Planck Institut für Festkörperforschung, Stuttgart, 1998.

(28) Israiloff, P.; Völlenkle, H.; Wittmann, A. *Monatsh. Chem.* **1974**, *105*, 1387–1404.

(29) Völlenkle, H.; Preisinger, A.; Nowotny, H.; Wittmann, A. *Z. Kristallogr.* **1967**, *124*, 9–25.

(30) Pauling, L. *The Nature of the Chemical Bond*, 3rd ed.; Cornell University Press: Ithaca, NY, 1960.

(31) Choe, W.; Miller, G. J.; Levin, E. M. *J. Alloys Compd.* **2001**, *329*, 121–130.

(32) Takeda, Y.; Kanamaru, F.; Shimada, M.; Koizumi, M. *Acta Crystallogr., Sect. B* **1976**, *32*, 2464–2466.

(33) Gardner, R. A.; Vlasse, M.; Wold, A. *Acta Crystallogr. Sect. B* **1969**, *25*, 781–787.

(34) Raju, N. P.; Greedan, J. E.; Ferguson, M. J.; Mar, A. *Chem. Mater.* **1998**, *10*, 3630–3635.

(35) Ferguson, M. J.; Hushagen, R. W.; Mar, A. *J. Alloys Compd.* **1997**, *249*, 191–198.

(36) Muro, Y.; Takeda, N.; Ishikawa, M. *J. Alloys Compd.* **1997**, *257*, 23–29.

(37) Jobiliong, E.; Brooks, J. S.; Choi, E. S.; Lee, H.; Fisk, Z. *Phys. Rev. B* **2005**, *72*, 104428-1–104428–9.

(38) Landrum, G. A.; Dronskowski, R. *Angew. Chem. Int. Ed.* **2000**, *39*, 1560–1585.

Chapter 5

Structure and Magnetic Properties of Hexagonal Perovskite-type Rare-Earth Vanadium Germanides *RE*VGe_3 (*RE* = La–Nd)*

5.1. Introduction

The dominance of transition-metal oxides in solid-state chemistry stems from the important physical phenomena, such as high-temperature superconductivity or colossal magnetoresistance, displayed by compounds whose structures are based largely on variations of the cubic perovskite-type ABO_3.[1] Perhaps less familiar are those compounds based on a different stacking of the component [AO_3] layers, yielding hexagonal structures containing chains of face-sharing octahedra, or fragments.[2,3] New types of electrical and magnetic behaviour are generated by the many combinations possible for the metal substituents *A* and *B*.[4,5] Although this hexagonal perovskite-type structure is formed for many oxides, chalcogenides, and halides,[6] little is known about the less ionic analogues in which the non-metal is replaced by a less electronegative element. In fact, the only examples of intermetallic compounds with the hexagonal perovskite-type structure are the recently discovered rare-earth transition-metal germanides *REM*Ge_3 (*RE* = La–Pr for *M* = Ti;[7,8] *RE* = La–Nd, Sm for *M* = Cr [9]). The electronic structure of these ternary rare-earth germanides is quite different from that of the oxides. Moreover, the magnetic properties of

* *A version of this chapter has been accepted for publication. Haiying Bie, Arthur Mar, 2009. Journal of Materials Chemistry.*

ternary rare-earth transition metal compounds in general are quite diverse, because of the varied interactions that can arise between the more localized f-electrons on the *RE* atoms and the more delocalized d-electrons on the *M* atoms.[10] Previous magnetic measurements revealed ferromagnetic ordering for $CeTiGe_3$ (T_C = 14 K)[8] and *RE*$CrGe_3$ (T_C ranging from 78 K for $LaCrGe_3$ to 155 K for $SmCrGe_3$).[9] Just as diverse properties can be exquisitely tuned through appropriate substitutions in the oxide perovskites *AB*O_3, it is of interest to investigate whether the magnetic properties of these intermetallic germanide analogues *REM*Ge_3 can also be modified in a similar manner.

In this chapter, we report the preparation of the intervening vanadium series, *RE*VGe_3 (*RE* = La–Nd). Their crystal structures have been refined and their magnetic properties have been measured, with the aim of comparing them to the isostructural *RE*$TiGe_3$ and *RE*$CrGe_3$ series. The effect of doping V or Mn into ferromagnetic $LaCrGe_3$ was also investigated.

5.2. Experimental Section

5.2.1. Synthesis

Starting materials for the preparation of *RE*VGe_3 were rare-earth pieces (*RE* = La–Nd; Hefa), vanadium ribbon (A. D. Mackay), and germanium ingot (Alfa), all with purities of 99.9% or better. Stoichiometric mixtures of the elements were arc-melted together in a Centorr 5TA tri-arc furnace on a water-cooled copper hearth under argon atmosphere in the presence of a Ti getter. A 5 at. % excess of vanadium was added to compensate for losses experienced during the arc-melting. The arc-melting procedure was carried out as before. The

ingots were sealed in evacuated fused-silica tubes and annealed at 800 °C for 3 weeks, and then quenched in cold water. Additional synthetic experiments to extend the substitution to other *RE* metals were unsuccessful. However, investigations into mixed transition-metal systems, through a similar synthesis procedure as above, resulted in the elucidation of two series of solid solutions $LaV_{1-x}Cr_xGe_3$ ($0 \leq x \leq 1$) and $LaCr_{1-x}Mn_xGe_3$ ($0 \leq x \leq 0.2$). These results indicate that that $LaMnGe_3$ could not be formed. Further experiments to attempt substitution with Fe did yield a ternary phase $LaFeGe_3$, but it adopts a different structure type ($BaNiSn_3$-type).[11]

5.2.2. Structure Determination

Powder X-ray diffraction patterns for *RE*VGe_3 (*RE* = La–Nd) were collected with Cu $K\alpha_1$ radiation on an Inel powder diffractometer equipped with a CPS 120 detector. The patterns agreed well with those simulated from the single-crystal structure data for *RE*$CrGe_3$,[9] from which initial atomic positions for *RE*VGe_3 were taken. The refinements were carried out with the full-profile Rietveld method with use of the program LHPM-Rietica.[12] The least-squares refinement included scale factor, background, zero point, cell parameters, pseudo-Voigt peak profile parameters, atomic coordinates, and isotropic displacement parameters. The Rietveld refinement results are summarized in Table 5–1 and the fits to powder patterns are shown in Figure 5–1. Atomic positions, standardized with the program STRUCTURE TIDY,[13] are listed in Table 5–2, and interatomic distances are listed in Table 5–3.

Table 5–1. Crystallographic data for *RE*VGe_3 (*RE* = La–Nd).

Formula	$LaVGe_3$	$CeVGe_3$	$PrVGe_3$	$NdVGe_3$
Formula mass (amu)	407.61	408.82	409.61	412.94
Space group		$P6_3/mmc$ (No. 194)		
a (Å)	6.2587(3)	6.2306(2)	6.2287(2)	6.2145(2)
c (Å)	5.6992(3)	5.6733(2)	5.6566(2)	5.6403(2)
V (Å^3)	193.34(2)	190.73(1)	190.06(1)	188.64(1)
Z	2	2	2	2
ρ_{calcd} (g cm^{-3})	6.999	7.115	7.154	7.267
Radiation		Cu Kα_1, λ = 1.54056 Å		
μ (mm^{-1})	127.62	135.03	141.30	148.29
2θ range	20.00–110.00°	20.00–110.00°	20.00–110.00°	20.00–110.00°
No. of data points	2759	2759	2759	2759
No. of reflections	51	50	50	50
No. of variables	20	20	20	20
Residuals [a]	R_B = 0.030 R_p = 0.052 R_{wp} = 0.070	R_B = 0.028 R_p = 0.044 R_{wp} = 0.069	R_B = 0.026 R_p = 0.053 R_{wp} = 0.076	R_B = 0.024 R_p = 0.039 R_{wp} = 0.061
GOF	3.27	7.51	3.94	7.58

[a] $R_B = \sum|I_o - I_c|/\sum I_o$; $R_p = \sum|y_o - y_c|/\sum y_o$; $R_{wp} = \left[\sum[w(y_o - y_c)]/\sum w y_o^2\right]^{1/2}$

Table 5–2. Atomic coordinates and isotropic displacement parameters (Å^2) for *RE*VGe$_3$ (*RE* = La–Nd).

	$LaVGe_3$	$CeVGe_3$	$PrVGe_3$	$NdVGe_3$
RE at 2*d* (1/3, 2/3, 3/4)				
B_{iso}	0.94(7)	1.00(7)	0.8(1)	0.82(8)
V at 2*a* (0, 0, 0)				
B_{iso}	0.9(2)	0.9(1)	1.4(2)	1.0(2)
Ge at 6*h* (*x*, 2*x*, 1/4)				
x	0.1952(2)	0.1959(2)	0.1970(3)	0.1955(2)
B_{iso}	0.79(7)	0.68(7)	0.40(9)	0.61(8)

Table 5–3. Selected interatomic distances (Å) in *RE*VGe$_3$ (*RE* = La–Nd).

	$LaVGe_3$	$CeVGe_3$	$PrVGe_3$	$NdVGe_3$
RE–Ge (×6)	3.1448(2)	3.1313(2)	3.1314(4)	3.1227(3)
RE–Ge (×6)	3.219(2)	3.201(1)	3.188(2)	3.186(1)
V–Ge (×6)	2.551(2)	2.546(2)	2.552(3)	2.534(2)
V–V (×2)	2.8496(2)	2.8367(1)	2.8283(1)	2.8202(1)
Ge–Ge (×2)	2.594(5)	2.568(4)	2.548(6)	2.569(5)

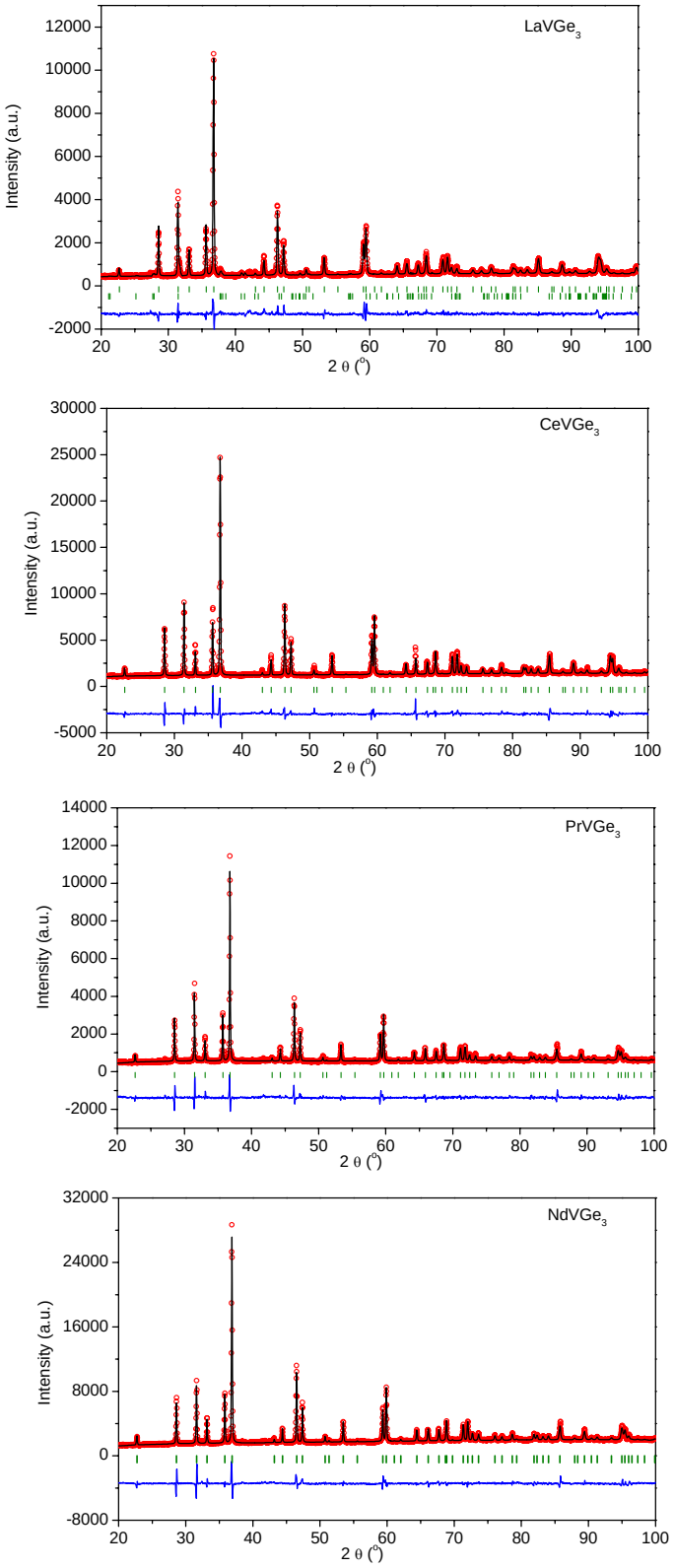

Figure 5–1. Rietveld refinement results for *RE*VGe_3 (*RE* = La-Nd). The observed profile is indicated by red circles and the calculated profile by the black solid lines. Bragg peak positions are located by the vertical green tick marks. (The second set of tick marks corresponds to trace amounts of $LaGe_{2-x}$ present in $LaVGe_3$.) The difference plot is shown at the bottom in blue.

5.2.3. Magnetic Measurements

Measurements of dc magnetic susceptibility were made on powder samples of *RE*VGe_3 (*RE* = La–Nd) and the solid solutions $LaV_{1-x}Cr_xGe_3$ ($0 \leq x \leq 1$) and $LaCr_{1-x}Mn_xGe_3$ ($0 \leq x \leq 0.2$), previously verified for phase purity by powder X-ray diffraction, between 2 and 300 K on a Quantum Design 9T-PPMS dc magnetometer / ac susceptometer. All susceptibility values were corrected for the holder and sample diamagnetism. Measurements of ac magnetic susceptibility were also made with a driving amplitude of 1 Oe and a frequency of 1000 Hz.

5.2.4. Band Structure Calculation

Tight-binding linear muffin tin orbital (TB-LMTO) band structure calculations were performed on $LaVGe_3$ within the local density and atomic spheres approximations using the Stuttgart TB-LMTO program.[14] The basis set consisted of La 6s/6p/5d/4f, V 4s/4p/3d, and Ge 4s/4p/4d orbitals, with the La 6p and Ge 4d orbitals being downfolded. Integrations in reciprocal space were carried out with an improved tetrahedron method; to allow an appropriate comparison, the same 95 irreducible *k* points within the first Brillouin zone were chosen as in the earlier calculation for $LaCrGe_3$.[9]

5.3. Results and Discussion

5.3.1. Structure and Bonding

Although ternary rare-earth germanides *RE*–*M*–Ge are now quite numerous,[15,16] there are still relatively few examples in which *M* is an early transition metal. In the *RE*–V–Ge systems, only a few Sc-containing phases ($Sc_xV_{5-x}Ge_3$, $Sc_2V_3Ge_4$, $Sc_{1+x}V_{5-x}Ge_5$) have been previously reported.[17–19] To our knowledge, the new ternary germanides $REVGe_3$ (*RE* = La–Nd) are the first examples in these systems in which *RE* is an f-element. The $REVGe_3$ series is isostructural to $RETiGe_3$ (*RE* = La–Pr)[7,8] and $RECrGe_3$ (*RE* = La–Nd, Sm),[9] which adopt the hexagonal perovskite-type structure ($BaNiO_3$-type or $BaVS_3$-type),[20,21] unusual for intermetallic compounds. As shown in Figure 5–2, the structure consists of chains of face-sharing VGe_6 octahedra extended along the *c* direction, with *RE* atoms situated in anticuboctahedral (CN12) interstices. Besides heteroatomic bonding interactions (*RE*–Ge, 3.12–3.22 Å; V–Ge, 2.53–2.55 Å) that are consistent with the sum of the metallic radii (La, 1.690 Å to Nd, 1.637 Å; V, 1.224 Å; Ge, 1.242 Å),[22] there are also homoatomic bonding interactions. Face-sharing of the VGe_6 octahedra leads to short V–V distances (2.82–2.85 Å), indicative of weak metal-metal bonding which counteracts the electrostatic repulsion between nominally cationic centres within the chains, as occurs in chalcogenide or halide representatives of hexagonal perovskites. However, the analogy ends here, as the bonding character in $REVGe_3$ is really quite different. In particular, the Ge–Ge distances are quite short (2.55–2.59 Å), suggestive of single bonds. That is, there is a polyanionic substructure in the form of triangular Ge_3 clusters, which serve to link adjacent chains of face-sharing octahedra.

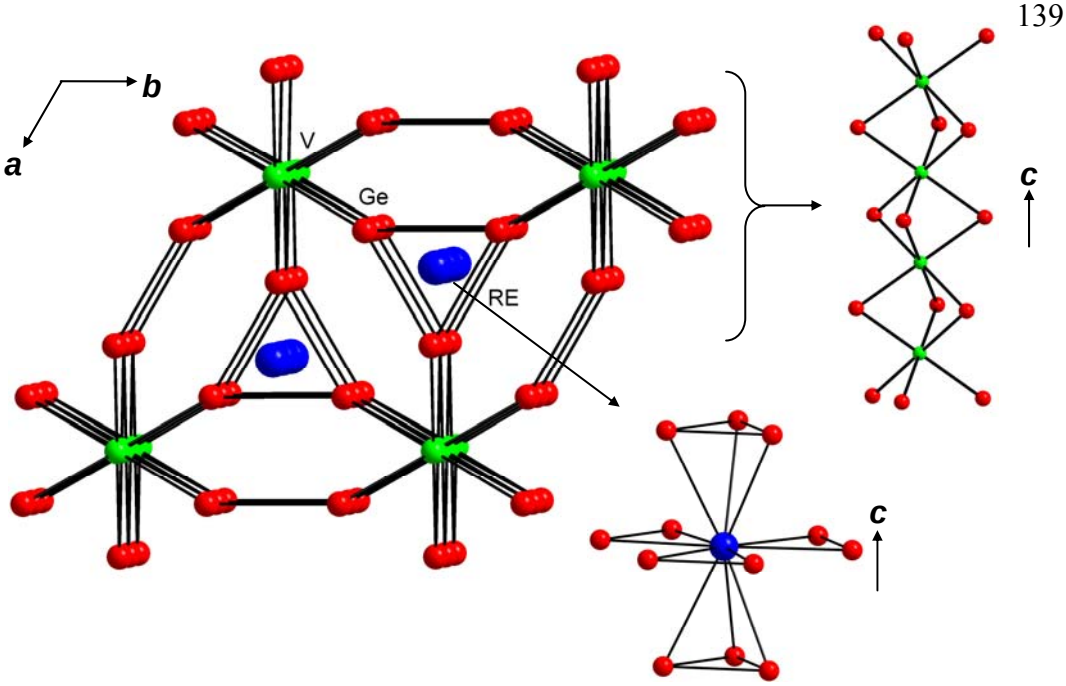

Figure 5–2. Structure of *RE*VGe_3 (*RE* = La–Nd) viewed down the *c* direction, emphasizing the V–Ge framework. The octahedral coordination around V atoms and the anticuboctahedral coordination around *RE* atoms are also highlighted. The blue, green, and red spheres are *RE*, V, and Ge atoms, respectively.

Although ionic character is certain to be low or absent in *RE*VGe_3, where electronegativity differences are small, it is nevertheless possible to propose a formulation based on the assumption of full electron transfer (Zintl-Klemm concept) that accounts for the structural features. Fulfilling the octet rule, a two-bonded Ge atom would be assigned as Ge^{2-}. Given trivalent *RE* atoms, the charge-balanced formulation that results is $RE^{3+}V^{3+}(Ge^{2-})_3$, with d-electrons remaining on the V atoms for metal-metal bonding. Whether such a formulation is realistic is another matter, to be ascertained later by band structure calculations. A warning that the ionic picture is misleading can be gauged by attempting to apply the conventional geometric arguments for stabilizing perovskite-related

structures, where the hexagonal form is favoured over the more common cubic form if the Goldschmidt tolerance factor, t, exceeds unity.[23] For $REMGe_3$, the problem of guessing an appropriate ionic radius for a hypothetical Ge^{2-} species can be overcome by working with the sum of metallic radii instead,[22] for the purpose of calculating $t = (r_{RE} + r_{Ge})/\sqrt{2}(r_M + r_{Ge})$. The values obtained for t range from 0.80 to 0.85 for $REMGe_3$ (*RE* = early rare-earth metal; *M* = Ti, V, Cr), in violation of the usual rule and suggesting that the ionic picture is invalid. Qualitatively, however, a size effect still operates in the sense that the substitution extends progressively to smaller *RE* atoms as *M* is a later transition metal (cf., $RETiGe_3$ (*RE* = La–Pr), $REVGe_3$ (*RE* = La–Nd), $RECrGe_3$ (*RE* = La–Nd, Sm)).

5.3.2. Magnetic Properties

It is helpful to begin by examining the magnetic properties of $LaVGe_3$, where no contribution from trivalent La atoms is expected. We have also prepared two series of solid solutions, a complete one in $LaV_{1-x}Cr_xGe_3$ ($0 \le x \le 1$) and a limited one in $LaCr_{1-x}Mn_xGe_3$ ($0 \le x \le 0.2$), to examine the effect of different numbers of d-electrons. Their unit cell parameters, obtained from powder X-ray diffraction data, are listed in Table 5–4. The unit cell volume generally decreases as Cr substitutes for V in $LaV_{1-x}Cr_xGe_3$, and as Mn substitutes for Cr in $LaCr_{1-x}Mn_xGe_3$. Figure 5–3 shows an interesting trend in which the *a*-parameter decreases while the *c*-parameter and the *c*/*a* ratio increase with greater substitution x in the $LaV_{1-x}Cr_xGe_3$ series, whereas little change occurs in the $LaCr_{1-x}Mn_xGe_3$ series. Figure 5–4 shows the dc magnetic susceptibility for $LaVGe_3$, $LaV_{1-x}Cr_xGe_3$ (x = 0.1, 0.4, 0.6, 0.9), and $LaCr_{1-x}Mn_xGe_3$ (x = 0.1, 0.2).

For $LaVGe_3$, the magnetic susceptibility is small, positive, and relatively temperature-independent, consistent with Pauli paramagnetism arising solely from the spins of conduction electrons. This behaviour implies the absence of localized unpaired d-electrons on the V atoms. For comparison, $LaCrGe_3$ was found to exhibit long-range ferromagnetic ordering at T_C = 78 K, with an effective magnetic moment of 1.4 μ_B/f.u arising from the itinerant d-electrons of the Cr atoms.[9] Doping of V atoms into $LaCrGe_3$ tends to suppress the Curie temperature (down to 60 K for 10% V), and when the majority of the Cr atoms are replaced, the ferromagnetic ordering vanishes completely (beyond 60% V). In contrast, doping of Mn atoms into $LaCrGe_3$ initially suppresses the Curie temperature (down to 60 K for 10% Mn) and then induces a transition (at 44 K for 20% Mn), as seen by the dramatic change in shape of the susceptibility curve. The transition is likely antiferromagnetic in origin, given that other rare-earth intermetallics containing Mn often exhibit antiferromagnetic ordering.[10]

Table 5–4. Hexagonal unit cell parameters for $LaV_{1-x}Cr_xGe_3$ and $LaCr_{1-x}Mn_xGe_3$ compounds.

Compound	*a* (Å)	*c* (Å)	*V* (Å^3)	*c*/*a* ratio
$LaV_{0.8}Cr_{0.2}Ge_3$	6.2972(1)	5.7371(1)	195.895(9)	0.9111
$LaV_{0.6}Cr_{0.4}Ge_3$	6.2601(1)	5.7446(1)	194.963(7)	0.9177
$LaV_{0.4}Cr_{0.6}Ge_3$	6.2390(1)	5.7414(1)	193.54(1)	0.9202
$LaV_{0.1}Cr_{0.9}Ge_3$	6.2145(1)	5.7588(1)	192.61(1)	0.9267
$LaCr_{0.9}Mn_{0.1}Ge_3$	6.2036(1)	5.7638(1)	192.098(9)	0.9291
$LaCr_{0.8}Mn_{0.2}Ge_3$	6.2019(1)	5.7637(1)	191.988(8)	0.9293

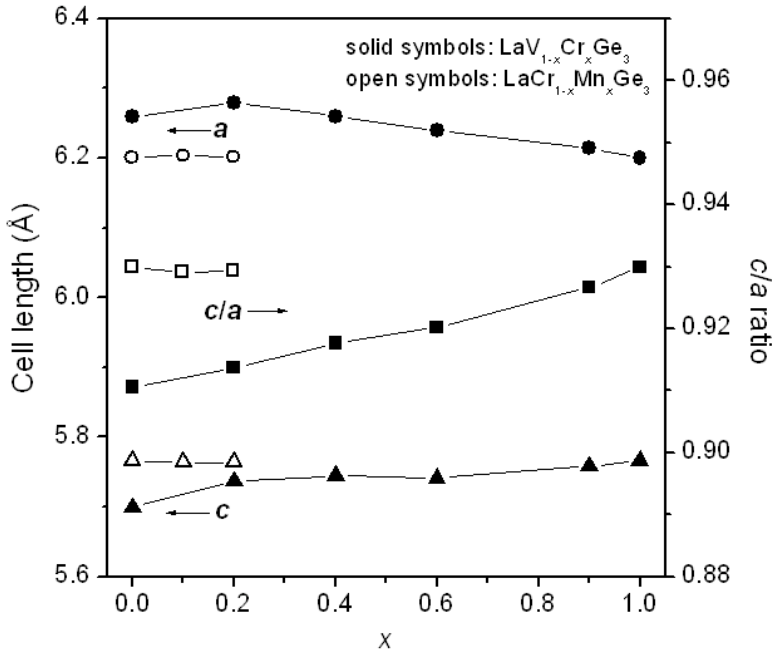

Figure 5–3. Plots of hexagonal cell parameters and *c/a* ratio vs *x* for two series of solid solutions, $LaV_{1-x}Cr_xGe_3$ and $LaCr_{1-x}Mn_xGe_3$.

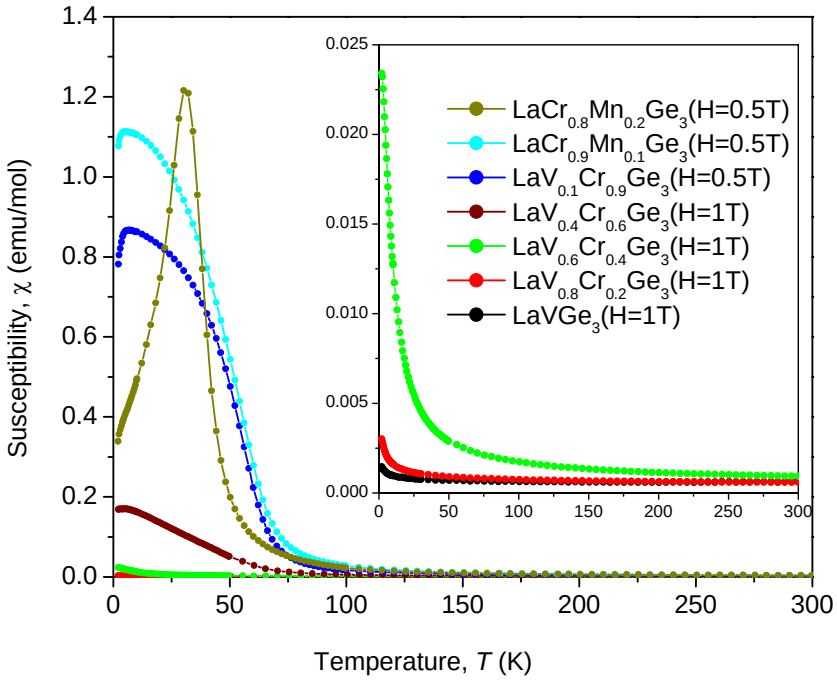

Figure 5–4. The dc magnetic susceptibility plots for $LaV_{1-x}Cr_xGe_3$ and $LaCr_{1-x}Mn_xGe_3$.

Table 5–5. Summary of magnetic data for *RE*VGe_3 (*RE* = Ce–Nd).

	$CeVGe_3$	$PrVGe_3$	$NdVGe_3$
T_N (K) from:			
$d(\chi T)/dT$ vs T plot	4	15.0	5.5
χ'_{ac} vs T plot	Not measured	13.1	3.6
θ_p (K)	–40(2)	–4.7(7)	–17(1)
χ_o (emu mol^{-1})	8.4×10^{-4}	5.9×10^{-4}	2.6×10^{-3}
$\mu_{eff, meas}$ (μ_B/f.u.)	2.21(2)	3.58(2)	3.71(2)
$\mu_{eff, theor}$ for RE^{3+} (μ_B)	2.54	3.58	3.62

The magnetic properties for the other *RE*VGe_3 (*RE* = Ce–Nd) members are summarized in Table 5–5. Plots of the temperature-dependent magnetic susceptibilities and field-dependent magnetizations are shown in Figure 5–5. Transition temperatures, T_N, were located from either dc or ac magnetic susceptibility curves, and effective magnetic moments were derived from the Curie constants obtained by fitting the high-temperature regime of the inverse magnetic susceptibility curves to the modified Curie-Weiss law, $\chi = C/(T-\theta_p) + \chi_o$. The negative Weiss temperatures (–40, –5, and –17 K for $CeVGe_3$, $PrVGe_3$, and $NdVGe_3$, respectively) and the absence of saturation behaviour in the magnetization curves imply antiferromagnetic coupling between the *RE* atoms, if the V atoms are assumed to carry no local moment given the results on $LaVGe_3$ presented above. The effective magnetic moments are slightly lower than the free-ion values for RE^{3+} in the case of $CeVGe_3$ (2.21 μ_B/f.u.) but are in good agreement in the cases of $PrVGe_3$ (3.58 μ_B/f.u.) and $NdVGe_3$ (3.71 μ_B/f.u.).

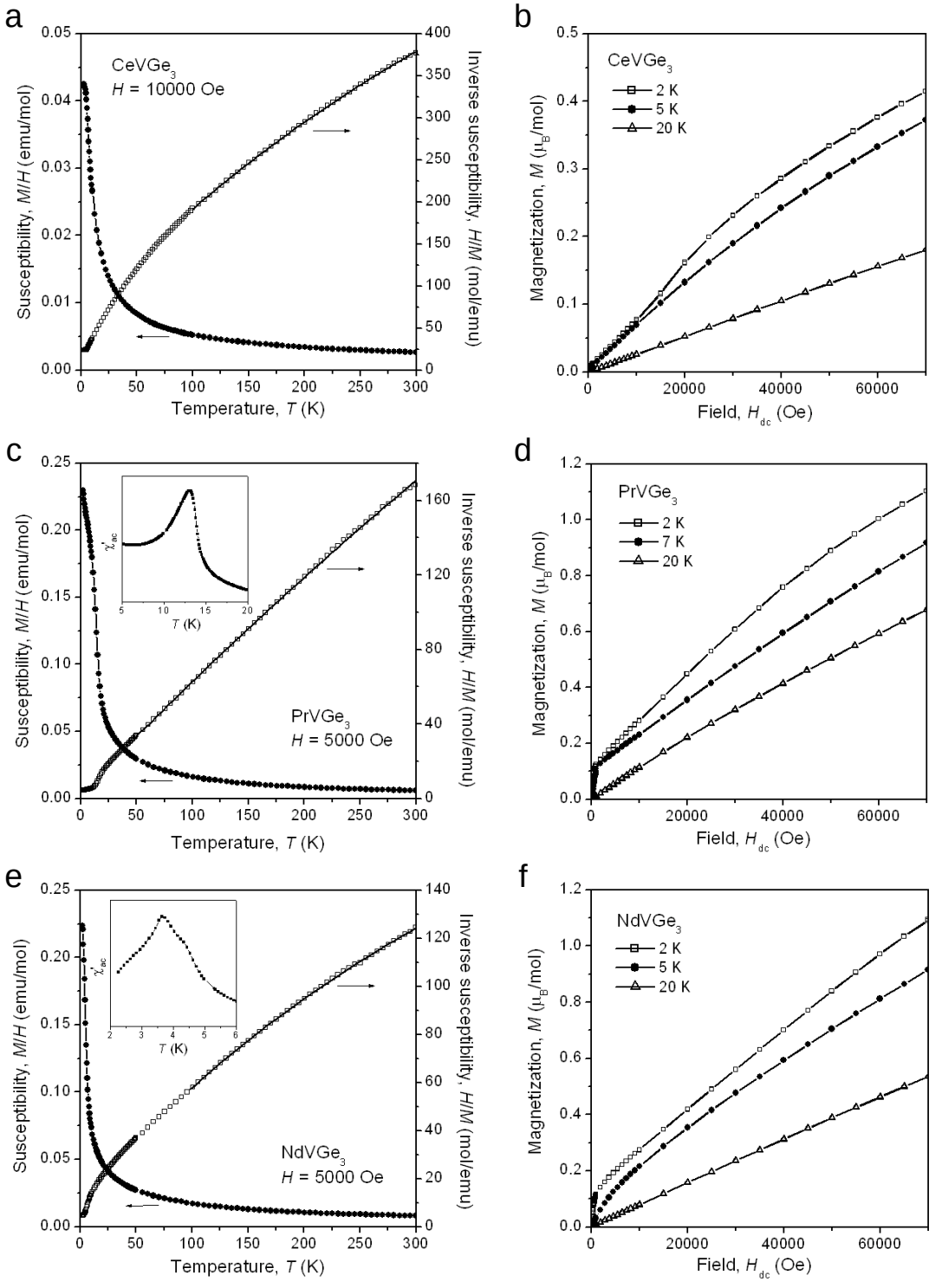

Figure 5–5. Magnetic data for (a)–(b) $CeVGe_3$, (c)–(d) $PrVGe_3$, and (e)–(f) $NdVGe_3$. The left panels show the zero-field-cooled dc magnetic susceptibility and its inverse as a function of temperature (with the insets highlighting low-temperature transitions in the ac magnetic susceptibility), and the right panels show isothermal magnetization curves at various temperatures.

The occurrence of mixed-valent Ce^{3+} and Ce^{4+} in $CeVGe_3$ is also suggested by the observation of the volume change from $LaVGe_3$ (193.34(2) $Å^3$) to $CeVGe_3$ (190.73(1) $Å^3$) to $PrVGe_3$ (190.06(1) $Å^3$). However, another possible explanation is that the use of polycrystalline samples may generate grain orientation effects under an applied magnetic field, such that the observed magnetization does not equal the average if there is strong magnetic anisotropy. Such a phenomenon was also observed for the related, but not isostructural, ternary antimonides *RE*VSb_3.[24–26] Above T_N, the magnetization curves depend linearly with applied field.

The magnetic behaviour of the germanide series *RE*VGe_3 and *RE*$CrGe_3$ parallels that of the antimonide series *RE*VSb_3 and *RE*$CrSb_3$.[24–32] The vanadium-containing compounds tend to be weakly antiferromagnetic with low transition temperatures (below ~20 K), whereas the chromium-containing ones are strongly ferromagnetic with high transition temperatures (above ~60 K). There are close structural similarities between *REM*Ge_3 and *REM*Sb_3: both contain chains of face-sharing *M*-centred octahedra, but whereas they are separated by Ge_3 clusters and retain their one-dimensional character in the former, they are condensed together through edge-sharing to form 2D layers in the latter.[33,34] The general mechanism for magnetic interactions is thus likely to be similar, involving indirect coupling of essentially local *RE* moments via the conduction electrons, to which the *M* atoms contribute. Evidence for these RKKY interactions normally comes from the observation of a linear relationship between the coupling strength (as measured by the transition temperature) and the de Gennes factor, (g–

$1)^2(J(J+1))$, but interestingly, this is observed neither in *RE*VGe_3 here nor in *RE*VSb_3, in contrast to both of the chromium-containing series. Strong CEF effects have been suggested to be responsible for the poor de Gennes scaling in *RE*VSb_3.[26] Both $LaCrGe_3$ and $LaCrSb_3$ also experience a similar suppression of ferromagnetism upon doping of the Cr atoms with V or Mn.[35]

5.3.3. Electronic Structure

The band structure calculation on $LaVGe_3$ reveals a density of states (DOS) curve (Figure 5–6a) that resembles that of $LaCrGe_3$, reported previously,[9] in the sense that the major change is simply a shift in the position of the Fermi level, in the approximation of a rigid band model. Most of the La states lie above the Fermi level, whereas many V and Ge states lie below. The strong mixing of states belies the ionic character suggested earlier in the Zintl formulation, but to the extent that there are many occupied Ge-based states, the presence of anionic Ge is confirmed. (Although charges derived from LMTO calculations are sensitive to the choice of Wigner-Seitz radii, the values of +1.5 for La, –0.03 for V, and –0.50 for Ge obtained are qualitatively consistent with the expected directions of electron transfer.) There is a large spike in the DOS near 0.7 eV, which is where the Fermi level would lie in the case for $LaCrGe_3$; this partially-filled narrow band is mostly based on transition-metal d-states, and, in accordance with the Stoner theory, has been shown to be responsible for the ferromagnetic behaviour in $LaCrGe_3$.[9] In contrast, with its fewer number of electrons, $LaVGe_3$

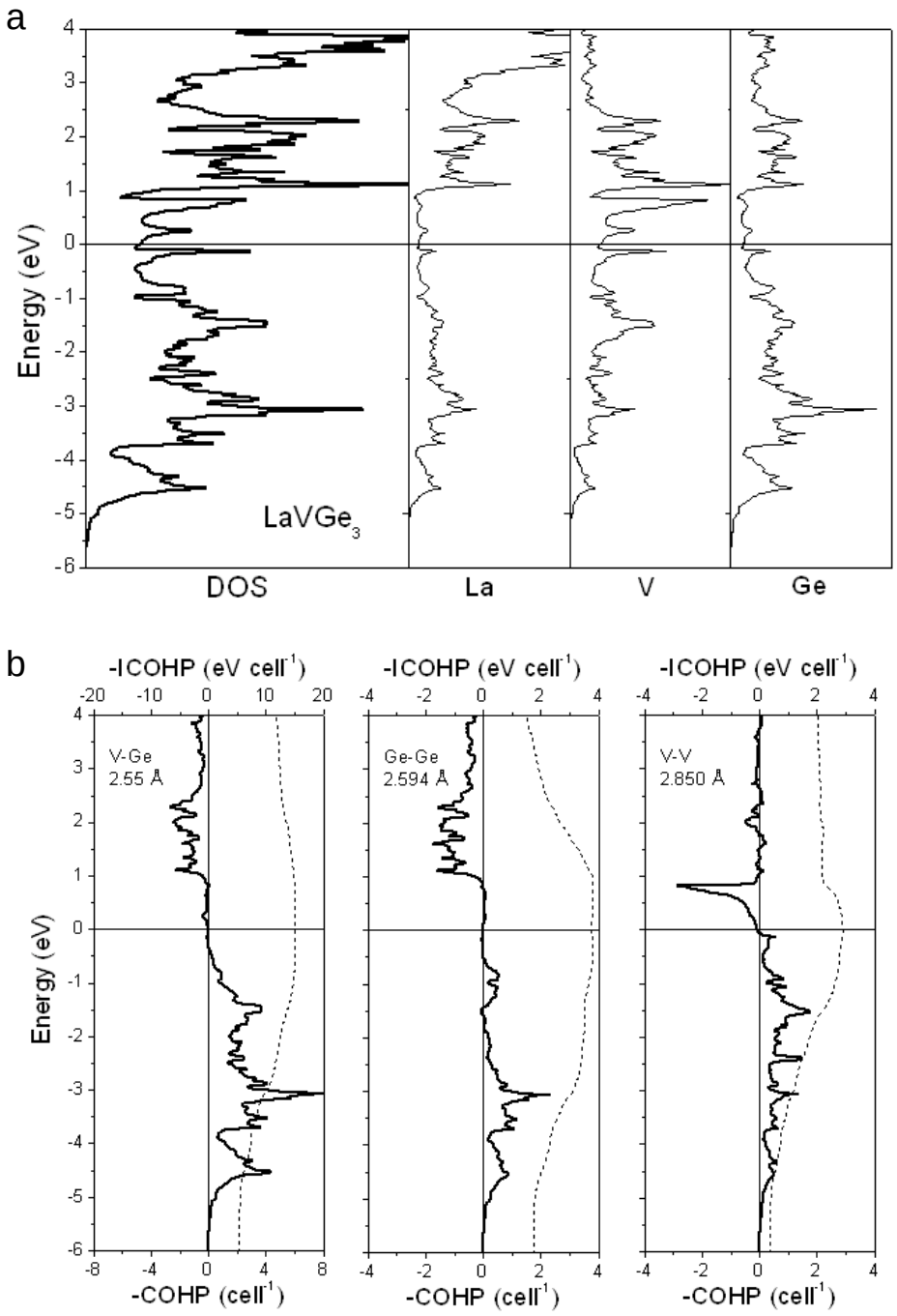

Figure 5–6. (a) Total density of states (DOS) and its La, V, and Ge projections in $LaVGe_3$. (b) Crystal orbital Hamilton populations (COHP) curves (solid lines) and integrated COHP curves (dashed lines) for V–Ge, Ge–Ge, and V–V contacts in $LaVGe_3$. The horizontal lines at 0 eV mark the Fermi level.

is not predicted to be ferromagnetically ordered because the Fermi level shifts to lower energy and high DOS across the Fermi level disappeared, consistent with the observation of Pauli paramagnetism in this compound.

The crystal orbital Hamilton population (COHP) curves (Figure 5–6b) for $LaVGe_3$ are also similar to those in $LaCrGe_3$.[9] The optimization of heteroatomic V–Ge bonding is to be expected and is quite strong, as gauged by its integrated COHP (–ICOHP) value of 2.5 eV/bond. The most interesting consequence of the lowering of the Fermi level in $LaVGe_3$ (relative to $LaCrGe_3$) is that the V–V interactions are also perfectly optimized, with all bonding levels filled and all antibonding levels unfilled. That is, the metal-metal bonding within the chains of face-sharing octahedra is strongest in $LaVGe_3$, where the –ICOHP attains its maximum value (1.4 eV per V–V bond), in contrast to that in $LaCrGe_3$ (1.1 eV per Cr–Cr bond). The presence of Ge–Ge bonding within the triangular Ge_3 clusters is also confirmed (1.3 eV/bond). In the vicinity of the Fermi level, the V–Ge and Ge–Ge interactions are essentially nonbonding, but the metal-metal interactions are sensitive to a change in electron count. Since the Ge–Ge bonds lie parallel to the *ab* plane whereas the metal-metal bonds lie parallel to the *c*-direction, increasing the electron count should lead to observable effects in the *a* and *c* parameters. As seen in Figure 5–3, increasing substitution of smaller sized Cr for V atoms in $LaV_{1-x}Cr_xGe_3$ is accompanied by a slight decrease in *a* (corresponding to a slight strengthening of Ge–Ge bonds, through occupation of a few rather weakly bonding levels – barely visible – located between 0 and 1 eV),

and an increase in *c* (corresponding to a weakening of metal-metal bonds, through occupation of the strongly antibonding levels clearly visible between 0 and 1 eV).

5.4. Conclusions

The series of ternary germanides *RE*VGe_3 completes the previously missing entry between *RE*$TiGe_3$ and *RE*$CrGe_3$, and suggests the possibility that further intermetallic representatives of the hexagonal perovskite-type structure may be worthwhile targeting. Emerging trends that can be generalized are: (i) The substitution extends to smaller *RE* atoms when the transition metal progresses to the right of the periodic table; (ii) The Zintl-Klemm formulation can explain the occurrence of homoatomic V–V bonding within the chains of face-sharing octahedra and triangular Ge–Ge bonding within the Ge_3 clusters; and (iii) The number of d-electrons in the transition metal site causes dramatic changes in their magnetic properties. The introduction of V or Mn into the ferromagnetic $LaCrGe_3$ tends to suppress the long-range ordering.

5.5. References

(1) Davies, P. K.; Wu, H.; Borisevich, A. Y.; Molodetsky I. E.; Farber, L. *Annu. Rev. Mater. Res.* **2008**, *38*, 369–401.

(2) Darriet J.; Subramanian, M. A. *J. Mater. Chem.* **1995**, *5*, 543–552.

(3) Stitzer, K. E.; Darriet J.; zur Loye, H.-C. *Curr. Opin. Solid State Mater. Sci.* **2001**, *5*, 535–544.

(4) Hébert, S.; Pralong, V.; Pelloquin D.; Maignan, A. *J. Magn. Magn. Mater.* **2007**, *316*, 394–399.

(5) Maignan, A.; Kobayashi, W.; Hébert, S.; Martinet, G.; Pelloquin, D.; Bellido N.; Simon, Ch. *Inorg. Chem.* **2008**, *47*, 8553–8561.

(6) Müller, U. *Inorganic Structural Chemistry*; Wiley: Chichester, 1993.

(7) Morozkin, A. V. *J. Alloys Compd.* **2004**, *370*, L1–L3.

(8) Manfrinetti, P.; Dhar, S. K.; Kulkarni R.; Morozkin, A. V. *Solid State Commun.* **2005**, *135*, 444–448.

(9) Bie, H.; Zelinska, O. Ya.; Tkachuk A. V.; Mar, A. *Chem. Mater.* **2007**, *19*, 4613–4620.

(10) Szytuła, A.; Leciejewicz, A. *Handbook of Crystal Structures and Magnetic Properties of Rare Earth Intermetallics*; CRC Press: Boca Raton, 1994.

(11) Tkachuk A. V.; Mar, A. *Acta Crystallogr., Sect. E* **2005**, *61*, i1–i2.

(12) Hunter, B. *LHPM-Rietica*, version 1.7.7, International Union of Crystallography Commission on Powder Diffraction Newsletter, no. 20 (summer), 1998 (www.rietica.org.).

(13) Gelato L. M.; Parthé, E. *J. Appl. Crystallogr.* **1987**, *20*, 139–143.

(14) Tank, R.; Jepsen, O.; Burkhardt A.; Andersen, O. K. *TB-LMTO-ASA Program*, version 4.7, Max Planck Institut für Festkörperforschung, Stuttgart, 1998.

(15) Salamakha, P. S.; Sologub, O. L.; Bodak, O. I. In *Handbook on the Physics and Chemistry of Rare Earths*; Gschneidner, Jr., K. A., Eyring, L., Eds.; Elsevier: Amsterdam, 1999; Vol. 27, pp 1–223.

(16) Salamakha, P. S. In *Handbook on the Physics and Chemistry of Rare Earths*; Gschneidner, K. A.; Jr., Eyring, L., Eds.; Elsevier: Amsterdam, 1999; Vol. 27, pp 225–338.

(17) Kotur, B. Ya.; Bodak, O. I.; Sikiritsa, M.; Bruvo, M. *Dopov. Akad. Nauk Ukr. RSR, Ser. B* **1983**, *10*, 46–49.

(18) Kotur, B. Ya.; Bodak, O. I.; Zavodnik, V. E. *Sov. Phys. Crystallogr.* **1986**, *31*, 513–516 (*Transl. Kristallografiya*, **1986**, *31*, 868–873).

(19) Kotur, B. Ya. *Inorg. Mater.* **1987**, *23*, 493–496 (*Transl. Izv. Akad. Nauk SSSR, Neorg. Mater.* **1987**, *23*, 558–561).

(20) Takeda, Y.; Kanamaru, F.; Shimada M.; Koizumi, M. *Acta Crystallogr.*, *Sect. B* **1976**, *32*, 2464–2466.

(21) Gardner, R. A.; Vlasse M.; Wold, A. *Acta Crystallogr. Sect. B*, **1969**, *25*, 781–787.

(22) Pauling, L. *The Nature of the Chemical Bond*, 3rd ed.; Cornell University Press: Ithaca, NY, USA, 1960.

(23) Søndenå, R.; Stølen, S.; Ravindran, P.; Grande T.; Allan, N. L. *Phys. Rev. B* **2007**, *75*, 184105-1–184105-10.

(24) Hartjes, K.; Jeitschko W.; Brylak, M. *J. Magn. Magn. Mater.*, **1997**, *173*, 109–116.

(25) Jackson, D. D.; Torelli M.; Fisk, Z. *Phys. Rev. B* **2001**, *65*, 014421-1–014421-6.

(26) Sefat, A. S.; Bud'ko, S. L.; Canfield, P. C. *J. Magn. Magn. Mater.* **2008**, *320*, 120–141.

(27) Raju, N. P.; Greedan, J. E.; Ferguson, M. J.; Mar, A. *Chem. Mater.* **1998**, *10*, 3630–3635.

(28) Leonard, M. L.; Dubenko, I. S.; Ali, N. *J. Alloys Compd.* **2000**, *303–304*, 265–269.

(29) Deakin, L.; Ferguson, M. J.; Mar, A.; Greedan, J. E.; Wills, A. S. *Chem. Mater.* **2001**, *13*, 1407–1412.

(30) Jackson D. D.; Fisk, Z. *Phys. Rev. B* **2006**, *73*, 024421-1–024421-7.

(31) Jackson, D. D.; McCall, S. K.; Karki, A. B.; Young, D. P. *Phys. Rev. B* **2007**, *76*, 064408-1–064408-5.

(32) Inamdar, M.; Thamizhavel, A.; Ramakrishnan, S. *J. Phys.: Condens. Matter* **2008**, *20*, 295226-1–295226-4.

(33) Brylak M.; Jeitschko, W. *Z. Naturforsch. B: Chem. Sci.* **1995**, *50*, 899–904.

(34) Ferguson, M. J.; Hushagen, R. W.; Mar, A. *J. Alloys Compd.* **1997**, *249*, 191–198.

(35) Dubenko, I. S.; Hill, P.; Ali, N. *J. Appl. Phys.* **2001**, *89*, 7326–7328.

Chapter 6

Structure and Magnetic Properties of Rare-Earth Chromium Germanides $RECr_xGe_2$ (RE = Sm, Gd–Er)*

6.1. Introduction

Ternary rare-earth transition-metal germanides *RE*–*M*–Ge represent a well-investigated class of intermetallics exhibiting a wide range of structures and physical properties,[1,2] as shown by our previous studies on the series of compounds $RECrGe_3$ [3] and $REVGe_3$.[4] The orthorhombic $CeNiSi_2$ structure type is adopted by many intermetallics with the composition REM_xTt_2 (*RE* = rare-earth elements, *M* = transition metal (Mn, Fe, Co, Ni, Cu, Ru, Rh, Re, Ir, Pd, Pt), *Tt* = Si, Ge, Sn (collectively, the "tetrels").[5,6] Most of these phases are nonstoichiometric, with the transition-metal content *x* generally increasing on proceeding to a heavier transition metal, or to a lighter tetrel. However, little is known about the nature of the deficiencies of the *M* sites. Surprisingly, detailed single-crystal structure studies have been scarce, and only recently has a modulated superstructure been implicated for $TbFe_{0.25}Ge_2$.[7] Much of the interest on these REM_xTt_2 phases has focused on their varied magnetic properties, which depend systematically on the component elements.[8]

One series has been missing to date is the Cr-containing $CeNiSi_2$-type

* *A version of this chapter has been published. Haiying Bie, Andriy V. Tkachuk, Arthur Mar, 2009. Journal of Solid State Chemistry, 182, 122–128. All work presented in this chapter was completed by myself with the experimental assistance of A.V. Tkachuk.*

compounds *RE*Cr_xGe_2. Continuing our studies of the *RE*–Cr–Ge system, in this chapter we report the new nonstoichiometric ternary germanides *RE*Cr_xGe_2, which form for the later *RE* elements (*RE* = Sm, Gd–Er). Some members could be successfully grown as single crystals through flux methods to permit structural investigations to determine the level of Cr deficiency in the $CeNiSi_2$-type structure adopted. Magnetic measurements were also performed for those members that could be prepared as phase-pure samples.

6.2. Experimental Section

6.2.1. Synthesis

Single crystals of $SmCr_xGe_2$ were first identified as byproducts in the synthesis of $SmCrGe_3$.[3] Single crystals of $GdCr_xGe_2$ and $DyCr_xGe_2$ were prepared in a similar manner, through a reaction of *RE*:Cr:Ge = 1:1:2 in the presence of a 10-fold molar excess of In placed within alumina crucibles jacketed by fused-silica tubes. The tubes were heated to 1000 °C over 10 h, cooled to 850 °C at a rate of 2 °C/h, held at this temperature for 2 d, and cooled to 300 °C over 2 d, at which point the liquid indium flux was centrifuged. EDX analyses on these crystals showed the presence of all three elements, and none of the flux elements, in ratios (31–35% *RE*, 7–10% Cr, 60–63% Ge) consistent with the formulas obtained from the structure determinations.

The extent of *RE* substitution was investigated by targeting samples of nominal composition *RE*$Cr_{0.3}Ge_2$, prepared by arc-melting mixtures of the elements. The alloys were placed in evacuated and sealed fused-silica tubes,

annealed at 800 °C for 20 days, and then quenched in cold water. *RE*$Cr_{0.3}Ge_2$ phases were obtained in essentially quantitative yield for *RE* = Gd–Er, as judged by their powder X-ray diffraction patterns. There was also evidence for the existence of $YbCr_{0.3}Ge_2$ (a = 4.0917(1) Å, b = 15.5214(5) Å, c = 3.9760(2) Å), but the sample contained other phases that could not be identified. The $DyCr_xGe_2$ series was selected to investigate the homogeneity range in Cr, through similar arc-melting and annealing reactions as above.

6.2.2. Structure Determination

Single-crystal X-ray diffraction data for *RE*Cr_xGe_2 (*RE* = Sm, Gd, Dy) were collected on a Bruker Platform / SMART 1000 CCD diffractometer at 22 °C using ω scans. Structure solution and refinement were carried out with use of the SHELXTL (version 6.12) program package.[9] Of the possible orthorhombic space groups *Cmcm*, *Cmc*2_1, and *Ama*2 suggested by the systematic absences, the centrosymmetric one *Cmcm* was chosen. Initial atomic positions were located by direct methods, revealing a $CeNiSi_2$-type structure commonly adopted by many *REM*$_x$*Tt*$_2$ phases. Refinements indicated partial occupancy, close to ¼, of the Cr site. However, the Cr–Ge2 distances (2.1–2.2 Å) are especially short and the Ge2 displacement ellipsoids are unusually oblate within square nets parallel to the *ac* plane. These features are characteristic of *REM*$_x$*Tt*$_2$ phases, where single-crystal structures have been refined.[10–12] Recently, a very weak superstructure for $TbFe_{0.25}Ge_2$ has been elucidated, based on a monoclinic supercell in space group $P2_1/n$.[7] Careful inspection of the intensity frames for *RE*Cr_xGe_2 did not reveal

any obvious additional reflections. Attempts were made to refine the structures in $P2_1/n$ according to the $TbFe_{0.25}Ge_2$ model, but the residual factors did not improve and the short Cr–Ge distances remained.

Powder X-ray diffraction data for all members $RECr_{0.3}Ge_2$ (*RE* = Gd–Er) were refined with the full-profile Rietveld method using the program LHPM-Rietica.[13] Initial positions were taken from the single-crystal structures described above. The occupancy of the Cr site was fixed at exactly 0.3, consistent with the initial stoichiometry of the loaded reactants to prepare these phase-pure samples. Only the results for $RECr_{0.3}Ge_2$ (*RE* = Tb, Ho, Er), where single-crystal data were unavailable, are reported here. Fits to the all powder patterns are shown in Figure 6–1. Atomic positions were standardized with the program STRUCTURE TIDY.[14] Crystal data and further details of the data collections are given in Table 6–1. Final values of the positional and displacement parameters are given in Table 6–2. Selected interatomic distances are listed in Tables 6–3.

6.2.3. Band Structure Calculation

Tight-binding linear muffin tin orbital (TB-LMTO) band structure calculations with atomic sphere approximation (ASA) were performed on $GdCr_{0.25}Ge_4$ within the local density and atomic spheres approximations using the Stuttgart TB-LMTO program.[15] Integrations in reciprocal space were carried out with an improved tetrahedron method over 54 independent *k* points within the first Brillouin zone. To avoid the problems with unfilled *f* electrons of late rare-earth elements, Y atoms were used in place of Gd for the calculation due to their similar sizes and trivalent oxidation states.

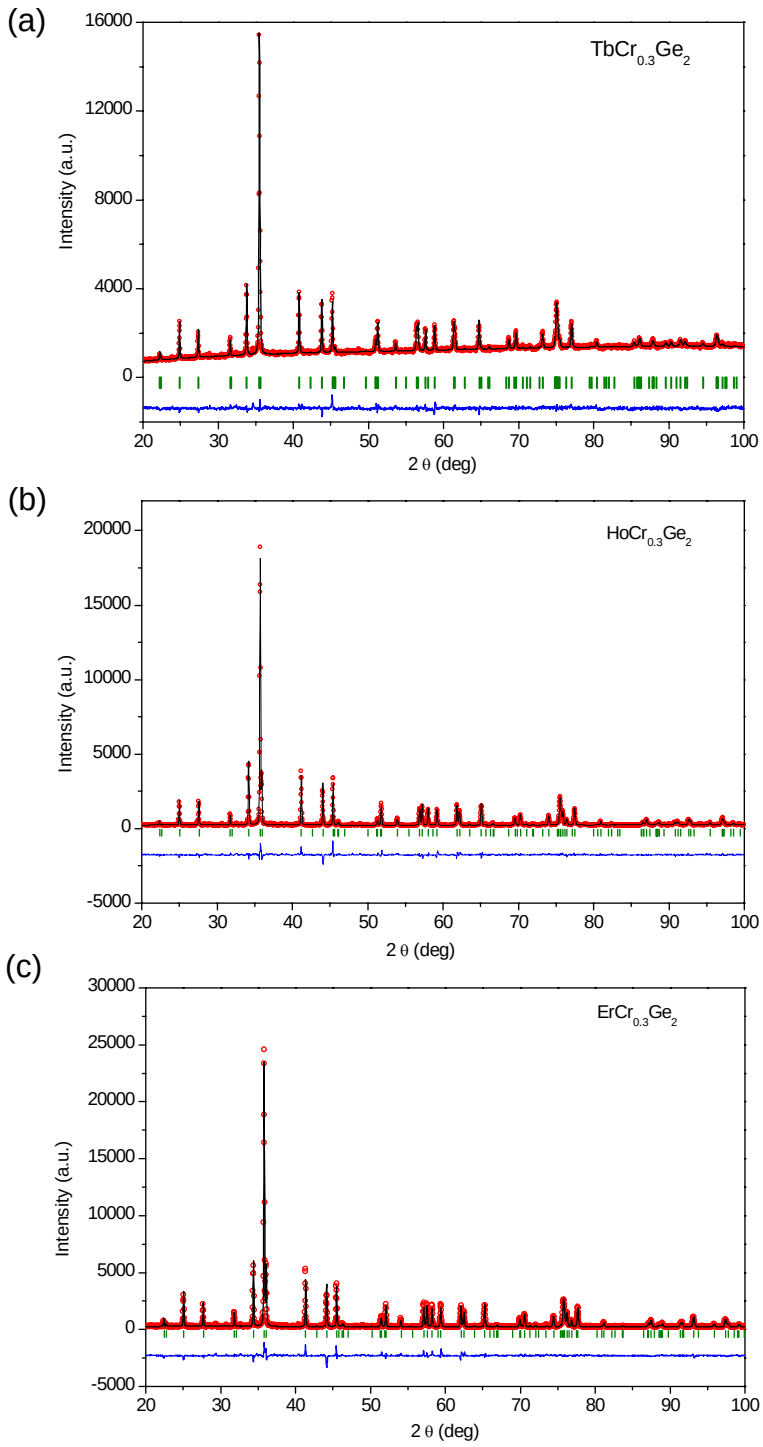

Figure 6–1. Rietveld refinement results for *RE*$Cr_{0.3}Ge_2$ (*RE* = (a) Tb, (b) Ho, (c) Er). The observed profile is indicated by red circles and the calculated profile by the black line. Bragg peak positions are located by the vertical tick green marks. The difference plot is shown at the bottom by blue lines.

Table 6–1. Crystallographic data for $RECr_xGe_2$ (*RE* = Sm, Gd–Er).

Formula	$SmCr_{0.29(1)}Ge_2$	$GdCr_{0.33(1)}Ge_2$	$TbCr_{0.3}Ge_2$	$DyCr_{0.25(1)}Ge_2$	$HoCr_{0.3}Ge_2$	$ErCr_{0.3}Ge_2$
Formula mass (amu)	310.66	319.72	319.71	320.58	325.71	328.04
Space group			*Cmcm* (No. 63)			
a (Å)	4.1939(5)	4.1694(13)	4.1335(3)	4.1303(8)	4.1117(2)	4.1016(2)
b (Å)	16.291(2)	16.136(5)	15.911(1)	15.839(3)	15.7384(8)	15.6579(6)
c (Å)	4.0598(5)	4.0495(13)	4.0107(3)	4.0112(8)	3.9951(2)	3.9876(2)
V (Å^3)	277.38(6)	272.43(15)	263.78(3)	262.42(9)	258.53(2)	256.09(2)
Z	4	4	4	4	4	4
ρ_{calcd} (g cm^{-3})	7.439	7.795	8.047	8.114	8.364	8.504
Radiation	Mo *K*α	Mo *K*α	Cu *K*α_1	Mo *K*α	Cu *K*α_1	Cu *K*α_1
μ (mm^{-1})	43.1	46.9	81.5	51.5	89.9	92.9
2θ range	5.0–60.9°	5.0–66.1°	20.0–100.0°	5.1–66.0°	20.0–100.0°	20.0–100.0°
No. of data collected	1617 (R_{int} = 0.037)	1800 (R_{int} = 0.049)	2759 data points	1741 (R_{int} = 0.024)	2759 data points	2759 data points
No. of unique data	264	321	90	303	89	89
	(256 with $F_o^2 > 2\sigma(F_o^2)$)	(294 with $F_o^2 > 2\sigma(F_o^2)$)	Bragg reflections	(296 with $F_o^2 > 2\sigma(F_o^2)$)	Bragg reflections	Bragg reflections
No. of variables	19	18	26	19	25	25
Residuals [a]	$R(F)$ = 0.021	$R(F)$ = 0.032	R_B = 0.018	$R(F)$ = 0.022	R_B = 0.046	R_B = 0.060
	$R_w(F^2)$ = 0.056	$R_w(F^2)$ = 0.069	R_p = 0.029	$R_w(F^2)$ = 0.047	R_p = 0.075	R_p = 0.091
			R_{wp} = 0.038		R_{wp} = 0.099	R_{wp} = 0.120

[a] $R(F) = \sum \| F_o | - | F_c \| / \sum | F_o |$; $R_w(F_o^2) = \left[\sum \left[w(F_o^2 - F_c^2)^2 \right] / \sum w F_o^4 \right]^{1/2}$; $R_B = \sum | I_o - I_c | / \sum I_o$; $R_p = \sum | y_o - y_c | / \sum y_o$; $R_{wp} = \left[\sum [w(y_o - y_c)] / \sum w y_o^2 \right]^{1/2}$, $w^{-1} = \left[\sigma^2 (F_o^2) + (Ap)^2 + Bp \right]$
where $p = \left[\max(F_o^2, 0) + 2F_c^2 \right] / 3$.

Table 6–2. Atomic coordinates and equivalent isotropic displacement parameters (Å^2) for *RE*Cr$_x$Ge$_2$ (*RE* = Sm, Gd–Er). [a]

	$SmCr_{0.29(1)}Ge_2$	$GdCr_{0.33(1)}Ge_2$	$TbCr_{0.3}Ge_2$	$DyCr_{0.25(1)}Ge_2$	$HoCr_{0.3}Ge_2$	$ErCr_{0.3}Ge_2$
RE						
y	0.3969(1)	0.3974(1)	0.3965(2)	0.3970(1)	0.3967(1)	0.3969(1)
U_{eq} or U_{iso}	0.0085(2)	0.0076(2)	0.015(1)	0.0099(2)	0.007(1)	0.011(1)
Cr						
occupancy	0.29(1)	0.33(1)	0.3	0.25(1)	0.3	0.3
y	0.1994(3)	0.2004(3)	0.1949(11)	0.1993(3)	0.1961(9)	0.1971(11)
U_{eq} or U_{iso}	0.0067(13)	0.0089(14)	0.009(4)	0.0057(14)	0.013(4)	0.025(5)
Ge1						
y	0.0497(1)	0.0506(1)	0.0510(3)	0.0522(1)	0.0522(2)	0.0527(2)
U_{eq} or U_{iso}	0.0097(2)	0.0093(2)	0.009(2)	0.0120(2)	0.004(1)	0.008(1)
Ge2						
y	0.7518(1)	0.7514(1)	0.7526(3)	0.7519(1)	0.7515(2)	0.7522(2)
U_{eq} or U_{iso}	0.0344(3)	0.0353(4)	0.017(2)	0.0306(3)	0.015(1)	0.015(1)

[a] All atoms are in Wyckoff position 4*c* (0, *y*, ¼); U_{eq} is defined as one-third of the trace of the orthogonalized U_{ij} tensor. U_{iso} applies to powder refinement samples.

Table 6–3. Selected interatomic distances (Å) in $RECr_xGe_2$ (*RE* = Sm, Gd–Er).

	$SmCr_{0.29(1)}Ge_2$	$GdCr_{0.33(1)}Ge_2$	$TbCr_{0.3}Ge_2$	$DyCr_{0.25(1)}Ge_2$	$HoCr_{0.3}Ge_2$	$ErCr_{0.3}Ge_2$
RE–Ge1 (×4)	3.046(1)	3.025(1)	2.999(2)	2.989(1)	2.977(1)	2.967(1)
RE–Ge2 (×2)	3.160(1)	3.141(2)	3.085(3)	3.090(1)	3.070(4)	3.056(1)
RE–Ge2 (×2)	3.160(1)	3.145(1)	3.106(5)	3.096(1)	3.074(2)	3.070(1)
RE–Ge1 (×2)	3.255(1)	3.234(1)	3.211(3)	3.210(1)	3.196(2)	3.187(1)
RE–Cr	3.217(5)	3.179(5)	3.21(2)	3.131(5)	3.16(1)	3.128(1)
RE–Cr (×4)	3.314(2)	3.307(3)	3.226(8)	3.258(2)	3.217(7)	3.217(1)
Cr–Ge2 (×2)	2.180(2)	2.169(2)	2.173(7)	2.149(2)	2.161(6)	2.146(1)
Cr–Ge2 (×2)	2.264(2)	2.241(2)	2.262(7)	2.227(2)	2.233(6)	2.225(1)
Cr–Ge1	2.439(5)	2.417(6)	2.29(2)	2.331(5)	2.27(1)	2.262(1)
Ge1–Ge1 (×2)	2.597(1)	2.601(2)	2.579(5)	2.599(1)	2.586(4)	2.587(1)
Ge2–Ge2 (×4)	2.919(1)	2.906(1)	2.881(1)	2.879(1)	2.867(1)	2.861(1)

6.2.4. Magnetic Measurements

Measurements of dc magnetic susceptibility were made on powders with the composition $RECr_{0.3}Ge_2$ (*RE* = Gd–Er), confirmed to be phase-pure by powder X-ray diffraction, between 2 and 300 K on a Quantum Design 9T–PPMS dc magnetometer / ac susceptometer. The susceptibility was corrected for contributions from the holder and underlying sample diamagnetism. Measurements of ac magnetic susceptibility were made with a driving amplitude of 1–10 Oe and a frequency of 2000 Hz.

6.3. Results and Discussion

6.3.1. Crystal Structure

The germanides REM_xGe_2 were previously known for first-row transition metals being restricted to *M* = Mn, Fe, Co, Ni, Cu,[2] and have now been extended to include an earlier transition metal, *M* = Cr, in the new series $RECr_xGe_2$. The range of *RE* substitution is narrower in $RECr_xGe_2$ (*RE* = Sm, Gd–Er, Yb), and gradually widens on progressing to $REMn_xGe_2$ (*RE* = Nd, Sm, Gd–Tm, Lu) and REM_xGe_2 (*M* = Fe, Co, Ni, Cu; *RE* = Y, La–Sm, Gd–Lu).[5,6] These compounds adopt the $CeNiSi_2$-type structure, which has been proposed to be more thermodynamically stable than the alternative $YIrGe_2$-type structure adopted by some representatives such as $RENiGe_2$.[16] Moreover, these $CeNiSi_2$-type phases typically display significant deficiencies on the transition metal site ($0 < x < 1$), unlike the $YIrGe_2$-type phases which are strictly stoichiometric. The stoichiometric compound $ScCrGe_2$ is also known, but it adopts an unrelated $ZrCrSi_2$-type (or $TiMnSi_2$-type) structure.[17,18] $DyCr_xGe_2$ was chosen as a

representative series to investigate the homogeneity range at 800 °C. The cell parameters increase monotonically with greater Cr content in the range $0.25 \leq x \leq 0.50$, beyond which multiphase products were observed (Figure 6–2). This result conforms to the general trend that x is smaller when M is an early transition-metal (cf., x increases gradually on progressing to a later transition metal, to as high as 1.0 in RENiGe$_2$). However, under the non-equilibrium conditions of the flux growth, other competing Cr-containing phases (such as Cr_3Ge and $RECr_6Ge_6$) were also formed, which may account for compositions of the ternary $RECr_xGe_2$ phases not reaching the maximum Cr content observed in arc-melting and annealing reactions.

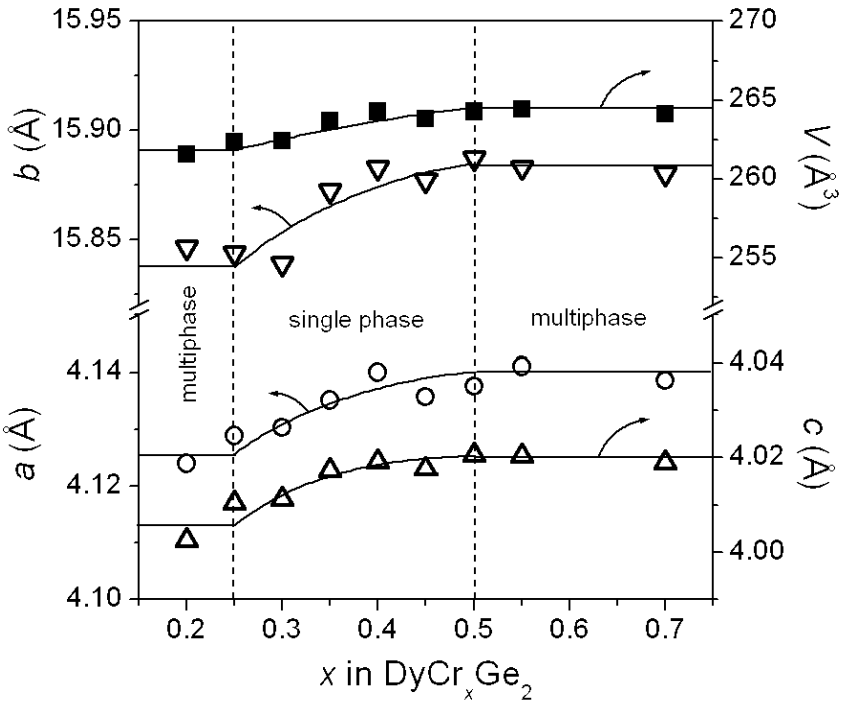

Figure 6–2. Plot of cell parameters vs. x for $CeNiSi_2$-type phase observed in reactions with nominal composition of $DyCr_xGe_2$.

The structure of *RE*Cr_xGe_2 consists of [Cr_xGe_2] layers parallel to the *ac* plane that are held together by zigzag chains of Ge1 atoms aligned along the *c* direction, forming a three-dimensional framework with channels occupied by *RE* atoms (Figure 6–3). The Ge–Ge distances within the zigzag chains of Ge1 atoms (~2.6 Å) are shorter and relatively invariant compared to those within the square nets of Ge2 atoms (~2.9 Å) forming part of the [Cr_xGe_2] layers. Each *RE* atom is coordinated by ten Ge atoms, eight at the corners of a square antiprism (four Ge1 and four Ge2) and two Ge1 atoms further away, at distances that gradually decrease with the lanthanide contraction (from 3.046(1)–3.255(1) Å in $SmCr_{0.3}Ge_2$ to 2.967(1)–3.187(1) Å in $ErCr_{0.3}Ge_2$). The Cr atoms are coordinated in square pyramidal geometry, with the distances to the four basal Ge2 atoms being anomalously short (2.146(1)–2.225(1) Å in $ErCr_{0.3}Ge_2$); even the distance to the apical Ge1 atom eventually becomes very short (2.439(5) Å in $SmCr_{0.3}Ge_2$ to 2.262(1) Å in $ErCr_{0.3}Ge_2$), when compared to typical distances of 2.4–2.5 Å in Cr–Ge binaries[19,20] or in *RE*$CrGe_3$,[3] or to the sum of the metallic radii (2.43 Å).[21] Many defect *REM*$_xGe_2$ structures exhibit these anomalously short *M*–Ge distances, but only in the case of $TbFe_{0.25}Ge_2$ has a modulated superstructure been resolved, in which the square Ge net distorts to form *cis*-*trans* chains that can accommodate more reasonable distances to the capping transition-metal atoms.[7] Attempts to detect a superstructure in *RE*Cr_xGe_2 were unsuccessful.

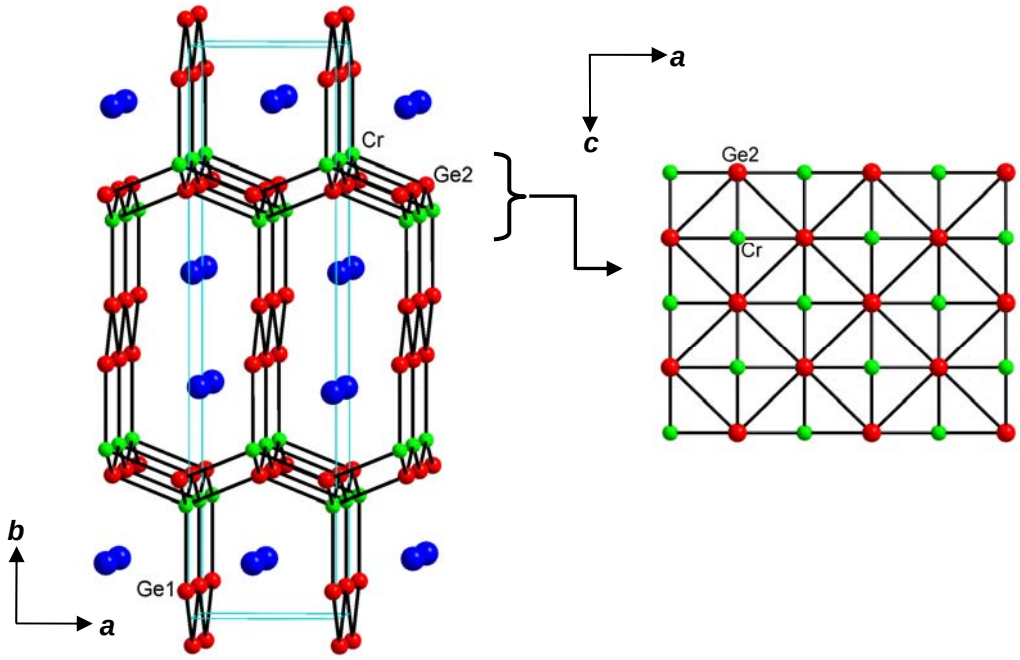

Figure 6–3. Average structure of *RE*Cr$_x$Ge$_2$ (*RE* = Sm, Gd–Er) viewed down the *c*-direction, and an excised [Cr$_x$Ge$_2$] slab viewed down the *b*-direction. The large blue spheres are *RE* atoms, the green spheres are Cr atoms, and the red spheres are Ge atoms.

6.3.2. Electronic Structure

With the understanding that only the average structure has been determined here, the Zintl-Klemm concept could be applied to draw some simple conclusions about the bonding in *RE*Cr$_x$Ge$_2$. If each of the two-bonded Ge1 atoms in the zigzag chains ($d_{(Ge–Ge)}$ = 2.601 Å) as single bond is assigned to be 2–, and the Ge2 atoms within the square nets ($d_{(Ge–Ge)}$ = 2.906 Å) are assumed to be isolated without involvement in homoatomic bonding, then a charge-balanced stoichiometric formulation "(RE^{3+})(Cr^{3+})($Ge1^{2-}$)($Ge2^{4-}$)" can be obtained. However, if the experimentally observed Cr deficiency (with x = ~ 0.3) is taken into account, then the formulation "(RE^{3+})(Cr^{3+})$_{0.33}$($Ge1^{2-}$)($Ge2^{2-}$)" leads to the interesting speculation that the square nets entail weak hypervalent bonding of the

Ge2 atoms, similar to that found in many polygermanides and in accordance with an ideal count of six electrons per atom in a square net.[22]

To evaluate the bonding in more detail, a band structure calculation on Y_4CrGe_8 was performed. As shown in Figure 6–4 (a), the DOS curve reveals metallic behaviour. Although most Y states are unoccupied and located above the Fermi level (E_f), some Y 4d states mix with Cr 3d and Ge 4s and 4p states found below. The crystal orbital Hamilton population (–COHP) curves for Ge1–Ge1 contacts in the zig-zag chains and Ge2–Ge2 contacts in the square sheets are shown in Figure 6–4 (b). The integrated –COHP up to E_f for the Ge1–Ge1 bonds within the zig-zag chains is 1.98 eV/bond, which is stronger than those in $LaCrGe_3$ (–ICOHP = 1.1 eV/bond) and is suggestive of single bonds.[3] In contrast, the Ge2–Ge2 contacts within the square sheets gives an integrated –COHP of 0.81 eV/bond up to E_f, which, although small, confirms the presence of real but weak bonding. Strong covalent Cr–Ge bonding is suggested by the integrated –COHP of 2.97 eV/bond up to E_f, which is much stronger than those observed in octahedral geometry in $LaCrGe_3$ (–ICOHP = 2.2 eV/bond).[3]

(a)

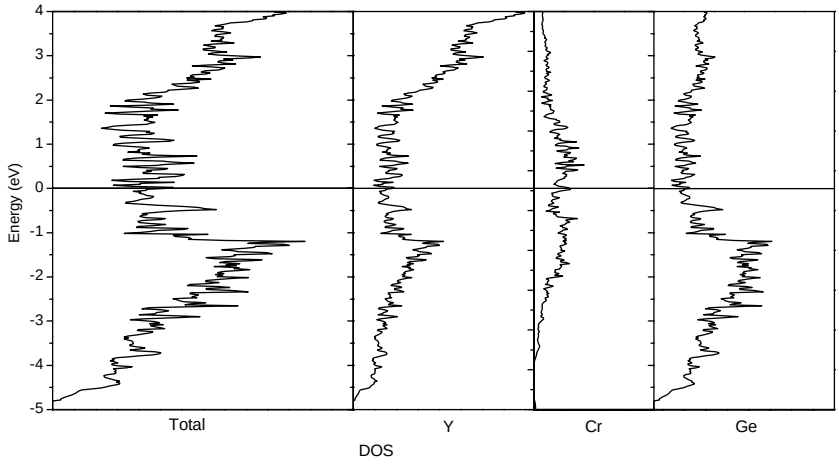

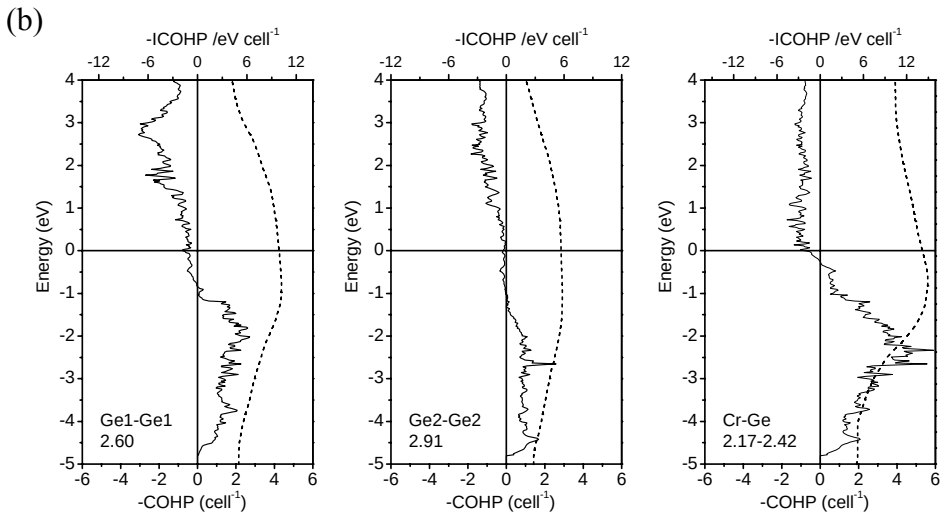

Figure 6–4. (a) Total density of states (DOS) for Y_4CrGe_8 and its Y, Cr, and Ge contributions; (b) Crystal orbital Hamilton population (COHP) curves for Ge1–Ge1 contacts in the zig-zag chains, Ge2–Ge2 interactions in the square sheets, and Cr–Ge contacts in the square pyramidal geometry. The Fermi level is marked by a horizontal line at 0 eV.

6.3.3. Magnetic Properties

Magnetic data for powder samples of $RECr_{0.3}Ge_2$ (*RE* = Gd–Er) are shown in Figure 6–5 and summarized in Table 6–4. The zero-field-cooled dc magnetic susceptibility curves measured under low applied magnetic fields (H = 1000 Oe (*RE* = Gd–Ho) or 5000 Oe (*RE* = Er)) reveal paramagnetic behaviour from 300 K down to relatively low temperatures (below 20 K), at which point downturns in the curves signal the onset of antiferromagnetic ordering. Néel temperatures were located either from plots of $d(\chi T)/dT$ vs T or from ac magnetic susceptibility curves. In the case of the Tb and Dy samples, a second transition at lower temperature is visible in the dc or ac magnetic susceptibility. Magnetic susceptibility measurements on single crystals of $TbFe_{0.25}Ge_2$ also showed two

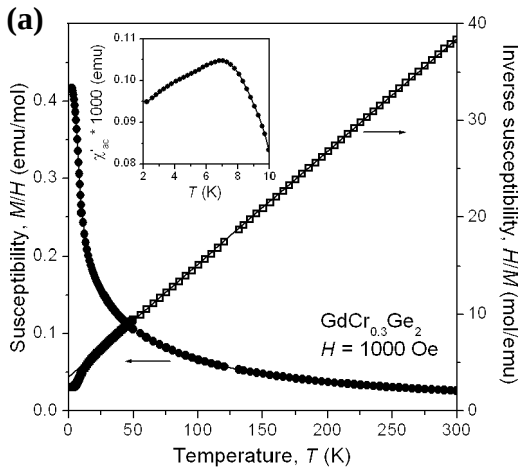
(a)
Susceptibility, M/H (emu/mol)
Inverse susceptibility, H/M (mol/emu)
Temperature, T (K)
GdCr0.3Ge2
H = 1000 Oe
χ'ac + 1000 (emu)
T (K)

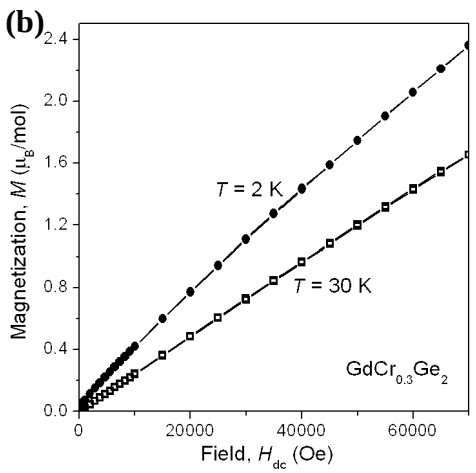
(b)
Magnetization, M (μB/mol)
Field, Hdc (Oe)
T = 2 K
T = 30 K
GdCr0.3Ge2

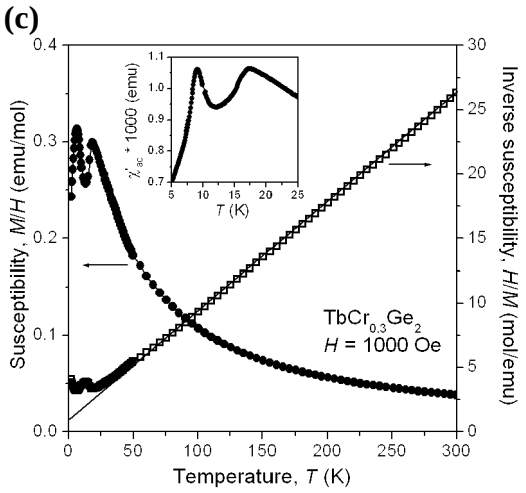
(c)
Susceptibility, M/H (emu/mol)
Inverse susceptibility, H/M (mol/emu)
Temperature, T (K)
TbCr0.3Ge2
H = 1000 Oe
χ'ac + 1000 (emu)
T (K)

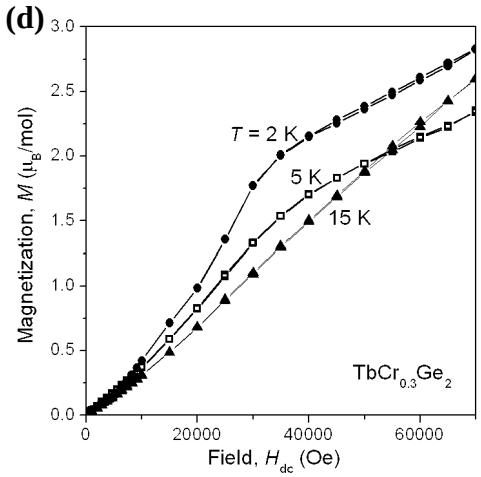
(d)
Magnetization, M (μB/mol)
Field, Hdc (Oe)
T = 2 K
5 K
15 K
TbCr0.3Ge2

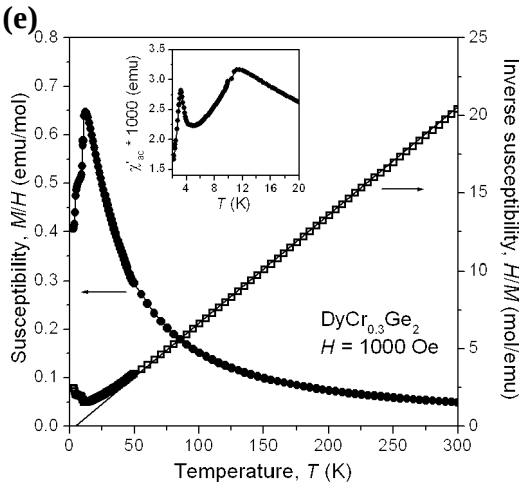
(e)
Susceptibility, M/H (emu/mol)
Inverse susceptibility, H/M (mol/emu)
Temperature, T (K)
DyCr0.3Ge2
H = 1000 Oe
χ'ac + 1000 (emu)
T (K)

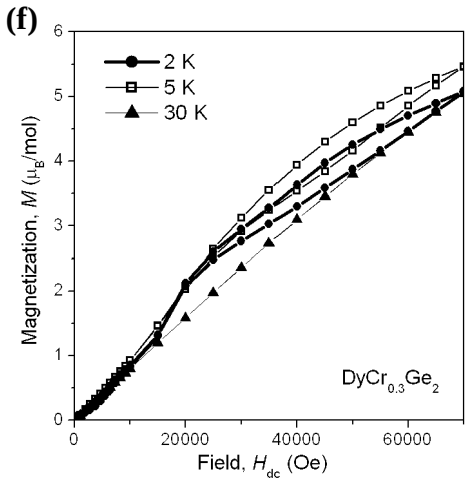
(f)
Magnetization, M (μB/mol)
Field, Hdc (Oe)
2 K
5 K
30 K
DyCr0.3Ge2

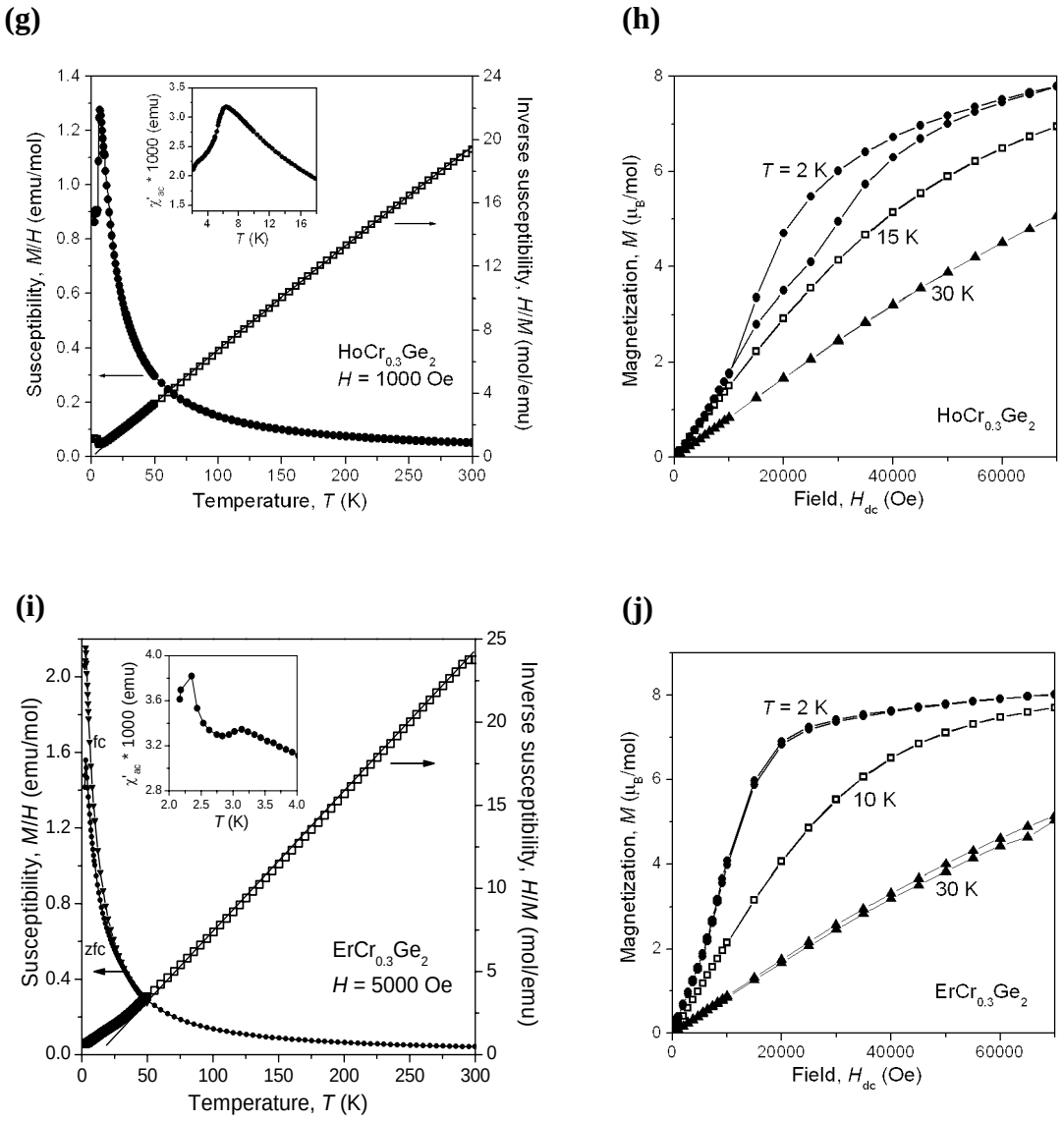

Figure 6–5. Magnetic data for $RECr_{0.3}Ge_2$ (*RE* = Gd–Er). The left panels show the zero-field-cooled dc magnetic susceptibility and its inverse as a function of temperature (with the insets highlighting low-temperature transitions in the ac magnetic susceptibility), and the right panels show isothermal magnetization curves at various temperatures.

Table 6–4. Summary of magnetic data for $RECr_{0.3}Ge_2$ (*RE* = Gd–Er).

	$GdCr_{0.3}Ge_2$	$TbCr_{0.3}Ge_2$	$DyCr_{0.3}Ge_2$	$HoCr_{0.3}Ge_2$	$ErCr_{0.3}Ge_2$
T_N (K) from:					
$d(\chi T)/dT$ vs T plot	10.2	4.3, 16.1	4.0, 9.9	5.5	2.5
χ'_{ac} vs T plot	7.0	9.1, 17.4	3.2, 11.2	6.4	3.1
θ_p (K)	–28.4(2)	–9.9(2)	4.5(2)	–2.3(2)	16.6(3)
$\mu_{eff,\ meas}$ (μ_B/f.u.)	8.26(1)	9.73(1)	10.76(1)	11.08(1)	9.67(1)
$\mu_{eff,\ theor}$ for RE^{3+} (μ_B)	7.94	9.72	10.65	10.61	9.58

transitions at 2.5 K and 19 K when the external magnetic field was applied parallel and perpendicular to the crystallographic *b*-axis, respectively.[7] The transitions were attributed to the Tb atoms experiencing a strong anisotropy between the interslab and intraslab magnetic interactions, as discussed below, and an analogous mechanism is likely operative in the isostructural $TbCr_{0.3}Ge_2$ and $DyCr_{0.3}Ge_2$ compounds here. In the case of the Er sample, a transition is seen at 2 K in the ac susceptibility but not the dc susceptibility curve. At the first glance, this may be attributable to trace amounts of ferrimagnetic $ErCr_6Ge_6$ impurities[23] found in this sample, but the saturation magnetization of 8 μ_B at 2 K is substantial (cf., theoretical value of 9.0 μ_B for Er^{3+}) and there is a divergence in the field-cooled vs. zero-field-cooled curves. This behaviour is similar to that seen in $ErCo_{0.47}Ge_2$ and $ErCu_{0.25}Ge_2$, whose detailed magnetic structures have been determined.[24,25]

In the high-temperature paramagnetic regime, the linear portion of the inverse magnetic susceptibility was fit to the Curie-Weiss law, $\chi = C / (T - \theta_p)$. The Weiss parameters θ_p are small and negative for *RE* = Gd, Tb, and Ho, implying antiferromagnetic coupling, but they are small and positive for *RE* = Dy and Er, implying ferromagnetic coupling. These trends are observed in related REM_xGe_2 compounds.[7,8,24–37] The effective magnetic moments determined from the Curie constants *C* are close to or slightly greater than the theoretical free-ion values for RE^{3+}. Thus, essentially all the magnetism originates from the magnetic moments of *f* electrons localized on the *RE* atoms. The *d* electrons on the Cr ions provide little or no contribution and are delocalized in the conduction states. Therefore, only long-range ordered *RE* atoms contribute to the overall magnetic behaviour of $RECr_xGe_2$ compounds. The isothermal magnetization curves at 2 K, below the Néel temperature, reveal an increasing tendency towards saturation behaviour on proceeding from *RE* = Gd to Er, and suggest the occurrence of metamagnetism in the case of *RE* = Tb, Dy, and Ho. The Dy and Ho samples display a slight hysteresis that is manifested only at intermediate fields (between 20 and 60 kOe) and vanishes as the applied field returns to zero.

Magnetic susceptibilities for different Cr contents (x = 0.25, 0.35, 0.45) in the $DyCr_xGe_2$ series have also been measured (Figure 6–6). Surprisingly, the transition at 12 K is little changed and the lower-temperature transition only tends to become slightly less prominent with greater Cr content. This relatively insensitivity may be attributed to the small change in unit cell parameters (~0.3% in the cell lengths and ~0.8% in cell volume) within the homogeneity range of

$DyCr_xGe_2$ (Figure 6–2). In contrast, a neutron diffraction study of the $TbNi_xGe_2$ (x = 0.6–1.0) series indicated a strong dependence with T_N increasing from 31 to 42 K with greater Ni content.[30]

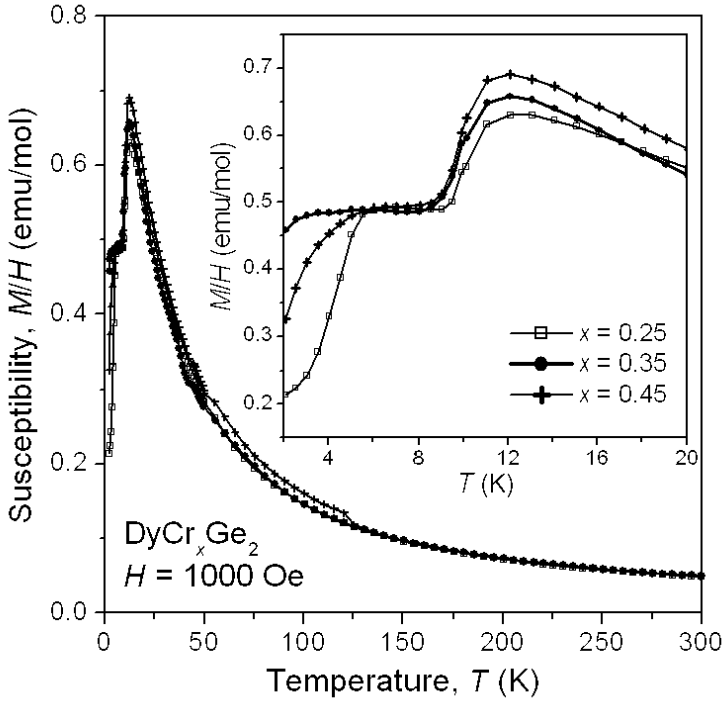

Figure 6–6. Zero-field-cooled dc magnetic susceptibility for several members of $DyCr_xGe_2$ (x = 0.25, 0.35, 0.45). The inset highlights the low-temperature transitions.

These results are generally consistent with the magnetic data previously reported for other REM_xGe_2 (M = Mn, Fe, Co, Ni, Cu) compounds with the $CeNiSi_2$-type structure.[7,8, 24–37] Most of these compounds are antiferromagnetic at similarly low temperatures (notable exceptions are $PrNiGe_2$ and $NdNiGe_2$, which are ferromagnetic) and exhibit effective magnetic moments close to the free-ion

RE^{3+} values (except for the Mn-containing compounds, where local Mn moments are observed).[26] The diverse magnetic behaviour originates from the competition of interactions between the *RE* atoms, which are arranged in double-layer slabs stacked along *b* (Figure 6–7). The *RE*–*RE* distances within these slabs are close to ~4.0 Å, whereas those between the slabs are ~5.6 Å. The *RE* atoms couple indirectly through spin polarization of conduction electrons from Cr atoms (RKKY model). Support for this mechanism in $RECr_xGe_2$ comes from the observation that T_N scales with the de Gennes factor (Figure 6–8). The deviation found for the Gd member is typically seen in other REM_xGe_2 series and normally attributed to contributions from crystalline electric field (CEF) effects. In most REM_xGe_2 compounds, the magnetic moments are coupled ferromagnetically within the slabs (parallel to the *ac* plane) and antiferromagnetically between them (along the *b* direction). Within this highly anisotropic arrangement of *RE* atoms, a variety of complex magnetic structures are possible depending on the relative strengths of these coupling interactions. Although the Cr atoms do not contribute to the total magnetic moment, the delocalized 3*d* electrons play an important role as the intermediary between the 4*f* moment coupling of the *RE* atoms.

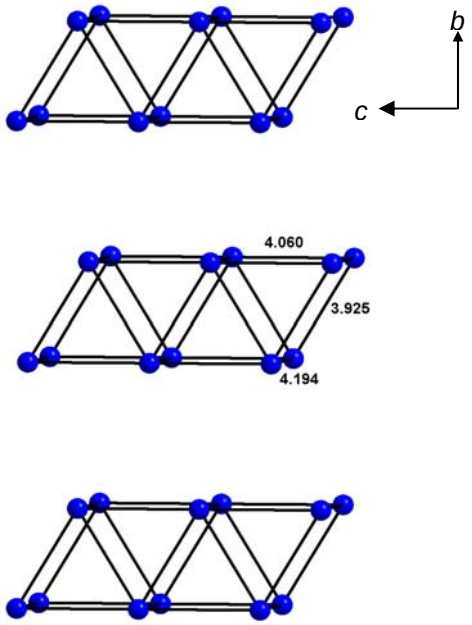

Figure 6–7. The *RE* arrangements in $RECr_xGe_2$.

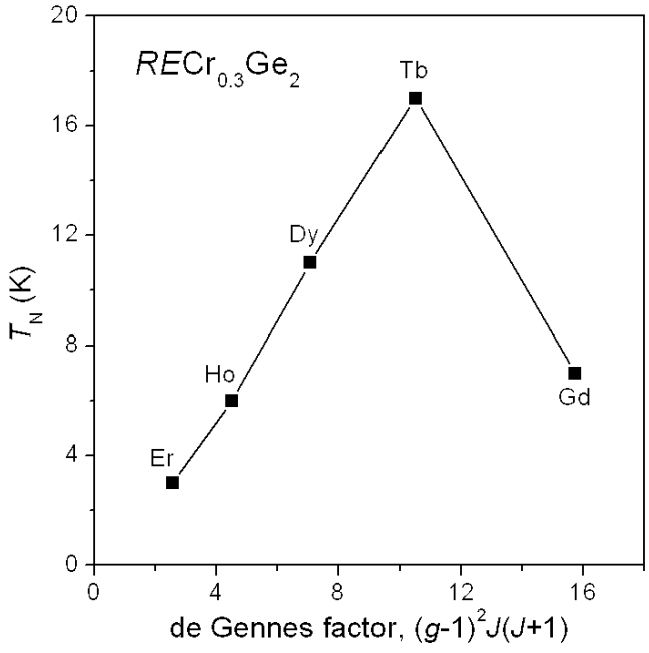

Figure 6–8. Magnetic ordering temperatures for $RECr_{0.3}Ge_2$ plotted vs the de Gennes factor.

6.4. Conclusions

The prevalent REM_xGe_2 phases with the $CeNiSi_2$-type structure have been extended to the earliest transition-metal representative thus far in $RECr_xGe_2$. We have attempted to prepare the corresponding silicides, $RECr_xSi_2$, but to no avail. The Zintl-Klemm formulation $RE^{3+}(Cr^{3+})_{0.33}(Ge^{2-})(Ge^{2-})$ helps rationalize the polygermanide bonding. The magnetic measurements show antiferromagnetic ordering at low T_N for all members from Gd to Er.

In recognition that only the average structure has been determined, as signalled by anomalously short Cr–Ge distances, it will be important to seek evidence for a superstructure through other methods such as electron diffraction. Analyses of the atomic pair distribution function obtained from synchrotron data might be helpful to understand the local structure around the Cr atoms. These compounds undergo antiferromagnetic ordering at low temperatures, with complex magnetic structures that will need to be elucidated in more detail by neutron diffraction studies.

6.5. References

(1) Salamakha, P. S.; Sologub, O. L.; Bodak, O. I. In *Handbook on the Physics and Chemistry of Rare Earths*; Gschneidner, K. A., Jr., Eyring, L., Eds.; Elsevier: Amsterdam, 1999; Vol. 27, pp 1–223.

(2) Salamakha, P. S. In *Handbook on the Physics and Chemistry of Rare Earths*; Gschneidner, K. A., Jr., Eyring, L., Eds.; Elsevier: Amsterdam, 1999; Vol. 27, pp 225–338.

(3) Bie, H.; Zelinska, O. Ya.; Tkachuk, A. V.; Mar, A. *Chem. Mater.* **2007**, *19*, 4613–4620.

(4) Bie, H.; Mar, A. *J. Mater. Chem.* (submitted).

(5) François, M.; Venturini, G.; Malaman, B.; Roques, B. *J. Less-Common Met.* **1990**, *160*, 197–213.

(6) Venturini, G.; François, M.; Malaman, B.; Roques, B. *J. Less-Common Met.* **1990**, *160*, 215–228.

(7) Zhuravleva, M. A.; Bilc, D.; Pcionek, R. J.; Mahanti, S. D.; Kanatzidis, M. G. *Inorg. Chem.* **2005**, *44*, 2177–2188.

(8) Szytuła, A.; Leciejewicz, J. *Handbook of Crystal Structures and Magnetic Properties of Rare Earth Intermetallics*; CRC Press: Boca Raton, 1994.

(9) Sheldrick, G. M. *SHELXTL*, Version 6.12; Bruker AXS Inc.: Madison, WI, 2001.

(10) Zeng, L.; Franzen, H. F. *J. Alloys Compd.* **1998**, *267*, 86–89.

(11) Paccard, L.; Paccard, D.; Allemand, J. *J. Less-Common Met.* **1990**, *161*, 295–298.

(12) Kończyk, J.; Demchenko, P.; Matvijishyn, R.; Pavlyuk, V.; Marciniak, B. *Acta Crystallogr. Sect. E* **2006**, *62*, i4–i6.

(13) Hunter, B. *LHPM-Rietica*, Version 1.7.7, International Union of Crystallography Commission on Powder Diffraction Newsletter, no. 20 (summer), 1998 (www.rietica, org.).

(14) Gelato, L. M.; Parthé, E. *J. Appl. Crystallogr.* **1987**, *20*, 139–143.

(15) Tank, R.; Jepsen, O.; Burkhardt, A.; Andersen, O. K. *TB-LMTO-ASA Program*, version 4.7; Max Planck Institut für Festkörperforschung: Stuttgart, 1998.

(16) Salvador, J. R.; Gour, J. R.; Bilc, D.; Mahanti, S. D.; Kanatzidis, M. G. *Inorg. Chem.* **2004**, *43*, 1403–1410.

(17) Kotur, B. Ya.; Kravs, A. B.; Andrusyak, R. I. *Russ. Metall.* **1988**, *6*, 192–195 (*Transl. Izv. Akad. Nauk SSSR*, *Metally*, **1988**, 198–201).

(18) Venturini, G.; Meot-Meyer, M.; Roques, B. *J. Less-Common Met.* **1985**, *107*, L5–L7.

(19) Israiloff, P.; Völlenkle, H.; Wittmann, A. *Monatsh. Chem.* **1974**, *105*, 1387–1404.

(20) Völlenkle, H.; Preisinger, A.; Nowotny, H.; Wittmann, A. *Z. Kristallogr.* **1967**, *124*, 9–25.

(21) Pauling, L. *The Nature of the Chemical Bond*, 3rd ed.; Cornell University Press: Ithaca, NY, 1960.

(22) Papoian, G. A.; Hoffmann, R. *Angew. Chem. Int. Ed.* **2000**, *39*, 2408–2448.

(23) Schobinger-Papamantellos, P.; Rodríguez-Carvajal, J.; Buschow, K. H. J. *J. Alloys Compd.* **1997**, *256*, 92–96.

(24) Baran, S.; Henkel, F.; Kaczorowski, D.; Hernandez-Velasco, J.; Penc, B.; Stüsser, A.; Szytuła, A.; Wawrzyńska, E. *J. Alloys Compd.* **2006**, *415*, 1–7.

(25) Gil, A.; Kaczorowski, D.; Hernandez-Velasco, J.; Penc, B.; Wawrzyńska, E.; Szytuła, A.; *J. Alloys Compd.* **2004**, *384*, L4–L6.

(26) Gil, A.; Leciejewicz, J.; Małetka, K.; Szytuła, A.; Tomkowicz, Z.; Wojciechowski, K. *J. Magn. Magn. Mater.* **1994**, *129*, L155–L159.

(27) Das, I.; Sampathkumaran, E. V. *Solid State Commun.* **1992**, *83*, 765–770.

(28) Ivanov, V.; Vinokurova, L.; Szytuła, A. *J. Alloys Compd.* **1995**, *218*, L24–L27.

(29) Ivanov, V.; Szytuła, A. *J. Alloys Compd.* **1997**, *252*, L22–L25.

(30) Schobinger-Papamantellos, P.; Buschow, K. H. J.; Ritter, C. *J. Alloys Compd.* **1999**, *287*, 51–56.

(31) Gil, A.; Hofmann, M.; Penc, B.; Szytuła, A. *J. Alloys Compd.* **2001**, *320*, 29–32.

(32) Pikul, A. P.; Kaczorowski, D.; Bukowski, Z.; Plackowski, T.; Gofryk, K. *J. Phys.: Condens. Matter* **2004**, *16*, 6119–6128.

(33) Gil, A.; Penc, B.; Hernandez-Velasco, J.; Wawrzyńska, E.; Szytuła, A. *J. Alloys Compd.* **2005**, *387*, L8–L10.

(34) Baran, S.; Gondek, Ł.; Hernandez-Velasco, J.; Kaczorowski, D.; Szytuła, A. *J. Magn. Magn. Mater.* **2005**, *285*, 188–192.

(35) Gil, A. *Mater. Sci. – Poland* **2006**, *24*, 577–583.

(36) Szytuła, A.; Penc, B.; Kaczorowski, D.; Arulraj, A.; Baran, S.; Stüsser, N.; Tomala, K. *J. Alloys Compd.* **2008**, *460*, 120–124.

(37) Gil, A.; Tubielewicz, K. *Metallofiz. Noveishie Tekhnol.* **2001**, *23*, 153–165.

Chapter 7

Ge Pairs and Sb Ribbons in Rare-Earth Germanium Antimonides $RE_{12}Ge_{7-x}Sb_{21}$ (*RE* = La–Pr)*

7.1. Introduction

Ternary rare-earth antimonides *RE*–*M*–Sb form a fascinating class of inorganic solids valued for their diverse structures and properties.[1] When *M* is a d-block element, these compounds exhibit desirable physical properties for applications as potential thermoelectric (e.g., REM_4Sb_{12})[2] or colossal magnetoresistive materials (e.g., $Eu_{14}MnSb_{11}$).[3] A characteristic feature in the structures of many antimonides is the presence of low-dimensional polyanionic units, such as Sb_4^{4-} squares in REM_4Sb_{12} or Sb_3^{7-} trimers in $Eu_{14}MnSb_{11}$.[4] When *M* is another p-block element (from Group 13 or 14), there is the possibility that anionic substructures may form involving both *M* and Sb atoms.[5] To what extent this occurs depends on the degree of electron transfer from the more electropositive *RE* atoms, and the relative electronegativities of the *M* and Sb atoms. This bonding situation differs from that in traditional Zintl compounds, such as ternary alkali or alkaline-earth metal antimonides, where the Zintl-Klemm electron-counting rule works well to account for the presence of trigonal planar or tetrahedral *M*-centred building blocks and the dominance of heteroatomic *M*–Sb

* *A version of this chapter has been accepted for publication. Haiying Bie, Arthur Mar, 2009. Chemistry—an Asian Journal.*

bonding in their structures.[6] Instead, these ternary rare-earth antimonides (*RE*–*M*–Sb; *M* = Ga, In, Ge, Sn) adopt quite complex structures involving (in addition to *M*–Sb bonding) extensive homoatomic *M*–*M* and Sb–Sb bonding,[5] as exemplified by $La_{13}Ga_8Sb_{21}$,[7] $RE_{12}Ga_4Sb_{23}$,[7] $REGaSb_2$,[8] $REIn_{1-x}Sb_2$,[9] $RE_6Ge_{5-x}Sb_{11+x}$,[10] and $RESn_{1-x}Sb_2$.[11] It is not straightforward to analyze the bonding, but a retrotheoretical approach has been helpful in highlighting the fragments, which may include non-classical units such as Sb ribbons or square sheets.[12]

The *RE*–Ge–Sb system presents an interesting example where the similar electronegativities and sizes of the two anionic components[13] give rise to a competition between Ge–Sb, Ge–Ge, and Sb–Sb bonding. Thus, in the Sb-rich phase $RE_6Ge_{5-x}Sb_{11+x}$, some of the anion sites exhibit partial disorder of Ge and Sb atoms.[10a] Understanding site preferences among the heavy p-block elements is part of a broader challenge (the "colouring problem") in crystal chemistry,[14] as seen in a related example of the study of $REGe_{1-x}Sn_{1+x}$.[15] In other cases, a metal-rich composition may lead to the absence of polyanionic bonding (La_5Ge_3Sb, $RE_5Ge_2Sb_2$)[16,17] or to apparent conformity with the Zintl-Klemm concept ($Yb_8Ge_3Sb_5$).[18] The only phase diagram investigations have been on the Ce–Ge–Sb system,[19] which confirm the existence of the $RE_6Ge_{5-x}Sb_{11+x}$-type phase.

In this chapter, we report the new series of phases $RE_{12}Ge_{7-x}Sb_{21}$ (*RE* = La–Pr) exhibiting a remarkable variety of anionic Ge and Sb substructures, which expands on known antimonides substructures. Magnetic data have also been measured for the La and Ce members of this series.

7.2. Experimental Section

7.2.1. Synthesis

Starting materials were *RE* pieces (Hefa), Ge pieces (Alfa) or powder (Cerac), and Sb pieces (Alfa-Aesar) or powder (Cerac), each with 99.9% purity or better. Products were characterized by powder X-ray diffraction and EDX analysis. In the course of investigating the La–Ge–Sb phase diagram, a new ternary phase was identified from EDX analysis on several polished arc-melted samples with an approximate composition of 30% La, 16% Ge, and 54% Sb. (Another new series of compounds $RE_5Ge_xSb_{3-x}$ was found and will be discussed in Chapter 8). Powder XRD confirmed that this phase was not the same as the previously known phase $La_6Ge_{2.8}Sb_{13.2}$ (or $La_6Ge_{5-x}Sb_{11+x}$ with $x = 2.2$).[10a] Single crystals were initially grown from reaction of the elements in a ratio (La:Ge:Sb = 35:20:45) judiciously chosen to avoid the formation of $La_6Ge_{2.8}Sb_{13.2}$. The mixture of the elements was placed in an inner alumina crucible jacketed by an outer fused-silica tube, which was then evacuated and sealed. The tube was heated at 650 °C over 1 day and then to 1050 °C for 1 day, kept at that temperature for 2 days, cooled to 800 °C over 4 days, kept at that temperature for 12 days, and then slowly cooled to 20 °C over 8 days. Powder XRD revealed that the product consisted of $La_{12}Ge_{7-x}Sb_{21}$ (with a diffraction pattern that matched well with the theoretical pattern subsequently determined from the single-crystal structure), LaSb, Ge, and importantly, none of the $La_6Ge_{5-x}Sb_{11+x}$ phase. Crystals of the ternary phase were shown to contain all three elements in a ratio (32% La,

18% Ge, 50% Sb) close to the formula refined from the structure determination (30% La, 17% Ge, 53% Sb), well within the usual uncertainties of EDX analysis.

Attempts were made to substitute other *RE* metals (*RE* = Ce–Nd, Sm, Gd–Er) in arc-melting reactions. For *RE* = Ce and Pr, the desired isostructural ternary phases were obtained, as verified by powder XRD analysis. For *RE* = Nd, Sm, and Gd–Tb, the products consisted of $RE_6Ge_{5-x}Sb_{11+x}$, *RE*Sb, and Ge. For *RE* = Dy–Er, the products consisted of binary and elemental phases.

Samples for magnetic measurements were prepared through arc-melting reactions of the elements in the ratio *RE*:Ge:Sb = 30:16:54, followed by annealing at 800 °C for 20 days. However, phase-pure samples only for the La and Ce containing members were obtained, and the Pr sample contained a mixture of $Pr_6Ge_{5-x}Sb_{11+x}$ and $Pr_{12}Ge_{7-x}Sb_{21}$.

7.2.2. Structure Determination

Single-crystal X-ray diffraction data for $RE_{12}Ge_{7-x}Sb_{21}$ (*RE* = La–Pr) were collected on a Bruker Platform / SMART 1000 CCD diffractometer at 22 °C using ω scans. Structure solution and refinement were carried out with use of the SHELXTL (version 6.12) program package.[20] Face-indexed numerical absorption corrections were applied. The treatment of the Pr member is discussed here as a representative example. The centrosymmetric space group *Immm* was initially chosen on the basis of intensity statistics, and starting positions for all atoms were found by direct methods. If all sites are fully occupied, the formula corresponds to "$Pr_{12}Ge_{10}Sb_{21}$". However, a refinement based on this model revealed

unreasonably large displacement parameters for Ge1 and Ge3. Moreover, unphysical Ge1–Ge1 and Ge3–Ge3 distances of ~0.5 and ~0.7 Å, respectively, result from the proximity of symmetry-equivalent sites related by a mirror plane normal to *a* or *b*, implying that the Ge1 or Ge3 site must be limited to a maximum occupancy of 0.50. Similar pathologies have been previously observed in $La_6Ge_{5-x}Sb_{11+x}$ [10a] and $Pr_{12}Ga_4Sb_{23}$.[7a] When refined, the occupancies of these sites converged to 0.365(2) for Ge1 and 0.504(4) for Ge3, and the displacement parameters were reduced to more reasonable values, although the ellipsoid for Ge1 was still somewhat elongated along *a*. In subsequent refinements, the occupancy for Ge1 was allowed to refine freely, whereas that for Ge3 was fixed at 0.50. Other models were also evaluated in which individual anion sites (e.g., Ge2 or Sb6) were allowed to contain a mixture of Ge and Sb atoms, but no disorder was implicated from the refinements. The final refinements for the three structures led to formulas of $La_{12}Ge_{6.66(1)}Sb_{21}$, $Ce_{12}Ge_{6.53(1)}Sb_{21}$, $Pr_{12}Ge_{6.46(1)}Sb_{21}$, in good agreement with the chemical compositions determined experimentally.

Attempts were made to refine the structures in lower symmetry space groups (*Imm*2, *I*222) in which one or more mirror planes are removed to resolve the disorder problem with the Ge1 and Ge3 sites. In the case of the Pr member, we were able to successfully refine an ordered model in *Im*2*m* in which the mirror plane normal to the 15 Å axis was removed. In this model, the unphysical Ge1–Ge1 or Ge3–Ge3 distances disappear. The Flack parameter of 0.51(3) indicates essentially equal twin components in which $GeSb_5$ square pyramids centred by the Ge3 atoms are oriented in opposite directions along this axis. However, the

Ge1 site remains partially occupied (0.738(5)) and its displacement ellipsoid is severely elongated normal to the $GeSb_3$ trigonal planar units, implying a slight puckering of these planes whose disorder is still unresolved within this space group. In the deposited crystal data, the structure is reported in its standard setting of *Imm*2, and with standardized atom labels and coordinates (Tables A2–1 and A2–2 in Appendix 2). In general, successful refinement of related antimonide structures in *Imm*2 has been restricted to a few cases (e.g. RE_6MSb_{15}),[21] whereas the majority have been reported in *Immm*. A recent refinement of $Ce_{12}Ge_{9-x}Sb_{23+x}$ (superstructure of $Ce_6Ge_{5-x}Sb_{11+x}$) required detection of very weak superstructure reflections and transformation to a larger orthorhombic cell.[19b] Attempts were made to search for superstructure in $RE_{12}Ge_{7-x}Sb_{21}$, but careful inspection of the frames revealed no obvious weak reflections.

Atomic positions were standardized with the program STRUCTURE TIDY.[22] In view of the disorder problem described above, we have opted to report the results as refined in *Immm*, with the understanding that these represent average structures. Crystal data and further details of the data collections are given in Table 7–1. Final values of the positional and displacement parameters are given in Table 7–2. Selected interatomic distances are listed in Table 7–3.

Table 7–1. Crystallographic data for $RE_{12}Ge_{7-x}Sb_{21}$ (*RE* = La–Pr).

Formula	$La_{12}Ge_{6.66(1)}Sb_{21}$	$Ce_{12}Ge_{6.53(1)}Sb_{21}$	$Pr_{12}Ge_{6.46(1)}Sb_{21}$
Formula mass (amu)	4707.12	4712.20	4716.60
Space group	*Immm* (No. 71)	*Immm* (No. 71)	*Immm* (No. 71)
a (Å)	4.3165(4)	4.2825(5)	4.2578(2)
b (Å)	15.2050(12)	15.0687(17)	14.9777(7)
c (Å)	34.443(3)	34.146(4)	33.938(2)
V (Å^3)	2260.6(3)	2203.5(4)	2164.3(2)
Z	2	2	2
ρ_{calcd} (g cm^{-3})	6.915	7.102	7.238
Crystal dimensions (mm)	0.35 × 0.09 × 0.04	0.14 × 0.01 × 0.01	0.28 × 0.10 × 0.04
μ(Mo Kα) (mm^{-1})	27.69	29.08	30.45
Transmission factors	0.034–0.351	0.197–0.704	0.036–0.325
2θ limits	4.44–66.22°	4.48–66.28°	4.52–66.32°
Data collected	$-6 \le h \le 6$,	$-6 \le h \le 6$,	$-6 \le h \le 6$,
	$-23 \le k \le 23$,	$-23 \le k \le 23$,	$-22 \le k \le 23$,
	$-52 \le l \le 51$	$-51 \le l \le 52$	$-50 \le l \le 51$
No. of data collected	15456	15365	15015
No. of unique data, including $F_o^2 < 0$	2486 (R_{int} = 0.041)	2441 (R_{int} = 0.096)	2397 (R_{int} = 0.040)
No. of unique data, with $F_o^2 > 2\sigma(F_o^2)$	2177	1559	2125
No. of variables	76	76	76
$R(F)$ for $F_o^2 > 2\sigma(F_o^2)$ [a]	0.032	0.038	0.025
$R_w(F_o^2)$ [b]	0.076	0.058	0.057
Goodness of fit	1.113	1.049	1.118
$(\Delta\rho)_{max}$, $(\Delta\rho)_{min}$ (e Å^{-3})	5.57, –3.48	3.63, –3.14	2.22, –1.71

[a] $R(F) = \sum \| F_o | - | F_c \| / \sum | F_o |$.

[b] $R_w(F_o^2) = \left[\sum \left[w(F_o^2 - F_c^2)^2 \right] / \sum w F_o^4 \right]^{1/2}$; $w^{-1} = \left[\sigma^2(F_o^2) + (Ap)^2 + Bp \right]$ where $p = \left[\max(F_o^2, 0) + 2F_c^2 \right] / 3$.

Table 7–2. Atomic coordinates and equivalent isotropic displacement parameters (Å^2) for $RE_{12}Ge_{7-x}Sb_{21}$ (*RE* = La–Pr).

Atom	Wyckoff position	Occupancy	*x*	*y*	*z*	U_{eq} [a]
$La_{12}Ge_{6.66(2)}Sb_{21}$						
La1	8*l*	1	0	0.21166(3)	0.42672(1)	0.0099(1)
La2	8*l*	1	0	0.35561(3)	0.31650(1)	0.0091(1)
La3	4*j*	1	½	0	0.07331(2)	0.0094(1)
La4	4*j*	1	½	0	0.29444(2)	0.0086(1)
Ge1	8*m*	0.414(4)	0.0686(5)	0	0.14702(5)	0.0169(8)
Ge2	8*l*	1	0	0.41657(5)	0.11426(2)	0.0124(2)
Ge3	4*g*	0.5	0	0.4791(2)	0	0.044(1)
Sb1	8*l*	1	0	0.13669(3)	0.33670(1)	0.0099(1)
Sb2	8*l*	1	0	0.14856(3)	0.10920(1)	0.0108(1)
Sb3	8*l*	1	0	0.28447(3)	0.22469(1)	0.0097(1)
Sb4	4*i*	1	0	0	0.22283(2)	0.0106(1)
Sb5	4*i*	1	0	0	0.44394(3)	0.0286(2)
Sb6	4*h*	1	0	0.35343(5)	½	0.0204(2)
Sb7	4*g*	1	0	0.29553(5)	0	0.0142(1)
Sb8	2*a*	1	0	0	0	0.0104(2)
$Ce_{12}Ge_{6.53(1)}Sb_{21}$						
Ce1	8*l*	1	0	0.21264(4)	0.42672(2)	0.0091(1)
Ce2	8*l*	1	0	0.35665(4)	0.31641(2)	0.0079(1)
Ce3	4*j*	1	½	0	0.07369(2)	0.0085(2)
Ce4	4*j*	1	½	0	0.29460(2)	0.0075(2)
Ge1	8*m*	0.382(3)	0.0634(9)	0	0.14728(8)	0.016(1)
Ge2	8*l*	1	0	0.41567(7)	0.11373(3)	0.0090(2)
Ge3	4*g*	0.5	0	0.4812(2)	0	0.015(1)
Sb1	8*l*	1	0	0.13763(4)	0.33647(2)	0.0087(1)
Sb2	8*l*	1	0	0.14911(5)	0.10927(2)	0.0104(1)
Sb3	8*l*	1	0	0.28455(4)	0.22438(2)	0.0086(1)
Sb4	4*i*	1	0	0	0.22352(3)	0.0100(2)
Sb5	4*i*	1	0	0	0.44438(3)	0.0185(2)
Sb6	4*h*	1	0	0.35313(7)	½	0.0194(2)
Sb7	4*g*	1	0	0.29755(6)	0	0.0122(2)
Sb8	2*a*	1	0	0	0	0.0093(3)
$Pr_{12}Ge_{6.46(1)}Sb_{21}$						
Pr1	8*l*	1	0	0.21265(2)	0.42656(1)	0.00935(7)
Pr2	8*l*	1	0	0.35685(2)	0.31639(1)	0.00856(6)
Pr3	4*j*	1	½	0	0.07392(1)	0.00903(8)
Pr4	4*j*	1	½	0	0.29485(1)	0.00816(8)
Ge1	8*m*	0.365(2)	0.0621(4)	0	0.14736(4)	0.0159(7)
Ge2	8*l*	1	0	0.41576(4)	0.11335(2)	0.0106(1)
Ge3	4*g*	0.5	0	0.4781(1)	0	0.0201(4)
Sb1	8*l*	1	0	0.13732(2)	0.33681(1)	0.00881(7)
Sb2	8*l*	1	0	0.14924(2)	0.10923(1)	0.01108(8)
Sb3	8*l*	1	0	0.28461(2)	0.22421(1)	0.00888(7)
Sb4	4*i*	1	0	0	0.22383(1)	0.01067(9)
Sb5	4*i*	1	0	0	0.44505(2)	0.0151(1)
Sb6	4*h*	1	0	0.35258(3)	½	0.0204(1)
Sb7	4*g*	1	0	0.29836(4)	0	0.0123(1)
Sb8	2*a*	1	0	0	0	0.0099(1)

[a] U_{eq} is defined as one-third of the trace of the orthogonalized U_{ij} tensor.

Table 7–3. Selected interatomic distances (Å) in $RE_{12}Ge_{7-x}Sb_{21}$ (*RE* = La–Pr).

	$La_{12}Ge_{6.66(2)}Sb_{21}$	$Ce_{12}Ge_{6.53(2)}Sb_{21}$	$Pr_{12}Ge_{6.46(1)}Sb_{21}$
*RE*1–Ge2 (×2)	3.2330(7)	3.1987(9)	3.1727(5)
*RE*1–Sb2 (×2)	3.2720(5)	3.2304(7)	3.2073(3)
*RE*1–Sb5	3.2726(5)	3.2604(7)	3.2462(3)
*RE*1–Sb1	3.3033(7)	3.2826(9)	3.2482(4)
*RE*1–Sb6	3.3192(7)	3.2775(9)	3.2563(4)
*RE*1–Sb7 (×2)	3.3227(4)	3.2968(5)	3.2819(2)
*RE*2–Ge1 (×2)	3.141(2)	3.114(3)	3.096(1)
*RE*2–Sb2 (×2)	3.3483(5)	3.3218(7)	3.3033(4)
*RE*2–Sb3 (×2)	3.3476(5)	3.3245(7)	3.3044(3)
*RE*2–Sb3	3.3419(7)	3.3247(9)	3.3103(5)
*RE*2–Sb4 (×2)	3.3634(4)	3.3331(6)	3.3155(3)
*RE*2–Sb1	3.4007(7)	3.3707(9)	3.3602(4)
*RE*3–Ge1 (×2)	3.149(2)	3.132(3)	3.113(2)
*RE*3–Sb8 (×2)	3.3218(5)	3.3039(7)	3.2902(3)
*RE*3–Sb2 (×4)	3.3599(5)	3.3330(7)	3.3114(3)
*RE*3–Sb6 (×2)	3.3678(7)	3.3509(9)	3.3419(5)
*RE*4–Sb4 (×2)	3.2775(7)	3.2366(9)	3.2159(5)
*RE*4–Sb1 (×4)	3.3311(5)	3.3060(6)	3.2849(3)
*RE*4–Sb3 (×2)	3.3428(5)	3.3107(8)	3.2902(4)
*RE*4–Ge2 (×2)	3.391(1)	3.378(1)	3.3612(7)
Ge1–Sb2 (×2)	2.624(1)	2.609(2)	2.5964(8)
Ge1–Sb4	2.628(2)	2.617(3)	2.609(2)
Ge2–Ge2	2.537(2)	2.541(2)	2.524(1)
Ge2–Sb1 (×2)	2.8576(7)	2.8498(9)	2.8328(4)
Ge2–Sb5 (×2)	3.207(1)	3.184(1)	3.171(1)
Ge3–Sb7	2.792(4)	2.768(4)	2.692(2)
Ge3–Sb5 (×4)	2.9132(8)	2.8762(8)	2.8493(4)
Sb1–Sb3 (×2)	3.2506(5)	3.2058(7)	3.1918(4)
Sb3–Sb3 (×2)	2.9659(7)	2.9546(9)	2.9449(5)
Sb6–Sb7 (×2)	3.1287(8)	3.121(1)	3.1054(5)
Sb6–Sb8 (×2)	3.1023(6)	3.0794(8)	3.0671(4)

7.2.3. Band Structure Calculation

Tight-binding linear muffin tin orbital (TB-LMTO) band structure calculations were performed within the local density and atomic spheres approximations using the Stuttgart TB-LMTO program.[23] An ordered model of "$La_{12}Ge_7Sb_{21}$" in *Imm*2 with no partial occupancies was examined. The basis set consisted of La 6s/6p/5d/4f, Ge 4s/4p/4d, and Sb 5s/5p/5d/4f orbitals, with the La 6p, Ge 4d, and Sb 5d/4f orbitals being downfolded. Integrations in reciprocal space were carried out with an improved tetrahedron method over 153 irreducible *k* points.

7.2.4. Magnetic Measurements

Measurements of dc magnetic susceptibility were made on powders of $RE_{12}Ge_{7-x}Sb_{21}$ (*RE* = La, Ce), for which phase-pure samples could be prepared, between 2 and 300 K on a Quantum Design 9T–PPMS dc magnetometer / ac susceptometer. The susceptibility was corrected for contributions from the holder and underlying sample diamagnetism.

7.3. Results and Discussion

7.3.1. Phase Composition

Information about phase relationships in the *RE*–Ge–Sb, or indeed in any of the *RE*–*M*–Sb (*M* = Group 13 or 14) systems, is sparse. Isothermal sections have been constructed only for the Ce–Ge–Sb system.[19] At 400 °C, the phases Ce_2GeSb_3, $Ce_5Ge_3Sb_2$, and Ce_3GeSb have been implicated, although some of

these may be doubtful.[19a] At 600 °C, the phase previously identified as $Ce_6Ge_{5-x}Sb_{11+x}$,[10a] but reformulated as $Ce_{12}Ge_{9-x}Sb_{23+x}$ in its superstructure form, has been confirmed; this phase was indicated to be stable between 400 and 800 °C.[19b] The new series $RE_{12}Ge_{7-x}Sb_{21}$ represents only the second Sb-rich phase found in any of the *RE*–Ge–Sb systems. As ascertained by various synthetic attempts, the extent of *RE* substitution in $RE_{12}Ge_{7-x}Sb_{21}$ (*RE* = La–Pr) appears to be considerably less than in $RE_6Ge_{5-x}Sb_{11+x}$ (*RE* = La–Nd, Sm, Gd–Dy). These ternary compounds were prepared through prolonged annealing at 800 °C, suggesting that they are stable at higher temperatures than compounds in the above phase diagram studies. From the crystallographic studies and EDX measurements, a Ge substoichiometry with $x = 0.4–0.5$ has been established for the single crystals examined. Although we have not attempted to determine the full range of nonstoichiometry, the formulation $RE_{12}Ge_{6.5–6.6}Sb_{21}$ likely represents the maximum Ge content, given that the syntheses of these crystals were performed with an excess of Ge relative to this composition.

7.3.2. Structure and Bonding

The structures of $RE_{12}Ge_{7-x}Sb_{21}$ (*RE* = La–Pr) have been determined by single-crystal X-ray diffraction in the orthorhombic space group *Immm* (Table 7–1). Unlike $RE_6Ge_{5-x}Sb_{11+x}$, there is no disorder between Ge and Sb atoms, although two of the Ge sites are partially occupied (Table 7–2). Bond distances (Table 7–3) are quoted in a general way for the entire series (*RE* = La–Pr) in the

discussion below, whereas more precise values are indicated for the Pr member in the figures.

$RE_{12}Ge_{7-x}Sb_{21}$ (*RE* = La–Pr) adopts a complex structure exhibiting a rich variety of bonding motifs. Although bonding extends in all three dimensions, the structure can be portrayed in a manner to highlight the polyanionic network built up of Ge and Sb atoms (Figure 7–1). This network defines large triangular channels extending along the *a* direction within which lie columnar assemblies of RE_6 trigonal prisms that are centred by additional Ge and Sb atoms. Among several ways to decompose the polyanionic network, a description in terms of ribbons or strips (Figure 7–2) is helpful in revealing structural relationships to other antimonides, as discussed later. The large triangular channels are outlined by two Ge/Sb ribbons (Sb5–Ge2–Sb1–Sb3–Sb3–Sb1–Ge2–Sb5) parallel to (011) and $(01\bar{1})$, and a five-atom-wide Sb ribbon bordered by Ge atoms (Ge3–Sb7–Sb6–Sb8–Sb6–Sb7–Ge3) parallel to (001). Alternatively, the diagonally oriented Ge/Sb ribbons, condensed together, may be considered to form a 2D kinked sheet derived from an infinite square net but folded at every seventh atom (at Sb5). The four-connected Sb atoms within these ribbons with the Sb–Sb distances (2.9–3.2 Å, longer than a typical Sb–Sb single bond length of ~ 2.7–2.8 Å) are indicative of the hypervalent bonding encountered in many solid-state polyantimonides.[12]

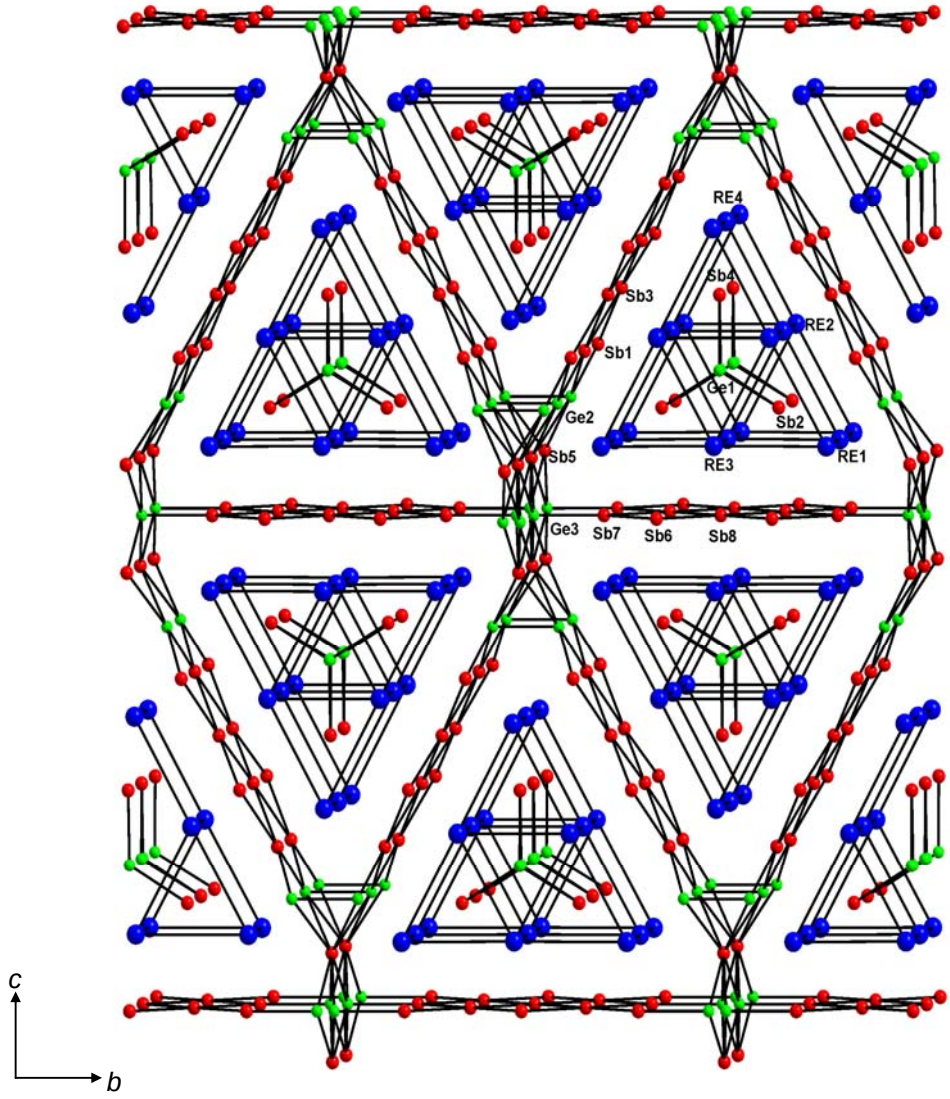

Figure 7–1. Structure of $RE_{12}Ge_{7-x}Sb_{21}$ (*RE* = La–Pr) viewed down the *a* direction. The blue spheres are *RE* atoms, the green spheres are Ge atoms, and the red spheres are Sb atoms. The solid lines between *RE* atoms outline the RE_6 trigonal prisms. The Ge3 site is only half-occupied.

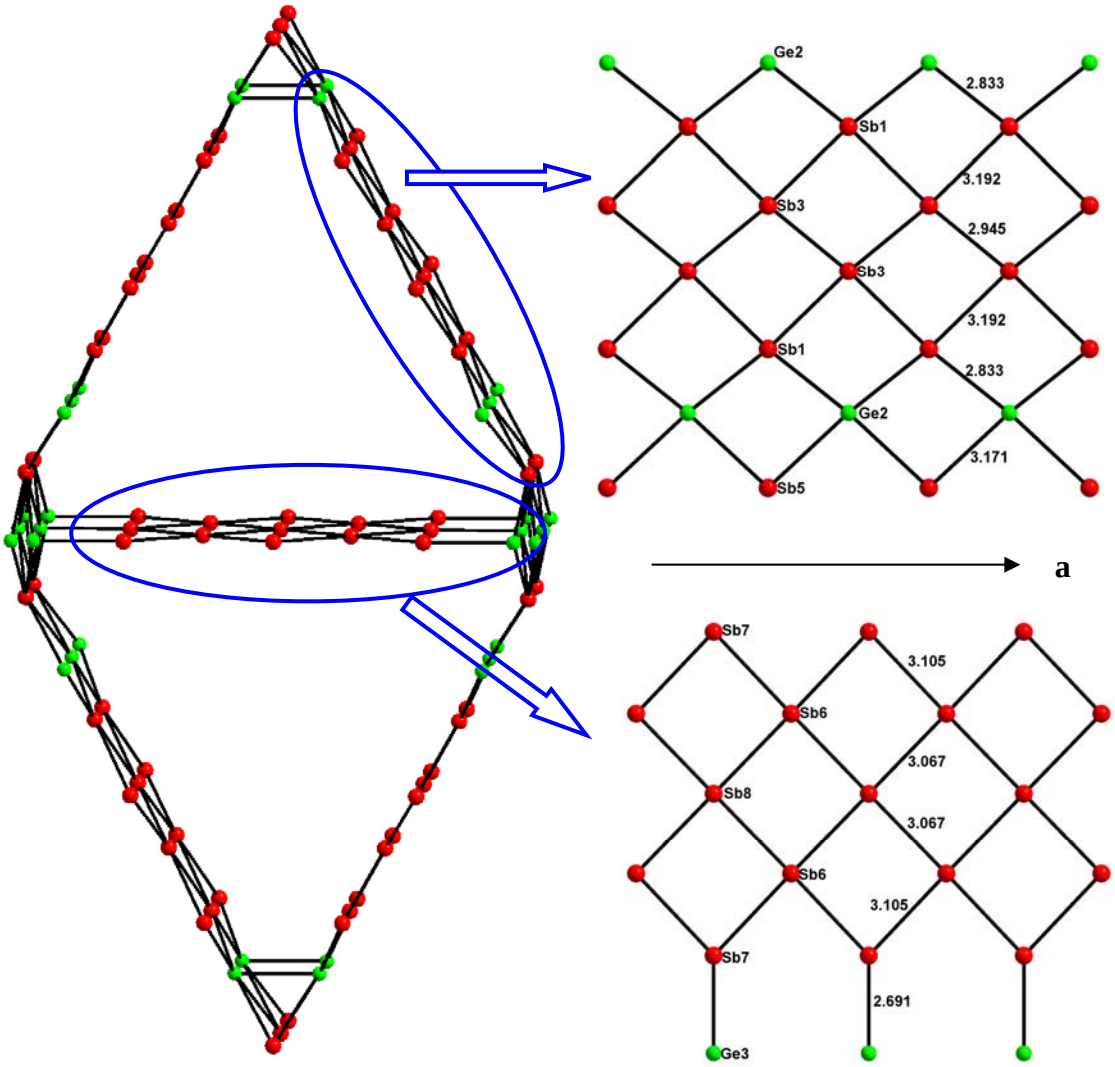

Figure 7–2. Deconstruction of the polyanionic network in $RE_{12}Ge_{7-x}Sb_{21}$ (*RE* = La–Pr) built up of ribbons containing Ge and Sb atoms extending along the *a* direction. The interatomic distances shown (in Å) here are for $Pr_{12}Ge_{6.5}Sb_{21}$.

Because Ge is another p-block element that can realize square nets, it is not obvious whether its introduction will lead to disorder with the Sb atoms or to heteroatomic bonding motifs. The Ge atoms occur in three different environments (Figure 7–3). The Ge1 atom is centred within a trigonal planar $GeSb_3$ unit embedded within the assemblies of RE_6 trigonal prisms. Analogous trigonal planar $GaSb_3$ units are found in classical Zintl phases (in combination with alkali and alkaline-earth metals)[6] such as Cs_6GaSb_3,[24] as well as in the rare-earth-containing phases $RE_{12}Ga_4Sb_{23}$, and $La_{13}Ga_8Sb_{21}$.[7] However, a Ge-centred analogue is apparently the first of its kind. The Ge1–Sb distances (2.60–2.63 Å) are quite short and consistent with single bonds. As implied by its *x* coordinate of ~0.06, the Ge atom is displaced from the plane by nearly 0.3 Å, indicating a slight puckering of these $GeSb_3$ units. The partial occupancy of these Ge1 sites accounts for the substoichiometry in $RE_{12}Ge_{7-x}Sb_{21}$. On proceeding from the La to the Pr member, the ensuing contraction of the surrounding RE_6 trigonal prisms leads to progressively shorter Ge1–Sb distances (down to 2.60 Å), which may account for the gradual decrease in the Ge1 occupancy and the relatively limited range of *RE* substitution in this series. The Ge2 atom is located just before the folding points in the 2D Ge/Sb kinked sheets. The full occupation of this site by Ge atoms contrasts with the disordering of Ge and Sb atoms within a similar site in $RE_6Ge_{5-x}Sb_{11+x}$, where similar kinked sheets are found.[10a] Two Ge2 atoms are brought into proximity at a distance of 2.52–2.54 Å, comparable to that in the covalently bonded Ge_2 dimers in Gd_2MgGe_2 (2.525(3) Å)[25] but slightly shorter than those in the Ge/Sb dimers in $RE_6Ge_{5-x}Sb_{11+x}$ (2.547(2)–2.615(2) Å).[10a]

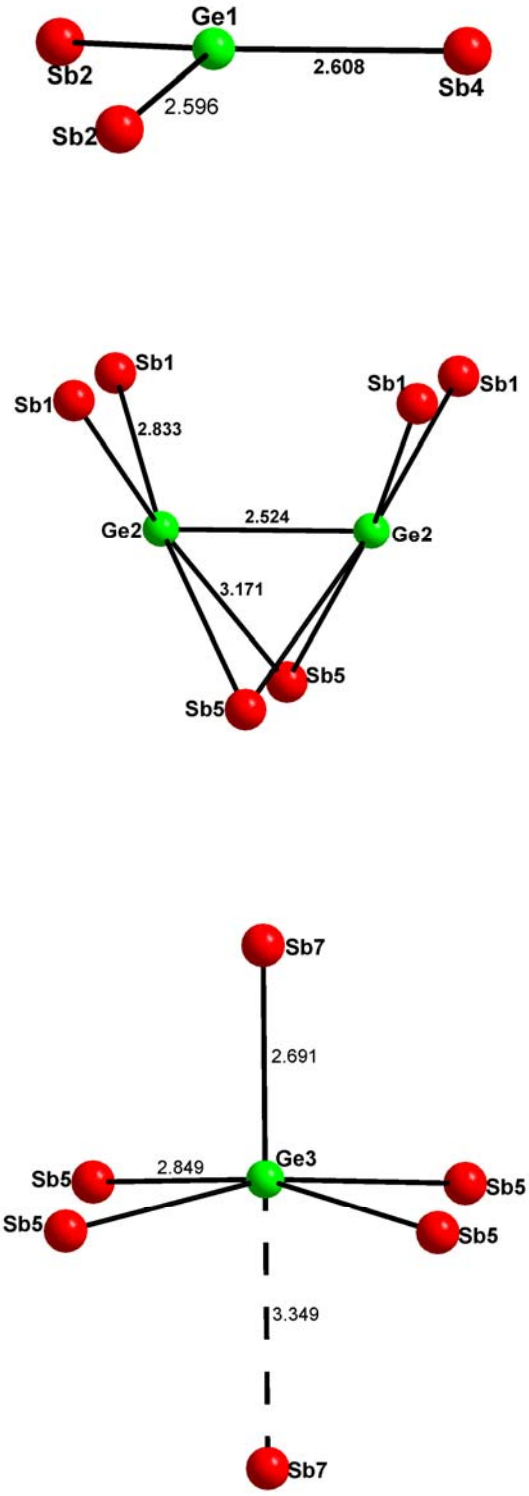

Figure 7–3. Coordination environments around the Ge atoms in $RE_{12}Ge_{7-x}Sb_{21}$ (*RE* = La–Pr).

Whether this short distance is an incidental result of the kinking or whether it results from a strong bonding interaction is a question to be resolved later through analysis of the band structure. The Ge3 atom, at first glance, appears to be located within a distorted octahedron, but the presence of a symmetry-equivalent Ge3 site related by a mirror plane normal to *b* limits the occupancy of these sites to 0.50. The Ge3 atoms are strongly displaced closer towards one than the other of the Sb7 atoms, so that the coordination geometry is perhaps more appropriately described as a square pyramid, with the distance to the apical Sb atom (2.69–2.79 Å) being shorter than to the four basal Sb atoms (2.85–2.91 Å). Although rare, square-pyramidal coordination of Ge is found in Ge_5F_{12}, for example.[26]

The *RE* atoms, portrayed earlier as vertices of the trigonal prisms forming large columnar assemblies, are actually surrounded by Ge and Sb atoms in environments with typically high CN of 9 or 10. Common to the structures of other *RE*–*M*–Sb (*M* = Ga, In, Ge, Sn) phases,[5] the coordination environments for all four *RE* sites are based on a square antiprism that may be monocapped or bicapped (Figure 7–4). The distances are generally shorter to the Ge atoms (3.1–3.2 Å) than to the Sb atoms (3.2–3.4 Å), with the exception being the *RE*4–Ge2 distances (3.4 Å).

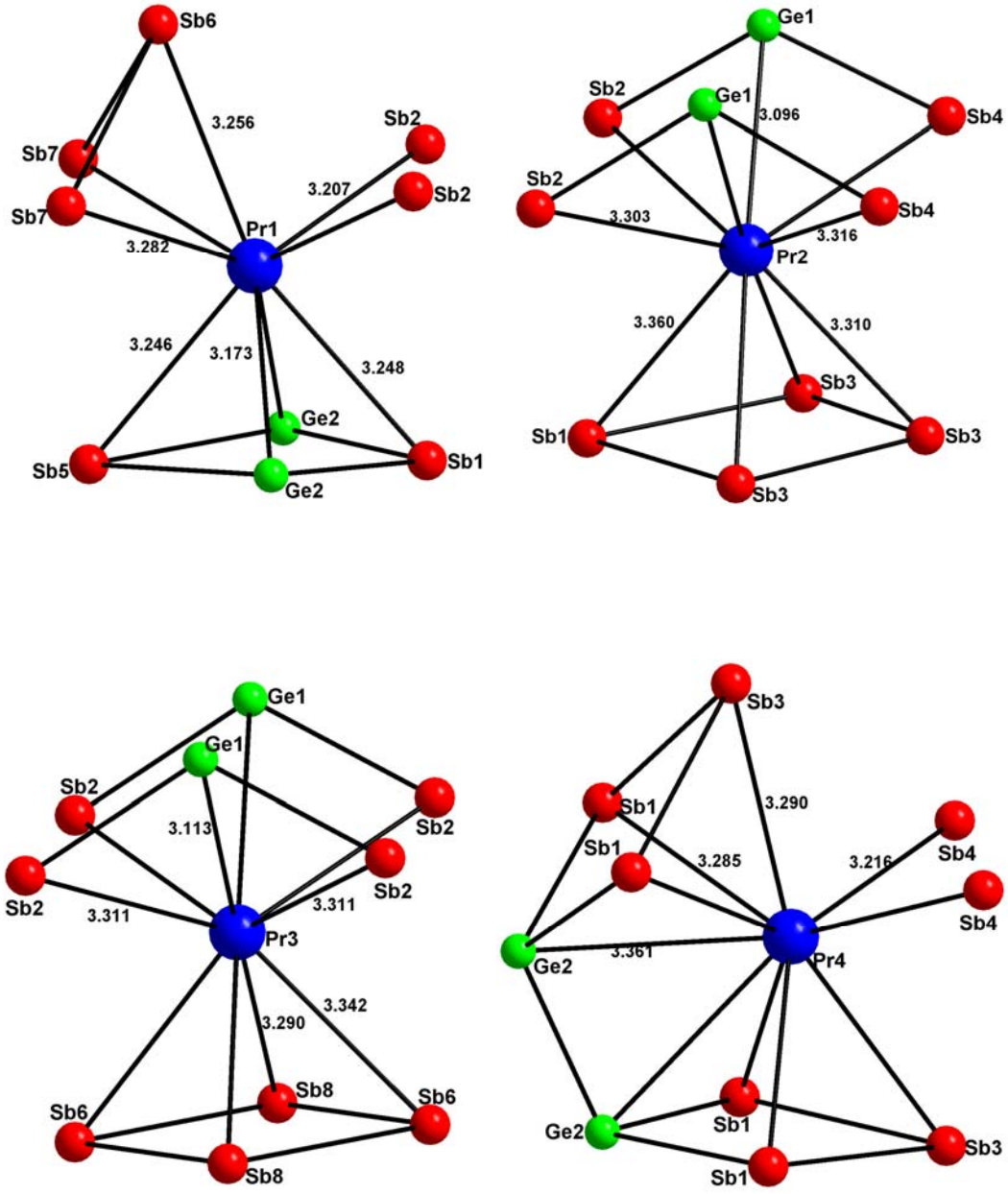

Figure 7–4. Coordination environments around the *RE* atoms in $RE_{12}Ge_{7-x}Sb_{21}$ (*RE* = La–Pr). Here $Pr_{12}Ge_{7-x}Sb_{21}$ is shown as an example.

The $RE_{12}Ge_{7-x}Sb_{21}$ series shares features with other ternary rare-earth polyantimonides (and, though still rare, polybismuthides) that are based on condensing ribbons of pnicogen atoms into 3D frameworks enclosing assemblies of centred RE_6 trigonal prisms. In particular, it integrates characteristics of the $RE_6Ge_{5-x}Sb_{11+x}$ [10a] and $RE_{12}Ga_4Sb_{23}$ [7a] structures (Figure 7–5). Like $RE_6Ge_{5-x}Sb_{11+x}$, the polyanionic network in $RE_{12}Ge_{7-x}Sb_{21}$ contains Ge_2 pairs (next to the folding points of the kinked sheets) and $GeSb_5$ square pyramids. They represent two members of an emerging homologous series ($RE_6Ge_{5-x}Sb_{11+x}$ (n = 1) and $RE_{12}Ge_{7-x}Sb_{21}$ (n = 2)) where the number of columns in the trigonal prismatic assemblies is equal to n^2. The width of each of the Sb ribbons also increases by two atoms on proceeding from $RE_6Ge_{5-x}Sb_{11+x}$ to $RE_{12}Ge_{7-x}Sb_{21}$. The result of this structural expansion is that the four-prism assemblies in $RE_{12}Ge_{7-x}Sb_{21}$ can now host $GeSb_3$ trigonal planes, in a manner similar to that in $RE_{12}Ga_4Sb_{23}$, where $GaSb_3$ trigonal planes and wider Sb ribbons are found. However, $RE_{12}Ga_4Sb_{23}$ belongs to a different structural lineage where Ga_2 pairs are found directly at the folding points of the kinked sheets. Further examples of the fascinating variations that can occur in this structural theme can be found elsewhere.[27]

It is not trivial to rationalize the bonding in $RE_{12}Ge_{7-x}Sb_{21}$. If the substoichiometry in Ge is neglected, then the assumption of trivalent *RE* atoms fully donating their valence electrons leads to the difficult task of how to partition the 36– charge per formula unit over the anionic substructure $[Ge_7Sb_{21}]$. Some of the structural motifs in $RE_{12}Ge_7Sb_{21}$ (idealized in the following discussion to be fully stoichiometric) have been treated through a retrotheoretical analysis in related compounds such as La_6MnSb_{15},[12a] $RE_{12}Ga_4Sb_{23}$,[7b] and $La_{13}Ga_8Sb_{21}$.[7b] The

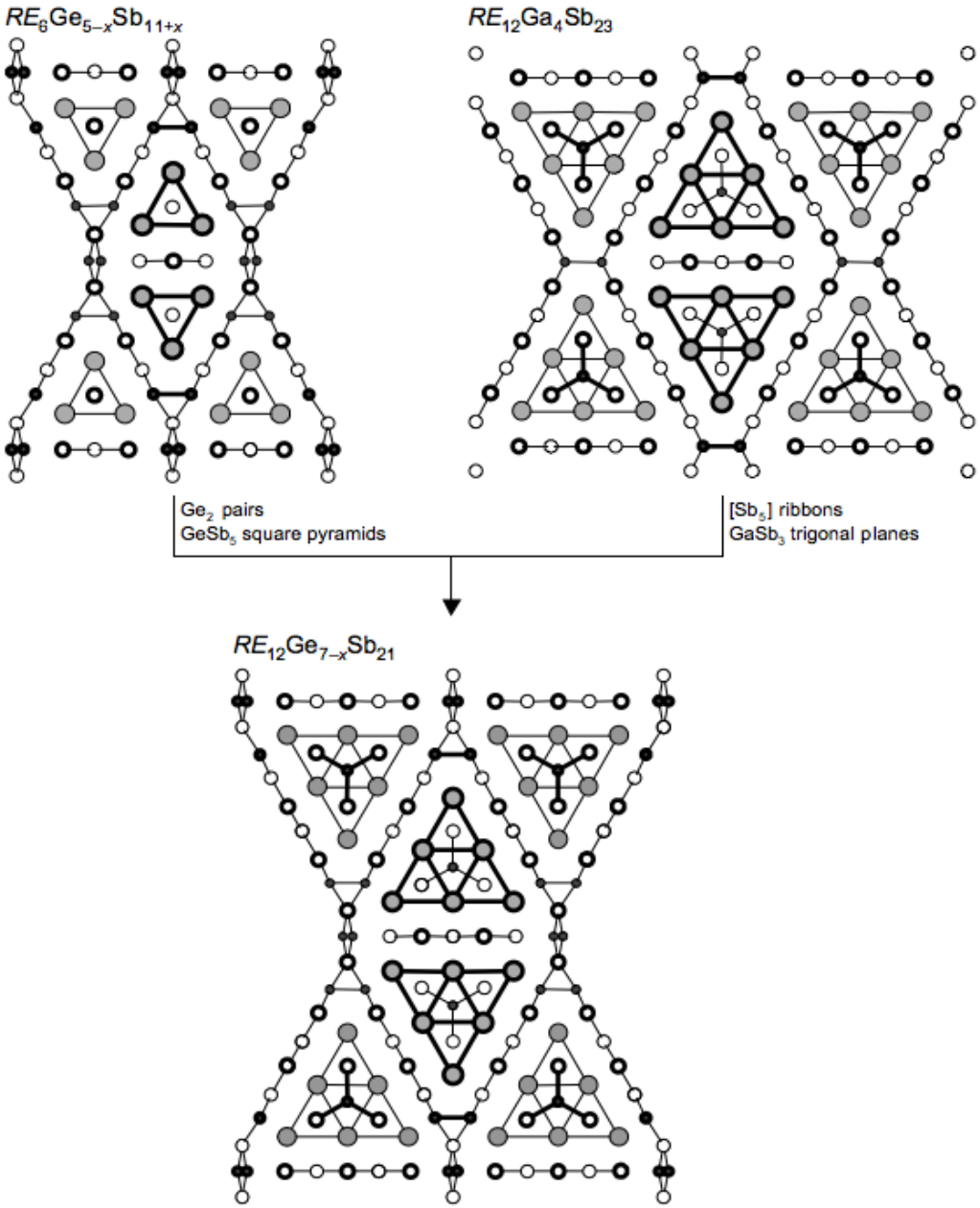

Figure 7–5. Derivation of $RE_{12}Ge_{7-x}Sb_{21}$ from the structures of $RE_6Ge_{5-x}Sb_{11+x}$ and $RE_{12}Ga_4Sb_{23}$, viewed in projection down the shortest cell axis. The large lightly shaded circles are *RE* atoms, the small solid circles are Ge or Ga atoms, and the medium open circles are Sb atoms. Circles with thicker rims indicate atoms located in planes displaced by half the short axis parameter.

simplest is the discrete trigonal planar $GeSb_3$ unit, analogous to the $GaSb_3$ unit in $RE_{12}Ga_4Sb_{23}$ and $La_{13}Ga_8Sb_{21}$. However, whereas an electron-deficient Ga centre in a $[GaSb_3]^{6-}$ unit (a 24-electron species, isoelectronic with boron trihalides) is consistent with planarity, a Ge centre in a $[GeSb_3]^{7-}$ unit (a 26-electron species) would have to support a lone pair and thereby favour a pyramidal distortion. The slight puckering observed in these trigonal planar units in $RE_{12}Ge_7Sb_{21}$ seems to provide evidence for this distortion. Molecular examples of trigonal planar Ge-centred radical species are known, but these must be stabilized by extremely bulky ligand groups.[28] A one-dimensional Sb_5 ribbon is also found in $RE_{12}Ga_4Sb_{23}$ and $La_{13}Ga_8Sb_{21}$.[7a] Through electron-counting rules developed initially for La_6MnSb_{15} and related compounds containing hypervalent Sb–Sb bonds (within square nets or fragments),[12] we arrive at an assignment of $[Sb_5]^{7-}$ units, with inner Sb atoms counted as 1– and terminal Sb atoms as 2–. The remaining $[Ge_5Sb_{10}]$ substructure forms the kinked sheets. Except for the Ge2–Ge2 pair, the interatomic distances within these sheets are about ~0.2 Å longer than expected for normal 2c–2e$^-$ bonds. Interpreting these distances to be 2c–1e$^-$ bonds instead would then lead to an assignment of $[Ge_5Sb_{10}]^{12-}$. The total charge for the anionic substructure $[Ge_7Sb_{21}]$ is thus 33– ($[GeSb_3]^{7-}$ $[GeSb_3]^{7-}$ $[Sb_5]^{7-}$ $[Ge_5Sb_{10}]^{12-}$). Clearly this is inconsistent with the 36+ charge provided by the *RE* atoms. The conclusion that can be drawn from this simplified bonding analysis is that $RE_{12}Ge_7Sb_{21}$ is not electron-precise, and the limits of applicability of the Zintl-Klemm approach are breached in a situation where bonding is of such low polarity.

Band structure calculations on $La_{12}Ge_7Sb_{21}$ reveal that although most of the La states are unoccupied, as seen in their large contribution to the density of states above the Fermi level, there is some mixing with Ge and Sb states, which dominate in the energy region from –5 eV to the Fermi level (Figure 7–6). The density of states curve is generally similar to those in $La_{12}Ga_4Sb_{23}$ and $La_{13}Ga_8Sb_{21}$.[7b] The crystal orbital Hamilton population (COHP) curves (Figure 7–7) reveal that heteroatomic Ge–Sb contacts account for most of the bonding stability in the structure (–ICOHP = 19.3 eV/cell = 0.6 eV/bond), followed by homoatomic Sb–Sb (–ICOHP = 11.4 eV/cell =0.4 eV/bond) and Ge–Ge contacts (–ICOHP = 2.4 eV/cell = 1.2 eV/bond). Interestingly, although they only constitute a small part of the structure, the Ge–Ge bonding (~2.5 Å) within pairs is optimized (all bonding levels and no antibonding levels occupied), indicating that these interactions are not a mere consequence of the folding of the kinked sheets described earlier. In contrast, some antibonding levels are occupied at the Fermi level for the Ge–Sb and Sb–Sb bonds.

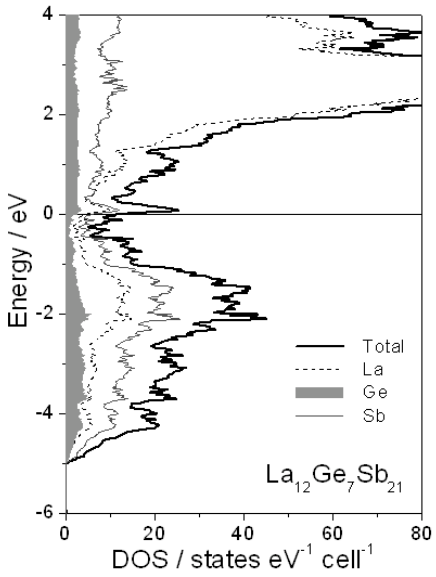

Figure 7–6. Total density of states (DOS) for $La_{12}Ge_7Sb_{21}$ (solid line) and its La, Ge, and Sb projections. The Fermi level is marked by the horizontal line at 0 eV.

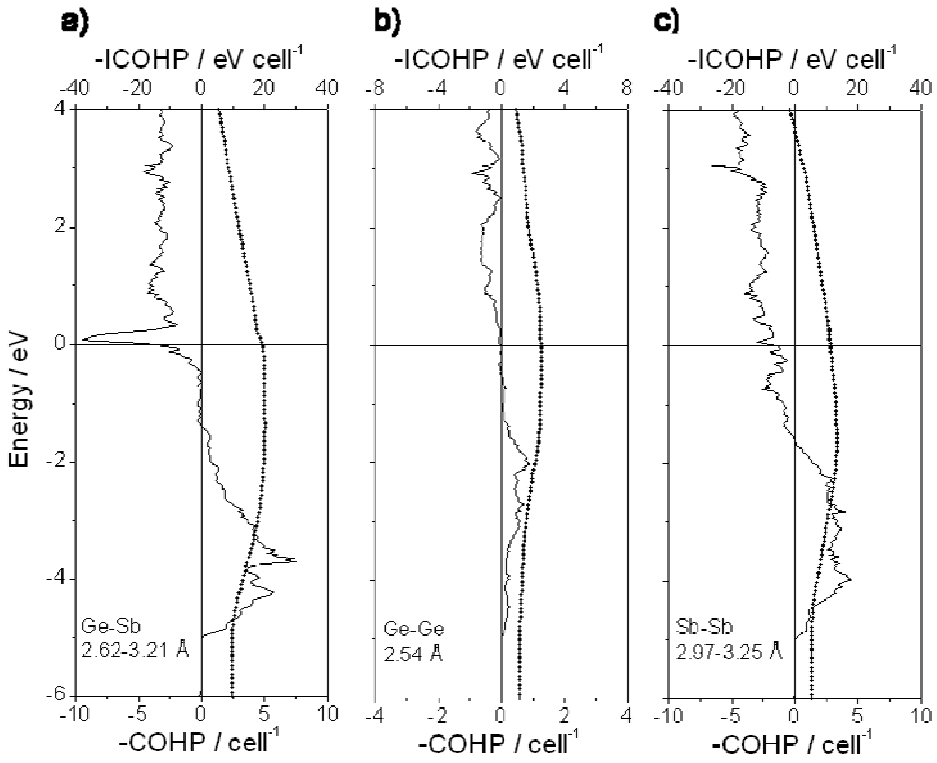

Figure 7–7. Crystal orbital Hamilton population (COHP) curves (solid line) and integrated COHP curves (dotted line) for (a) Ge–Sb, (b) Ge–Ge, and (c) Sb–Sb contacts in $La_{12}Ge_7Sb_{21}$. The Fermi level is marked by the horizontal line at 0 eV.

7.3.3. Magnetic Properties

Magnetic measurements have been made for the La and Ce members of $RE_{12}Ge_{7-x}Sb_{21}$. $La_{12}Ge_{6.7}Sb_{21}$ exhibits a relatively large temperature-independent Pauli paramagnetism (χ_o = 0.0034 emu/mol), consistent with trivalent La and the absence of localized unpaired electrons (Figure A2–1 in Appendix 2). The magnetic susceptibility of $Ce_{12}Ge_{6.5}Sb_{21}$ under an applied field of 1 *T* continues to increase as the temperature is lowered to 2 K (Figure 7–8a). With its pronounced curvature, the inverse susceptibility can be fit to the modified Curie-Weiss law, $\chi = C/(T-\theta_p) + \chi_o$. The effective magnetic moment derived from the Curie constant is μ_{eff} = 2.65(1) μ_B/Ce, similar to the expected value of 2.54 μ_B for Ce^{3+}. The Weiss parameter, θ_p = –3.2(5) K, suggests weak antiferromagnetic coupling, although no long-range ordering was observed in the temperature dependence of the magnetic susceptibility down to 2 K. Isothermal magnetization measurements reveal the appearance of saturation behaviour as the temperature is lowered below 10 K (Figure 7–8b). At 2 K, the magnetization approaches a saturation value of 1.2 μ_B/Ce as the applied field is increased up to 70000 Oe. In related compounds such as $RE_6Ge_{5-x}Sb_{11+x}$,[10b] RE_6MnSb_{15},[21] and $RE_6Zn_{1+x}Sb_{14}$,[27c] the presence of *RE* atoms within single columns of trigonal prisms gives rise to long-range antiferromagnetic ordering with relatively low T_N values (e.g., 4 K for $Ce_6Ge_{5-x}Sb_{11+x}$), possibly as a result of a ferrimagnetic spin arrangement. The presence of larger assemblies of trigonal prisms in $Ce_{12}Ge_{6.5}Sb_{21}$ leads to more complex arrangements of Ce 4f moments that would have to be analyzed in detail through further experiments.

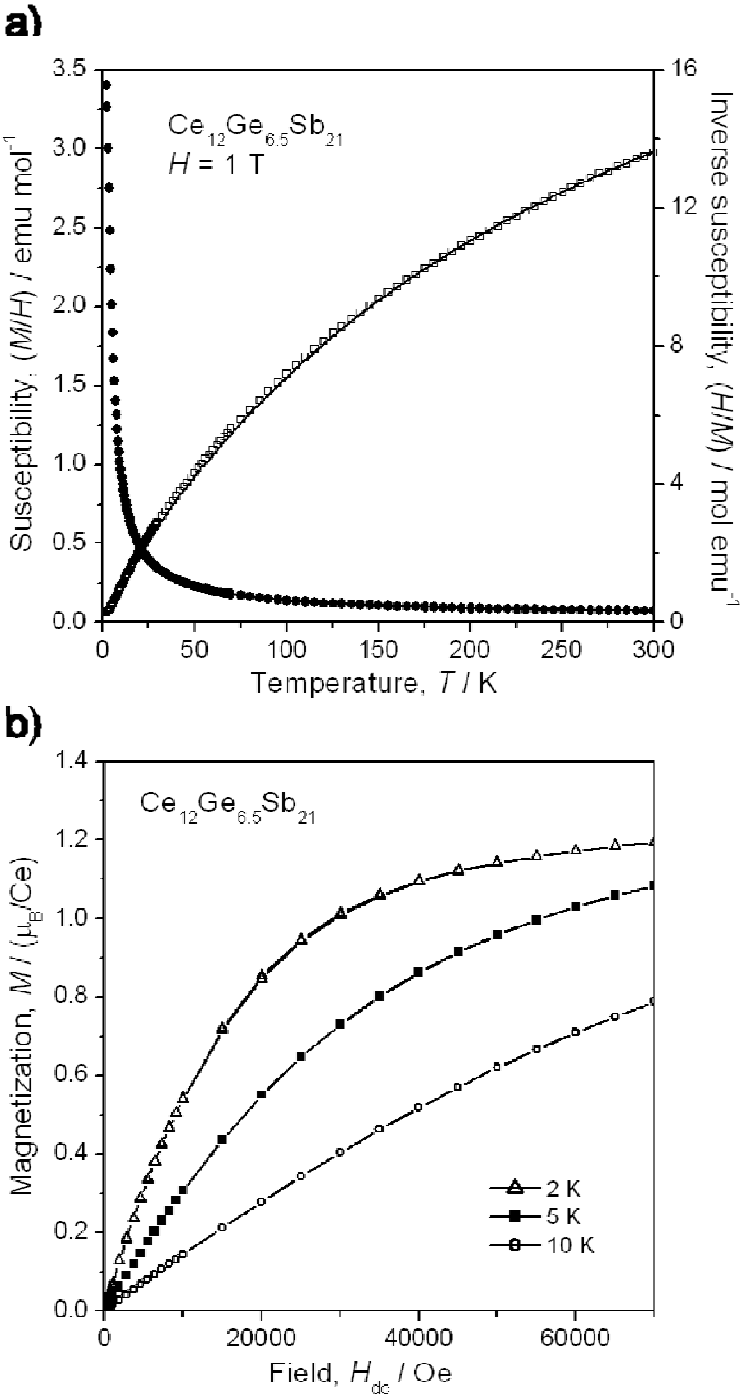

Figure 7–8. Magnetic data for $Ce_{12}Ge_{6.5}Sb_{21}$. (a) Magnetic susceptibility and its inverse, with a fit to the modified Curie-Weiss law indicated by the solid line. (b) Isothermal magnetization at different temperatures.

7.4. Conclusions

The ternary rare-earth germanium antimonides $RE_{12}Ge_{7-x}Sb_{21}$ (*RE* = La–Pr; x = 0.4–0.5) were synthesized by direct reactions of the elements. Single-crystal X-ray diffraction studies indicated that they adopt a new structure type, integrating complex features found in $RE_6Ge_{5-x}Sb_{11+x}$ and $RE_{12}Ga_4Sb_{23}$. A 3D polyanionic framework consisting of Ge pairs, Sb ribbons, and 2D Ge/Sb layers outlines large channels occupied by columns of face-sharing RE_6 trigonal prisms. These trigonal prisms are centred by additional Ge and Sb atoms to form $GeSb_3$ trigonal planar units. A bonding analysis attempted through the Zintl-Klemm concept suggests that full electron transfer from the *RE* atoms to the anionic substructure cannot be assumed. Band structure calculations reveal the presence of Ge–Ge, Ge–Sb and Sb–Sb bonding. Magnetic measurements on $Ce_{12}Ge_{6.5}Sb_{21}$ indicate antiferromagnetic coupling but no long-range ordering down to 2 K.

Given its resemblance to the previously known phase $RE_6Ge_{5-x}Sb_{11+x}$, it may be worthwhile targeting the third member of what may be a homologous structural series with the general formula $RE_{n^2+3n+2}Ge_{n^2-n+5}Sb_{n^2+7n+3}$, in which assemblies of centred RE_6 trigonal prisms (of which there are n^2 condensed together) are delimited by an anionic network of Ge and Sb atoms. If fully ordered structures are assumed, the next member following $RE_6Ge_5Sb_{11}$ (n = 1) and $RE_{12}Ge_7Sb_{21}$ (n = 2) would have the hypothetical formula "$RE_{20}Ge_{11}Sb_{33}$" (n = 3). The structure of such a compound would be predicted to contain assemblies of nine condensed RE_6 trigonal prisms (Figure 7–9). Centring these prisms would then lead to a cyclic Ge_3Sb_6 unit.

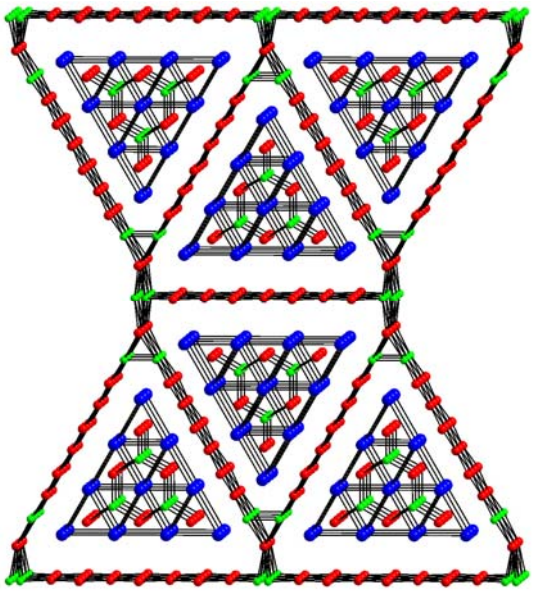

Figure 7–9. Hypothetical structure of $RE_{20}Ge_{11}Sb_{33}$, with assemblies of nine condensed RE_6 trigonal prisms. The labelling scheme is the same as in Figure 7–5.

7.5. References

(1) Sologub, O. L.; Salamakha, P. S. In *Handbook on the Physics and Chemistry of Rare Earths*; Gschneidner, K. A., Jr., Bünzli, J.-C. G., Pecharsky, V. K., Eds.; Elsevier: Amsterdam, 2003; Vol. 33, pp 35–146.

(2) Nolas, G. S.; Morelli, D. T.; Tritt, T. M. *Annu. Rev. Mater. Sci.* **1999**, *29*, 89–116.

(3) Chan, J. Y.; Kauzlarich, S. M.; Klavins, P.; Shelton, R. N.; Webb, D. J. *Chem. Mater.* **1997**, *9*, 3132–3135.

(4) Xu, J.; Kleinke, H. *J. Comput. Chem.* **2008**, *29*, 2134–2143.

(5) Mills, A. M.; Lam, R.; Ferguson, M. J.; Deakin, L.; Mar, A. *Coord. Chem. Rev.* **2002**, *233–234*, 207–222.

(6) Eisenmann, B.; Cordier, G. In *Chemistry, Structure, and Bonding of Zintl Phases and Ions*; Kauzlarich, S. M., Ed.; VCH Publishers: New York, 1996; pp 61–137.

(7) a) Mills, A. M.; Mar, A. *Inorg. Chem.* **2000**, *39*, 4599–4607; b) Mills, A. M.; Deakin, L.; Mar, A. *Chem. Mater.* **2001**, *13*, 1778–1788.

(8) Mills, A. M.; Mar, A. *J. Am. Chem. Soc.* **2001**, *123*, 1151–1158.

(9) Ferguson, M. J.; Ellenwood, R. E.; Mar, A. *Inorg. Chem.* **1999**, *38*, 4503–4509.

(10) a) Lam, R.; McDonald, R.; Mar, A. *Inorg. Chem.* **2001**, *40*, 952–959; b) Deakin, L.; Lam, R.; Mar, A. *Inorg. Chem.* **2001**, *40*, 960–965.

(11) a) Ferguson, M. J.; Hushagen, R. W.; Mar, A. *Inorg. Chem.* **1996**, *35*, 4505–4512; b) Norén, L.; Withers, R. L.; Brink, F. J. *J. Solid State Chem.* **2005**, *178*, 2133–2143.

(12) a) Papoian, G. A.; Hoffmann, R. *J. Solid State Chem.* **1998**, *139*, 8–21; b) Papoian, G. A.; Hoffmann, R. *Angew. Chem. Int. Ed.* **2000**, *39*, 2408–2448; c) Papoian, G.; Hoffmann, R. *J. Am. Chem. Soc.* **2001**, *123*, 6600–6608.

(13) Pauling, L. *The Nature of the Chemical Bond*, 3rd ed.; Cornell University Press: Ithaca, NY, 1960.

(14) Miller, G. J. *Eur. J. Inorg. Chem.* **1998**, 523–536.

(15) Tobash, P. H.; Meyers, J. J.; DiFilippo, G.; Bobev, S.; Ronning, F.; Thompson, J. D.; Sarrao, J. L. *Chem. Mater.* **2008**, *20*, 2151–2159.

(16) Guloy, A. M.; Corbett, J. D. *Inorg. Chem.* **1993**, *32*, 3532–3540.

(17) Kozlov, A. Yu.; Pavlyuk, V. V.; Davydov, V. M. *Intermetallics*, **2004**, *12*, 151–155.

(18) Salvador, J. R.; Bilc, D.; Mahanti, S. D.; Hogan, T.; Guo, F.; Kanatzidis, M. G. *J. Am. Chem. Soc.* **2004**, *126*, 4474–4475.

(19) a) Stetskiv, A. O.; Pavlyuk, V. V.; Bodak, O. I. *Pol. J. Chem.* **1998**, *72*, 956–958; b) Nasir, N.; Grytsiv, A.; Rogl, P.; Saccone, A.; Giester, G. *J. Solid State Chem.* **2009**, *182*, 645–656.

(20) Sheldrick, G. M. *SHELXTL*, version 6.12; Bruker AXS Inc.: Madison, WI, 2001.

(21) Sologub, O.; Vybornov, M.; Rogl, P.; Hiebl, K.; Cordier, G.; Woll, P. *J. Solid State Chem.* **1996**, *122*, 266–272.

(22) Gelato, L. M.; Parthé, E. *J. Appl. Crystallogr.* **1987**, *20*, 139–143.

(23) Tank, R.; Jepsen, O.; Burkhardt, A.; Andersen, O. K. *TB-LMTO-ASA Program*, version 4.7, Max Planck Institut für Festkörperforschung, Stuttgart, 1998.

(24) Blase, W.; Cordier, G.; Somer, M.; *Z. Kristallogr.* **1992**, *199*, 277–278.

(25) Choe, W.; Miller, G. J.; Levin, E. M. *J. Alloys Compd.* **2001**, *329*, 121–130.

(26) Taylor, J. C.; Wilson, P. W. *J. Am. Chem. Soc.* **1973**, *95*, 1834–1838.

(27) a) Crerar, S. J.; Morgan, M. G.; Mar, A. *J. Solid State Chem.* **2003**, *171*, 137–142; b) Tkachuk, A. V.; Tam, T.; Mar, A. *Chem. Met. Alloys* **2008**, *1*, 76–83; c) Liu, Y.; Chen, L.; Li, L.-H.; Wu, L.-M.; Zelinska, O. Ya.; Mar, A. *Inorg. Chem.* **2008**, *47*, 11930–11941.

(28) a) Sekiguchi, A.; Fukawa, T.; Nakamoto, M.; Lee, V. Ya.; Ichinohe, M. *J. Am. Chem. Soc.* **2002**, *124*, 9865–9869; b) Drost, C.; Griebel, J.; Kirmse, R.; Lönnecke, P.; Reinhold, J. *Angew. Chem. Int. Ed.* **2009**, *48*, 1–5.

Chapter 8

Structures and Magnetic Properties of $RE_5Tt_xSb_{3-x}$ (*RE* = La–Nd; *Tt* = Si, Ge)*

8.1. Introduction

In giant magnetocaloric materials such as the intermetallic compounds based on Gd_5Ge_4, a ferromagnetic ordering should be accompanied by a structural phase transition.[1] These structural changes can be induced not only by controlling physical variables such as temperature or magnetic field, but also by manipulating the chemical composition through varying the valence electron concentration (e.g., $Gd_5Ga_xGe_{4-x}$),[2] cation or anion size (e.g., $Gd_{5-x}Y_xGe_4$, $Gd_5Si_xGe_{4-x}$),[3,4] or both (e.g., $La_{5-x}Ca_xGe_4$, $Gd_5Sb_xGe_{4-x}$).[5,6] Recently, efforts have been made to prepare ternary derivatives based on another class of intermetallic compounds, the binary rare-earth antimonides RE_5Sb_3, as potential magnetocaloric materials.[7] The binary RE_5Sb_3 phases adopt different crystal structures depending on the *RE*.[8] The hexagonal Mn_5Si_3-type structure predominates for most of the *RE* elements, but the very similar orthorhombic β-Yb_5Sb_3-type and Y_5Bi_3-type structures are also found less commonly, usually for the later *RE* elements.[9] (Although it is now recognized that the eponymous "β-Yb_5Sb_3" does not exist as a true binary but rather as a hydrogen-stabilized phase,[10,11] the name of this structure type has

*A version of this chapter has been accepted for publication. Haiying Bie, Arthur Mar, 2009. European Journal of Inorganic Chemistry.

conventionally been retained to describe other genuine binary phases.) Interestingly, chemical substitution of the Sb atoms in RE_5Sb_3 results in nonstoichiometric $RE_5M_xSb_{3-x}$ (*RE* = Gd–Er, Y; *M* = Fe, Co, Ni, Cu; $x \leq 1$) phases that adopt the β-Yb_5Sb_3-type structure.[7,12–15] To date, the substitution has been limited to transition metals for *M*, whereas substitution by p-block elements has not been attempted.

In this chapter, we report the existence of new $RE_5Tt_xSb_{3-x}$ series containing an early rare-earth (*RE* = La–Nd) and a p-block element from group 14 (a tetrel, *Tt* = Si, Ge). This substitution, which changes both the electron count and anion size, stabilizes the formation of the orthorhombic β-Yb_5Sb_3-type structure, different from those of the parent binaries (RE_5Sb_3, RE_5Si_3, or RE_5Ge_3). Band structure calculations were carried out to gain further understanding of the factors influencing the structure and bonding of these compounds. As initial steps to characterize their materials properties, magnetic measurements were also made.

8.2. Experimental Section

8.2.1. Synthesis

Initial reactions were performed in the course of investigating the La–Si–Sb and La–Ge–Sb phase diagrams. Starting materials were *RE* pieces (Hefa), Si lumps (Alfa-Aesar), Ge ingots (Alfa Inorganics, Ventron), and Sb ingots (Alfa-Aesar), each with 99.9% purity or better. Samples were prepared by arc-melting of the elemental components in various ratios, annealed at 800 °C for 20 days and then quenched in cold water. Phase identification was performed through powder

X-ray diffraction on ground samples and quantitative EDX analysis on polished samples.

Single crystals of $La_5Si_xSb_{3-x}$ and $La_5Ge_xSb_{3-x}$ were found in the quenched alloys prepared from the molar ratio La:(Si or Ge):Sb = 65:15:20. After the structures of these crystals were established from single-crystal X-ray diffraction studies, attempts were made to substitute other *RE* metals (*RE* = Ce–Nd, Sm, Gd) through similar arc-melting and annealing reactions with various loading compositions. These reactions were successful for *RE* = Ce–Nd, but not for *RE* = Sm and Gd, where only binary phases were obtained. Elemental compositions were determined on polished samples through quantitative electron probe microanalysis (EPMA) (Table 8–1).

Table 8–1. Atomic compositions (%) determined from X-ray diffraction data and electron probe microanalysis data for $RE_5Tt_xSb_{3-x}$ (*RE* = La–Nd; *Tt* = Si, Ge).

Formula from X-ray data	Expected			Observed		
	RE	*Tt*	Sb	*RE*	*Tt*	Sb
$La_5Si_{1.40(2)}Sb_{1.60(2)}$	62.5	17.5	20.0	not measured		
$Ce_5Si_{1.4}Sb_{1.6}$ [a]	62.5	17.5	20.0	62.4(4)	18.2(6)	19.3(4)
$Pr_5Si_{1.20(3)}Sb_{1.800(8)}$	62.5	15.0	22.5	63(1)	17(1)	20(1)
$Nd_5Si_{1.2}Sb_{1.8}$ [a]	62.5	15.0	22.5	63.9(4)	14.6(8)	22(1)
$La_5Ge_{1.32(6)}Sb_{1.68(4)}$	62.5	16.5	21.0	64.5(5)	14.2(5)	21.3(5)
$Ce_5Ge_{0.9}Sb_{2.1}$ [a]	62.5	11.3	26.2	66.4(3)	10.8(5)	22.7(6)
$Pr_5Ge_{1.68(6)}Sb_{1.32(4)}$	62.5	21.0	16.5	64.7(4)	18.8(4)	16.4(1)
$Nd_5Ge_{1.14(6)}Sb_{1.86(4)}$	62.5	14.3	23.2	65(1)	15(1)	21(1)

[a] Occupancies of the *Tt* and Sb sites in these Rietveld refinements were fixed on the basis of the observed atomic compositions.

The $La_5Ge_xSb_{3-x}$ series was selected for further investigation of the homogeneity range. Different samples in the range $0 \le x \le 3$ were prepared by arc-melting and annealing reactions. Phase analysis and evolution of cell parameters established the solid solubility range to be $0.9 \le x \le 1.6$ (Figure 8–1 and Table A3–1 in Appendix 3).

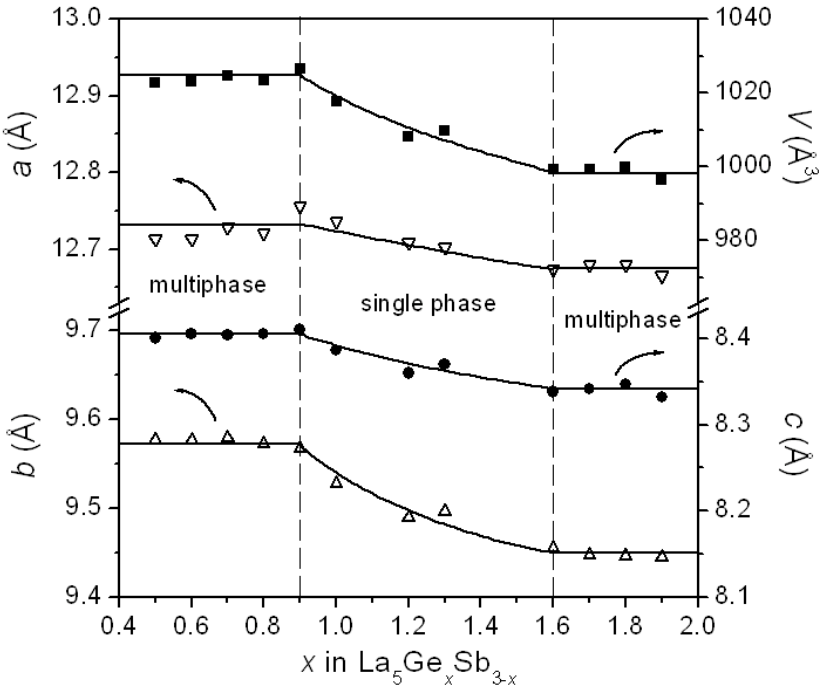

Figure 8–1. Plot of cell parameters vs. x for the β-Yb_5Sb_3-type phase obtained in reactions with nominal composition $La_5Ge_xSb_{3-x}$. In addition to the ternary phase, La_5Sb_3 and La_4Sb_3 were also formed below $x = 0.9$, and La_4Ge_3 was formed above $x = 1.6$.

8.2.2. Structure Determination

Suitable single crystals of $RE_5Si_xSb_{3-x}$ (*RE* = La, Pr) and $RE_5Ge_xSb_{3-x}$ (*RE* = La, Pr, Nd) were selected from reactions with various loading compositions for $RE_5Tt_xSb_{3-x}$. Single-crystal X-ray diffraction data were collected on a Bruker Platform / SMART 1000 CCD diffractometer at 22 °C using ω scans. Structure solution and refinement were carried out with use of the SHELXTL (version 6.12)

program package.[16] Face-indexed numerical absorption corrections were applied. For all compounds, the centrosymmetric space group *Pnma* was chosen on the basis of intensity statistics. Initial atomic positions found by direct methods were consistent with the β-Yb_5Sb_3-type structure,[17] and refinements generally proceeded in a straightforward manner. Refinements on the occupancy factors confirmed that all *RE* sites are fully occupied. However, the distribution of *Tt* atoms in the two possible Sb sites (4*c* and 8*d*) had to be evaluated carefully. The refinement of $La_5Si_xSb_{3-x}$ is described here as an example. The idealized formula La_5SiSb_2 could be proposed initially and such a formula suggests the 4*c* site is occupied exclusively by Si atoms and the 8*d* site by Sb atoms. Refinement of this ordered model, with the possibility of substoichiometry being permitted, led to partial occupancies of 0.94(1) Si in the 4*c* site and 0.850(3) Sb in the 8*d* site. Alternatively, substitutional disorder was invoked in which both sites were allowed to be occupied by a mixture of Si and Sb sites, subject to the restraint that the occupancies sum to 1.00(1) in each site. Refinement of this disordered model led to occupancies of 1.00(1) Si and 0.000(5) Sb in the 4*c* site, and 0.20(1) Si and 0.802(5) Sb in the 8*d* site. The third possible situation, in which both sites are substitutionally disordered and underoccupied, was not considered to be likely, given that related $RE_5M_xSb_{3-x}$ (*M* = Fe, Co, Ni, Cu) structures exhibit full occupancies in both sites and *M*/Sb disorder in only one site.[7,12–15] Guided in this manner, we have fixed the 4*c* site to be fully occupied exclusively by Si atoms and restrained the 8*d* site to be fully occupied by a mixture of Si and Sb atoms in the final refinement. The diffraction data for the other isostructural compounds were treated in a similar way, leading to refined formulas that agreed well with the EPMA results (Table 8–1). The possibility that interstitial impurities such as hydrogen atoms might be present was discounted on the basis that the parent

binary trivalent rare-earth antimonides with the β-Yb_5Sb_3-type structure are definitively hydrogen-free.[9]

Because suitable single crystals of $RE_5Si_xSb_{3-x}$ (*RE* = Ce, Nd) and $Ce_5Ge_xSb_{3-x}$ were unavailable, their structures were refined from powder X-ray diffraction data, collected over 5 hours on the powder diffractometer. Initial positions were taken from the single-crystal structures determined above, and the full-profile Rietveld method was applied with use of the program LHPM-Rietica.[18] Because site occupancies are normally difficult to treat in the Rietveld method, they were not refined but rather fixed on the basis of the EPMA results (Table 8–1), with the assumption as before that the 4*c* site is fully occupied by *Tt* atoms and the 8*d* site by a mixture of *Tt* and Sb atoms. (Attempts were made to refine the occupancy, but these were considered to be unjustified because the results were not found to be sensitive to the occupancy parameters.) Both sites were constrained to have equal isotropic displacement parameters. The least-squares refinement included scale factor, background, zero point, cell parameters, occupancies, atomic coordinates, and isotropic displacement parameters. For $Ce_5Ge_xSb_{3-x}$, the sample chosen was at the lower bound of the solid solution range (x = 0.9), which is below that for the idealized formula Ce_5GeSb_2 (x = 1.0). In this instance, the disorder of Ge and Sb atoms must be invoked in the 4*c* site and not in the 8*d* site, analogous to the case in $RE_5M_xSb_{3-x}$ (*M* = Fe, Co, Ni, Cu).

Atomic positions were standardized with the program STRUCTURE TIDY.[19] Crystal data and further details of the data collections are given in Table 8–2. Final values of the positional and displacement parameters are given in Table 8–3. A detailed listing of interatomic distances is available in Table A3–2 in Appendix 3, and an abridged version is given in Table 8–4.

Table 8–2. Crystallographic data for $RE_5Tt_xSb_{3-x}$ (RE = La–Nd; Tt = Si, Ge).

$RE_5Si_xSb_{3-x}$				
Formula	$La_5Si_{1.40(2)}Sb_{1.60(2)}$	$Ce_5Si_{1.4}Sb_{1.6}$	$Pr_5Si_{1.20(3)}Sb_{1.800(8)}$	$Nd_5Si_{1.2}Sb_{1.8}$
Formula mass (amu)	928.68	934.73	957.41	974.06
Space group	*Pnma* (No. 62)	*Pnma* (No. 62)	*Pnma* (No. 62)	*Pnma* (No. 62)
a (Å)	12.6724(13)	12.5029(5)	12.401(2)	12.2970(6)
b (Å)	9.4205(10)	9.3597(4)	9.3328(16)	9.2798(5)
c (Å)	8.3191(9)	8.1872(3)	8.1740(14)	8.1208(4)
V (Å^3)	993.1(2)	958.09(7)	946.0(3)	926.68(8)
Z	4	4	4	4
ρ_{calcd} (g cm^{-3})	6.211	6.477	6.722	6.979
Radiation	Mo Kα, λ = 0.71073 Å	Cu Kα$_1$, λ = 1.54056 Å	Mo Kα, λ = 0.71073 Å	Cu Kα$_1$, λ = 1.54056 Å
μ (mm^{-1})	25.38	215.70	30.35	251.25
2θ range	5.86–66.28°	20.00–110.00°	5.96–66.22°	20.00–110.00°
Refinement method	SHELXTL	Rietveld	SHELXTL	Rietveld
No. of data collected	11793	3103 data points	12383	3103 data points
No. of unique data	1970 (R_{int} = 0.097) (1426 with $F_o^2>2\sigma(F_o^2)$)	639 Bragg reflections	1875 (R_{int} = 0.083) (1498 with $F_o^2>2\sigma(F_o^2)$)	620 Bragg reflections
No. of variables	45	35	45	36
Residuals [a]	$R(F)$ ($F_o^2 > 2\sigma(F_o^2)$) = 0.039 $R_w(F_o^2)$ = 0.074	R_B = 0.015 R_p = 0.023 R_{wp} = 0.030	$R(F)$ ($F_o^2 > 2\sigma(F_o^2)$) = 0.032 $R_w(F_o^2)$ = 0.057	R_B = 0.011 R_p = 0.022 R_{wp} = 0.029

$RE_5Ge_xSb_{3-x}$				
Formula	$La_5Ge_{1.32(6)}Sb_{1.68(4)}$	$Ce_5Ge_{0.9}Sb_{2.1}$	$Pr_5Ge_{1.68(6)}Sb_{1.32(4)}$	$Nd_5Ge_{1.14(6)}Sb_{1.86(4)}$
Formula mass (amu)	994.91	1021.61	987.21	1030.41
Space group	*Pnma* (No. 62)	*Pnma* (No. 62)	*Pnma* (No. 62)	*Pnma* (No. 62)
a (Å)	12.669(5)	12.5020(8)	12.337(6)	12.2982(11)
b (Å)	9.457(4)	9.4361(6)	9.283(4)	9.3222(9)
c (Å)	8.339(3)	8.2378(5)	8.144(4)	8.1599(8)
V (Å^3)	999.0(7)	971.8(1)	932.7(7)	935.5(2)
Z	4	4	4	4
ρ_{calcd} (g cm^{-3})	6.615	6.979	7.030	7.316
Radiation	Mo Kα, λ = 0.71073 Å	Cu Kα$_1$, λ = 1.54056 Å	Mo Kα, λ = 0.71073 Å	Mo Kα, λ = 0.71073 Å
μ (mm^{-1})	29.17	224.78	34.58	36.01
2θ range	5.84–66.20°	20.00–110.00°	6.00–66.00°	6.00–66.28°
Refinement method	SHELXTL	Rietveld	SHELXTL	SHELXTL
No. of data collected	13100	3103 data points	12163	12244
No. of unique data	1988 (R_{int} = 0.074) (1582 with $F_o^2 > 2\sigma(F_o^2)$)	646 Bragg reflections	1847 (R_{int} = 0.088) (1405 with $F_o^2 > 2\sigma(F_o^2)$)	1868 (R_{int} = 0.063) (1531 with $F_o^2 > 2\sigma(F_o^2)$)
No. of variables	45	36	45	45
Residuals [a]	$R(F)$ ($F_o^2 > 2\sigma(F_o^2)$) = 0.033 $R_w(F_o^2)$ = 0.063	R_B = 0.017 R_p = 0.028 R_{wp} = 0.036	$R(F)$ ($F_o^2 > 2\sigma(F_o^2)$) = 0.032 $R_w(F_o^2)$ = 0.060	$R(F)$ ($F_o^2 > 2\sigma(F_o^2)$) = 0.027 $R_w(F_o^2)$ = 0.050

[a] $R(F) = \sum \| F_o | - | F_c \| / \sum | F_o |$; $R_w(F_o^2) = \left[\sum \left[w(F_o^2 - F_c^2)^2 \right] / \sum w F_o^4 \right]^{1/2}$, $w^{-1} = \left[\sigma^2(F_o^2) + (Ap)^2 + Bp \right]$ where $p = \left[\max(F_o^2, 0) + 2F_c^2 \right] / 3$;

$R_B = \sum | I_o - I_c | / \sum I_o$; $R_p = \sum | y_o - y_c | / \sum y_o$; $R_{wp} = \left[\sum \left[w(y_o - y_c) \right] / \sum w y_o^2 \right]^{1/2}$.

Table 8–3. Atomic coordinates and equivalent isotropic displacement parameters (Å^2) for $RE_5Tt_xSb_{3-x}$ (RE = La–Nd; Tt = Si, Ge).

Atom	Wyckoff position	Occupancy	x	y	z	U_{eq} or U_{iso} [a]
$La_5Si_{1.40(2)}Sb_{1.60(2)}$						
La1	8*d*	1	0.06534(4)	0.04007(5)	0.19305(5)	0.0149(1)
La2	4*c*	1	0.00061(5)	¼	0.53559(8)	0.0161(1)
La3	4*c*	1	0.21353(5)	¼	0.84177(8)	0.0151(1)
La4	4*c*	1	0.29443(5)	¼	0.36269(8)	0.0149(1)
Si1/Sb1	8*d*	0.20(1)/0.802(5)	0.32629(5)	0.00820(5)	0.07503(7)	0.0108(2)
Si2	4*c*	1	0.4849(3)	¼	0.5712(4)	0.0180(7)
$Ce_5Si_{1.4}Sb_{1.6}$						
Ce1	8*d*	1	0.0640(3)	0.0396(5)	0.1948(5)	0.020(1)
Ce2	4*c*	1	–0.0025(7)	¼	0.5287(8)	0.014(1)
Ce3	4*c*	1	0.2172(7)	¼	0.8389(9)	0.022(2)
Ce4	4*c*	1	0.2952(6)	¼	0.3620(8)	0.015(2)
Si1/Sb1	8*d*	0.2/0.8	0.3254(3)	0.0084(8)	0.0755(6)	0.007(1)
Si2	4*c*	1	0.484(2)	¼	0.573(3)	0.007(1)
$Pr_5Si_{1.20(3)}Sb_{1.800(8)}$						
Pr1	8*d*	1	0.06469(3)	0.04151(4)	0.19032(4)	0.0125(1)
Pr2	4*c*	1	0.00116(4)	¼	0.53725(6)	0.0135(1)
Pr3	4*c*	1	0.21478(4)	¼	0.83970(6)	0.0132(1)
Pr4	4*c*	1	0.29435(4)	¼	0.36394(6)	0.0124(1)
Si1/Sb1	8*d*	0.10(1)/0.900(4)	0.32648(4)	0.00953(4)	0.07477(6)	0.0106(1)

Si2	4*c*	1	0.4849(2)	¼	0.5735(3)	0.0138(5)
$Nd_5Si_{1.2}Sb_{1.8}$						
Nd1	8*d*	1	0.0661(4)	0.0426(5)	0.1926(6)	0.018(1)
Nd2	4*c*	1	–0.0044(9)	¼	0.5312(9)	0.018(2)
Nd3	4*c*	1	0.2192(6)	¼	0.8391(9)	0.008(2)
Nd4	4*c*	1	0.2973(6)	¼	0.3623(9)	0.013(2)
Si1/Sb1	8*d*	0.1/0.9	0.3265(4)	0.0099(8)	0.0756(7)	0.015(1)
Si2	4*c*	1	0.480(3)	¼	0.590(4)	0.015(1)

$La_5Ge_{1.32(6)}Sb_{1.68(4)}$						
La1	8*d*	1	0.06507(3)	0.04199(4)	0.19496(4)	0.0151(1)
La2	4*c*	1	0.00102(4)	¼	0.53162(6)	0.0154(1)
La3	4*c*	1	0.21526(4)	¼	0.84016(6)	0.0146(1)
La4	4*c*	1	0.29368(4)	¼	0.35956(6)	0.0144(1)
Ge1/Sb1	8*d*	0.15(3)/0.84(2)	0.32589(3)	0.00766(4)	0.07326(5)	0.0117(1)
Ge2	4*c*	1	0.48239(8)	¼	0.5746(1)	0.0178(2)
$Ce_5Ge_{0.9}Sb_{2.1}$						
Ce1	8*d*	1	0.0640(4)	0.0430(5)	0.1978(6)	0.011(1)
Ce2	4*c*	1	0.0013(11)	¼	0.5245(9)	0.010(2)
Ce3	4*c*	1	0.2197(7)	¼	0.8357(9)	0.008(2)
Ce4	4*c*	1	0.2929(6)	¼	0.3553(9)	0.006(2)
Sb1	8*d*	1	0.3270(4)	0.0041(9)	0.0766(7)	0.020(1)

Ge2/Sb2	4*c*	0.9/0.1	0.482(1)	¼	0.582(2)	0.020(1)
$Pr_5Ge_{1.68(6)}Sb_{1.32(4)}$						
Pr1	8*d*	1	0.06634(3)	0.04351(4)	0.19371(4)	0.0133(1)
Pr2	4*c*	1	0.00144(4)	¼	0.53281(6)	0.0152(1)
Pr3	4*c*	1	0.21752(4)	¼	0.83488(6)	0.0139(1)
Pr4	4*c*	1	0.29306(4)	¼	0.35475(6)	0.0142(1)
Ge1/Sb1	8*d*	0.34(3)/0.66(2)	0.32611(4)	0.00777(5)	0.06983(6)	0.0109(2)
Ge2	4*c*	1	0.48116(8)	¼	0.5763(1)	0.0144(2)
$Nd_5Ge_{1.14(6)}Sb_{1.86(4)}$						
Nd1	8*d*	1	0.06502(2)	0.04345(3)	0.19011(4)	0.0120(1)
Nd2	4*c*	1	0.00178(3)	¼	0.53498(5)	0.0119(1)
Nd3	4*c*	1	0.21689(3)	¼	0.83644(5)	0.0126(1)
Nd4	4*c*	1	0.29386(3)	¼	0.36039(5)	0.0118(1)
Ge1/Sb1	8*d*	0.07(3)/0.93(2)	0.32637(3)	0.00954(4)	0.07231(5)	0.0101(1)
Ge2	4*c*	1	0.48252(7)	¼	0.5784(1)	0.0130(2)

[a] U_{iso} applies to $Ce_5Si_{1.4}Sb_{1.6}$, $Nd_5Si_{1.2}Sb_{1.8}$, and $Ce_5Ge_{0.9}Sb_{2.1}$, for which Rietveld refinements were performed. U_{eq} is defined as one-third of the trace of the orthogonalized U_{ij} tensor.

Table 8–4. Ranges of interatomic distances (Å) in $RE_5Tt_xSb_{3-x}$ (*RE* = La–Nd; *Tt* = Si, Ge).[a]

	$La_5Si_{1.40(2)}Sb_{1.60(2)}$	$Ce_5Si_{1.4}Sb_{1.6}$	$Pr_5Si_{1.20(3)}Sb_{1.800(8)}$	$Nd_5Si_{1.2}Sb_{1.8}$
*RE*1–*Tt*2	2.984(2)–3.127(3)	2.951(9)–3.11(2)	2.948(1)–3.069(2)	2.90(1)–3.18(3)
*RE*1–Sb1	3.462(1)–3.604(1)	3.423(4)–3.539(5)	3.394(1)–3.536(1)	3.354(6)–3.509(7)
*RE*1–*RE*2	3.564(1)	3.470(5)	3.528(1)	3.466(7)
*RE*2–*Tt*2	3.227(4)	3.27(2)	3.188(3)	3.08(3)
*RE*2–Sb1	3.292(1)–3.304(1)	3.236(9)–3.302(9)	3.245(1)–3.251(1)	3.168(9)–3.276(9)
*RE*3–*Tt*2	2.986(3)	3.01(3)	2.938(3)	3.00(3)
*RE*3–Sb1	3.316(1)–3.331(1)	3.270(6)–3.284(7)	3.263(1)–3.289(1)	3.224(8)–3.273(8)
*RE*4–*Tt*2	2.972(3)	2.92(3)	2.918(3)	2.91(3)
*RE*4–Sb1	3.328(1)–3.373(1)	3.280(6)–3.343(6)	3.284(1)–3.329(1)	3.242(7)–3.337(9)
Sb1–*RE*	3.292(1)–3.604(1)	3.236(9)–3.539(5)	3.245(1)–3.536(1)	3.168(9)–3.509(7)
*Tt*2–*RE*	2.972(3)–3.277(4)	2.92(3)–3.27(2)	2.918(3)–3.188(3)	2.90(3)–3.18(3)

	$La_5Ge_{1.32(6)}Sb_{1.68(4)}$	$Ce_5Ge_{0.9}Sb_{2.1}$	$Pr_5Ge_{1.68(6)}Sb_{1.32(4)}$	$Nd_5Ge_{1.14(6)}Sb_{1.86(4)}$
*RE*1–*Tt*2	2.990(1)–3.165(1)	2.980(5)–3.19(1)	2.946(1)–3.101(1)	2.942(1)–3.088(1)
*RE*1–Sb1	3.472(1)–3.609(1)	3.434(6)–3.517(6)	3.372(1)–3.550(1)	3.370(1)–3.532(1)
*RE*1–*RE*2	3.523(1)	3.417(7)	3.456(1)	3.497(1)
*RE*2–*Tt*2	3.292(2)	3.25(2)	3.193(2)	3.164(1)
*RE*2–Sb1	3.296(1)–3.308(1)	3.25(1)–3.29(1)	3.216(1)–3.230(1)	3.227(1)–3.232(1)
*RE*3–*Tt*2	3.034(2)	3.04(1)	3.004(2)	2.965(1)
*RE*3–Sb1	3.316(1)–3.341(1)	3.263(9)–3.335(9)	3.242(1)–3.267(1)	3.247(1)–3.284(1)
*RE*4–*Tt*2	2.988(1)	3.02(1)	2.940(2)	2.924(1)
*RE*4–Sb1	3.334(1)–3.378(1)	3.292(8)–3.364(8)	3.257(1)–3.310(1)	3.273(1)–3.321(1)
Sb1–*RE*	3.296(1)–3.609(1)	3.25(1)–3.517(6)	3.216(1)–3.550(1)	3.227(1)–3.532(1)
*Tt*2–*RE*	2.988(1)–3.292(2)	2.980(5)–3.25(2)	2.940(2)–3.193(2)	2.924(1)–3.164(1)

[a] The labels Sb1 and *Tt*2 refer to the majority component in these sites which may accommodate a mixture of both atoms.

8.2.3. Band Structure Calculation

Tight-binding linear muffin tin orbital (TB-LMTO) band structure calculations were performed within the local density and atomic spheres approximations using the Stuttgart TB-LMTO program as before.[20] To understand the bonding and solubility range in $La_5Ge_xSb_{3-x}$, three idealized ordered models at different levels of substitution x were examined: (i) $La_5Ge_{0.5}Sb_{2.5}$ (with Ge atoms in half of the 4*c* sites) was modeled in space group $P2_1/m$, (ii) La_5GeSb_2 (with Ge atoms in the 4*c* sites and Sb atoms in the 8*d* sites) was retained in space group *Pnma*, and (iii) $La_5Ge_{1.5}Sb_{1.5}$ (with Ge atoms in the 4*c* sites and a quarter of the 8*d* sites) was modeled in space group $P\bar{1}$. The density of states (DOS) curves were calculated with use of a basis set consisting of La 6s/6p/5d/4f, Ge 4s/4p/4d, and Sb 5s/5p/5d/4f orbitals, with the La 6p, Ge 4d, and Sb 5d/4f orbitals being downfolded. Integrations in reciprocal space were carried out with an improved tetrahedron method over 36 irreducible k points for the model in *Pnma*. Inspection of the DOS curves revealed that the La 4f orbitals only contribute to conduction states, located well above the Fermi level, and do not participate in bonding interactions below the E_f. For the purpose of determining crystal orbital Hamilton population (COHP) curves, these La 4f orbitals were additionally downfolded. This downfolding was necessary because the La 4f orbitals are too diffuse to allow overlap populations to be computed. (A representative DOS curve for La_5GeSb_2 with downfolded La 4f orbitals is shown in Figure A3–1 in Appendix 3.)

8.2.4. Magnetic Measurements

Samples with a constant substitutional level, $RE_5Tt_{1.2}Sb_{1.8}$, were synthesized according to the procedure described earlier and their purity was checked by powder X-ray diffraction. An additional sample, $Pr_5Ge_{1.7}Sb_{1.3}$, was prepared for comparison to $Pr_5Ge_{1.2}Sb_{1.8}$ to study the effect of different substitutional levels. Measurements of dc magnetic susceptibility were made on powders of all samples except for the Ce-containing ones (which contained a small amount of Ce_2Sb impurity) between 2 and 300 K on a Quantum Design 9T–PPMS dc magnetometer / ac susceptometer. All susceptibility values were corrected for contributions from the holder and underlying sample diamagnetism. Measurements of ac magnetic susceptibility were also made with a driving amplitude of 1 Oe and a frequency of 1000 Hz.

8.3. Results and Discussion

8.3.1. Phase Diagram

Because limited information was previously available about phase relationships in the *RE*–Si–Sb systems (whose phase diagrams have been determined only for *RE* = Ce, Dy, and Y),[21–23] initial investigations were carried out to elaborate the La–Si–Sb phase diagram. Through powder X-ray diffraction and EDX analysis of 37 arc-melted samples, the isothermal section at 800 °C was constructed (Figure 8–2). The existence of expected binary La–Si and La–Sb phases and the absence of binary Si–Sb phases were confirmed.[24] In the La–Si system, two Si-rich phases exhibited slight homogeneity ranges. In $LaSi_2$ ($ThSi_2$-type, space group $I4_1/amd$), a deficiency of up to 10% Si was observed. In $LaSi_{2-x}$ ($GdSi_{1.4}$-type, space group *Imma*), a homogeneity range of $0.3 \leq x \leq 0.5$ was

found. Of the two modifications known for LaSi, only the high-temperature form (FeB-b-type, space group *Pnma*) was formed. La_5Si_3 also adopts two possible modifications, but only the tetragonal form (Cr_5B_3-type, space group *I*4/*mcm*) was observed. In the La–Sb system, the phases formed at 800 °C are consistent with our recent investigation of the La–Ti–Sb phase diagram.[24]

A new ternary phase $La_5Si_xSb_{3-x}$ was identified in the vicinity of the composition La:Si:Sb = 65:15:20 in the La–Si–Sb phase diagram. The germanium-containing analogue $La_5Ge_xSb_{3-x}$ was also identified in the La–Ge–Sb phase diagram, which is more complicated and whose investigation is still in progress.[25] Because La_5Sb_3 and La_5Ge_3 are isostructural, both adopting the hexagonal Mn_5Si_3-type structure, the initial thought was that the ternary phase represented a solid solution of the component binary phases. However, analysis of the products obtained from arc-melting reactions with various loading compositions $La_5Ge_xSb_{3-x}$ ($0 \le x \le 3$) revealed that the solid solubility extends only within the range $0.9 \le x \le 1.6$ (Figure 8–1), and that the structure is of the orthorhombic β-Yb_5Sb_3-type, different from those of the parent binaries RE_5Sb_3 (Mn_5Si_3-type), RE_5Si_3 (Cr_5B_3-type), or RE_5Ge_3 (Mn_5Si_3-type) for *RE* = La–Nd.

These ternary phases represent the first examples of cases where the β-Yb_5Sb_3-type structure can be stabilized by replacement of Sb with another p-block element instead of a transition metal.[7,12–15] Interestingly, attempts to synthesize the analogous ternary $RE_5Tt_xSb_{3-x}$ (*Tt* = Si, Ge) phases with other rare-earth metals indicated that the range of substitution is limited to the earlier or larger members (*RE* = La–Nd), in contrast to the $RE_5M_xSb_{3-x}$ (*M* = Fe, Co, Ni, Cu)

phases which are stabilized in the presence of the later or smaller members (*RE* = Gd–Er, Y). Examples of compounds characterized in this study by X-ray diffraction and elemental analysis are listed in Table 8–1.

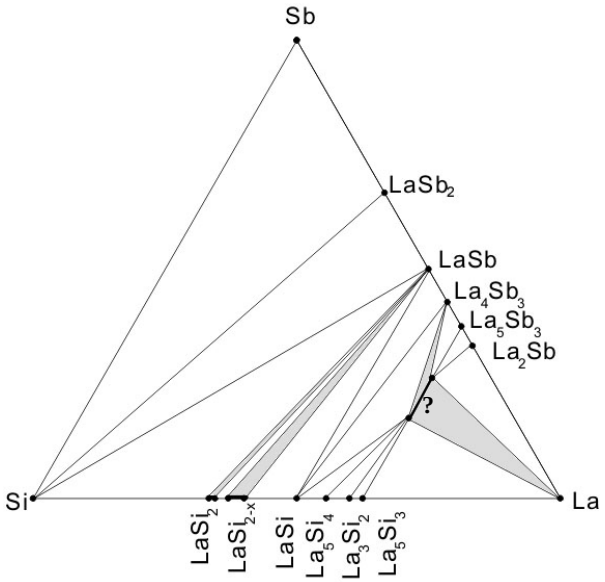

Figure 8–2. Isothermal section at 800 °C for the La–Si–Sb system. The ternary phase is identified to be $La_5Si_xSb_{3-x}$, with a homogeneity width estimated to be similar to that in $La_5Ge_xSb_{3-x}$ ($0.9 \le x \le 1.6$).

Among the binary antimonides RE_5Sb_3, the Mn_5Si_3-type structure is found for the majority of the trivalent *RE* elements.[8] The hydrogen-free β-Yb_5Sb_3-type structure has now been established with certainty for two trivalent *RE* members (Er and Tm), and the closely related Y_5Bi_3-type structure is found for *RE* = Er, Tm, and Lu.[9] Some of these binary antimonides (e.g., Y_5Sb_3, Er_5Sb_3) or the related ternary variants (e.g., $Gd_5Ni_xBi_{3-x}$) undergo complex temperature-dependent phase transitions among these structure types.[7,12,14] To test whether polymorphism might occur in the $RE_5Tt_xSb_{3-x}$ series, the thermal stability of two representative members, $Pr_5Si_xSb_{3-x}$ and $Pr_5Ge_xSb_{3-x}$, was examined at

temperatures lower than their original formation at 800 ºC. Annealing them at 600 ºC or 400 ºC for two-week periods did not reveal any changes in the powder X-ray diffraction patterns. This observation suggests that either $RE_5Tt_xSb_{3-x}$ undergoes no phase transformation at lower temperature.

8.3.2. Structure and Bonding

The crystal structures of eight members of the $RE_5Tt_xSb_{3-x}$ series have been determined by single-crystal or powder X-ray diffraction in the orthorhombic space group *Pnma* (Table 8–2; Figures A3–2 and A3–3). The structure type adopted, that of β-Yb_5Sb_3,[17] has a ternary ordered variant called the Ce_5RuGe_2-type where Ru occupies a 4*c* site and Ge an 8*d* site in place of the Sb atoms in the former.[26] Although analogous ternary germanides, antimonides, and bismuthides were initially assumed to be similarly ordered, it is now recognized that they can exhibit a relatively wide homogeneity range arising from disorder within these sites.[7,14,27,28] In transition-metal-containing antimonides $RE_5M_xSb_{3-x}$ (*RE* = Gd–Er, Y; *M* = Fe, Co, Ni, Cu), the value of *x* is always smaller than 1 and the mixing of *M* and Sb atoms occurs only in the 4*c* site while the 8*d* site accommodates Sb atoms exclusively.[7,12–15] In contrast, in the new tetrel-containing antimonides $RE_5Tt_xSb_{3-x}$ (*RE* = La–Nd; *Tt* = Si, Ge), the value of *x* is normally *larger* than 1 and the situation is reversed, with the 4*c* site being occupied only by *Tt* atoms while the 8*d* site accommodates a mixture of *Tt* atoms with the majority Sb atoms (Table 8–3).

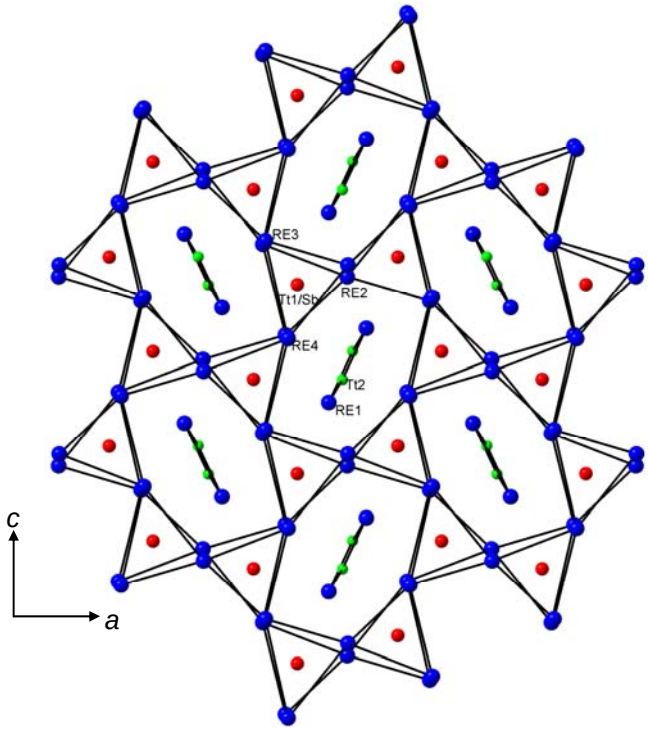

Figure 8–3. Structure of $RE_5Tt_xSb_{3-x}$ (*RE* = La–Nd; *Tt* = Si, Ge), emphasizing the connectivity of RE_6 trigonal prisms, viewed down the *b* direction. The blue circles are *RE* atoms, the green circles are *Tt*2 atoms (4*c*), and the red circles are mixture of *Tt*1 and Sb atoms (8*d*).

A simple way to visualize the structure of $RE_5Tt_xSb_{3-x}$ is to assemble it from RE_6 trigonal prisms (Figure 8–3). These trigonal prisms share opposite triangular faces along the *b* direction to form infinite columns, which then fuse along edges to form a three-dimensional framework outlining large distorted hexagonal channels. The mixture of *Tt*/Sb atoms (8*d* site, labelled as *Tt*1/Sb1 but referred to simply as Sb1 for brevity in subsequent discussion) fills the centres of the RE_6 trigonal prisms, whereas *Tt* atoms (4*c* site, labelled as *Tt*2) are connected to *RE*1 atoms to form a ribbon of [RE_2Tt] rhombs extending down the large hexagonal channels (Figure 8–4a).

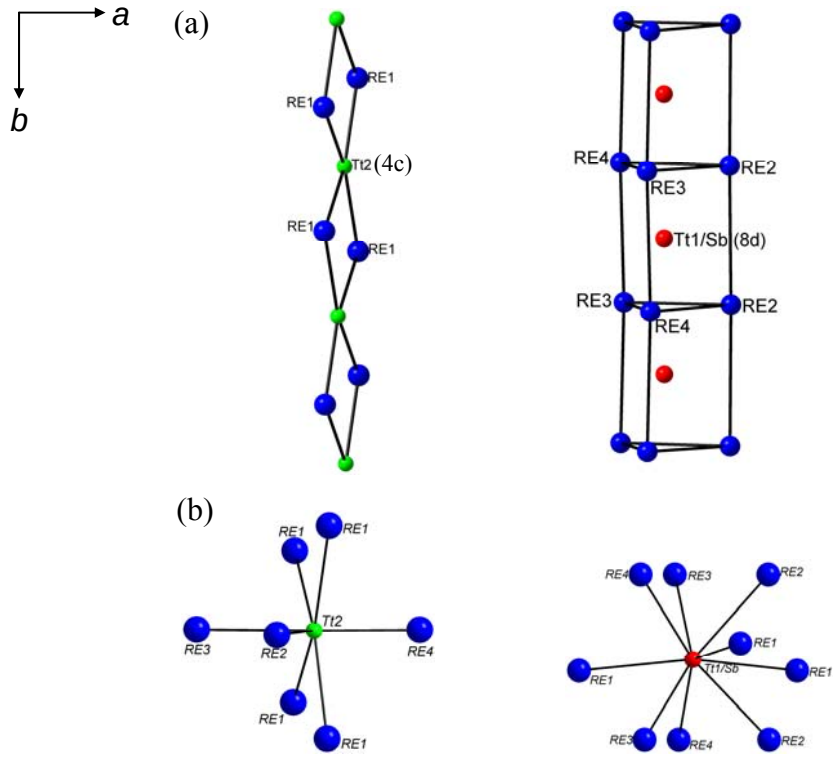

Figure 8–4. (a) One-dimensional ribbons of [RE_2Tt] rhombs and columns of confacial RE_6 trigonal prisms extending along the *b* direction. (b) Local coordination environments around the *Tt*2 (4*c*) and *Tt*1/Sb1 (8*d*) sites.

The distinctions noted between the $RE_5Tt_xSb_{3-x}$ (*RE* = La–Nd; *Tt* = Si, Ge; usually $x \geq 1$) and $RE_5M_xSb_{3-x}$ (*RE* = Gd–Er, Y; *M* = Fe, Co, Ni, Cu; $x \leq 1$) series indicate that size effects, perhaps in the form of radius ratio rules, may be one factor controlling the formation of this structure. Examination of the local coordination environments in $RE_5Tt_xSb_{3-x}$ (Figure 8–4b) clearly reveals that the 8*d* site (CN9, tricapped trigonal prismatic) is preferred by the larger Sb atoms whereas the 4c site (CN7, capped distorted octahedral) accommodates only the smaller *Tt* atoms. The limiting radius ratios are 0.73 for a tricapped trigonal prismatic site and 0.59 for a capped octahedral site.[29] As confirmed by inspection of Table 8–4, the distances of surrounding *RE* atoms to the Sb1 site (3.2–3.6 Å)

are generally longer than those to the *Tt*2 site (2.9–3.3 Å), consistent with the relative sizes of atoms (Pauling metallic radii R_1 of 1.17 Å for Si, 1.24 Å for Ge, and 1.39 Å for Sb).[30] If neutral atoms are assumed and Pauling metallic radii are chosen, the ratio r_{Sb}/r_{RE} always lies, no matter what the *RE* metal, in the range 0.82–0.88, which exceeds the critical value of 0.73 required to support the occupation of Sb atoms within the tricapped trigonal prismatic (8*d*) sites, consistent with the site preference observed in either the $RE_5Tt_xSb_{3-x}$ or $RE_5M_xSb_{3-x}$ series. Similarly, the ratios r_{Si}/r_{RE} = 0.69–0.72 for $RE_5Si_xSb_{3-x}$ (*RE* = La–Nd), r_{Ge}/r_{RE} = 0.74–0.76 for $RE_5Ge_xSb_{3-x}$ (*RE* = La–Nd), and r_M/r_{RE} = 0.71–0.74 for $RE_5M_xSb_{3-x}$ (*RE* = Gd–Er, Y) exceed the critical value of 0.59 required to fill the capped octahedral (4*c*) sites. It is tempting to suggest that the Ge atoms in $RE_5Ge_xSb_{3-x}$ can mix in the 8*d* sites because r_{Ge}/r_{RE} also exceeds 0.73, but then the same line of argument fails to explain the observed site preferences of Si atoms in $RE_5Si_xSb_{3-x}$ or *M* atoms in $RE_5M_xSb_{3-x}$. However, it does not account for the existence, for example, of $RE_5Tt_xSb_{3-x}$ for the late *RE*, or $RE_5M_xSb_{3-x}$ for the early *RE* metals, since their radius ratios do not seem to preclude their formation. Lastly, despite their formation with the later or smaller *RE* elements, the corresponding distances in $RE_5M_xSb_{3-x}$ (*M* = Fe, Co, Ni, Cu) are surprisingly not much shorter (e.g., 3.1–3.5 Å (Sb–Y) and 2.9–3.1 Å (Ni/Sb–Y) in $Y_5Ni_{0.38}Sb_{2.62}$) than in $RE_5Tt_xSb_{3-x}$.[12]

One way to improve the arguments based on size effects is to consider the role of electron transfer. Although the approximation of neutral atoms and metallic radii is certainly more realistic than that of fully charged species and

ionic radii, it is clear that some degree of electron transfer must take place, but the directions will differ depending on the presence of a main-group vs. a transition metal. In $RE_5Tt_xSb_{3-x}$, the *RE* atoms will donate electrons to both *Tt* and Sb atoms, whereas in $RE_5M_xSb_{3-x}$, the *RE* and *M* atoms will donate electrons to the Sb atoms. That is, the *Tt* atoms are likely anionic and have larger radii than the neutral species, whereas the *M* atoms are cationic and have smaller radii than the neutral species. In the discussion above, the key ambiguity can be traced to the fact that the r_{Tt}/r_{RE} or r_M/r_{RE} ratios are all quite close to 0.73, the critical value above which mixing of *Tt* atoms in the 8*d* site may take place. If r_{Tt} is replaced with larger and r_M with smaller values, then there should be an enhanced differentiation in the radius ratios, to the extent that r_{Tt}/r_{RE} may become >0.73 in $RE_5Tt_xSb_{3-x}$ and r_M/r_{RE} may become <0.73 in $RE_5M_xSb_{3-x}$. These corrections then account for the occurrence of mixing of *Tt* but not *M* atoms in the 8*d* site.

Interestingly, the lower bound for *x* was actually found to be slightly less than 1 in the investigation of the solid solubility in $La_5Ge_xSb_{3-x}$ ($0.9 \leq x \leq 1.6$). The Ge-poorest end-member for the solid solution in the Ce-containing series, $Ce_5Ge_{0.9}Sb_{2.1}$, showed the expected low Ge content (Table 8–1). In the crystal structure of $Ce_5Ge_{0.9}Sb_{2.1}$ (Table 8–3), the site occupation is now analogous to that in $RE_5M_xSb_{3-x}$ (*M* = Fe, Co, Ni, Cu), with 10% of the Ge atoms within the [RE_2Ge] rhombs statistically substituted by Sb atoms.

Closer consideration of the electronic structure and bonding is helpful in determining what other factors besides size effects influence the structural stability in $RE_5Tt_xSb_{3-x}$ and $RE_5M_xSb_{3-x}$. Unlike the hydrogen-stabilized β-

Yb_5Sb_3-type binary antimonides formed with divalent *RE* metals (e.g., Eu_5Sb_3H, Yb_5Sb_3H),[10,11] these ternary antimonides are not electron-precise. According to the Zintl-Klemm concept, electron counting for the idealized stoichiometric model "La_5GeSb_2" containing isolated Ge and Sb atoms implies the formulation $(La^{3+})_5(Ge^{4-})(Sb^{3-})_2(e^-)_5$, the five excess electrons remaining on the La atoms for use in metal-metal bonding. The 4*c* and 8*d* site preferences has been confirmed through previous band structure calculations on both binary (Tm_5Sb_3, Y_5Sb_3) and ternary antimonides ($Y_5Ni_xSb_{3-x}$) with this structure type.[9,12] Calculations on a hypothetical model of $Y_5Ni_xSb_{3-x}$ in which Ni atoms are placed in the 8*d* site have suggested that doing so would destabilize the heteroatomic Y–Ni and Y–Sb interactions; structural relaxation to counteract these effects are also disfavoured by destabilizing the Y–Y interactions.[12]

To evaluate the site preferences in $RE_5Tt_xSb_{3-x}$, three ordered models of $La_5Ge_xSb_{3-x}$ were examined in which the Ge atoms occupy: (i) half of the 4*c* sites (x = 0.5 or $La_5Ge_{0.5}Sb_{2.5}$), (ii) all of the 4*c* sites (x = 1 or La_5GeSb_2), or (iii) all of the 4*c* and one-quarter of the 8*d* sites (x = 1.5 or $La_5Ge_{1.5}Sb_{1.5}$). The density of states (DOS) curves calculated for these models are similar (Figure 8–5). Although most of the La states are unoccupied and lie above the Fermi level, there are significant contributions below the Fermi level which mix with the Ge and Sb states, indicating that La–Ge and La–Sb bonding interactions will be important in stabilizing the structure. The crystal orbital Hamilton population (–COHP) curves for La–La, La–Ge, and La–Sb interactions for La_5GeSb_2 are shown in Figure 8–6. Homoatomic La–La bonding interactions are found

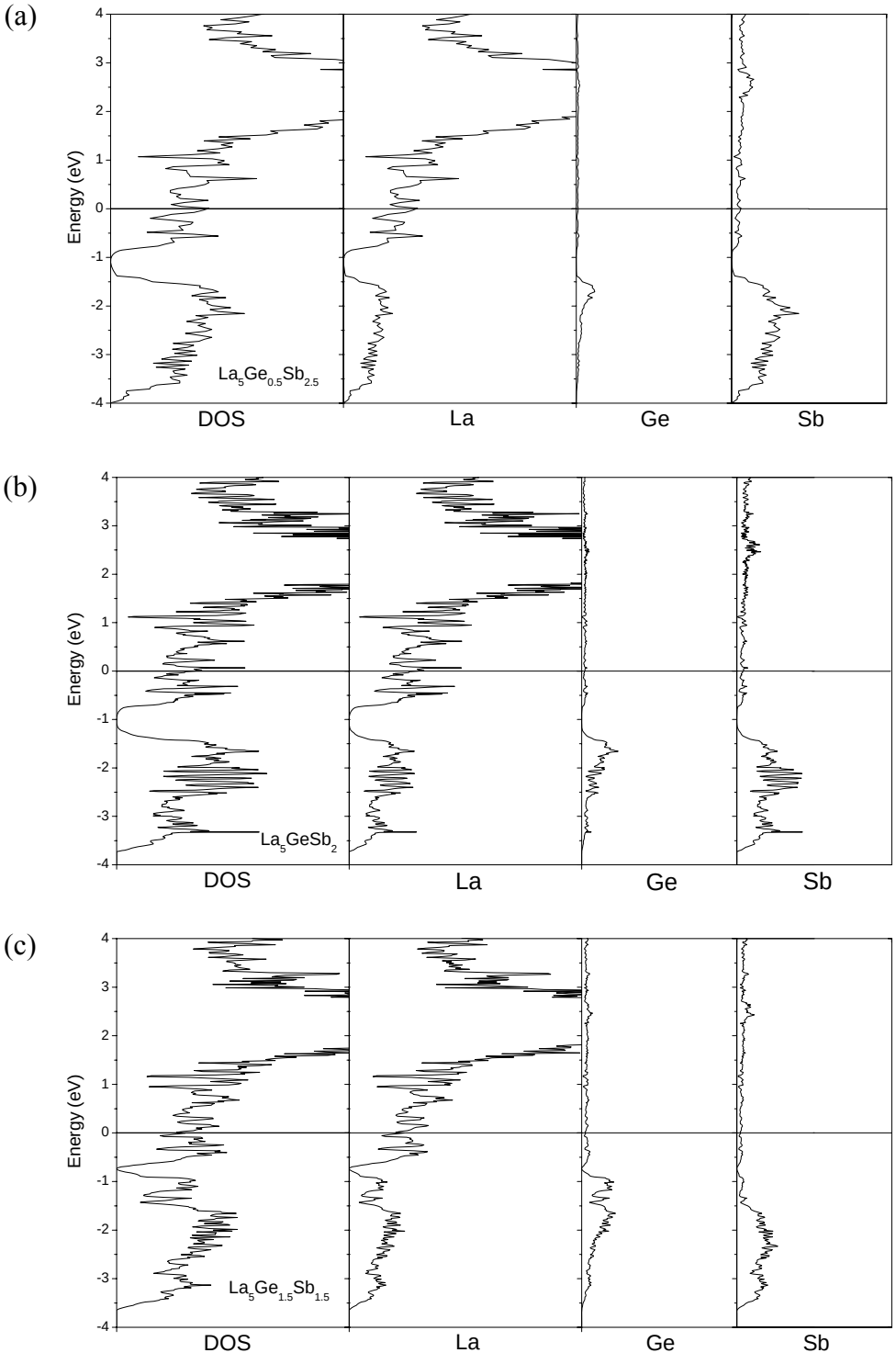

Figure 8–5. Density of states (DOS) and its La, Ge, and Sb projections for ordered models of (a) $La_5Ge_{0.5}Sb_{2.5}$, (b) La_5GeSb_2, and (c) $La_5Ge_{1.5}Sb_{1.5}$. The horizontal line at 0 eV marks the Fermi level.

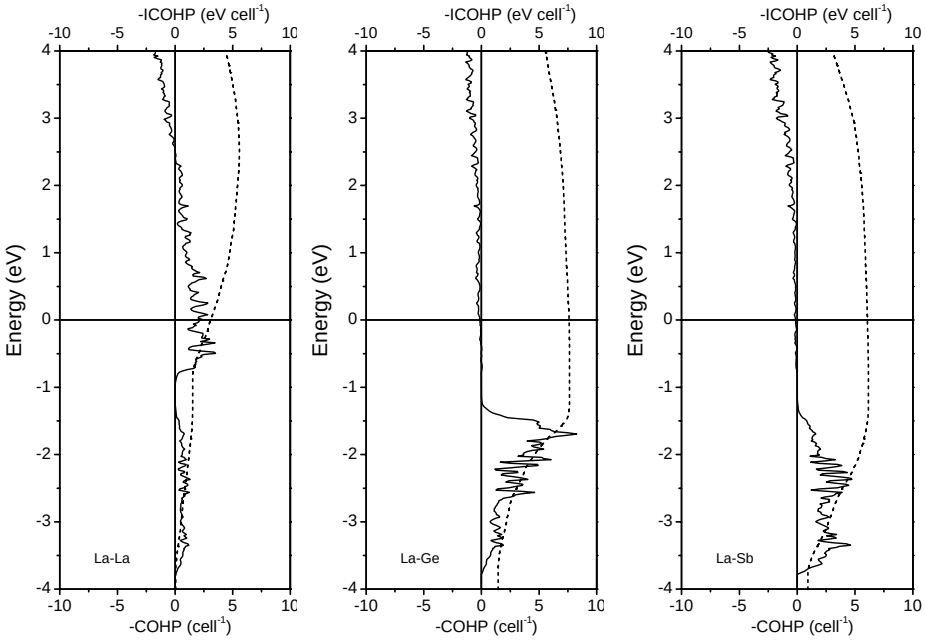

Figure 8–6. Crystal orbital Hamilton population (COHP) curves (solid line) and integrated COHP curves (dotted line) for (a) La–La, (b) La–Ge, and (c) La–Sb contacts in La_5GeSb_2. The horizontal line at 0 eV marks the Fermi level.

primarily above the gap at –1 eV, whereas strong heteroatomic La–Ge and La–Sb bonding interactions are found below. Increasing the degree of Ge substitution, from $x = 0.5$ to $x = 1.5$, reduces the number of electrons in the system, so that the Fermi level is shifted down closer to the gap near –1 eV (Figure 8–5). However, a rigid band approximation cannot be simply applied here to form conclusions about the change in bond strengths, because the relative contribution of Ge-based states below the Fermi level also becomes more important. The average integrated COHP values (–ICOHP), which are a measure of bond strength, for these interactions in the three models are listed in Table 8–5. The average –ICOHP values for La–La interactions differ slightly, but those for La–Ge and La–

Table 8–5. Average integrated crystal orbital Hamilton population (–ICOHP) (eVbond^{-1}) in different models for $La_5Ge_xSb_{3-x}$.

Contact [a]	$La_5Ge_{0.5}Sb_{2.5}$	La_5GeSb_2	$La_5Ge_{1.5}Sb_{1.5}$
La–La	0.183	0.238	0.153
La–Ge	0.196	1.086	0.638
La–Sb	0.258	0.675	0.419

[a] For distances less than 4.2 Å.

Sb change dramatically. Optimal bonding is observed in La_5GeSb_2 where all the –ICOHP values are maximized. In contrast, the weakness of all contacts in hypothetical $La_5Ge_{0.5}Sb_{2.5}$ strongly disfavours its formation; for example, La–Ge contacts are inherently weakest (0.196 eV/bond). In $La_5Ge_{1.5}Sb_{1.5}$, both La–Ge and La–Sb bonding are also weakened relative to La_5GeSb_2, but not to the extreme extent as in $La_5Ge_{0.5}Sb_{2.5}$. Although this calculation shows that the composition can deviate from La_5GeSb_2, it is more favourable to do so towards the Ge-rich instead of the Ge-poor range, consistent with the observed solubility range of $0.9 \leq x \leq 1.6$ in $La_5Ge_xSb_{3-x}$.

8.3.3. Magnetic Properties

Magnetic measurements have been made for several representatives of the $RE_5Tt_xSb_{3-x}$ series, with the expectation that the only contributions to the magnetism will originate from f-electrons on the *RE* atoms. The La-containing compounds, $La_5Si_{1.2}Sb_{1.8}$ and $La_5Ge_{1.2}Sb_{1.8}$, exhibit temperature-independent Pauling paramagnetism with little dependence on the identity of the tetrel (χ_o = 0.001–0.002 emu/mol), consistent with trivalent La and the absence of localized

unpaired electrons (Figure A3–4 in Appendix 3). The Ce-containing compounds could not be prepared in pure form to permit measurements. For the Pr- and Nd-containing compounds, the zero-field-cooled dc magnetic susceptibilities (measured under an applied field of H = 5000 Oe), field-dependent magnetizations (measured at different temperatures), and ac susceptibilities indicate complex magnetic behaviour. Transition temperatures were located either from dc or ac magnetic susceptibility curves (Table 8–6).

Table 8–6. Summary of magnetic data for $RE_5Tt_xSb_{3-x}$ (RE = Pr, Nd; Tt = Si, Ge).

	$Pr_5Si_{1.2}Sb_{1.8}$	$Pr_5Ge_{1.2}Sb_{1.8}$	$Pr_5Ge_{1.7}Sb_{1.3}$	$Nd_5Si_{1.2}Sb_{1.8}$	$Nd_5Ge_{1.2}Sb_{1.8}$
T_C (K) from:					
χ_{dc} curve	9, 30	4, 31	4, 30	10, 20, 62	11, 22, 65
χ'_{ac} curve	16, 28	not measured	29	25, 40, 62	15, 27, 64
θ_p (K)	17.2(6)	32.2(2)	20.8(4)	58.0(7)	58.8(3)
$\mu_{eff, meas}$ (μ_B/RE)	3.56(1)	3.69(1)	3.81(1)	3.75(1)	3.69(1)
$\mu_{eff, theor}$ for RE^{3+} (μ_B)	3.58	3.58	3.58	3.62	3.62

Two members in the $Pr_5Ge_xSb_{3-x}$ series were measured to examine the effect of different Ge contents (x = 1.2 and 1.7). In $Pr_5Ge_{1.2}Sb_{1.8}$, the magnetic susceptibility curve shows two transitions at 4 K and ~30 K (Figure 8–7a). When the Ge content increases in $Pr_5Ge_{1.7}Sb_{1.3}$, the magnetic susceptibility is generally attenuated but the ~30 K transition becomes more prominent. The high-temperature paramagnetic regions of both curves are similar. The linear portions of the inverse magnetic susceptibility can be fit to the Curie-Weiss law, $\chi = C/(T-\theta_p)$. The effective magnetic moments (3.7 or 3.8 μ_B) derived from the Curie

constant are slightly greater than the theoretical free-ion value for Pr^{3+} (3.58 μ_B) and the Weiss parameters θ_p are positive (32 or 21 K) for $Pr_5Ge_{1.2}Sb_{1.8}$ and $Pr_5Ge_{1.7}Sb_{1.3}$, respectively, indicating ferromagnetic coupling of the Pr^{3+} moments. Despite these similarities, the isothermal magnetization curves reveal possibly different low-temperature magnetic structures: an approach to saturation for $Pr_5Ge_{1.2}Sb_{1.8}$ (Figure 8–7b) but metamagnetic behaviour for $Pr_5Ge_{1.7}Sb_{1.3}$ (Figure 8–7c) below ~30 K, and the appearance of hysteresis for both compounds at 2 K.

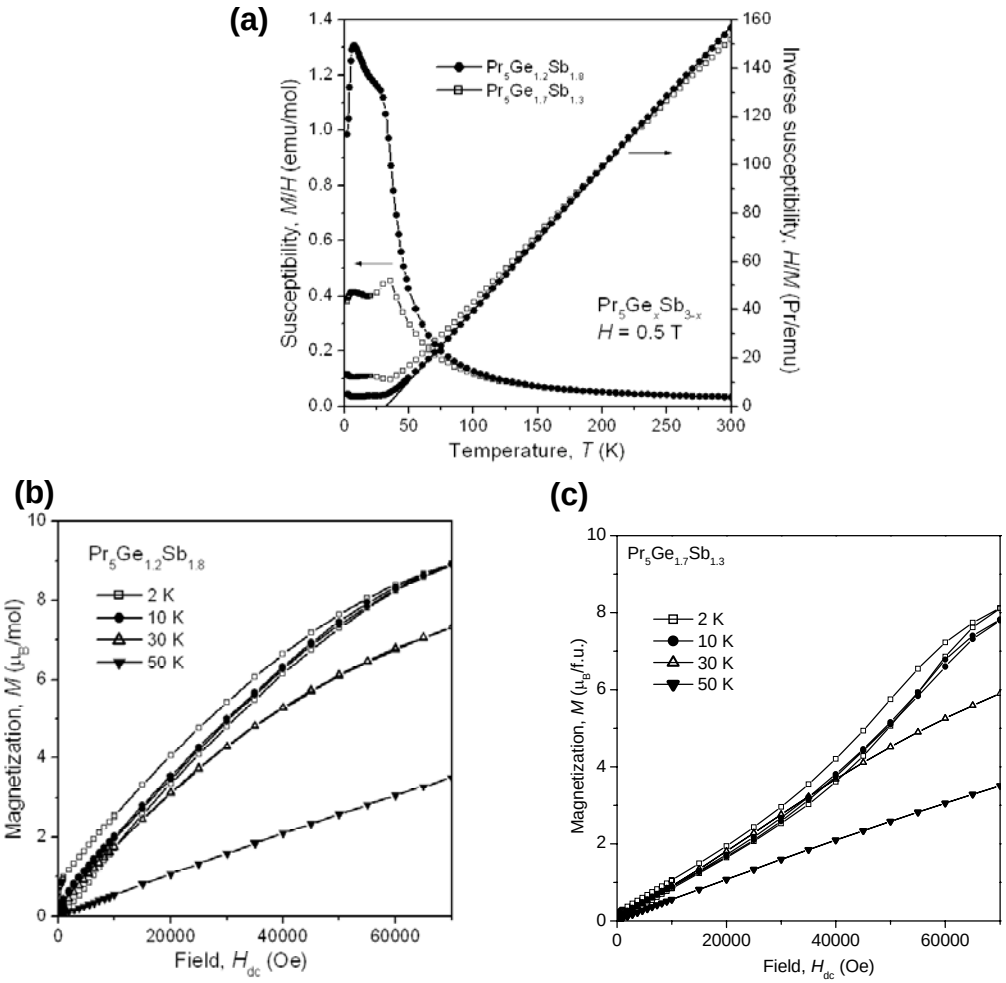

Figure 8–7. Magnetic data for $Pr_5Ge_xSb_{3-x}$ (x = 1.2, 1.7). (a) Magnetic susceptibility and its inverse, with a fit to the Curie-Weiss law indicated for $Pr_5Ge_{1.2}Sb_{1.7}$ by the solid line. (b) Isothermal magnetization at different temperatures for $Pr_5Ge_{1.2}Sb_{1.7}$. (c) Isothermal magnetization at different temperatures for $Pr_5Ge_{1.7}Sb_{1.3}$.

The magnetic behaviour for $Pr_5Si_{1.2}Sb_{1.8}$ resembles that for $Pr_5Ge_{1.2}Sb_{1.8}$ except that the ~30 K transition is strongly suppressed (although it is still barely visible in the ac susceptibility curve) and the Weiss parameter has decreased from 32 K to 17 K (Figure 8–8a). The magnetization curves are also similar (Figure 8–8b). The magnetic behaviour of $Nd_5Si_{1.2}Sb_{1.8}$ and $Nd_5Ge_{1.2}Sb_{1.8}$ is quite complex (Figures 8–8c–8f). There are now at least three transitions, some ill-defined, seen in the magnetic susceptibility curves. Fitting of the inverse magnetic susceptibility in the paramagnetic regions yields similar effective magnetic moments (3.62 μ_B) and Weiss parameters (58–59 K) for both compounds. On the other hand, the magnetization curves show several step-like features at low temperatures, indicative of multiple metamagnetic states as a function of applied field.

Comparison to the parent binaries (RE_5Si_3, RE_5Ge_3, or RE_5Sb_3) provides little guidance because they adopt different structure types from $RE_5Tt_xSb_{3-x}$. For example, the Mn_5Si_3-type phases RE_5Ge_3[31–34] and RE_5Sb_3 (*RE* = Pr, Nd)[35] order antiferromagnetically, whereas the Cr_5B_3-type phases RE_5Si_3 (*RE* = Pr, Nd) order ferromagnetically.[32,36,37] Magnetic measurements on related ternary antimonides with the β-Yb_5Sb_3-type structure are limited to those on Gd_5NiSb_2, where ferromagnetic ordering at 115 K was observed and the contribution of Ni atoms to the effective magnetic moment was considered to be negligible.[7] An important feature in these β-Yb_5Sb_3-type compounds is the presence of many close *RE*–*RE* contacts, as short as 3.4 Å in $RE_5Tt_xSb_{3-x}$ (Table 8–4), which gives rise to complex and strong magnetic interactions through direct coupling, in addition to indirect coupling via spin polarization of the conduction electrons.

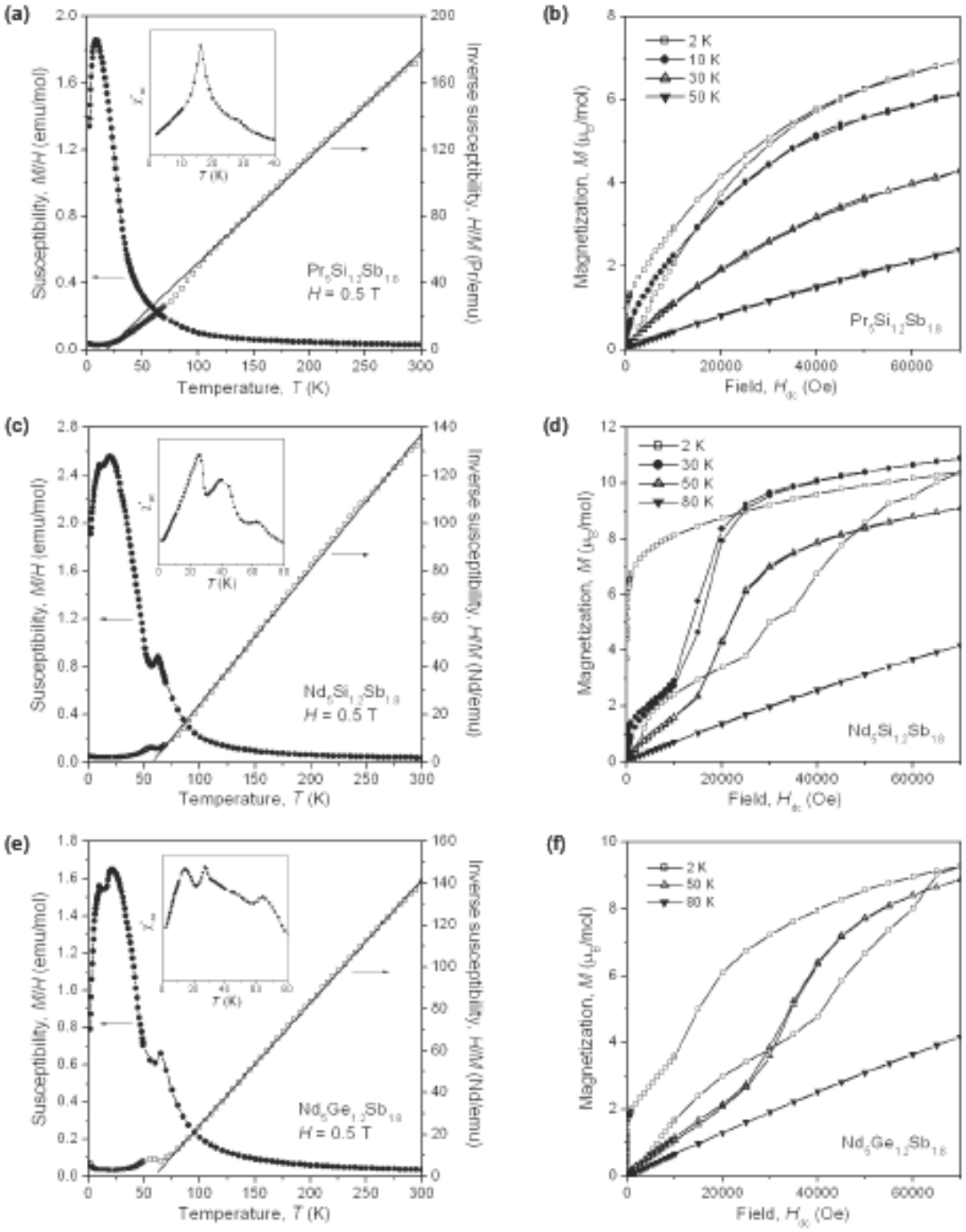

Figure 8–8. Magnetic data for (a)–(b) $Pr_5Si_{1.2}Sb_{1.8}$, (c)–(d) $Nd_5Si_{1.2}Sb_{1.8}$, and (e)–(f) $Nd_5Ge_{1.2}Sb_{1.8}$. The left panels show the zero-field-cooled dc magnetic susceptibility and its inverse as a function of temperature (with the insets highlighting low-temperature transitions in the ac magnetic susceptibility), and the right panels show isothermal magnetization curves at various temperatures.

8.4. Conclusions

The partial substitution of Sb with Si or Ge in $RE_5Tt_xSb_{3-x}$ (*RE* = earlier rare-earth) stabilizes the formation of β-Yb_5Sb_3-type structure, previously found for only a few binary rare-earth antimonides RE_5Sb_3 (*RE* = later rare-earth) and some ternary transition-metal antimonides $RE_5M_xSb_{3-x}$. The range of solid solubility determined for a representative series, $La_5Ge_xSb_{3-x}$, is $0.9 \leq x \leq 1.6$. The disorder arises largely from the partial substitution of *Tt* atoms into Sb 8*d* sites centred within RE_6 trigonal prisms. Columns of confacial RE_6 trigonal prisms are connected to each other through edge-sharing to form a three-dimensional framework outlining hexagonal channels filled by ribbons of [RE_2Tt] rhombs. Band structure calculations provide qualitative support for these site preferences. Magnetic measurements on $RE_5Tt_xSb_{3-x}$ (*RE* = La, Pr, Nd) revealed Pauli paramagnetic behaviour for the La members and multiple low-temperature transitions (likely involving ferromagnetic ordering) for the Pr and Nd members.

8.5. References

(1) Gschneidner Jr., K. A.; Pecharsky, V. K. *Annu. Rev. Mater. Sci.* **2000**, *30*, 387–429.

(2) Mozharivskyj, Y.; Choe, W.; Pecharsky, A. O.; Miller, G. J. *J. Am. Chem. Soc.* **2003**, *125*, 15183–15190.

(3) Misra, S.; Miller, G. J. *J. Am. Chem. Soc.* **2008**, *130*, 13900–13911.

(4) Pecharsky, V. K.; Gschneidner, K. A. Jr. *J. Alloys Compd.* **1997**, *260*, 98–106.

(5) Wu, L.-M.; Kim, S.-H.; Seo, D.-K. *J. Am. Chem. Soc.* **2005**, *127*, 15682–15683.

(6) Chernyshov, A. S.; Mudryk, Ya. S.; Pecharsky, V. K.; Gschneidner, K. A. Jr. *J. Appl. Phys.* **2006**, *99*, 08Q102-1–08Q102-3.

(7) Svitlyk, V.; Fei, F.; Mozharivskyj, Y. *J. Solid State Chem.* **2008**, *181*, 1080–1086.

(8) Sologub, O. L.; Salamakha, P. S. In *Handbook on the Physics and Chemistry of Rare Earths*; Gschneidner, K. A., Jr., Bünzli, J.-C. G., Pecharsky, V. K., Eds.; Elsevier: Amsterdam, 2003; Vol. 33, pp 35–146.

(9) Gupta, S.; León-Escamilla, E. A.; Wang, F.; Miller, G. J.; Corbett, J. D. *Inorg. Chem.* **2009**, *48*, 4362–4371.

(10) León-Escamilla, E. A.; Corbett, J. D. *J. Alloys Compd.* **1998**, *265*, 104–114.

(11) León-Escamilla, E. A.; Corbett, J. D. *Chem. Mater.* **2006**, *18*, 4782–4792.

(12) Mozharivskyj, Y.; Franzen, H. F. *J. Alloys Compd.* **2001**, *319*, 100–107.

(13) Morozkin, A. V.; Nirmala, R.; Malik, S. K. *J. Alloys Compd.* **2005**, *394*, L9–L11.

(14) Zelinska, M.; Zhak, O.; Oryshchyn, S.; Babizhetskyy, V.; Pivan, J.-Y.; Guérin, R. *J. Alloys Compd.* **2007**, *437*, 133–139.

(15) Verbovytsky, Yu.; Łątka, K. *J. Alloys Compd.* **2008**, *450*, 272–275.

(16) Sheldrick, G. M. *SHELXTL*, Version 6.12; Bruker AXS Inc.: Madison, WI, 2001.

(17) Brunton, G. D.; Steinfink, H. *Inorg. Chem.* **1971**, *10*, 2301–2303.

(18) Hunter, B. *LHPM-Rietica*, version 1.7.7, International Union of Crystallography Commission on Powder Diffraction Newsletter, no. 20 (summer), 1998 (www.rietica.org).

(19) Gelato, L. M.; Parthé, E. *J. Appl. Crystallogr.* **1987**, *20*, 139–143.

(20) Tank, R.; Jepsen, O.; Burkhardt, A.; Andersen, O. K. *TB-LMTO-ASA Program*, version 4.7, Max Planck Institut für Festkörperforschung, Stuttgart, 1998.

(21) Stetskiv, A. O.; Pavlyuk, V. V.; Bodak, O. I. *Ukr. Khim. Zh.* **1999**, *65*, 87–89.

(22) Morozkin, A. V. *J. Alloys Compd.* **2003**, *358*, L6–L8.

(23) Kozlov, A. Yu.; Pavlyuk, V. V. *J. Alloys Compd.* **2004**, *370*, 192–197.

(24) a) Villars, P., Ed., *Pauling File Binaries Edition*, Version 1.0; ASM International: Materials Park, OH, 2002; b) Bie, H.; Moore, S. H. D.; Piercey, D. G.; Tkachuk, A. V.; Zelinska, O. Ya.; Mar, A. *J. Solid State Chem.* **2007**, *180*, 2216–2224.

(25) Bie, H.; Mar, A. *Chem. – Asian J.*, in press.

(26) Gladyshevskii, R. E.; Cenzual, K.; Zhao, J. T.; Parthé, E. *Acta Crystallogr., Sect. C: Cryst. Struct. Commun.* **1992**, *48*, 221–225.

(27) Sologub, O. L.; Salamakha, P. S.; Godart, C. *J. Alloys Compd.* **2000**, *307*, 31–39.

(28) Sologub, O. L.; Salamakha, P. S.; Alleno, E.; Godart, C. *J. Magn. Magn. Mater.* **2001**, *226–230*, 170–172.

(29) Holleman, A. F.; Wiberg, E. *Inorganic Chemistry*; Academic Press: San Diego, 2001.

(30) Pauling, L. *The Nature of the Chemical Bond*, 3rd ed.; Cornell University Press: Ithaca, NY, 1960.

(31) Buschow, K. H. J.; Fast, J. F. *Phys. Stat. Sol.* **1967**, *21*, 593–600.

(32) Narasimhan, K. S. V. L.; Steinfink, H.; Ganapathy, E. V. *J. Appl. Phys.* **1969**, *40*, 51–54.

(33) Schobinger-Papamantellos, P.; Buschow, K. H. J. *J. Magn. Magn. Mater.* **1985**, *49*, 349–356.

(34) Joshi, D. A.; Thamizhavel, A.; Dhar, S. K. *Phys. Rev. B* **2009**, *79*, 014425-1–014425-7.

(35) Yakinthos, J. K.; Semitelou, I. P. *J. Magn. Magn. Mater.* **1983**, *36*, 136–140.

(36) Boulet, P.; Weitzer, F.; Hiebl, K.; Noël, H. *J. Alloys Compd.* **2001**, *315*, 75–81.

(37) Pinguet, N.; Weitzer, F.; Hiebl, K.; Schuster, J. C.; Noël, H. *J. Alloys Compd.* **2003**, *348*, 1–11.

Chapter 9

Conclusions

In this thesis, several new series of ternary rare-earth antimonides and germanides have been synthesized. Their major characteristics are summarized in Table 9–1. Exploration of these new polar ternary intermetallics offers us the opportunity to study their unique bonding character containing both homoatomic and heteroatomic bonding. In this chapter, we present some general observations regarding structures and bonding of antimonides and germanides. The presence of less electronegative rare-earth atoms, as well as transition-metal atoms capable of variable oxidation states, represents an intermediate situation between the extremes of Hume-Rothery phases and Zintl phases where bonding is challenging to rationalize. The limits of applicability of the Zintl-Klemm concept to these compounds have been addressed. Finally, we summarize some of the general physical properties displayed by these antimonides and germanides.

9.1. Structure and Bonding

The new ternary compounds synthesized in this thesis can be divided into two classes: (i) *RE*–*M*–(Ge, Sb) where one component is a d-block element (*M* = Ti, V, Cr) and (ii) *RE*–(Si, Ge)–Sb where two components are p-block elements. In both cases, electronegativity differences are less pronounced than in traditional

Table 9–1. Summary of the bonding characters of all compounds synthesized in this thesis.

Compound	Structure type	Homoatomic substructures		Heteroatomic geometry	Electron counting scheme	Properties	
$RE_2Ti_7Sb_{12}$	Own type	Disordered Sb fragments	2D Ti layers	$TiSb_6$ octahedra	$(La^{3+})_2(Ti^{2.8+})_7(Sb_{12})^{25.9-}$		
$RE_2Ti_{11-x}Sb_{14+x}$	Own type	1D linear, zig-zag chains, pairs	1D Ti linear chain	$TiSb_7$ pentagonal bipyramids $TiSb_6$ octahedra	$(RE^{3+})_2(Ti^{2.6+})_{11}(Sb^{2.5-})_{14}$	Metallic	
$RECrGe_3$	Hexagonal perovskite	Triangular Ge_3 cluster	1D Cr linear chains	$CrGe_6$ octahedra	$RE^{3+}Cr^{3+}(Ge^{2-})_3$	Metallic	FM
$REVGe_3$	Hexagonal perovskite	Triangular Ge_3 cluster	1D V linear chains	VGe_6 octahedra	$RE^{3+}V^{3+}(Ge^{2-})_3$		AFM
$RECr_xGe_2$	$CeNiSi_2$	1D zig-zag chains, 2D square sheets	None	$CrGe_5$ square pyramids	$RE^{3+}(Cr^{3+})_{0.33}(Ge^{2-})(Ge^{2-})$		AFM
$RE_5Ge_xSb_{3-x}$	β-Yb_5Sb_3	None	None	None	$(RE^{3+})_5(Ge^{4-})(Sb^{3-})_2(5e^-)$		FM
$RE_{12}Ge_{7-x}Sb_{21}$	Own type	Five-atom-wide Sb ribbons	Ge pairs	$GeSb_3$ trigonal planes $GeSb_5$ square pyramids	$(RE^{3+})_{12}[(GeSb_3)^{7-}]_2(Sb_5)^{7-}$ $(Ge_5Sb_{10})^{12-}(3e^-)$		AFM

Zintl phases, but the components play different roles in charge assignment and bonding. Whereas d-block elements tend to lose their valence electrons to form cations, a p-block metalloid element such as Si and Ge normally gains electrons to form anions. In this way, a rich variety of metalloid substructures can be formed adopting many remarkable bonding arrangements, such as Sb pairs, chains, and five-atom-wide ribbons; Ge pairs, trigonal planes, zigzag chains, and 2D square sheets; and 2D Ge/Sb layers. Despite these bonding similarities, Ge tends to adopt a higher coordination number than Sb, such as 5-coordinated square pyramidal $GeSb_5$ units, because of the higher valence of Ge.

The structures of $RE_2Ti_7Sb_{12}$ and $RE_2Ti_{11-x}Sb_{14+x}$, which contain the valence-electron-poor d-block element Ti, are characterized by many long Sb–Sb distances (Tables 2–5 and 3–4). In $RE_2Ti_7Sb_{12}$, there is considerable disorder (split sites, partial occupancies), making it difficult to identify localized Sb substructures. In contrast, in $RE_2Ti_{11-x}Sb_{14+x}$, there are readily identifiable 1D linear chains ($d_{(Sb4–Sb4)}$ = 2.86 Å), zig-zag chains ($d_{(Sb2–Sb2)}$ = 3.28 Å), and pairs ($d_{(Sb5–Sb8)}$ = 3.09 Å), all participating in hypervalent bonding. (The shorter distance of 2.86 Å observed is probably the result of a matrix effect, and may be considered to be a hypervalent bond.) Although both compounds are quite metal-rich, the metal components have transferred electrons to reduce some of the Sb atoms to form isolated Sb^{3-} units or not very extensive polyanionic substructures containing only weak Sb–Sb bonding. Despite the superficial similarity between Ge and Sb, which are related diagonally in the periodic table, the crystal structures of $REVGe_3$ and $RECrGe_3$ (hexagonal perovskite type) are different from those of $REVSb_3$ and $RECrSb_3$ ($CeCrSb_3$-type); nevertheless, both structure

types consist of chains of face-sharing $CrSb_6$ or $CrGe_6$ octahedra.[1] The *RE*VGe_3 and *RE*$CrGe_3$ compounds contain trigonal planar Ge_3 clusters, an unusual substructure not found in the binary Zintl phases A_xGe_y (Figure 1–8). In these clusters, the Ge–Ge distances of 2.5–2.6 Å correspond to typical single bonds. In the ternary *RE*Cr_xGe_2 compounds, extensive anionic Ge substructures are found in the form of 1D zigzag chains ($d_{(Ge–Ge)}$ = ~ 2.5–2.6 Å single bonds) and 2D square sheets ($d_{(Ge–Ge)}$ = ~ 2.8–2.9 Å hypervalent bonds). Both of these substructures are observed in the related compounds *M*Ge_2 (*M* = Zr, Hf) and $TmGe_2$, but the hypervalent bonds of 2.8–2.9 Å in the 2D square sheets are much longer than those in *M*Ge_2 ($d_{(Ge–Ge)}$ = 2.6–2.7 Å) and $TmGe_2$ ($d_{(Ge–Ge}$ = 2.78 Å), probably because of further reduction caused by introducing additional electrons from the transition-metal atoms.[2,3]

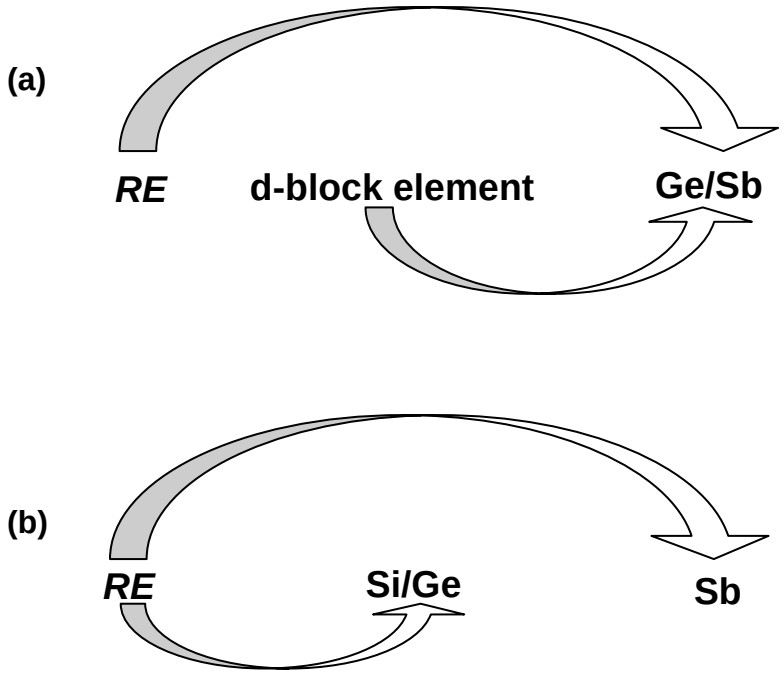

Figure 9–1. The electron transfers in (a) *RE*–(Ti, V, Cr)–(Ge, Sb) and (b) *RE*–(Si, Ge)–Sb compounds. The width and arrows indicates the magnitude and direction of electron transfer.

As shown in Figure 9–1, there are differences in the magnitude and direction of electron transfer between the *RE*–*M*–(Ge, Sb) and *RE*–(Si, Ge)–Sb compounds. In the compounds discussed above, *RE*–(Ti, V, Cr)–(Ge, Sb), the presence of electropositive d-block elements causes an additional transfer of electrons to the metalloid components, leading to their further reduction and thus the observation of isolated or low-dimensional polyanionic Ge or Sb substructures. In contrast, in compounds that contain a p-block element as the second component, *RE*–(Si, Ge)–Sb, the *RE* metal atoms are the only contributor of valence electrons which are then transferred to both metalloid atoms. This interesting bonding situation, especially for metalloids with similar electronegativities leads to a competition for the transferred valence electrons from the *RE* atoms, resulting in the formation of more complex substructures.[4] Thus, in $RE_{12}Ge_{7-x}Sb_{21}$, which integrates the bonding characteristics of $RE_6Ge_{5-x}Sb_{11+x}$[5] and $RE_{12}Ga_4Sb_{23}$,[6] there are five-atom-wide Sb ribbons, 2D kinked Ge/Sb sheets, and Ge pairs. Singly-bonded Ge–Ge pairs are quite common in Zintl phase binary compounds, such as AE_5Ge_3 (*M* = Ca, Ba, Sr) as well as in $RE_6Ge_{5-x}Sb_{11+x}$ although Ge is found to mix with Sb in this position. Of course, there is a limit to this complexity.[5,7–9] In the highly metal-rich compounds $RE_5Ge_xSb_{3-x}$, the many *RE* atoms provide more than enough electrons for the full reduction to isolated Ge^{4-} and Sb^{3-} units, with the remaining electrons participating in *RE*–*RE* bonding.

The homoatomic metal-metal bonding substructures are observed whenever there are extra electrons in the electropositive components. Thus, Ti–Ti

(1D linear chain, 2D layer), V–V (1D linear chain), Cr–Cr (1D linear chain) substructures are found in the compounds containing transition-metal components.

The occurrence of heteroatomic bonding should not be forgotten, of course. Indeed, in the transition-metal-containing compounds, the more conventional way to view their structures is to focus on these bonds (*M*–Ge or *M*–Sb) as we discussed in the previous chapters. Different *M*-centred polyhedra (MGe_n or MSb_n) are connected together to form an extended framework, resulting in large empty spaces that are filled by the *RE* atoms. No heteroatomic bonding occurs in $RE_5Tt_xSb_{3-x}$ where isolated Ge^{4-}/$Si^{4-}$and Sb^{3-} atoms are well separated by walls of *RE* atoms, but it does occur in $RE_{12}Ge_{7-x}Sb_{21}$ in the form of trigonal planar $GeSb_3$ and square pyramidal $GeSb_5$ units. In spite of the similarities between Ge and Sb, no mixing is found, which is distinct from the situation in the compound $RE_6Ge_{5-x}Sb_{11+x}$.[5]

9.2. Limits of the Zintl-Klemm Concept

The Zintl-Klemm concept provides a simple and efficient way to explain the structure and bonding of alkali or alkaline-earth metal antimonides and germanides with large electronegativity difference (Chapter 1). However, the assumption of complete electron transfer from the electropositive metals to electronegative metalloid atoms fails when the electronegativity difference is smaller, as in the case of rare-earth and transition metal compounds. Nevertheless, it serves as a good starting point to explain the presence of homoatomic bonding (*M*–*M*, Ge–Ge, or Sb–Sb bonding) based on the degree of the electron transfer, as has been applied successfully to $RE_2Ti_7Sb_{12}$, $RE_2Ti_{11-x}Sb_{14+x}$, $RECrGe_3$, $REVGe_3$,

RECr_xGe_2, and $RE_{12}Ge_{7-x}Sb_{21}$ (Table 9–1 and individual chapters). Despite these successes, there are limitations to the Zintl-Klemm concept.

First, the degree of electron transfer is already overestimated in attempts to explain the geometry of the substructures and the bonding in many polar intermetallics. The concept of complete transfer definitely becomes an unreasonable claim when less electropositive rare-earth or transition metals are present, e.g., $RE_{12}Ge_{7-x}Sb_{21}$ where the rare-earth atoms do not really transfer all 36 valence electrons to the anionic substructures. In addition, inconsistent with the presence of a band gap as would be predicted by full electron transfer and localized electrons in traditional Zintl phases, most of these polar intermetallic compounds exhibit metallic behaviour suggesting delocalized electrons, as shown by magnetic or electrical measurements. Although the definition has now been expanded to include the idea of "metallic Zintl phases", as long as the bonding substructures can be rationalized,[10] the idea of complete electron transfer is clearly invalid. For instance, the Zintl-Klemm formalism $La^{3+}Cr^{3+}(Ge^{2-})_3$ and $La^{3+}V^{3+}(Ge^{2-})_3$ accounts nicely for the occurrence of 2b-Ge_3 trigonal planar clusters. However, it still does not explain the depressed magnetic moments in $LaCrGe_3$ and Pauli paramagnetic behavior in $LaVGe_3$ if V^{3+} or Cr^{3+} is assigned.

Second, the Zintl-Klemm concept is not a predictive tool in the sense that it cannot determine the structure of an unknown compound in advance. It ignores the important role of the size of the cations, which are simply considered to be guests to fill empty space. In fact, the cations do influence the structure of a material, and the ratio between cations and anions is an important parameter to determine the final structure of a product. For instance, $BaGe_2$ ($BaSi_2$ type) and

$CaGe_2$ ($CaSi_2$ type) contain different Ge substructures: a tetragonal cluster in the former vs. a 2D brick-like layer in the latter (Table 1–2).[11,12] Similarly, Sb^- is present in both $CaSb_2$ and KSb, but in the form of different Sb substructures: a zig-zag chain in the former vs. a helical chain in the latter (Table 1–2).[13,14] Both examples cannot be explained solely by the Zintl-Klemm concept. A cationic size effect seems to be observed in $RE_2Ti_7Sb_{12}$ vs. $RE_2Ti_{11-x}Sb_{14+x}$, which are stabilized by different-sized *RE* components. It has also been seen that size effects, in the form of r_{Tt}/r_{RE} and r_M/r_{RE} ratios, may be important in influencing the different solubility ranges in $RE_5Tt_xSb_{3-x}$ ($x > 1$) and $RE_5M_xSb_{3-x}$ ($x < 1$).

9.3. Physical Properties

The electrical resistivities and magnetic properties of the synthetically available compounds have been measured. As mentioned in Chapter 1, resistivity measurements help us to test the validity of the proposed bonding schemes and to understand their electronic structures. Since the crystals obtained in most cases were not big enough, only $RECrGe_3$ and $RE_2Ti_{11-x}Sb_{14+x}$ samples have been measured. They exhibit metallic behaviour, implying that the electrons are delocalized, and not localized as would be expected by the traditional Zintl-Klemm concept.

Magnetic properties have been measured for compounds where a pure phase can be obtained. Due to the existence of unpaired f- or d-electrons, or both, these compounds exhibit interesting magnetic properties. The magnetic investigations help us to determine the oxidation states of magnetic centers, and also provide a way to identify the properties that might be useful in industrial applications.

The series of compounds *RE*$CrGe_3$ (*RE* = La–Nd, Sm) exhibit band ferromagnetic behaviour with relatively high T_C values ranging from 60 K to 155 K. Although on an absolute scale, these T_C values are still low (cf. 770°C for Fe), there may be potential for improvement through appropriate modifications. The conduction 3d electrons from the transition-metal component play an important role in influencing the magnetic interaction between 4f localized magnetic moments in these compounds. The isostructural *RE*VGe_3 compounds exhibit antiferromagnetic behaviour due to their changed electronic structure originating from the altered d-electrons in the V centres. The magnetic measurements on the quaternary variants $LaCr_{1-x}M_xGe_3$ (*M* = V, Mn) show that the Curie temperature is, unfortunately, depressed by V- or Mn-doping. The *RE*Cr_xGe_2 (*RE* = Sm, Gd–Er) compounds exhibit antiferromagnetic behaviour with low transition temperatures. This behaviour originates from the competition of possible *RE*–*RE* interactions within and between the double-layer slabs. With their low occupancy, the Cr atoms do not contribute to the total magnetic moment, but their delocalized 3d electrons do play an important role serving as the intermediary between the 4f moment coupling of the *RE* atoms, which are proved to be trivalent. Complicated magnetic behaviour with more than one transition temperature has been observed in $RE_5Tt_xSb_{3-x}$, where many short *RE*–*RE* distances are present. Analysis of the magnetic moments suggests that all *RE* atoms are trivalent. Weak antiferromagnetic coupling occurs in $Ce_{12}Ge_{7-x}Sb_{21}$ due to the presence of *RE* atoms within four face-sharing columns of trigonal prisms with *RE*–*RE* distances of ~ 4.3 Å. The observed magnetic moment is attributable to Ce^{3+}.

9.4. Future Directions

This work has uncovered a fruitful area of research in solid-state chemistry, raising the possibility for further investigations. It has been shown that cationic size is an important factor that influences the structure of a product. Therefore, it would be interesting to investigate the system of alkaline-earth titanium antimonides. Preliminary investigation of the Ba–Ti–Sb system has led to the discovery of a new compound $Ba_5Ti_{12}Sb_{19+x}$,[15] in which both cationic size and valence electron concentration might play important roles. More experiments can be envisioned involving the substitution of other alkaline-earth metals, such as Ca or Sr. The results of this thesis, combined with previous results as reviewed in Chapter 1, have shown the diversity of Ge and Sb substructures. But what about the neighbouring valence-electron-poor element Ga? The unique characters of multicentre bonding and polyhedral clusters are present in the Ga substructures, distinct from electron-rich Sb substructures.[10] It would be of great interest to investigate the *RE*–(Ti, V, Cr)–Ga system to identify new types of Ga substructures. In addition, the magnetic measurements described in this thesis have been made on powder samples. Magnetic anisotropy would be expected because of the low-dimensional *RE* arrangements, and further neutron diffraction is required to understand their magnetic structures in greater detail.

9.5. References

(1) a) Ferguson, M. J.; Hushagen, R. W.; Mar, A. *J. Alloys Comp.* **1997**, *249(1-2)*, 191–198; b) Brylak, M.; Jeitschko, W. *Z. Naturforsch., B*: *Chem. Sci.* **1995**, *50(6)*, 899–904.

(2) Smith, J. F.; Bailey, D. M. *Acta Crystallogr.* **1957**, *10*, 341–342.

(3) Tobash, P. H.; Meyers, J. J.; DiFilippo, G.; Bobev, S.; Ronning, F.; Thompson, J. D.; Sarrao, J. L. *Chem. Mater.* **2008**, *20*, 2151–2159.

(4) Mills, A. M.; Lam, R.; Ferguson, M. J.; Deakin, L.; Mar, A. *Coord. Chem. Rev.* **2002**, *233–234*, 207–222.

(5) Lam, R.; McDonald, R.; Mar, A. *Inorg. Chem.* **2001**, *40*, 952–959.

(6) Mills, A. M.; Mar, A. *Inorg. Chem.* **2000**, *39*, 4599–4607.

(7) Eisenmann, B.; Schäfer, H. *Z. Naturforsch., B*: *Anorg. Chem. Org. Chem.* **1974**, *29 (7-8)*, 460–463.

(8) Nesper, R.; Zürcher, F. *Z. Kristallogr. – New Cryst. Struct.* **1999**, *214(1)*, 22.

(9) Nesper, R.; Zürcher, F. *Z. Kristallogr. – New Cryst. Struct.* **1999**, *214(1)*, 21.

(10) Kauzlarich, S. M., Ed. *Chemistry, Structure and Bonding of Zintl Phases and Ions*; VCH Publishers: New York, 1996.

(11) Vaughey, J. T.; Miller, G. J.; Gravelle, S.; Leon-Escamilla, E. A.; Corbett, J. D. *J. Solid State Chem.* **1997**, *133*, 501–507.

(12) Tobash, P. H.; Bobev, S. *J. Solid State Chem.* **2007**, *180*, 1575–1581.

(13) Deller, K.; Eisenmann, B. *Z. Anorg. Allg. Chem.* **1976**, *425(2)*, 104–108.

(14) Hönle, W.; von Schnering, H. G. *Z. Kristallogr.* **1981**, *155*, 307–314.

(15) Bie, H.; Mar, A. 92nd Canadian Chemistry Conference and Exhibition, Hamilton, Ontario, Canada, May 30–June 3, 2009.

Appendix 1

Supplementary data for Chapter 4

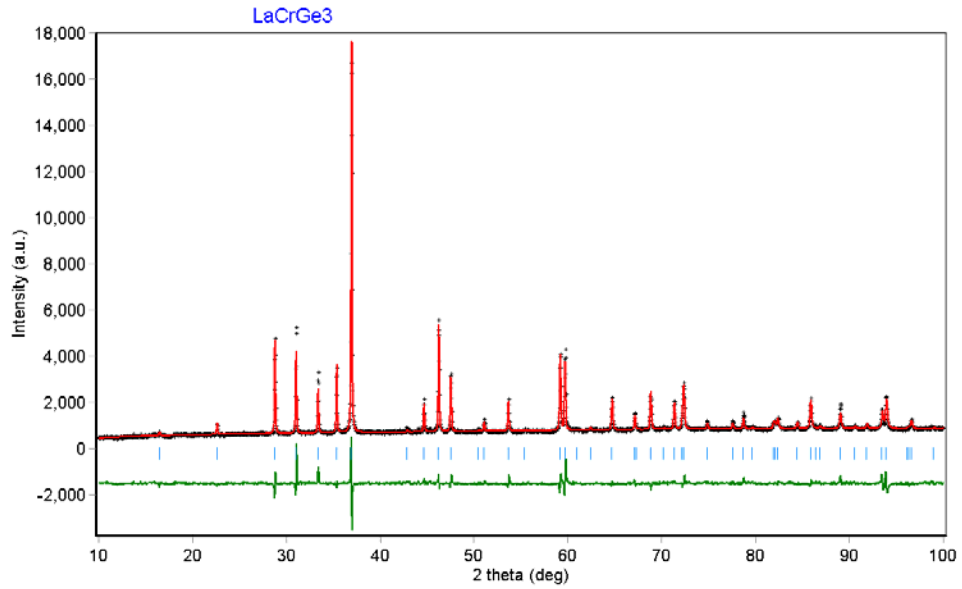

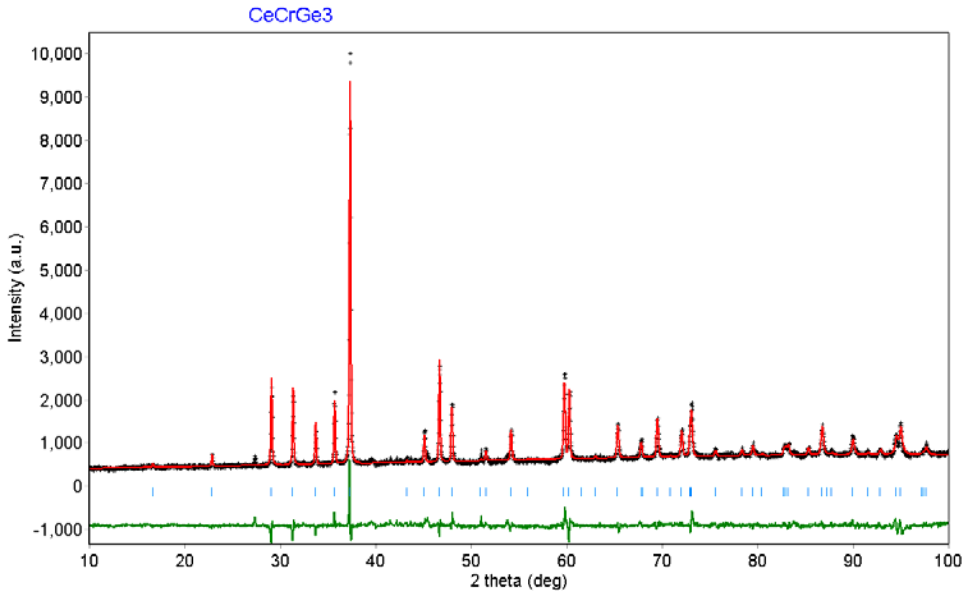

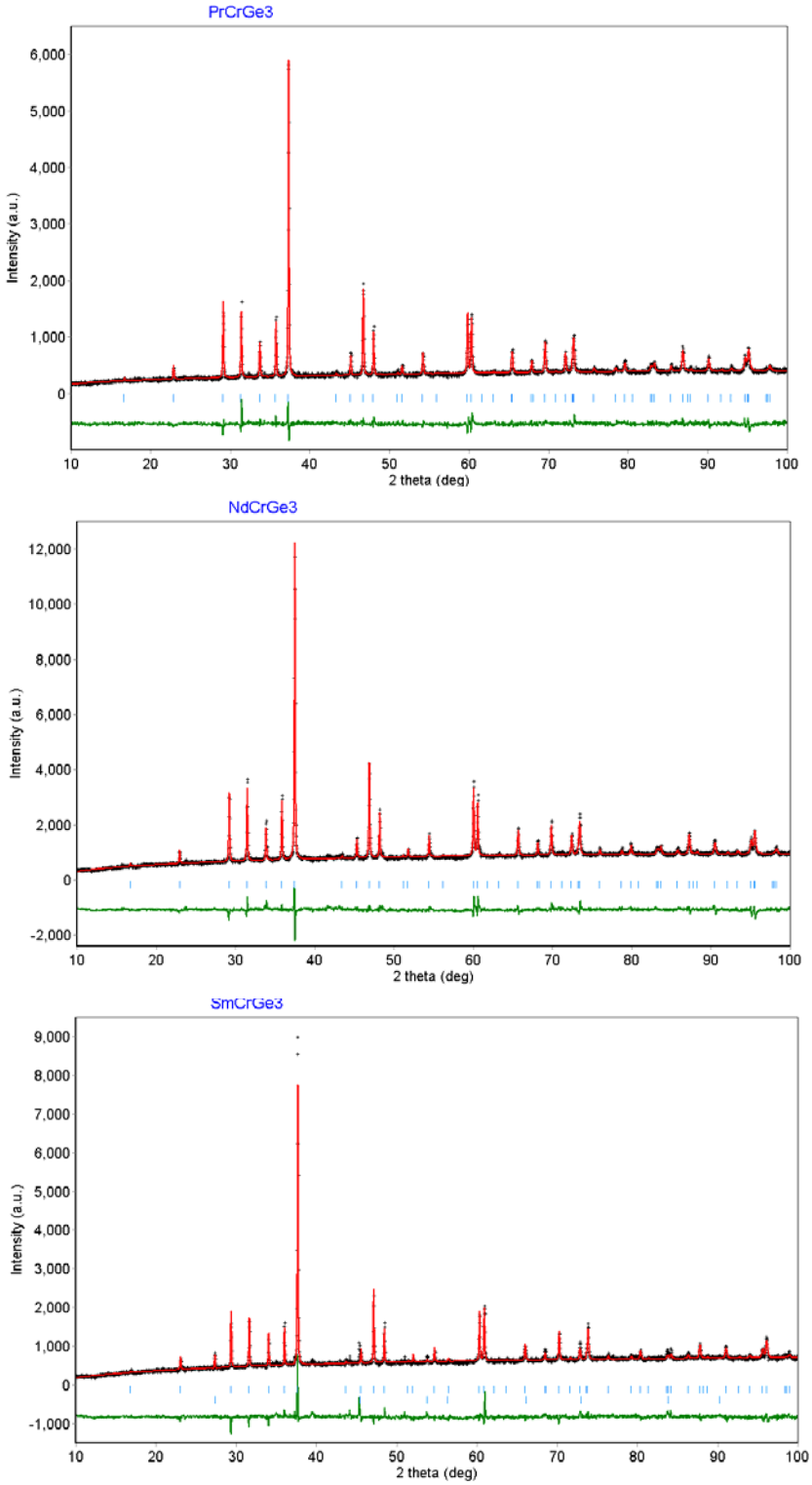

Figure A1–1. Rietveld refinement results for *RE*$CrGe_3$ (*RE* = La–Nd, Sm). The observed profile is indicated by black crosses and the calculated profile by the solid red line. Bragg peak positions are located by the vertical blue tick marks. The difference plot is shown at the bottom.

Table A1–1. Crystallographic data for *RE*$CrGe_3$ (*RE* = La–Nd, Sm) from Rietveld refinements on arc-melted samples.

Compound	*a* (Å)	*c* (Å)	*V* (Å^3)	R_P	R_{wp}	R_B	ρ_{calcd} (g cm^{-3})
$LaCrGe_3$	6.1901(3)	5.7546(3)	190.96(2)	4.97	7.37	3.69	7.104
$CeCrGe_3$	6.1390(5)	5.7063(5)	186.24(3)	4.72	6.42	4.60	7.306
$PrCrGe_3$	6.1291(4)	5.6939(4)	185.24(2)	5.03	6.53	2.94	7.359
$NdCrGe_3$	6.1116(3)	5.6817(3)	183.79(2)	4.13	5.46	2.85	7.478
$SmCrGe_3$	6.0812(3)	5.6594 (3)	181.25(2)	4.60	6.47	5.04	7.694

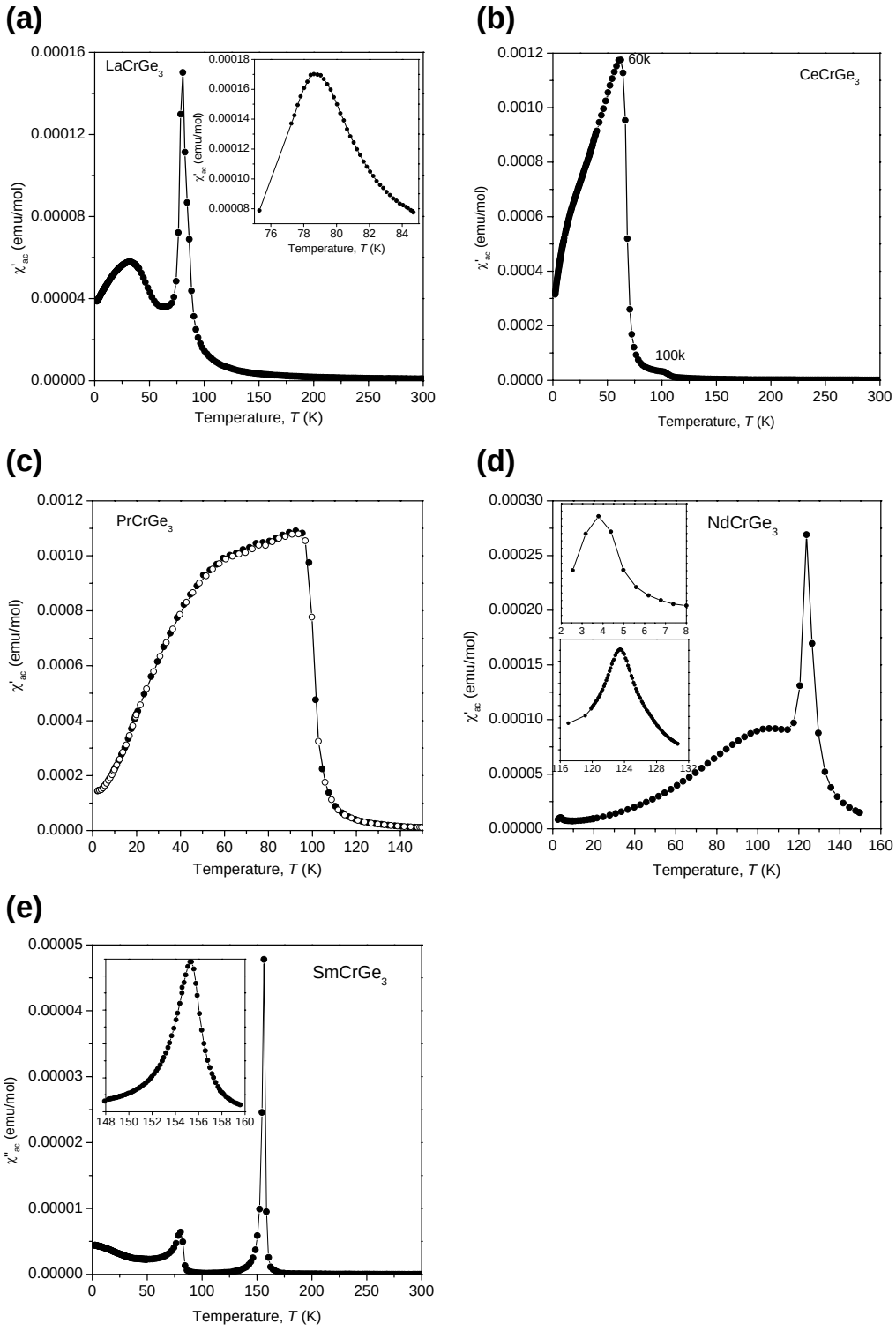

Figure A1–2. Plots of ac magnetic susceptibility for *RE*$CrGe_3$ (*RE* = La–Nd, Sm).

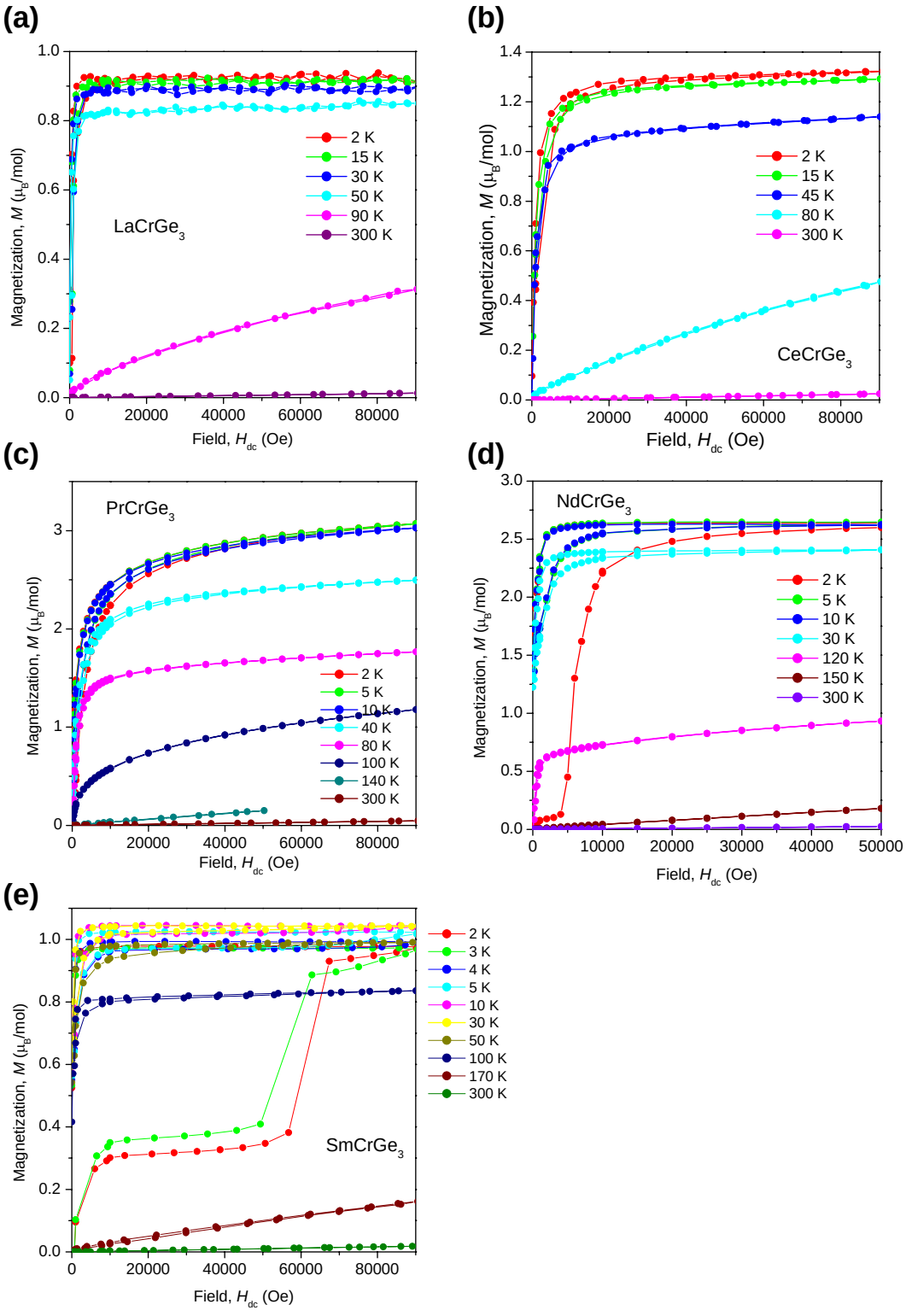

Figure A1–3. Plots of isothermal magnetization for *RE*CrGe$_3$ (*RE* = La–Nd, Sm).

Appendix 2

Supplementary data for chapter 7

Table A2–1. Crystallographic data for $Pr_{12}Ge_{6.48(1)}Sb_{21}$ refined in space group *Imm2*.

Formula	$Pr_{12}Ge_7Sb_{21}$
Formula mass (amu)	4755.80
Space group	*Imm2* (No. 44)
a (Å)	4.2578(2)
b (Å)	33.938(2)
c (Å)	14.9777(7)
V (Å^3)	2164.3(2)
Z	2
ρ_{calcd} (g cm^{-1})	7.240
Crystal dimensions	0.28×0.10×0.04
μ (Mo Kα) (mm^{-1})	30.46
Transmission factors	0.036–0.325
2θ limits	4.52°–66.32°
Data collected	$-6 \le h \le 6$, $-50 \le k \le 51$, $-23 \le l \le 23$,
No. of data collected	15015
No. of unique data, including $F_o^2<0$	4570 (R_{int} = 0.036)
No. of unique data, with $F_o^2>2\sigma(F_o^2)$	3880
No. of variables	130
$R(F)$ for $F_o^2>2\sigma(F_o^2)$ [a]	0.028
$R_w(F_o^2)$ [b]	0.066
Goodness of fit	1.081
$(\Delta\rho)_{max}$, $(\Delta\rho)_{min}$ (eÅ^{-3})	4.31, –3.38

[a] $R(F) = \sum \| |F_o| - |F_c| \| / \sum |F_o|$;

[b] $R_w(F_o^2) = \left[\Sigma \left[w(F_o^2 - F_c^2)^2 \right] / \Sigma w F_o^4 \right]^{1/2}$; $w^{-1} = \left[\sigma^2(F_o^2) + (Ap)^2 + Bp \right]$ where $p = \left[\max(F_o^2, 0) + 2F_c^2 \right] / 3$.

Table A2–2. Atomic coordinates and equivalent isotropic thermal displacement parameters (Å^2) for $Pr_{12}Ge_{6.48(1)}Sb_{21}$ refined in space group *Imm2*.

Atom	Wyckoff position	occupancy	*x*	*y*	*z*	U_{eq} [a]
Pr1	4*d*		0	0.20515(1)	0.50031(11)	0.00803(9)
Pr2	4*d*		0	0.31637(4)	0.35691(6)	0.0086(2)
Pr3	4*d*		0	0.31640(3)	0.64318(6)	0.0083(2)
Pr4	4*d*		0	0.42609(1)	0.4999(1)	0.00897(7)
Pr5	4*d*		0	0.42654(4)	0.21268(6)	0.0092(2)
Pr6	4*d*		0	0.42657(4)	0.78737(6)	0.0093(2)
Sb1	4*d*		0	0.10917(4)	0.14911(9)	0.0112(2)
Sb2	4*d*		0	0.10930(4)	0.85063(9)	0.0109(2)
Sb3	4*d*		0	0.22383(1)	–0.0005(1)	0.01050(9)
Sb4	4*d*		0	0.22417(4)	0.28471(7)	0.0093(3)
Sb5	4*d*		0	0.22425(4)	0.71554(7)	0.0084(3)
Sb6	4*d*		0	0.33679(4)	0.13710(7)	0.0087(2)
Sb7	4*d*		0	0.33684(4)	0.86238(8)	0.0088(2)
Sb8	4*d*		0	0.44506(2)	0.00001(1)	0.0149(1)
Sb9	2*b*		0	½	0.3531(1)	0.0212(4)
Sb10	2*b*		0	½	0.6479(1)	0.0194(4)
Sb11	2*a*		0	0	–0.0001(2)	0.0097(1)
Sb12	2*a*		0	0	0.2983(1)	0.0126(4)
Sb13	2*a*		0	0	0.7016(1)	0.0122(4)
Ge1	4*d*		0	0.11339(7)	0.4167(1)	0.0131(4)
Ge2	4*d*		0	0.11334(7)	0.5851(1)	0.0085(4)
Ge3	4*d*	0.738(5)	0	0.14739(4)	0.0001(3)	0.0484(7)
Ge4	2*a*		0	0	0.4783(1)	0.0239(4)

[a] U_{eq} is defined as one-third of the trace of the orthogonalized U_{ij} tensor.

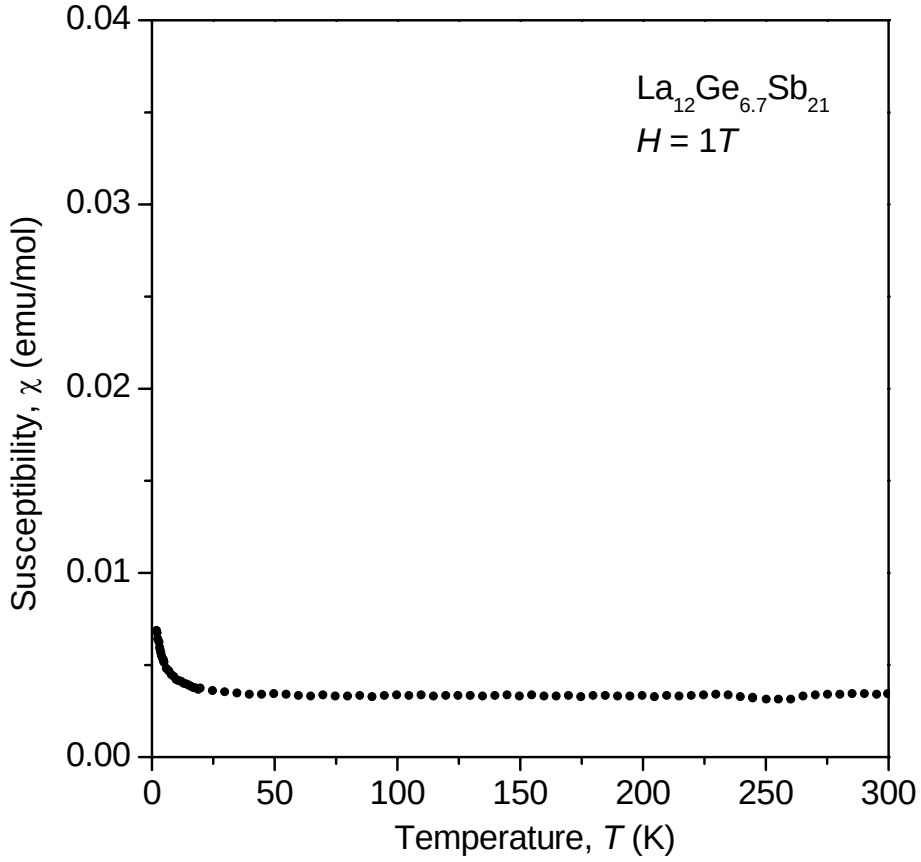

Figure A2–1. Molar magnetic susceptibility for $La_{12}Ge_{6.7}Sb_{21}$ in an applied field of 1 T.

Appendix 3

Supplementary data for chapter 8

Table A3–1. Synthesis and cell parameters of $La_5Ge_xSb_{3-x}$ phases.[a]

Loading composition	Phases obtained	*a* (Å)	*b* (Å)	*c* (Å)	*V* (Å^3)
$La_5Ge_{0.5}Sb_{2.5}$	$La_5Ge_xSb_{3-x}$, La_5Sb_3, La_4Sb_3	12.7132(6)	9.5768(5)	8.4007(4)	1022.7(1)
$La_5Ge_{0.6}Sb_{2.4}$	$La_5Ge_xSb_{3-x}$, La_5Sb_3, La_4Sb_3	12.7136(6)	9.5732(4)	8.4057(5)	1023.0(1)
$La_5Ge_{0.7}Sb_{2.3}$	$La_5Ge_xSb_{3-x}$, La_5Sb_3, La_4Sb_3	12.7282(6)	9.5788(6)	8.4039(4)	1024.6(1)
$La_5Ge_{0.8}Sb_{2.2}$	$La_5Ge_xSb_{3-x}$, La_5Sb_3, La_4Sb_3	12.7213(4)	9.5718(4)	8.4053(3)	1023.5(1)
$La_5Ge_{0.9}Sb_{2.1}$	$La_5Ge_xSb_{3-x}$, trace La_4Sb_3	12.7562(6)	9.5668(4)	8.4104(3)	1026.4(1)
$La_5Ge_{1.0}Sb_{2.0}$	$La_5Ge_xSb_{3-x}$	12.7362(4)	9.5278(3)	8.3866(3)	1017.7(1)
$La_5Ge_{1.2}Sb_{1.8}$	$La_5Ge_xSb_{3-x}$	12.7085(6)	9.4896(6)	8.3602(4)	1008.2(1)
$La_5Ge_{1.3}Sb_{1.7}$	$La_5Ge_xSb_{3-x}$	12.7024(7)	9.4963(6)	8.3702(5)	1009.7(1)
$La_5Ge_{1.6}Sb_{1.4}$	$La_5Ge_xSb_{3-x}$	12.6733(7)	9.4554(7)	8.3384(5)	999.2(1)
$La_5Ge_{1.7}Sb_{1.3}$	$La_5Ge_xSb_{3-x}$, La_4Ge_3	12.6794(6)	9.4473(6)	8.3419(4)	999.2(1)
$La_5Ge_{1.8}Sb_{1.2}$	$La_5Ge_xSb_{3-x}$, La_4Ge_3	12.6798(6)	9.4464(5)	8.3473(4)	999.8(1)
$La_5Ge_{1.9}Sb_{1.1}$	$La_5Ge_xSb_{3-x}$, La_4Ge_3	12.6650(5)	9.4440(5)	8.3317(4)	996.5(1)

[a] Syntheses were performed by arc-melting of the component elements with the indicated loading compositions, followed by annealing at 800 °C. Cell parameters of $La_5Ge_xSb_{3-x}$ phases were obtained by Rietveld refinement of powder X-ray diffraction patterns.

Table A3–2. Interatomic distances (Å) in $RE_5Tt_xSb_{3-x}$ (*RE* = La–Nd; *Tt* = Si, Ge).

	$La_5Si_{1.40(2)}Sb_{1.60(2)}$	$Ce_5Si_{1.4}Sb_{1.6}$	$Pr_5Si_{1.20(3)}Sb_{1.800(8)}$	$Nd_5Si_{1.2}Sb_{1.8}$
*RE*1–*Tt*2	2.984(2)	2.951(9)	2.948(1)	2.90(1)
*RE*1–*Tt*2	3.127(3)	3.11(2)	3.069(2)	3.18(3)
*RE*1–Sb1	3.462(1)	3.423(4)	3.394(1)	3.354(6)
*RE*1–Sb1	3.492(1)	3.439(5)	3.453(1)	3.415(7)
*RE*1–Sb1	3.604(1)	3.539(5)	3.536(1)	3.509(7)
*RE*1–*RE*2	3.564(1)	3.470(5)	3.528(1)	3.466(7)
*RE*1–*RE*2	3.642(1)	3.614(4)	3.609(1)	3.603(6)
*RE*1–*RE*1	3.692(1)	3.645(1)	3.585(1)	3.612(9)
*RE*1–*RE*4	3.786(1)	3.756(1)	3.730(1)	3.700(8)
*RE*1–*RE*1	3.955(1)	3.938(1)	3.892(1)	3.849(9)
*RE*1–*RE*4	3.989(1)	3.923(1)	3.902(1)	3.850(8)
*RE*1–*RE*3	3.997(1)	4.005(3)	3.932(1)	3.936(8)
*RE*2–*Tt*2	3.277(4)	3.27(2)	3.188(3)	3.08(3)
*RE*2–Sb1 (×2)	3.292(1)	3.302(9)	3.245(1)	3.276(9)
*RE*2–Sb1 (×2)	3.304(1)	3.236(9)	3.251(1)	3.168(9)
*RE*2–*RE*1 (×2)	3.564(1)	3.470(5)	3.528(1)	3.466(7)
*RE*2–*RE*1 (×2)	3.642(1)	3.614(4)	3.609(1)	3.603(6)
*RE*2–*RE*3	3.711(1)	3.741(8)	3.624(1)	3.72(1)
*RE*2–*RE*3	3.778(1)	3.668(9)	3.691(1)	3.56(1)
*RE*2–*RE*4	3.992(1)	3.964(9)	3.902(1)	3.96(1)
*RE*3–*Tt*2	2.986(3)	3.01(3)	2.938(3)	3.00(3)
*RE*3–Sb1 (×2)	3.316(1)	3.270(6)	3.263(1)	3.224(8)
*RE*3–Sb1 (×2)	3.331(1)	3.284(7)	3.289(1)	3.273(8)
*RE*3–*RE*2	3.711(1)	3.741(8)	3.624(1)	3.72(1)
*RE*3–*RE*2	3.778(1)	3.668(9)	3.691(1)	3.56(1)
*RE*3–*RE*1 (×2)	3.997(1)	4.005(3)	3.932(1)	3.936(8)
*RE*4–*Tt*2	2.972(3)	2.92(3)	2.918(3)	2.91(3)
*RE*4–Sb1 (×2)	3.328(1)	3.280(6)	3.284(1)	3.242(7)
*RE*4–Sb1 (×2)	3.373(1)	3.343(6)	3.329(1)	3.337(9)
*RE*4–*RE*1 (×2)	3.786(1)	3.756(1)	3.730(1)	3.700(8)
*RE*4–*RE*2	3.992(1)	3.964(9)	3.902(1)	3.96(1)
*RE*4–*RE*1 (×2)	3.989(1)	3.923(1)	3.902(1)	3.850(8)
Sb1–*RE*2	3.292(1)	3.302(9)	3.245(1)	3.276(9)
Sb1–*RE*2	3.304(1)	3.236(9)	3.251(1)	3.168(9)
Sb1–*RE*3	3.316(1)	3.270(6)	3.263(1)	3.224(8)
Sb1–*RE*4	3.328(1)	3.280(6)	3.284(1)	3.242(7)
Sb1–*RE*3	3.331(1)	3.284(7)	3.289(1)	3.273(8)
Sb1–*RE*4	3.373(1)	3.343(6)	3.329(1)	3.337(9)
Sb1–*RE*1	3.462(1)	3.423(4)	3.394(1)	3.354(6)
Sb1–*RE*1	3.492(1)	3.439(5)	3.453(1)	3.415(7)
Sb1–*RE*1	3.604(1)	3.539(5)	3.536(1)	3.509(7)
*Tt*2–*RE*4	2.972(3)	2.92(3)	2.918(3)	2.91(3)
*Tt*2–*RE*1 (×2)	2.984(2)	2.951(9)	2.948(1)	2.90(3)
*Tt*2–*RE*3	2.986(3)	3.01(3)	2.938(1)	3.00(3)
*Tt*2–*RE*1 (×2)	3.127(3)	3.11(2)	3.069(2)	3.18(3)
*Tt*2–*RE*2	3.277(4)	3.27(2)	3.188(3)	3.08(3)

	$La_5Ge_{1.32(6)}Sb_{1.68(4)}$	$Ce_5Ge_{0.9}Sb_{2.1}$	$Pr_5Ge_{1.68(6)}Sb_{1.32(4)}$	$Nd_5Ge_{1.14(6)}Sb_{1.86(4)}$
*RE*1–*Tt*2	2.990(1)	2.980(5)	2.946(1)	2.942(1)
*RE*1–*Tt*2	3.165(1)	3.19(1)	3.101(1)	3.088(1)
*RE*1–Sb1	3.472(1)	3.456(5)	3.376(2)	3.370(1)
*RE*1–Sb1	3.476(1)	3.434(6)	3.372(1)	3.428(1)
*RE*1–Sb1	3.609(1)	3.517(6)	3.550(1)	3.532(1)
*RE*1–*RE*2	3.523(1)	3.417(7)	3.456(1)	3.497(1)
*RE*1–*RE*2	3.678(1)	3.680(5)	3.617(1)	3.632(1)
*RE*1–*RE*1	3.731(1)	3.719(1)	3.645(2)	3.583(1)
*RE*1–*RE*4	3.760(1)	3.701(3)	3.636(1)	3.682(1)
*RE*1–*RE*1	3.934(2)	3.907(1)	3.834(2)	3.851(1)
*RE*1–*RE*4	3.987(1)	3.936(1)	3.898(1)	3.873(1)
*RE*1–*RE*3	4.030(1)	4.062(7)	3.962(1)	3.940(1)
*RE*2–*Tt*2	3.292(2)	3.25(2)	3.193(2)	3.164(1)
*RE*2–Sb1 (×2)	3.296(1)	3.25(1)	3.216(1)	3.227(1)
*RE*2–Sb1 (×2)	3.308(1)	3.29(1)	3.230(1)	3.232(1)
*RE*2–*RE*1 (×2)	3.523(1)	3.417(7)	3.456(1)	3.497(1)
*RE*2–*RE*1 (×2)	3.678(1)	3.680(5)	3.617(1)	3.632(1)
*RE*2–*RE*3	3.740(1)	3.74(1)	3.627(1)	3.612(1)
*RE*2–*RE*3	3.775(2)	3.70(1)	3.665(2)	3.657(1)
*RE*2–*RE*4	3.976(1)	3.90(1)	3.879(1)	3.864(1)
*RE*3–*Tt*2	3.034(2)	3.04(1)	3.004(2)	2.965(1)
*RE*3–Sb1 (×2)	3.316(1)	3.335(9)	3.242(1)	3.247(1)
*RE*3–Sb1 (×2)	3.341(1)	3.263(9)	3.267(1)	3.284(1)
*RE*3–*RE*2	3.740(1)	3.74(1)	3.627(1)	3.612(1)
*RE*3–*RE*2	3.775(2)	3.70(1)	3.665(2)	3.657(1)
*RE*3–*RE*1 (×2)	4.030(1)	4.062(7)	3.962(1)	3.940(1)
*RE*4–*Tt*2	2.988(1)	3.02(1)	2.940(2)	2.924(1)
*RE*4–Sb1 (×2)	3.334(1)	3.292(8)	3.257(1)	3.273(1)
*RE*4–Sb1 (×2)	3.378(1)	3.364(8)	3.310(1)	3.321(1)
*RE*4–*RE*1 (×2)	3.760(1)	3.701(3)	3.636(1)	3.682(1)
*RE*4–*RE*2	3.976(1)	3.90(1)	3.879(1)	3.864(1)
*RE*4–*RE*1 (×2)	3.987(1)	3.936(1)	3.898(1)	3.873(1)
Sb1–*RE*2	3.296(1)	3.25(1)	3.216(1)	3.227(1)
Sb1–*RE*2	3.308(1)	3.29(1)	3.230(1)	3.232(1)
Sb1–*RE*3	3.316(1)	3.335(9)	3.242(1)	3.247(1)
Sb1–*RE*4	3.334(1)	3.292(8)	3.257(1)	3.273(1)
Sb1–*RE*3	3.341(1)	3.263(9)	3.267(1)	3.284(1)
Sb1–*RE*4	3.378(1)	3.364(8)	3.310(1)	3.321(1)
Sb1–*RE*1	3.471(1)	3.456(5)	3.376(2)	3.370(1)
Sb1–*RE*1	3.476(1)	3.434(6)	3.372(1)	3.428(1)
Sb1–*RE*1	3.609(1)	3.517(6)	3.550(1)	3.532(1)
*Tt*2–*RE*4	2.988(1)	3.02(1)	2.940(2)	2.924(1)
*Tt*2–*RE*1 (×2)	2.999(1)	2.980(5)	2.946(1)	2.942(1)
*Tt*2–*RE*3	3.034(2)	3.04(1)	3.004(2)	2.965(1)
*Tt*2–*RE*1 (×2)	3.165(1)	3.19(1)	3.101(1)	3.088(1)
*Tt*2–*RE*2	3.292(2)	3.25(2)	3.193(2)	3.164(1)

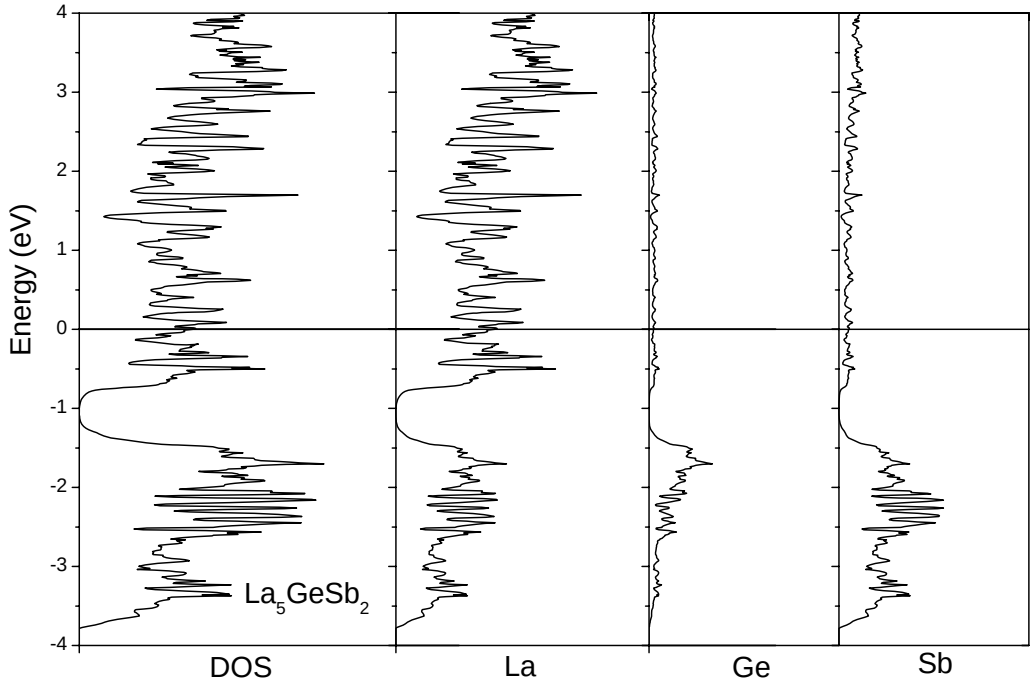

Figure A3–1. Density of states (DOS) and its La, Ge, and Sb projections for La_5GeSb_2, with La 4f orbitals being downfolded. The horizontal line at 0 eV marks the Fermi level.

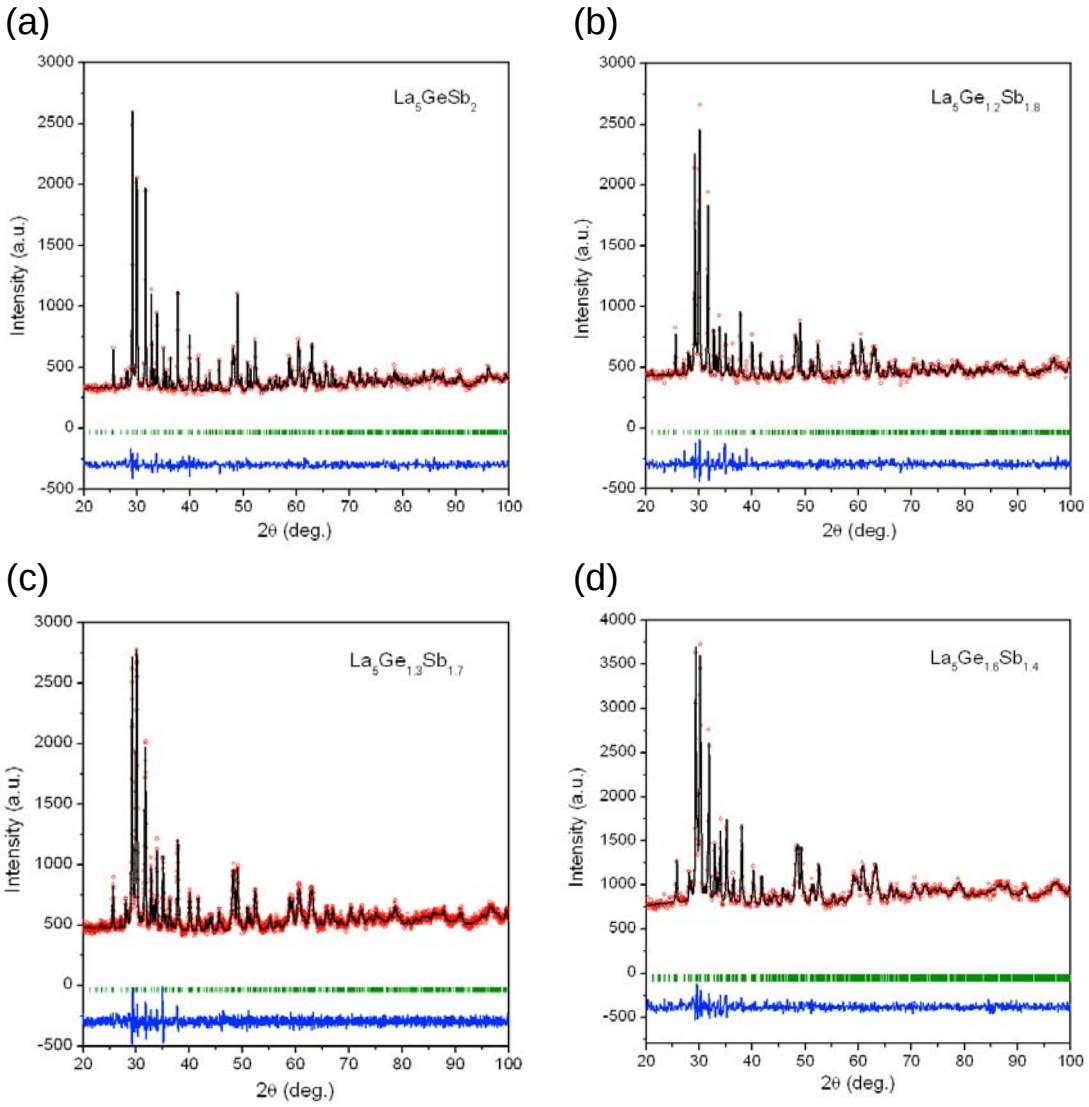

Figure A3–2. Rietveld refinement results for pure samples of $La_5Ge_xSb_{3-x}$, with x = (a) 1.0, (b) 1.2, (c) 1.3, and (d) 1.6. The observed profile is indicated by circles and the calculated profile by the solid line. Bragg peak positions are located by the vertical tick marks. The difference plot is shown at the bottom.

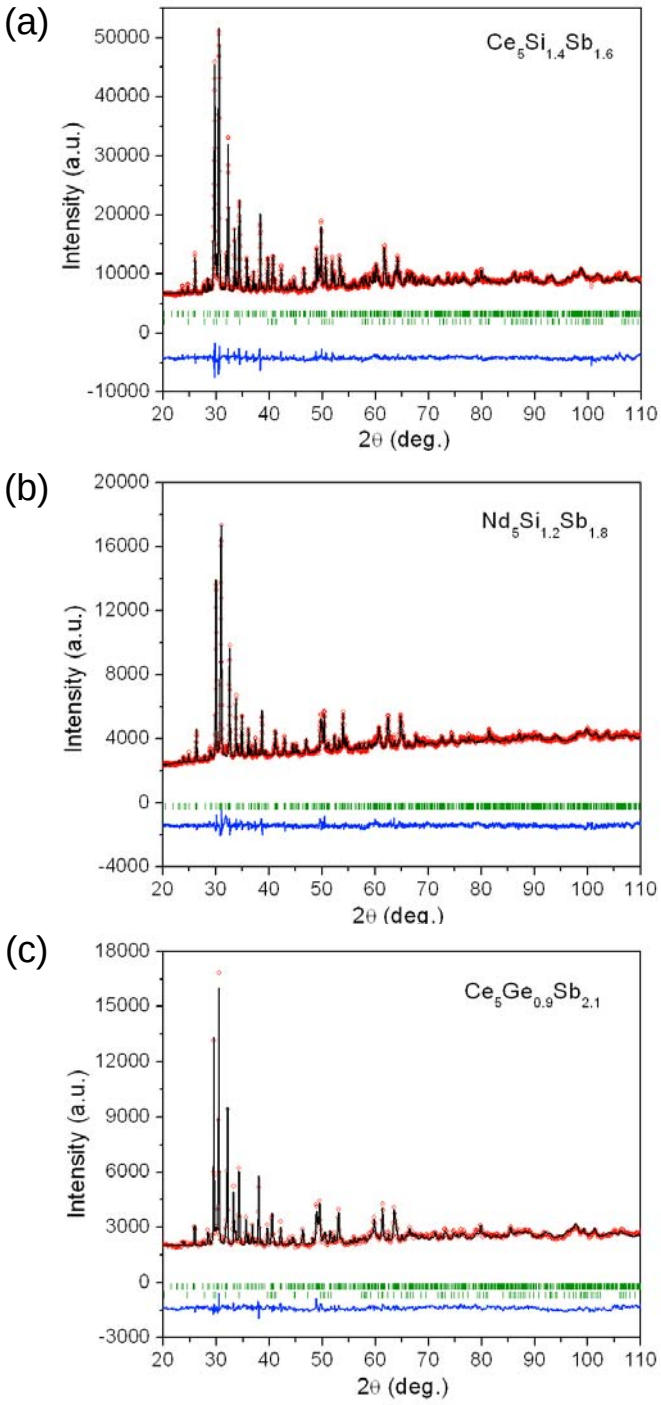

Figure A3–3. Rietveld refinement results for (a) $Ce_5Si_{1.4}Sb_{1.6}$, (b) $Nd_5Si_{1.2}Sb_{1.8}$, and (c) $Ce_5Ge_{0.9}Sb_{2.1}$. The observed profile is indicated by circles and the calculated profile by the solid line. Bragg peak positions are located by the vertical tick marks. The difference plot is shown at the bottom. Trace amounts of Ce_2Sb are also present in (a) and (c).

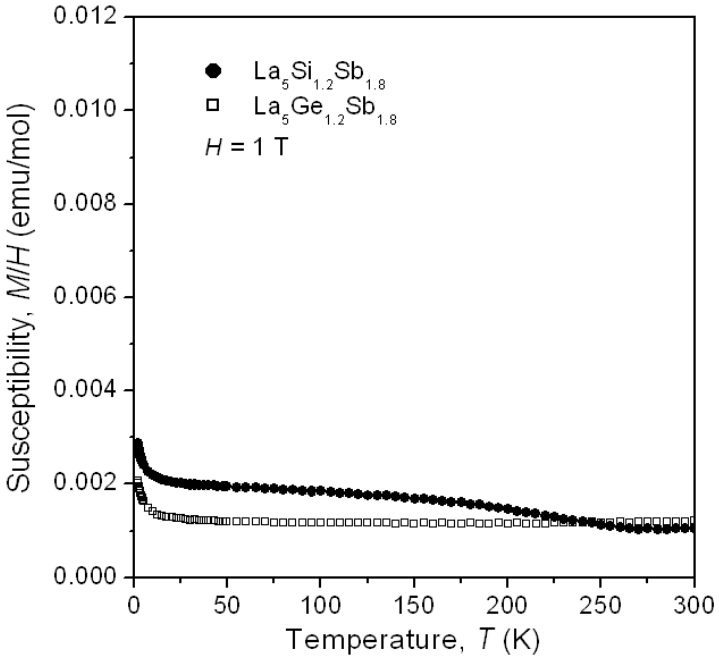

Figure A3–4. Molar magnetic susceptibility for $La_5Si_{1.2}Sb_{1.8}$ and $La_5Ge_{1.2}Sb_{1.8}$ in an applied field of 1 *T*.